Geometrical Optimisation of Receivers for Concentrating Solar Thermal Systems

Charles-Alexis Asselineau

A thesis submitted for the degree of
Doctor of Philosophy
The Australian National University

November 2017

Except where otherwise indicated, this thesis is my own original work.

Charles-Alexis Asselineau

10 November 2017

Acknowledgements

I would like to thank:

- Dr. John Pye for giving me the opportunity to conduct my doctoral research in the topic I wished to study and for always having his door open for discussions.
- Dr. Joe Coventry for the support and constructive discussions as well as the engineering insights throughout the research.
- Prof. Wojciech Lipinski and the whole Solar Thermal Group, past and present, at the Australian National University for the positive work atmosphere during these years of research.
- The Australian REnewable ENergy Agency (ARENA), and the former Australian Solar Institute (ASI) for funding the research in concentrated solar power that made my PhD work a reality through the "USASEC Cavity receiver performance improvement project" project and the Australian Solar Thermal Research Initiative (ASTRI).
- Dr. Clifford Ho for welcoming me as a visiting scholar at the National Solar Thermal Test Facility at Sandia National Laboratories in Albuquerque, New Mexico.
- Dr. Sylvie Thiebaux from Data61 and Prof. Hussein Abbas from the University of New South Wales Canberra campus for helpful discussions and insights into the confusing world of optimisation research.

Abstract

In concentrated solar thermal technologies, the receiver converts concentrated solar radiation into high-temperature heat. Solar receivers are commonly simulated with a stochastic integration method: Monte-Carlo ray-tracing. The optimisation of the geometry of receivers is challenging when using existing optimisation methods for two reasons: each receiver evaluation using Monte-Carlo ray-tracing requires significant computational effort and the outcome of a simulation involves uncertainty.

A series of novel optimisation techniques are proposed to enable gradient-free, stochastic and multi-objective optimisation adapted to such problems. These techniques address the computational load difficulty and the challenge of conducting stochastic optimisation based on uncertain evaluations by introducing the concepts of “Progressive Monte-Carlo Evaluation (PMCE)”, “Intermediate Ray Emission Source (IRES)” and adaptive view-factor calculation. A new “Multi-Objective and Evolutionary PMCE Optimisation (MOE-PMCE-O)” method is then built around PMCE to enable multi-objective geometrical optimisation of receivers.

PMCE is shown to be able to reduce the computational time of a random search optimisation by more than 90% and is used in the geometrical design of a new receiver for the Australian National University SG4 dish concentrator that achieved 97.1% (±2.2%) of thermal efficiency during on-sun testing. MOE-PMCE-O is applied to a multi-objective tower receiver problem where liquid sodium is used as the receiver heat-carrier in a surround configuration heliostat field. A series of useful geometrical concepts emerge from the results, with geometrical features able to maintain high efficiency while keeping acceptable incident peak flux values with a moderate receiver total mass.

Finally, a more fundamental look at the impact of the interaction of concentrating optics on the exergy of radiation available at the receiver location highlights the major role played by concentrator surface slope error in lowering the exergy in concentrated solar thermal systems and quantifies the exergy loss associated with non-ideal match between flux and surface temperature in receivers.

List of publications

(a) C.-A. Asselineau and J. Pye. Exergetic efficiency of point focus concentrators under realistic angular radiation distributions. In *Proceedings of the APSRC 2015*, 2015.

(b) C.-A. Asselineau, E. Abbasi and J. Pye. Open cavity receiver geometry influence on radiative losses. In Solar2014, editor, *Proceedings of Solar2014, 52nd Annual Conference of the Australian Solar Energy Society*. Melbourne, May 2014.

(c) C.-A. Asselineau, J. Zapata and J. Pye. Integration of Monte-Carlo ray tracing with a stochastic optimisation method: application to the design of solar receiver geometry. *Optics Express*, 23 (11): A437–A443, 2015. doi: 10.1364/OE.23.00A437.

(d) C.-A. Asselineau, J. Zapata and J. Pye. Geometrical Shape Optimization of a Cavity Receiver Using Coupled Radiative and Hydrodynamic Modeling. *Energy Procedia*, 69: 279 – 288, 2015. ISSN 1876-6102. doi: 10.1016/j.egypro.2015.03.032. SolarPACES 2014.

(e) C.-A. Asselineau, C. Corsi, J. Coventry and J. Pye. Geometrical exploration of a flux-optimised sodium receiver through multi-objective optimisation. In *Proceedings of SolarPACES 2016*, Abu Dhabi, UAE, 2016.

(f) C.-A. Asselineau, J. Pye and J. Coventry. Multi-objective method for receiver design optimization using n-dimensional stochastic pareto front detection. In *ASME 2016 Power & Energy conference*, Charlotte, USA, June 2016.

(g) J. Coventry, M. Arjomandi, C. Asselineau, A. Chinnici, C. Corsi, D. Davis, J. Kim, A. Kumar, W. Lipinski, W. Logie, G. Nathan, J. Pye and W. Saw. Development of ASTRI high-temperature solar receivers. In *Proceedings of SolarPACES 2016*, 2016.

(h) W. Logie, C.-A. Asselineau, J. Pye and J. Coventry. Temperature and heat flux distributions in sodium receiver tubes. In *Proceedings of the APSRC 2015*, 2015.

(i) W. Logie, C.-A. Asselineau, J. Pye and J. Coventry. Thermal stress in sodium receiver tubes. In *Proceedings of SolarPACES 2016*, Abu Dhabi, UAE, 2016.

(j) J. Pye, G. Hughes, J. Zapata, C.-A. Asselineau, J. Coventry, E. Abbasi, M. Kaufer and F. Venn. Improved tubular receivers for point-focus concentrators. In *Light, Energy and the Environment*, page RW3B.4. Optical Society of America, 2014. doi: 10.1364/OSE.2014.RW3B.4.

(k) J. Pye, M. Zheng, J. Zapata, C.-A. Asselineau and J. Coventry. An exergy analysis of tubular solar-thermal receivers with different working fluids. In *Proceedings of SolarPACES 2014*, Beijing, China, 2014.

(l) J. Pye, G. Hughes, E. Abbasi, C.-A. Asselineau, G. Burgess, J. Coventry, W. Logie, F. Venn and J. Zapata. Development of a higher-efficiency tubular cavity receiver for direct steam generation on a dish concentrator. In *Proceedings of SolarPACES 2015*, Cape Town, South Africa, 2015.

(m) J. Pye, J. Coventry, F. Venn, J. Zapata, E. Abbasi, C.-A. Asselineau, G. Burgess, G. Hughes and W. Logie. Experimental testing of a high-flux cavity receiver. In *Proceedings of SolarPACES 2016*, Abu Dhabi, UAE, 2016.

(n) Y. Wang, C.-A. Asselineau, J. Coventry and J. Pye. Optical performance of bladed receivers for csp systems. In *Proceedings of ASME Power & Engineering 2016*, 2016. doi: 10.1115/ES2016-59693.

(o) J. Zapata, C.-A. Asselineau, J. Pye, M. Kaufer and G. Hughes. An integrated optical and thermal model of cavity receivers for paraboloidal dish concentrators. In *Proceedings of the APSRC 2014*, 2014.

Contents

List of Figures

List of Tables

Nomenclature

Variables, Latin:

$\mathbf{r}$	Vector in three dimensional space	[m]
L	Length	[m]
r	Radius	[m]
A	Area	[m^2]
V	Volume	[m^3]
n	Refractive index	[1]
q, Q	Energy	[J]
I	Radiative intensity	[$W.sr.m^{-1}$]
H	Irradiance	[$W.m^{-2}$]
G	Solar direct normal irradiance	[$W.m^{-2}$]
E	Emittance	[$W.m^{-2}$]
C	Optical concentration	[1]
C_g	Geometrical concentration	[1]
T	Temperature	[K]
p	Pressure	[Pa]
h	Specific enthalpy	[$J.kg^{-1}.K^{-1}$]
H	Enthalpy	[$J.K^{-1}$]
m	Mass	[kg]
v	Velocity	[$m.s^{-1}$]
k	Thermal conductivity	[$W.m^{-1}.K^{-1}$]
Cp	Heat capacity	[$J.kg^{-1}.K^{-1}$]
u	Convective heat transfer coefficient	[$W.m^{-2}.K^{-1}$]
$\Re$	Uniform random variate belonging to the interval $[0,1]$	[1]
S	Entropy	[$J.K^{-1}$]

J	Radiosity	[W.m^{-2}]
ℓ	Flow-path variable	[m]

Variables, Greek:

θ, φ	Angles	[rad]
ω	Solid angle	[sr]
λ	Wavelength	[m^{-1}]
ρ	Density	[kg.m^{-3}]
ν	Kinematic viscosity	[m^2.s^{-1}]
μ	Dynamic viscosity	[Pa.s]
β	Thermal expansion coefficient	[K^{-1}]
α_d	Thermal diffusivity	[m^2.s^{-1}]
χ	Circumsolar ratio	[1]
γ	Exergy to energy ratio	[1]

Variable modification:

$\lvert x \rvert$	Absolute value of x
$\lVert \mathbf{x} \rVert$	Norm of the vector **x**
$\lfloor x \rfloor$	floor rounded value of x
$\lceil x \rceil$	ceiling rounded value of x
$\bar{x}$	Average value of x
$\hat{x}$	Normalised value of x
$\dot{x}$	Time derivation of x
x'	Derivation of x by one dimension of space
x''	Derivation of x by two dimensions of space
Δx	Difference in the value of x

Set notations:

$p = \{x\}$	Set p containing the object x

$\lvert p \rvert$	Cardinal of the set p
$\cup$	Set union operator
$\setminus$	Set difference operator
$\mathbb{R}$	Real numbers set
$P(x)$	Cumulative distribution function (CDF) of the variable x

Constants:

c	Speed of light in vacuum	$c = 299,792,458$ m.s^{-1}
h_P	Plank constant	$h_P = 6.6261 \times 10^{-34}$ J.s
k_B	Boltzmann constant	$k_B = 1.3807 \times 10^{-23}$ J.K^{-4}
σ	Stefan-Boltzmann constant	$\sigma = 5.67 \times 10^{-8}$ W.m^{-2}.K^{-4}
g	Earth gravitational acceleration approximation	$g \approx 9.81$ m.s^{-2}

1 Introduction and motivations

In this introduction chapter, the fundamental aspects of Concentrated Solar Power technologies are presented and a review of research around receiver design and optimisation is carried out. The literature references present in this chapter are meant to offer an overview of the state-of-the art as of the start of 2015.

1.1 CSP collectors

1.1.1 Collector fundamentals

CSP collectors optically concentrate direct normal irradiance (DNI) which is the fraction of solar radiation that is reaching the surface of the Earth without being absorbed or deviated in the atmosphere. CSP systems are typically classified according to the type of collector they use. The first distinction is made between line or point focus optics. Line focus optical concentrators track the sun rotating on a single axis and reflect solar radiation onto a line while point focus concentrator track the sun in two dimensions and focus solar radiation on a point. The ideal line focus concentrator is the cylindro-parabolic concentrator also named "parabolic trough" and the ideal point focus concentrator is a paraboloid of revolution also named "parabolic dish" (Figure 1-1).

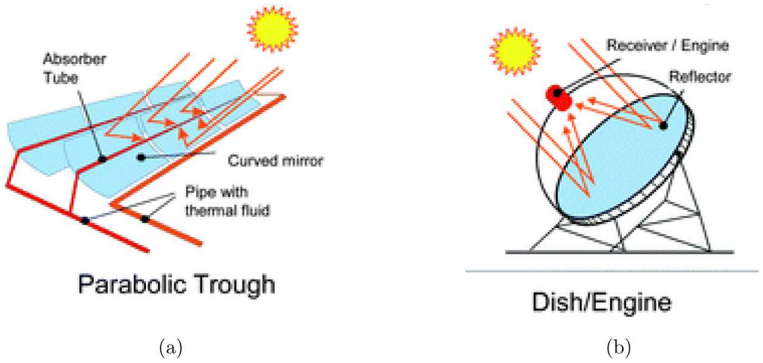

Figure 1-1: (a) Parabolic trough and (b) parabolic dish concentrator schematics [127].

For a wide range of technical and economical reasons, the ideal concentrator profile is not always desirable and alternative versions of the ideal parabolic concentrators have been developed. Inspired from Fresnel optical discretisation, the ideal parabolic shapes are sectioned into segments that are dropped on the same plane and independently actuated to track the sun. The results of this transformation are the Linear Fresnel Reflector (LFR), which is an approximation of the parabolic trough concentrator, and the heliostat field, which is an approximation of the ideal point focus concentrator (Figure 1-2).

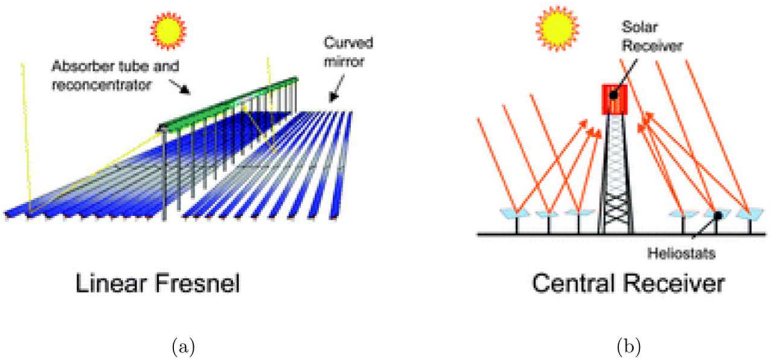

Figure 1-2: Schematics of: (a) Linear Fresnel reflector, Fresnel approximation of the parabolic trough and (b) heliostat field concentrator, Fresnel approximation of the parabolic dish [127].

Point focus concentrators can reach higher concentration levels than line focus concentrators [92]. The concentration provided by a CSP collector is usually quantified in "suns" which corresponds to a multiplier of the received DNI. Two definitions of concentration are commonly used, whether they consider the geometry of the concentrator or local values at the focus, and are presented in details in Chapter 2. The temperature of operation and the efficiency of the CSP system depend on the level of concentration at the focus of the concentrator [92, 124]. While the methods developed in the present research are applicable to any type of CSP system, this research work addresses point focus concentrators because of their potential to achieve higher concentrations and therefore efficiencies.

The potential of high concentration motivated the first research efforts at the ANU on dish concentrators [75]. The ANU possesses significant expertise in parabolic dish design and operation with approximately 40 years of research on the topic that led to the construction and operation of the largest parabolic dish concentrator in the world [93]. The recent rise of heliostat field based CSP systems, often called Central Receiver Systems (CRS), at the commercial scale on the global market is another illustration of the technological shift towards higher concentrations. Heliostat fields are expected to replace parabolic trough technologies as the leading commercial CSP application in the coming years.

1.1.2 Collector optical loss mechanisms

Several optical energy loss mechanisms impact the performance of concentrators. Part of the solar radiation intercepted by the optics reaches the collector surfaces while the remaining part intersects objects that do not participate in the concentration process and casts shade on the concentrator. This process is known as shading and is important because it influences the layout of collectors in a field. In some systems, shading is caused by the receiver itself and can therefore be associated to receiver design. As explained in Chapter 2, shading can be considered as a concentrator energy loss if the system definition is based on the land area occupied.

The non-shaded radiative flux coming from the sun to the reflective surfaces of the concentrator is reflected towards the receiver or blocked on its way and lost. This process is known as blockage can impact significantly the distribution of irradiance at the receiver depending on the sun position in the sky. A detail description of the concentrator loss mechanisms can be found in Chapter 2.

The position of the sun in the sky changes throughout the day and impacts the efficiency of solar concentrators. Dish concentrators are relatively independent to this effect as they point directly at the sun during the whole day. Heliostat fields' optical performance depends strongly on the position of the sun in the sky. In general, heliostat fields perform best at solar noon and have gradually less efficiency as the sun position deviates from solar noon [144].

1.2 CSP Receivers

1.2.1 Receiver fundamentals

Receivers convert concentrated radiation into another form of energy. Two major types of receivers exist depending on their function in the CSP system:

- Receiver-reactors: a thermochemical reaction is performed in the volume of the receiver and heat is converted into chemical energy [80, 127].
- Thermal receivers: heat is transported out of the receiver volume by a Heat (or thermal energy) Carrier (HC) and no chemical reaction is performed. This heat is usually converted to work and subsequently to electricity in a thermodynamic engine.

Alternative ways to convert concentrated radiation into useful work exist. Concentrated PhotoVolatics (CPV) use small multiple-junctions photovoltaic cells to convert radiation into electricity through photoelectric conversion and are relatively well developed with a few commercial plants in operations. On a more exploratory level, Thermo-PhotoVoltaics (TPV) use an intermediate emitter to modify the spectrum of the incoming sunlight through absorption and thermal emission to an array of specifically designed photovoltaic cells tuned to the emitted spectrum. Photo-Enhanced Thermionic Emissions (PETE) alternatively seeks to produce electrical current through radiation and thermionic emissions combined. Thermionic emission is the extraction of charge carriers from a hot electrode under the effect of thermal excitation.

1.2.2 Receiver energy loss mechanisms

The work developed in this doctoral thesis focuses on thermal receivers. A simplified thermal receiver operation diagram is presented in Figure 1-3.

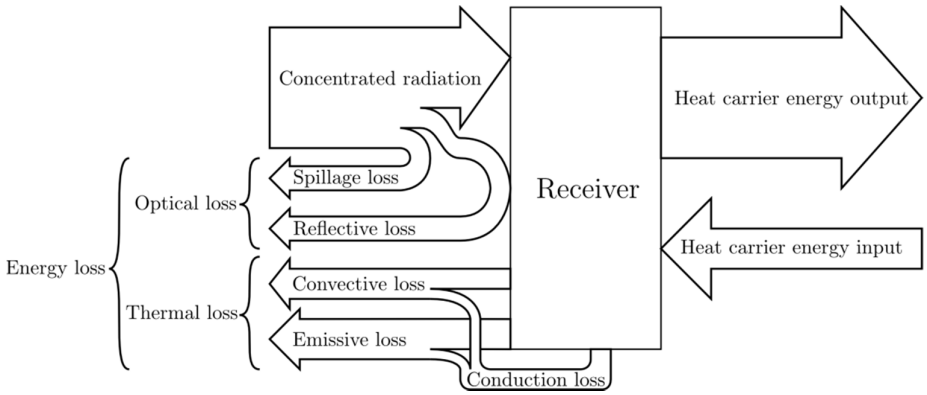

Figure 1-3: Receiver energy flow diagram scheme.

From the concentrated radiation incident on the receiver only a fraction is transferred to the heat carrier (HC) flowing in the receiver and the remaining part is lost to the environment through four main energy loss mechanisms:

- The spillage loss: After being reflected by the concentrator, a fraction of the non-blocked radiation may miss the receiver completely and be lost. This loss mechanism is often considered as a concentrator loss but is a function of the capacity of the receiver to intercept most of the incoming radiation and is associated with the receiver. Spillage loss is illustrated on a commercial Aora receiver in .
- The reflective losses: the fraction that is reflected and not absorbed by the receiver because receiver surfaces are not perfect absorbers.
- The emissive losses: the fraction that is emitted to the surroundings due to the Stefan-Boltzmann law and not absorbed again by the receiver surface.
- The convective losses: the fraction that transferred to the surrounding air through convective heat transfer with the external surface of the tubes.

The term optical loss is used to refer to the combination of spillage and reflective loss which are mostly independent of the temperature of the receiver. Thermal loss refers to the combination of emissive and convective loss. In addition, it is common to refer to conductive losses for the loss of energy from the receiver through the rest of the supporting structure by heat conduction. Conductive losses are ultimately lost to the surroundings through convective heat transfer with the surrounding air and radiative emissions. The thermal energy loss is a function of the temperature distribution in the receiver.

The relative importance of each of the loss mechanisms is shown in Figure 1-4 for an illustrative surface element taking into account standard values for the parameters considered [29].

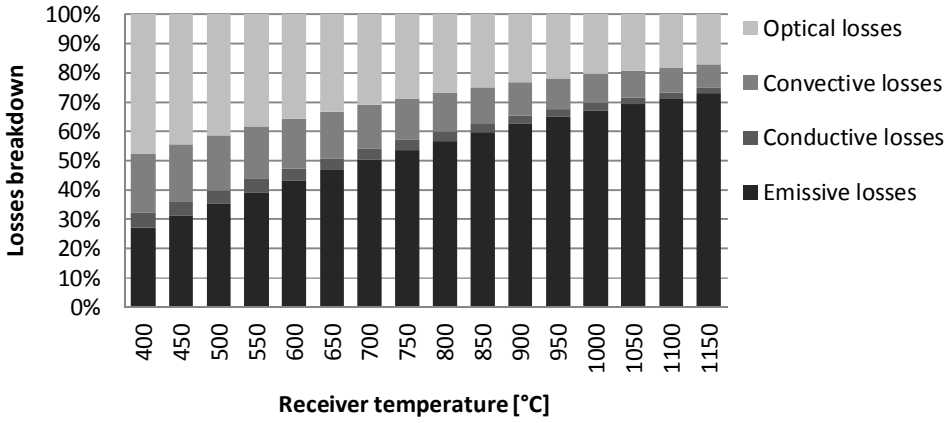

Figure 1-4: Losses breakdown for a reference flat receiver surface element. Assumptions: emissivity is 0.9, receiver optical efficiency is 0.95, insulation thickness is 1 m, thermal conductivity of the insulation is 5 $W.m^{-1}.K^{-1}$, convective loss coefficient is 20 $Wm^{-2}.K^{-1}$, heat transfer coefficient from the irradiated wall to the heat transfer fluid is 500 $W.m^{-2}.K^{-1}$, temperature of the surroundings I 300 K.

With increased surface temperature, the relative importance of thermal emission loss increases significantly. Mitigation of thermal emissions has a dominating role in improving the performance of high-temperature receivers.

The temperature at the outlet of the receiver sets the hot source temperature of the thermodynamic energy conversion as stated by the Carnot principle. The higher the temperature of the HC at the outlet of the receiver, the better the efficiency of the conversion of heat into work. On the other side, increasing the temperature of the HC requires a higher temperature in the receiver and therefore higher thermal losses. A trade-off between thermally driven loss mechanisms and thermodynamic efficiency of the system appears [34, 133] and an optimal temperature of conversion can be determined for any isothermal receiver, as shown in Figure 1-5, for a black-body surface.

The advantage of using highly concentrated flux appears clearly in Figure 1-5 where higher concentration can lead to significantly higher efficiencies. The optimal theoretical receiver temperature for a given highly concentrated flux can be high; economical and practical factors relating to materials and HCs with suitable thermal stability also have to be considered. In a more realistic model, the combined impact of all mechanisms on the efficiency needs to be taken into account to assess a more realistic upper bound on the amount of work that can be produced by the system.

Temperatures over 900 °C are a challenge on the material side. The need for high temperatures has motivated some research in secondary concentrators that provide a second stage of optical concentration between the concentrator and the receiver. There are theoretical limitations to what secondary optics can achieve [24] and their practicality for large scale systems has not been demonstrated. Systems without secondary concentrators are in

fact already capable of reaching concentration levels over 2000 suns without secondary optics [131].

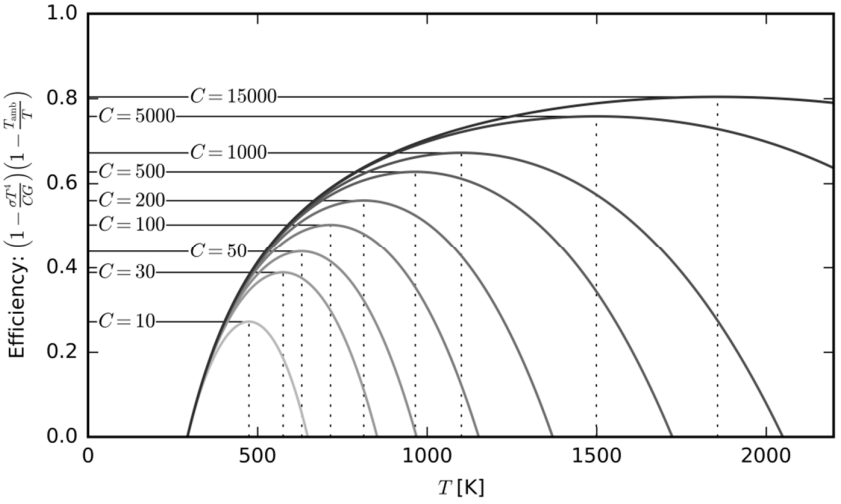

Figure 1-5: Efficiency of the conversion of radiation into work by a black-body surface as a function of the surface temperature and for several optical concentration levels with the irradiance G = 1000 W.m^{-2} and the ambient temperature T_{amb} = 20 °C.

The concentration levels at the receiver directly depend on the optics and solar radiation conditions and therefore the amount of work that can be produced by a system is also impacted by the optical concentration process. Exergy is the fraction of an energy quantity that can be converted into work. For energy in the form of heat, exergy is related to energy through the Carnot efficiency; when the energy is in the form of radiation, the relationship between exergy and energy is different and has been independently established by different researchers [85, 114, 117]. Radiative intensity, unlike heat, is a function of the propagation direction and so is the exergy of radiation. The impact of the direction of propagation of radiation on radiation exergy has been studied for simple configurations involving isotropic radiation or uniform angular distribution [58, 72, 85, 110, 114, 153]. Landsberg and Badescu [83] suggested a geometrical factor to take into account the geometrical property of the radiation source and quantified the exergy of radiation coming from a specific solar radiation angular distribution. The evaluation of the maximum amount of work that can eb extracted from solar radiation has been recently reviewed [3, 8, 87, 94, 155] however, no effort was spent on understanding the influence of the concentration process on solar radiation exergy, a topic which is not addressed in the literature.

1.2.3 Photo-thermal interface

Many point-focus receiver concepts have been proposed in the literature with the objective to minimise the receiver energy losses and consequently improve the performance of the CSP system [61]. A first distinction that can be made between all proposed concepts is

between directly and indirectly irradiated receivers. For directly irradiated receivers, concentrated solar radiation is absorbed by the HC itself while for indirectly irradiated receivers, an intermediate medium; the absorber, absorbs it and transfers it to the HC as heat.

For indirectly irradiated receivers a physical barrier exists between the HC and the environment, which has the advantage of allowing better control of the conditions of the absorption of concentrated radiation because of a fixed and engineered geometry of the absorber. All commercial applications of CSP technologies have used indirectly irradiated receivers up to now. This choice is also motivated by historical reasons: receivers were first, and still generally are, considered as 'inside-out' boilers and have been manufactured and designed using boiler engineering knowledge that led to simple absorber geometries (generally a bank of tubes). However, a major limitation of indirectly irradiated receivers is the thermo-mechanical limitations of the containment material.

Directly irradiated receivers have the potential to reach higher energy efficiencies by removing the absorber and the associated heat transfer resistance from the system. Key challenges are reliably containing and controlling the flow of the HC and the heat transfer conditions. When specific conditions, such as a specific chemical composition in the receiver volume, are desired in directly irradiated receivers it is common to use a transparent window through which radiation is transmitted to the absorption medium. This solution, useful for lab-scale and small experiments, tends to be avoided in larger systems due to the fragility of those windows [76, 98]. Directly irradiated receivers have mostly been used in laboratories, at the very small scale, to study high-temperature thermochemical reactions. Below is a list of research projects currently working on demonstration-scale prototypes:

- CSIRO Newcastle as part of the Australian Solar Thermal Research Initiative (ASTRI) is investigating directly irradiated stage falling particle receivers.
- Sandia National Laboratories currently has a program developing a directly irradiated falling particle receiver [138].
- San Diego State University is working on a directly irradiated Small Particle Heat Exchange Receiver (SPHER) as part of the Sunshot initiative [43].
- Laboratory scale experiments have been conducted on directly irradiated reactive materials at ETH Zurich in Switzerland [60] and Niigata University in Japan [2].
- The Solar Expanded Vortex Receiver is a directly irradiated receiver where small particles are circulated using a vortex flow and is under development at the University of Adelaide in Australia [27].

- The King Saud University in Ryadh, Saudi Arabia, is investigating directly irradiated obstructed flow falling particle curtains [88].
- A rotating drum particle receiver developed by the German aerospace agency DLR is at the prototype scale testing in Jülich, Germany [156].

1.2.4 Heat carriers

Heat carriers in solid, liquid and gas phases have been suggested and tested for CSP applications [14]. Considering the heat carrier role in a CSP system, it shoucl qualitatively have the following characteristics:

- Good thermal conductivity properties to extract and release heat efficiently.
- High heat capacity to limit the mass flow needed to carry the heat out of the receiver volume.
- Chemical stability at high temperatures to be able to use higher efficiency thermodynamic cycles.
- The lowest possible corrosive behaviour with common containment materials, particularly metals.
- Can be easily transported and circulated.
- Be relatively cheap.

In addition, if the HC is used as a directly irradiated medium, it needs to have a high absorptivity in the concentrated sunlight wavelengths and as low as possible emissions in the wavelengths corresponding to thermal emissions. This combination of radiative characteristics is usually labeled spectral selectivity and improves the performance of the receiver. Table 1-1 presents the temperature of operations for commercial HCs.

Table 1-1: Temperature of operation limits for commercial CSP systems heat carriers [14].

Heat carrier		Temperature range [°C]
Water/steam		0–550
Thermal oil	Therminol VP-1	12–400
Molten salts	HITEC	140–530
	HITEC XL	130–550
	Solar salt	260-600

Commercial linear concentrator systems operate at lower temperatures due to the lower concentration levels and traditionally use thermal oil as their heat carrier. The relatively

low density and heat capacity of thermal oils makes them less attractive than molten salts for energy storage. This limitation has motivated research towards using molten salts in linear concentration systems.

State-of–the-art heliostat field based systems use higher temperature HCs: molten salts (Solar Reserve Tonopah plant, Torresol Energy Gemasolar plant) or water/steam (Brightsource Ivanpah plant). The heat transfer properties of water are very good in the boiling region and make it a viable option, however, when water turns into superheated steam, the heat transfer coefficients to the receiver surfaces drop significantly making it a much less efficient HC. High-temperature steam tends to become corrosive which poses problems for the pipes. Molten salt eutectic mixtures have very good heat capacities and are progressively becoming the standard for CSP as both a HC and a thermal storage material. Molten salts suffer from two disadvantages:

- Their relatively high melting temperature requires the use of “heat-tracing”, a network of resistive heating tape running on all the HC circulation ducts of the system to prevent solidification of the salt when the whole system cools down at night time or during transient cut-off of the solar radiation due to clouds.
- They start to decompose at ~550 °C which is limiting the performance of CRS plants which would otherwise be able to reach higher temperature of operation [14].

The development of new molten salts mixtures with lower solidification temperature and stable to higher temperature is an active area of research [142]. Higher efficiency CSP systems will need HCs able to reach higher temperatures. Demonstrated and promising HC options include:

- Inert solid particles used in a falling particle curtain directly exposed to radiation or as a fluidised medium [39, 61]. The advantages are high heat capacities and high-temperature thermal stability.
- Air as a compressed fluid in a tubular receiver or in volumetric receiver concepts [6].
- Liquid metals and among them liquid sodium [30, 131] which is stable at higher temperatures than commercial HCs and has unmatched heat transfer properties provided by a very high thermal conductivity.

1.2.5 Receiver geometry

Another important differentiation that exists between receiver concepts relates to the general geometry of the receiver. External receivers are the commercial state-of-the-art and consist of cylindrical or cubical arrangements of tube banks as illustrated in Figure 1-6. As long

as the external temperature of the receiver tubes does not exceed temperatures of roughly 650°C, thermal emissions remain relatively moderate and external receivers can be used without sacrificing too much performance.

(a) (b)

Figure 1-6: (a) the cylindrical tubular molten-salts receiver at the Solar Reserve Crescent Dunes plant in the USA[1] and (b), one of the three identical external receivers of the Brightsource Energy Ivanpah solar power plant[2].

For higher receiver temperatures, thermal emissions become a significant contributor to the overall energy loss. In order to mitigate this loss mechanism, the hot tubes of the receiver can be placed in an insulated cavity with a reduced aperture opening to the environment. The radiative exposure to the "cold" surroundings is then reduced and emissive losses mitigated. This effect is generally known as the "cavity effect". In addition, cavity receivers reduce reflective losses through the same mechanism: reflected sunlight is contained in the cavity and a part of it is reflected back to the absorber surface, emulating an increase in effective absorptivity as a seen from the focal plane. This effect is known as "light-trapping". External receivers are relatively simpler to build and install than cavity receivers, particularly for large scale CSP systems.

The most important geometrical parameter of a CSP receiver is the "aperture" which is the virtual surface through which radiation enters and leaves the receiver volume. The optimal aperture size for isothermal cavities with planar apertures has been studied in the literature as shown in Figure 1-7 [140]. The optimal aperture dimensions are a function of the temperature of the cavity and the focal plane flux distribution. Knowing the focal plane flux distribution, the aperture dimensions can be set to maximise the trade-off between added energy input and increased surface area for thermal emissions. The result is an aperture that maximises the energy absorbed on the walls of the cavity for a given temperature.

[1] Source: http://www.solarreserve.com
[2] Source: www.brightsourceenergy.com

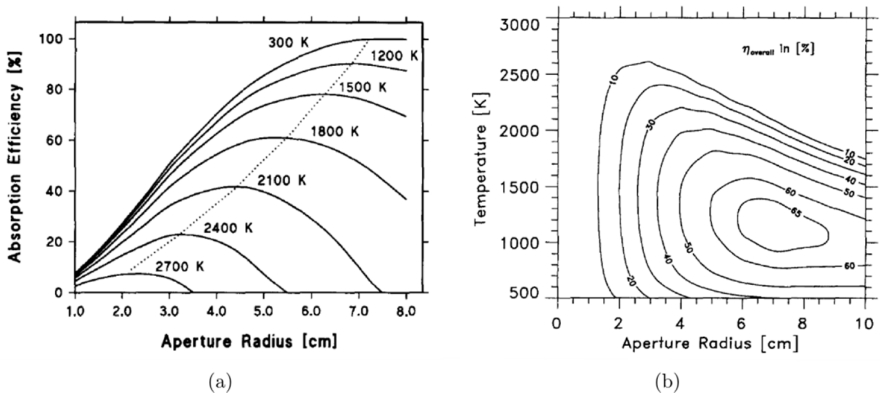

Figure 1-7: (a) Energy absorption efficiency as a function of the aperture radius, for various cavity-receiver temperatures. (b) Overall system efficiency as a function of the aperture radius and temperature using a measured solar flux distribution, extracted from [140].

External receiver geometries presented in the literature belong in general to three categories: planar, cylindrical and cubical arrangement of tubes, and are usually simplified heavily and included in heliostat field layout studies. Commercially, tower receivers have cavities made of planar tube banks arranged in a concave shape and placed in an insulated enclosure as shown in Figure 1-8 (b). The need to design CRS with higher temperature receivers and concentration levels has led to the development of tower volumetric receiver concepts with multiple apertures for multiple small scale cavity receivers [132].

Figure 1-8: (a) Cavity receiver placed at the focus of the SG3 concentrator at the ANU STG facilities in Canberra (Australia) and (b) Abengoa Solar's PS20 "cavity" receiver in Spain.

Cavity receivers are frequently considered isothermal or approximated to an equivalent isothermal grey body positioned at the aperture. From a theoretical standpoint the fundamental objective of thermal receivers is to increase the temperature of a HC, and consequently the isothermal approximation frequently used in cavity receiver design needs to be relaxed for accurate performance modelling. The temperature distribution in the receiver is established by local energy balances between the absorbed concentrated radiation, the energy extracted by the HC and the thermal loss mechanisms. Non-isothermal receivers with a temperature distribution matched to the flux distribution have been suggested as a theoretical

concept to reduce thermal losses and reach a high temperature of HC efficiently [124]. In Figure 1-9 a multi-stage receiver with a finite set of thermal zones has been developed by fractioning the focal plane aperture of the receiver into independent sections, each with their own temperature, as an application of the previous concept [82]. This concept was subsequently built and tested with success, heating air up to 1200 °C at 20 bar of pressure [81].

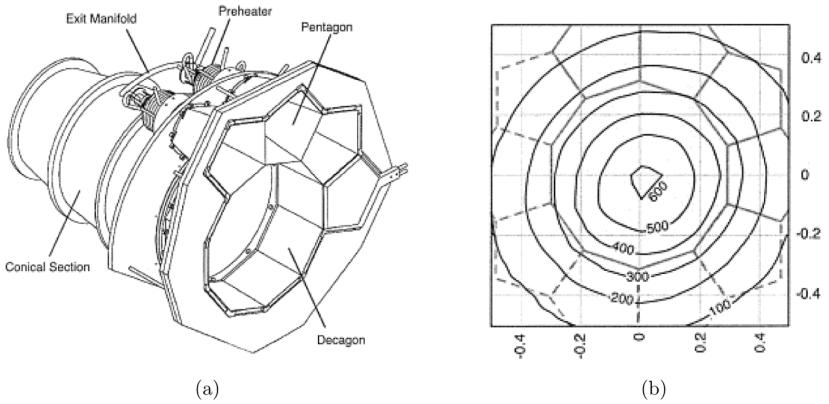

Figure 1-9: (a) Multi-stage solar receiver, experimental prototype of non-isothermal receiver and (b) the distribution of the apertures (in grey) of the different components over a focal plane fluxmap [82].

Cavity receiver systems in the literature and in commercial operations use simple geometries and rely on having a high ratio of internal surface area to aperture surface area to promote both the cavity and the light-trapping effects previously mentioned. The most common geometries for small systems (<1 MWth) are cylinders or cones whose aspect ratio (ratio of diameter on length) is “optimised”, or more generally, evaluated through parametric studies to obtain the sufficient cavity effect [57, 59, 103, 147]. Seminal work on dish concentrator systems from Sandia National Laboratories in Albuquerque (USA) looked at different classes of geometries by modelling the performance of arbitrarily chosen ellipsoidal, hetero-conical and spherical geometries, and concluded that the geometry had little influence on the first law efficiency but a strong influence on internal wall flux distributions [56]. The major energy input of the system, the incoming radiative flux distribution, has a strong influence on local energy balances and has been shown to be strongly dependent on the receiver geometry as recently demonstrated by Shuai et al. in Figure 1-10 [136]. In Figure 1-10 (b), the normalised axial radiative flux distribution changes significantly depending on the cavity geometry. From this series of works, it is understood that:

- Higher concentrations are necessary to reach higher efficiencies at higher receiver temperatures.
- Receiver geometry can help manipulate the flux distribution at the receiver location.

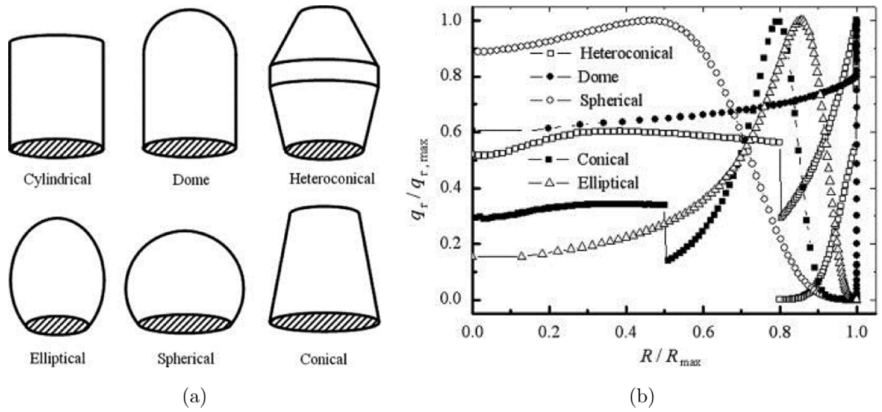

Figure 1-10: Illustration of the influence of receiver geometry on the surface flux distribution for a set of receivers placed at the focal plane of a dish concentrator [136]. The shape of the receivers (a) strongly influences the normalized incident flux distribution on the walls (b).

The link between receiver geometry and photo-thermal conversion efficiency is not fully explored in the literature where simplified assumptions are considered in general for geometry, temperature and flux distributions. To understand these interactions, fully coupled models including both the external side and HC side are necessary as they are the only way to evaluate accurately the local net heat flux and temperatures. The influence of the geometry of the absorbing surfaces of a receiver, as opposed to the aperture, on the amount of work that can be extracted from the HC has not been studied and explained.

Some difficulties arise when large thermal gradients are observed in receivers and thermal stresses overcome the allowable stress limit of the materials, causing material failure. While it is hard to find experimental data on commercial or experimental receiver failure, generally because of “bad press” consequences, thermal stresses in receivers have been the subject of a few studies in the literature focusing on thermal stress in tubes under specific irradiation conditions [40, 41, 107, 116, 126]. Thermo-mechanical analysis is rarely included at the receiver geometry design stage in the literature. While non-isothermal receivers can provide improved photo-thermal conversion efficiency, they are potentially more subject to high thermal stresses due to the greater temperature and flux variations expected if geometries are designed to increase concentration.

Cavity receivers tend to be preferred when focal flux concentrations are high enough to overcome the thermo-mechanical limits of materials. This is because, in cavities, radiation is redistributed over a larger surface without greatly increasing radiative losses [144]. For dish concentrators, simple cavity receiver geometries like cylinders and cones suffer from highly non uniform incident flux distribution [56, 136]. This non-uniform flux distribution tends to create non-uniform temperature distributions which can have detrimental effects on receiver reliability and resistance to thermo-mechanical stresses [41]. This can be alleviated by re-aligning the concentrator mirror facets [5]. In the case of CRS, complex heliostats aiming

strategies are used to adapt the receiver flux distribution and therefore mitigate the thermal stresses. The use of detailed design of receiver geometry aiming at mitigating the thermal stress issues is not found in the literature.

1.3 Receiver simulation

Considering the complexity of a CSP system, the temperature levels involved, the cost of the equipment and variability of the resource, receiver design relies extensively on simulations prior to any experiment. Receiver performance depends on coupled local and system energy balances involving radiative, convective and conduction heat transfer which generally form non-linear systems of equations. Analytical resolution of this type of problem is usually challenging, particularly when receiver surfaces radiate between each other.

When the receiver geometry is convex, no radiative heat transfer occurs between receiver surfaces and modelling the radiation component of the energy balance is simpler. For such systems, cone optics simulation technics based on geometrical projections and convolution of distributions of flux can be efficiently used to obtain fast and relatively accurate results [45].

The most common method to simulate radiative heat transfer in non-trivial geometries and heat-transfer conditions is Monte-Carlo Ray Tracing (MCRT) [65, 101]. MCRT is a stochastic method suitable to simulate the propagation of light, approximated as bundles of rays, in a three-dimensional scene. It presents the advantage of being able to relatively easily adapt to any type of macroscopical radiative heat transfer problem but can suffer from slow convergence rates and high computation cost in complex scenes. Typically the convergence rate of MCRT methods follows a $1/\sqrt{n}$ trend where n is the number of rays cast, meaning that the precision of the result doubles for a number of rays multiplied by 4 [36].

A wide range of implementations of MCRT methods for radiative heat transfer has been suggested in the literature to improve convergence rates or accelerate simulations [101]. These methods usually involve two strategies: variance reduction via stochastic importance sampling, control variate and integral formulation techniques [36] and the development of dedicated algorithms for the resolution of specific problems [65].

For problems involving only diffuse surfaces, a common assumption for rough surfaces in CSP problems, the radiosity method is commonly used to evaluate radiative heat-transfer balances involving thermal emissions [63]. The radiosity method isolates the geometrical relations between the elements in the scene in a matrix of view factors, established via analytical methods or numerical integration (MCRT for example) from the thermal boundary conditions. One can consequently modify the thermal boundary condition without any

modification to the matrix of view factors, to study the influence of the temperature distribution in the scene on the radiative losses of a receiver. View factor computations are computationally expensive and many methods have been suggested to accelerate their computation such as the hemisphere method, finite element approximations, pseudo Monte-Carlo methods, reciprocity and summation rule enforcements [145] or the use of shape primitives [146].

Convective heat transfer is notoriously complicated to evaluate as its theory relies on the resolution of the Navier-Stokes equation system, which is yet to be demonstrated in its full 3D form (it is one of the millennium problems and a 1,000,000 USD prize is offered for its solution[3]). Receiver convective loss to the environment is through heat exchange with the surrounding air under natural, forced and mixed convection regimes. Forced convection regimes are usually associated with wind blowing on receiver surfaces and are the source of an intermittent loss depending on the location of the system and the atmospheric conditions. Natural convection is driven by the buoyancy created by the temperature gradients between the hot air in contact with the receiver surfaces and the surrounding air. These phenomena have been studied experimentally and numerically and are still active research topics [108, 134, 154]. In high-temperature receiver studies, convective heat loss to the environment tends to be dominated by radiative heat loss, because radiative loss is a function of the temperature to the power 4 while convection is only proportional to the temperature of the surface, and approximate methods using correlations derived from experiment and dimensionless numbers characterising the system are adopted to simplify the analysis.

Internal convection in receivers occurs in the HC volume. In indirectly irradiated receivers, heat is generally transferred to the HC via convection between the absorber and the HC. Correlations exists, depending on the geometry of the ducts or pipe in which the HC circulates and the flow conditions. For directly irradiated receivers, convection is more critical and understanding it usually requires case specific studies.

In the absence of a suitable correlation or analytical solution, Computational Fluid Dynamics (CFD) codes are used to numerically solve the energy, mass and momentum equations in the problem of choice. CFD relies on finite volume methods applied to a discrete version of the problem.

Heat conduction is governed by the Fourier law of conduction. For problems without analytical solution, well known finite differences or finite elements methods are commonly

[3] Source : http://www.claymath.org/millennium-problems

used. Heat conduction is important for indirectly irradiated receivers as the absorbed heat is first conducted through the absorber material before being extracted by the HC [63].

Every problem is unique in its geometry and setting the boundary conditions, control volumes and discretisation schemes is a critical phase of coupled heat transfer modeling. Examples of coupled heat transfer modeling of solar receivers can be found in the literature [31, 37, 68, 89, 112, 128]. The usual focus of the existing work is on the modeling of experimental results or detailed evaluation of a pre-determined design [11].

Energy efficiency is usually used to evaluate the performance of a receiver design; however, the temperature level of the HC at the outlet of a receiver has a strong influence on the amount of work that can ultimately be extracted from it, as a consequence of the second law of thermodynamics. Exergy is the fraction of energy that can be transformed into work and can be determined for thermal devices such as heat exchangers, turbines, boilers and thermal strorage systems. Most exergy analysis studies in the solar thermal energy literature focus on system analysis and components are not modelled in great detail [53, 77, 158, 160, 162]. Applying exergy analysis to the solar receiver field should provide interesting insights into optimal receiver designs without having to evaluate the performance of the whole CSP system. One study on the exergy efficiency of receiver tubes for solar collectors can be found in the literature using a range of simplifications [69]. The influence of the geometry and radiative properties of concentrators on the exergy provided by solar radiation has not been analysed in detail in the literature and is of importance to understand how to design receivers efficiently. In addition, the impact of the temperature distribution in complex receiver shapes and their impact on the exergy levels in the receiver have not been analysed in detail in the literature.

1.4 Receiver optimisation

1.4.1 Optimisation fundamentals

The general optimisation problem is summarised in the following expression:

$$\min_{x \in X} F(x) \tag{1-1}$$

Where x is a vector of variables and X the feasible region. When no condition is imposed on the feasible region, the optimisation problem is unconstrained, otherwise the problem is known as constrained optimisation. Depending on the nature of the function F and the amount of available information about it, different techniques can be used to solve the problem. These techniques are regrouped into two sub-fields of research: Mathematical Programming and Simulation-Optimisation. Mathematical programming relies on progressing

towards the minimisation of F by making assumptions over the nature of F, typically local or global convexity/concavity and gradient estimations.

In some problems, some of the variables are stochastic and introduce uncertainty in the evaluation of $F(x)$. $F(x)$ is not accessible directly but only through sampling of another function $f(x,\rho)$ of the vector of finite variables x and uncertain or random variables ρ. Eq. 1-1 becomes:

$$\min_{x \in X} E\left[f(x,\rho)\right] \tag{1-2}$$

In Eq. 1-2, $E\left[f(x,\rho)\right]$ is the expectation of $f(x,\rho)$. Traditional mathematical programing methods generally need to be modified to process the stochastic nature of the function evaluation and stochastic optimisation methods are used [64]. Sample average approximation and related methods rely on turning an uncertain problem into a deterministic one on which gradient estimates are obtained and used to progress towards the problem solution. Another approach relies on stochastic approximation methods that mimic gradient methods for non-linear problems. When no gradient or information is available on F, due to the non-derivability, complexity of the problem or non-practicality of estimating low uncertainty values of $F(x)$ for example, random search methods can be useful [4]. Heuristics and metaheuristics are specific subclasses of random search methods that establish logical scenarii to solve approximate optimisation problems where the objective to find good enough results within acceptable time constraints rather than the exact optimal candidates. Heuristics and metaheuristics tend to focus on population-based optimisation approaches where the optimisation result is searched using a population of “candidates” instead of a single point of evaluation. Data processing on this population of candidates is performed at each step of the procedure to generate a new “evolved” population of candidates that is expected to help the progression towards a final result. This “learning” step unlocks evolutionary strategies in heuristics and metaheuristics which perform well at navigating complex and unknown solution spaces with large numbers of local minima. Genetic algorithms and particle swarm algorithms are well known metaheuristics already widely used methods in deterministic optimisation [48].

In some complex problems, F is unknown and $F(x)$ values are estimated with computer simulations. Simulation-Optimisation (SO) regroups the different types of optimisation methods used to solve such “black-box” problems [25]. A general introduction to SO methods is found in Fu et al. [44].

In the great majority of examples found in the literature, stochastic optimisation is conducted for a single objective function. In most complex design problems however,

performance over multiple objective functions is sought after. As an example, some objective functions for a good solar receiver could be the energy efficiency, the cost of the receiver and the life expectancy of the device. Multi-objective optimisation is the sub-field of optimisation that focuses on the issue of optimising a problem with a set of objective functions. In most situations, interesting designs appear by analysing the trade-offs between the objective functions. In some situations, several optimisation metrics are "scalarised" or regrouped into a single value which is then optimised using single objective methods. Scalarisation requires the decision maker to pre-establish some relationship between the different objective functions and therefore impose some bias on the trade-offs that will be identified between competing objective functions. In the "black-box" problem situation, scalarisation should be avoided as the decision maker cannot rely on any information from the problem and could therefore significantly influence the results by choosing an arbitrary scalarisation method that does not suit the problem. The non-biased way of conducting multi-objective optimisation is by using the concept of Pareto dominance. The multi-objective optimisation problem is:

$$\max_{x \in X} \left\{ F_1(x), F_2(x), \ldots, F_m(x) \right\} \tag{1-3}$$

In eq. 1-3, $F_i : X \to \mathbb{R} \left(i =, \ldots, m \right)$ are the m objective functions considered. Here max is used instead of min as the aim is to maximise performance. In this problem, $\alpha \in X$ is non-dominated if there is no $\beta \in X$ at least as good as α in all the objective functions and strictly better than α in at least one of them. The set of non-dominated, or Pareto optimal, points of a problem forms a Pareto front and constitutes the result of a multi-objective optimisation. The benefit of the multi-objective approach is that instead of a single optima design, a range of Pareto optimal designs illustrating the best possible performance in every objective independently is obtained (Figure 1-11). The decision maker can then evaluate the trade-offs between conflictive objective functions and choose the best compromise. The combination of both stochastic optimisation and multi-objective optimisation is much less developed than each of them separately in the literature [54]. The methods from both fields, however, cannot be simply combined a priori and active research is ongoing to develop methods to solve this class of problems.

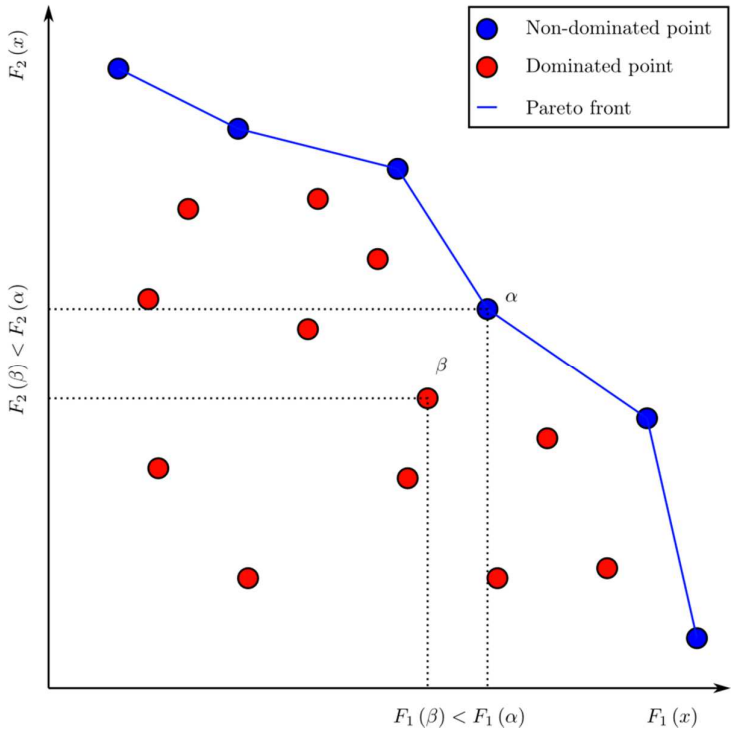

Figure 1-11: 2D Pareto front construction example. α dominates β as it has better performance in both $F_1(x)$ and $F_2(x)$. There is no point that has better performance than α in both objective functions at the same time.

1.4.2 Optimisation of receiver geometry

In the CSP literature, most of the geometrical optimisation studies have focused on concentrator design. Optimisation of receivers, past the aperture design, is in fact very rarely undertaken and parametric studies are preferred. The main technical reason to explain this gap is that radiative heat transfer simulations are computationally intensive and limit the number of alternative configurations that can be evaluated. More fundamentally, coupled heat transfer models such as the ones taking place in receivers are usually non-linear functions of the geometry of the problem and can present a large, and unknown, number of local minima, virtually preventing the use of steepest gradient based optimisation methods. In addition, the study of non-classical geometries imposes the use of complex volumetric integration methods to evaluate radiative heat transfers. The most common integration method, Monte-Carlo ray-tracing, is stochastic and prevents the use of classical optimisation methods unable to consider uncertainty in the evaluation of the objective functions. A fundamental distinction needs to be made between the mathematical optimisation problem, as defined in the previous section and numerical optimisation tools, which one can uses to solve an optimisation problem. Numerical optimisation tools inherently introduce some "noise" or uncertainty in the calculations. Numerical optimisation tools dedicated to the solution of non-stochastic problems use different techniques to handle this imprecision. In a stochastic simulation optimisation problem, whether the uncertainty comes from noise or

statistical variation in the estimation of the objective is irrelevant as it is not possible to distinguish between them.

Every coupled heat transfer model cited in the previous section uses CFD to solve the overall energy balance of the system including external convection. This method can provide accurate results for the simulation of a single receiver but is difficult to integrate in optimisation where the evaluation of numerous candidates is necessary to explore the parameter space because of the computational effort required. The usual approach to receiver design in the literature consists of parametric studies in which every receiver candidate is simulated to a high level of precision to be compared with the others by a decision maker.

The optimisation of the geometry of the gas channels in a dish cavity receiver for maximum work output was undertaken using a deterministic “leap frog” algorithm [102]. However, the study used analytic approximations for the overall radiation input to the receiver and no detailed flux distribution was considered.

Two examples of optimisation problems involving Monte-Carlo ray-tracing can be found. A deterministic steepest gradient optimisation associated with a stochastic sampling method was used to study specular radiant cavities and linear concentrator profiles [32, 96]. A significant limitation of these studies is their limitation to convex optimisation problems due to the optimisation strategy used.

Howell et al. [65] highlight the fact that optimisation is the only viable solution method solve radiative enclosure design problems where the geometry is an integration variable. In addition the capability of metaheuristics to integrate arbitrary constraints in the formulation of the problems is considered to provide economical solutions of complex problems.

An inspirational study from the Harbin Institute of Technology in China determined an ideal cavity shape to intercept a quasi-homogeneous flux at every location of a cavity receiver placed at the focal plane of a dish concentrator. The study started from a spherical cavity receiver and procedurally progressed by adapting the local radius for a minimum flux variation with the previous element. Figure 1-12 shows the result of such a study for a cavity receiver for a dish concentrator. This result confirms the large influence of the receiver geometry on the flux distribution in solar receivers. While some approximate models exist for simple receiver shapes, detailed radiative heat transfer models such as MCRT are necessary to study receiver geometries in detail.

Cavity shapes that are optimized for specific flux and temperature distributions can therefore be envisioned. The manufacturability and cost of these cavity receivers is a potential issue and needs to be evaluated systematically to produce efficient and feasible concepts. The

procedural determination of the optimal shape of a receiver taking into account detailed heat transfer conditions at the surface and potential constraints such as efficiency, thermo-mechanical limits of the materials and cost, is not found in the literature.

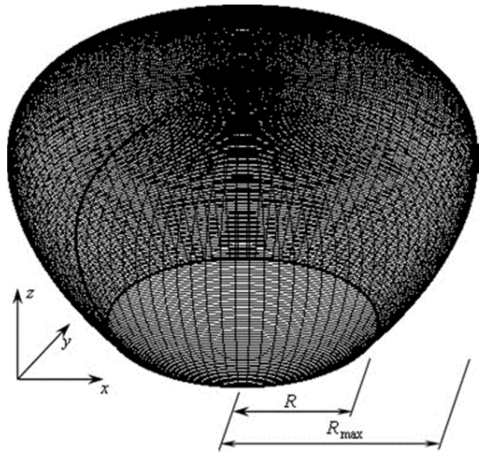

Figure 1-12: Upside-down pear shape with pseudo-homogenous incident flux from a dish concentrator [136].

All the studies mentioned in this section focused on the optimisation of a single objective function which can be a significant constraint in systems design. The geometrical optimisation of receivers using multi-objective approach has not been performed in the literature at this time.

1.5 Research contribution

1.5.1 Research statement

Heat transfer processes driven by the incident concentrated flux determine the energy efficiency and thermo-mechanical stress in the receiver. Coupled heat transfer models, while relatively rare in the receiver literature, are needed to carefully assess the performance of a receiver design.

The geometry of receivers has a strong influence on the incident flux distribution and consequently can impact the energy efficiency and thermo-mechanical stress simultaneously. However, the detailed influence of the geometry of the absorbing surfaces of a receiver is identified as a relatively unexplored research area and opportunities exist for more systematic analyses than is currently found in the literature.

The optimisation of receivers is very rarely found and parametric studies are preferred by most authors for their simplicity and to avoid the complications brought by the stochastic

nature of MCRT simulations. Among the very few optimisation studies found, all focused on single objective optimisation[4].

These observations lead to the following research statement: **New methods are needed to rigorously analyse and optimise the geometry of solar thermal receivers against multiple competing performance indicators.** The work developed in this dissertation is a contribution of the author to address this gap. The outcome of the research is to enable geometrical optimisation of high-temperature receivers and provide tools to design, cheaper, more efficient and more reliable receivers. To achieve this goal, the work follows two streams:

- The development of a framework for coupled heat transfer modelling of indirectly irradiated receivers of diverse geometries.
- The development of multi-objective and stochastic simulation optimisation methods and their application to receiver geometric optimisation.

The methods are applied to a series of point focus concentrator and receiver examples to demonstrate the feasibility of multi-objective receiver optimisation and some of the potential benefits associated.

1.5.2 Thesis outline

The work presented hereafter is divided in four main chapters. In Chapter 2 “Receiver model” fundamentals of CSP receiver modelling are presented, covering both the theory and the simulation tools used. In Chapter 3 “Receiver model applications” the application of the elements discussed in Chapter 2 is presented on two examples of receiver coupled heat transfer models. Chapter 4 “Optimisation of Receiver Design” presents in a chronological manner, the optimisation studies developed during the research and the progression towards more rigorous and polyvalent optimisation methods able to tackle problems involving complex and stochastically simulated systems such as concentrated solar receivers. Chapter 5 “Applied exergy analysis in CSP” proposes a method to analyse the value of optical concentration using the second law of thermodynamics.

[4] The review process for this manuscript brough two recent publications on the topic, published after the date at which this review was written :

- Moghimi, M.A., Craig, K.J. & Meyer, J.P., Simulation-based optimisation of a Linear Fresnel Collector mirror field and receiver for optical, thermal and economic performance, Solar Energy, Vol. 153, pp.655-678, 2017.
- Moghimi, M.A., Craig, K.J. & Meyer, J.P., Optimization of a trapezoidal cavity absorber for the LinearFresnel Reflector, Solar Energy, Vol. 119, pp.343-361, 2015.2

1.5.3 Simulation and modelling tools

For flexibility, sharing, transparency and cost reasons, the modelling work is developed using open-source code exclusively. All the tools developed in this PhD are coded in Python language and make extensive use of the NumPy [143] and SciPy [71] libraries. The open source "Tracer" library is used for ray-tracing [99]. The numerous additions and improvements brought to the Tracer library are available on a copy of the code available on the Internet: https://github.com/casselineau/Tracer. An occasional use of SolarPILOT, a free but closed source CSP optical simulation package from NREL can be found for validation purposes or quick evaluation of flux distributions.

2 Receiver modelling

This chapter contains the full description a mathematical model and simulation methods used to solve coupled heat transfer receiver problems. The model will then be used for case studies and optimisation in subsequent chapters.

2.1 The Sun as a source of radiative energy

2.1.1 The Sun

The Sun is a white dwarf star located at the center of the solar system which provides the great majority of the energy input to the Earth in the form of radiative energy. The Sun is a sphere of $r_{\text{Sun}} = 695{,}700$ km of radius positioned at a mean distance of $D_{\text{Sun}} = 1.496 \times 10^8$ km of the Earth[5]. Taking into account the distance between the Sun and the Earth, the average extraterrestrial irradiance, also known as solar constant, amounts to 1360,8 W/m^2 [34]. Seen from the surface of the Earth, the Sun appears as a small disc of varying spatial brightness in the sky. Solar radiation is consequently not collimated and exhibits an angular dependency. Extraterrestrial solar radiation interacts with the atmosphere it traverses on its way to the surface of the planet. The spectrum of the radiation incident on the surface of the planet is different to the extraterrestrial one, mostly due to the absorption bands of ozone, dioxygen, water and carbon dioxide. Figure 2-1 presents the extraterrestrial solar spectrum, the surface direct normal incident spectrum and the blackbody approximation of the solar spectrum. The blackbody spectrum for a constant refractive index is described by Planck's law:

$$E_{b\lambda}(T,\lambda) = \frac{2\pi h_P c^2}{n^2 \lambda^5 \left(e^{\frac{h_P c}{n\lambda k_B T}} - 1 \right)} \tag{2-1}$$

With T the temperature, λ the wavelength, c the speed of light in vacuum, h_P the Plank constant, k_b the Boltzmann constant and n the refractive index of the medium. The overall emission of radiation from black-body surfaces is given by the Stefan-Boltzman law:

$$E_b(T) = \sigma T^4 \tag{2-2}$$

[5] Source : http://solarsystem.nasa.gov

The Sun can be approximated to a blackbody at a temperature between 5500 K and 6000 K depending on the references and approximations taken. Considering a solar irradiance G the equivalent blackbody temperature of the sun is given by the following expression:

$$T_{\text{Sun}}(G) = \sqrt[4]{\frac{G}{\sigma \sin^2(\theta_{\text{Sun}})}} \tag{2-3}$$

With θ_{Sun} the angle subtended by the sun in the sky and related to the sun dimensions with:

$$\theta_{\text{Sun}} = \tan^{-1}(r_{\text{Sun}}/D_{\text{Sun}}) \tag{2-4}$$

For extraterrestrial solar radiation, the solar constant is $G = 1360.8$ W.m^{-2} giving $T_{\text{Sun}}(1360.8) = 5772$ K. The comparison between the measured and approximated spectra is shown in Figure 2-1.

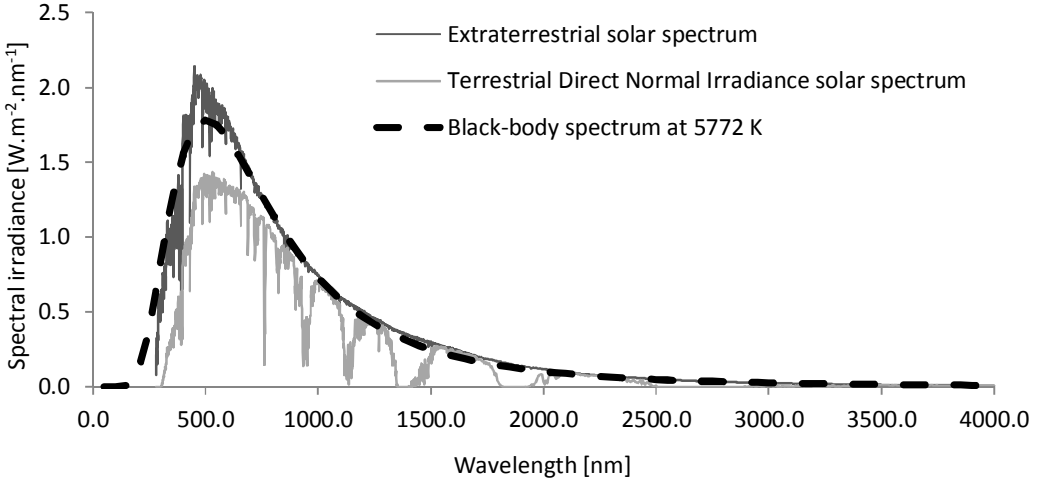

Figure 2-1: Extraterrestrial and DNI spectra (ASTM G173-03 Reference Spectra Derived from SMARTS v. 2.9.2) compared with the black-body emission spectrum at 5772 K. Spectral data from Gueymard et al. [52].

The typical direct normal irradiance (DNI) finally reaching the surface of the earth is generally closer to 1000 W/m^2 which is the value chosen as 1 sun.

The angular distribution of the solar radiation is also impacted by the interaction with the atmosphere through numerous and complex absorption, reflection, emission and scattering processes. The angular distribution of radiation, also known as “sunshape”, is important for concentrating optics because it influences the spatial distribution of radiation, as will be developed in sections 2.1.2 and 2.1.3.

The position of the sun in the sky changes depending on the time of the day and the day of the year. It is common to characterise the sun position relatively to a point on the surface of the earth using $\hat{\mathbf{d}}_{\text{sun}}$ the solar unit direction vector or “solar vector”. In CSP, the use of the

azimuth angle (or its complementary zenith angle) and the elevation angle, as illustrated in Figure 2-2, is common practice.

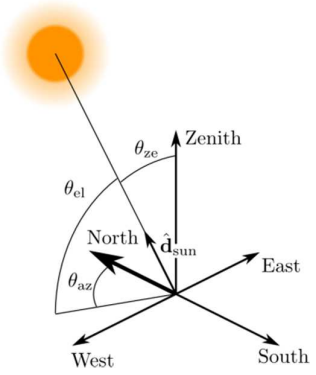

Figure 2-2: Solar vector construction illustation for a southern hemisphere location.

$$\hat{\mathbf{d}}_{sun}(\mathbf{r},t) = \cos(\theta_{el})\sin(\theta_{az})\hat{\mathbf{x}} + \cos(\theta_{el})\cos(\theta_{az})\hat{\mathbf{y}} + \sin(\theta_{el})\hat{\mathbf{z}} \quad (2\text{-}5)$$

Several studies in the literature describe numerical algorithms to determine the solar vector in local coordinates [17, 49].

2.1.2 Sunshape distributions

2.1.2.1 Sunshape definition

Solar radiation reaches the surface of the Earth with a specific angular intensity distribution influenced by three major factors:

- A geometrical effect: the sun is not a point source. As a consequence, solar radiation from different locations on the sun reaches any point on the atmosphere of the Earth with a corresponding incident angle.
- Limb-darkening: a physical effect caused by the temperature and optical depth gradients in stars when seen from distant locations that diminishes the radiance from the outermost regions of the solar disc [15].
- Atmospheric scattering: Solar radiation interacts with the particles contained in the earth's atmosphere before reaching any concentrating device at the surface and has its angular intensity profile modified. Mie [100], describes a particular phenomenon called small angle forward scattering that occurs when the diameter of the particles met by solar radiation is large in comparison to the wavelengths of the photons. As a consequence, a fraction of the solar intensity distribution is seen as coming from outside the solar disc, often labelled *solar aureole* or *circumsolar region*.

The angular intensity distribution on the surface of the earth is called "sunshape" in CSP research. Buie et al. (2003) [21] give a good overview of the motivations and development of the different sunshape models and measurements. The strongest motivation to use accurate

sunshape models is the reported 20% variation in optical performance of the system due to changes in the sunshape alone.

2.1.2.2 Sunshape analytical expression

The radiative flux received by any point of a surface is the integrated intensity over the hemisphere at this location:

$$\dot{q}''(\mathbf{r}) = \cos(\theta_{in}) \int_0^{2\pi} I(\mathbf{r},\omega)\cos(\theta)\, d\omega \tag{2-6}$$

with θ_{in} the angle between the normal vector of the surface considered and the solar vector as shown in Figure 2-3 and θ an angle formed between the solar vector and any point on the sun surface.

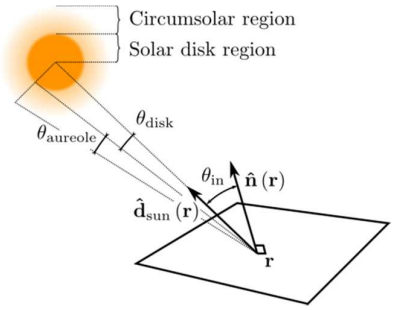

Figure 2-3: Angular conventions for sunshape declaration.

Sunshapes are axisymmetric distributions around the solar vector:

$$\dot{q}''(\mathbf{r}) = \cos(\theta_{in}) 2\pi \int_0^{\pi/2} I(\mathbf{r},\theta)\cos(\theta)\sin(\theta)\, d\theta \tag{2-7}$$

Sunshapes are generally expressed as normalised angular radiation intensity distributions $\hat{I}_{sunshape}(\theta)$, also labelled brightness by some authors.

$$I(\mathbf{r},\theta) = I(\mathbf{r},\theta=0)\hat{I}_{sunshape}(\theta) \tag{2-8}$$

The simplest sunshape model, still used in many 1st order simulations, is the uniform angular intensity distribution model, often labelled *pillbox* sunshape. Pillbox sunshapes are straight-forward to implement in simulation tools but generally fail in providing realistic solar flux distributions because only the geometrical effect mentioned in the previous section is considered. The pillbox sunshape analytical expression is the following:

$$\begin{cases} \hat{I}_{\text{pillbox}}(\theta) = 1 & \text{for } \theta \in [0, \theta_{\text{disc}}] \\ \hat{I}_{\text{pillbox}}(\theta) = 0 & \text{for } \theta > \theta_{\text{disc}} \end{cases} \tag{2-9}$$

θ_{disk} accounts for the half angle subtended by the sun in the sky. θ_{disk} is comprised in an interval between 4.584 mrad and 4.742 mrad due to the elliptic orbit of the earth but an average value of 4.65 mrad is usually considered representative of the size of the sun disc in the sky over a year. Buie et al. explain that atmospheric scattering, mostly determined by geographical atmospheric conditions, influences the sunshape and plays a significant role in determining flux distributions at the final target. Atmospheric scattering of incoming solar radiation has an impact on the choice of the acceptance angle of solar concentrators [20]. Using the Lawrence Berkeley Laboratory's sunshapes database, collected from 11 sites across the United States between 1976 and 1981 [105], and sunshape data from the German Aerospace Centre (DLR) correlating three European sites, they propose a sunshape model that is independent of geographic location. The Buie sunshape model describes angular distribution of the solar intensity as a function of the circumsolar ratio (CSR) χ, defined as the ratio of flux coming from the solar aureole $\dot{q}''_{aureole}$ over the total incident flux $\dot{q}''_{in}$:

$$\chi = \frac{\dot{q}''_{aureole}}{\dot{q}''_{in}} \tag{2-10}$$

Figure 2-4 illustrates the comparison between the Buie sunshape model and some of the DLR sunshape measurements.

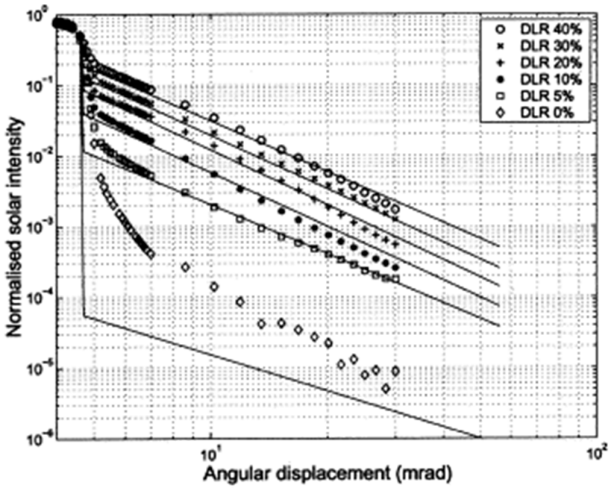

Figure 2-4: Buie sunshape model compared with experimental measurements for several CSR input values [21].

The total incident flux is the sum of the flux coming from the solar disc and from the circumsolar region:

$$\dot{q}''_{in} = \dot{q}''_{disc} + \dot{q}''_{aureole} \tag{2-11}$$

Using the conventions from Buie et al. [21]:

$$\dot{q}''_{Buie}(\theta) = \dot{q}''_{Buie}(\theta = 0)\hat{\dot{q}}''_{Buie}(\theta) \tag{2-12}$$

$$\begin{cases} \hat{\hat{q}}''_{\text{Buie}}(\theta) = \dfrac{\cos(0.326\theta)}{\cos(0.308\theta)} & \text{for } \theta \in [0, \theta_{\text{disc}} = 4.65 \text{ mrad}] \\ \hat{\hat{q}}''_{\text{Buie}}(\theta) = e^{\kappa}\theta^{\gamma} & \text{for } \theta \in [\theta_{\text{disc}} = 4.65 \text{ mrad}, \theta_{\text{aureole}} = 43.6 \text{ mrad}] \end{cases} \quad (2\text{-}13)$$

with γ and κ detailed in the following equations:

$$\gamma = 2.2\ln(0.52\chi)\chi^{0.43} - 0.1 \quad (2\text{-}14)$$

$$\kappa = \ln(13.5\chi)\chi^{-0.3} \quad (2\text{-}15)$$

2.1.3 Sunshape declarations for Monte-Carlo ray-tracing models

2.1.3.1 Ray sources in Monte-Carlo ray-tracing.

In MCRT, radiation is approximated as a bundle of rays. The geometry of each ray is defined by a starting position vector $\mathbf{r}$ and a unit direction vector $\hat{\mathbf{d}}$. The positions and directions of all rays are randomly declared according to probability density functions that realistically describe the radiation source considered and propagated through the system of concern. Ray starting positions are declared on surfaces large enough to cover the entire optical aperture of the system considered. These surfaces are labelled “sources" in the rest of this dissertation. Source declaration requires:

- A function to determine the starting position of the rays according to the source geometry considered.
- A function to determine the direction of the rays according to the sunshape considered.
- A value for G, the Direct Normal Irradiance (DNI) to determine the energy carried by each ray.
- A number of rays N_{rays}.

It is generally convenient to use planar sources of uniform radiative flux to simulate the solar input to a system in CSP. The most common geometries are discs and rectangles. In the following section the source declarations consider that every ray carries the same fraction of the total energy of the source:

$$\dot{q}_{\text{ray}} = \frac{GA_{\text{source}}}{N_{\text{rays}}} \quad (2\text{-}16)$$

Spatially uniform radiation is obtained using a uniform probability density function for the ray starting position $\mathbf{r}$. The ray starting position is defined as:

$$\mathbf{r} = x_r\hat{\mathbf{x}} + y_r\hat{\mathbf{y}} + z_r\hat{\mathbf{z}} \quad (2\text{-}17)$$

The unit direction vector in 3D space is:

$$\hat{\mathbf{d}} = x_d\hat{\mathbf{x}} + y_d\hat{\mathbf{y}} + z_d\hat{\mathbf{z}} \tag{2-18}$$

The components of the position and direction vectors are obtained from sampling values from known distributions able to describe the physics involved. This sampling is done by determination of the cumulative distribution function (CDF) $P(x,y)$ of a given distribution function $f_d(x,y)$ and relating it to one uniform random variates per random variable, $\Re_x$ and $\Re_y$ here. The multivariate cumulative distribution function is obtained from the distribution considered.

$$P(x,y) = \frac{\int_{-\infty}^{x}\int_{-\infty}^{y} f_d(t,u)\,dtdu}{\int_{-\infty}^{+\infty}\int_{-\infty}^{+\infty} f_d(x,y)\,dxdy} \tag{2-19}$$

The CDF related to a single variable only is obtained by integrating the distribution function over the range of definition of all other variables:

$$\begin{cases} P(x) = \dfrac{\int_{-\infty}^{x}\int_{-\infty}^{+\infty} f_d(t,u)\,dtdu}{\int_{-\infty}^{+\infty}\int_{-\infty}^{+\infty} f_d(x,y)\,dxdy} \\ P(y) = \dfrac{\int_{-\infty}^{+\infty}\int_{-\infty}^{y} f_d(t,u)\,dtdu}{\int_{-\infty}^{+\infty}\int_{-\infty}^{+\infty} f_d(x,y)\,dxdy} \end{cases} \tag{2-20}$$

Finally, Monte-Carlo sampling of values within these CDFs is obtained with the following expressions [65, 101]

$$\begin{cases} P(x) = \Re_x \\ P(y) = \Re_y \end{cases} \tag{2-21}$$

2.1.3.2 Rectangular source ray position declaration

For a rectangular source of dimensions L_x on the (x) axis and L_y on the (y) axis, the CDF are:

$$P_{\text{rectangle}}(x,y) = \frac{\int_{0}^{x}\int_{0}^{y} dtdu}{\int_{0}^{L_x}\int_{0}^{L_y} dxdy} = \frac{xy}{L_xL_y} \tag{2-22}$$

$$P_{\text{rectangle}}(x)=\frac{x}{L_x} \tag{2-23}$$

$$P_{\text{rectangle}}(y)=\frac{y}{L_y} \tag{2-24}$$

Similarly to Eq. 2-21:

$$\begin{cases} x_{\text{r}}=L_x\Re_x \\ y_{\text{r}}=L_y\Re_y \end{cases} \tag{2-25}$$

The random uniformly distributed ray starting position on a rectangular source is:

$$\mathbf{r}_{\text{rectangle}}=L_x\Re_x\hat{\mathbf{x}}+L_y\Re_y\hat{\mathbf{y}} \tag{2-26}$$

2.1.3.3 Disc source ray position declaration

Here the uniform positions on disc geometries are given. In planar cylindrical coordinates:

$$\begin{cases} x_{\text{r}}=r\cos(\varphi) \\ y_{\text{r}}=r\sin(\varphi) \end{cases} \tag{2-27}$$

For a disc source of radius R_{disc}, the CDF is:

$$P_{\text{disc}}(r,\varphi)=\frac{\int_0^{\varphi}\int_0^{r} u\,du\,dt}{\int_0^{2\pi}\int_0^{R_{\text{disc}}} r\,dr\,d\varphi}=\frac{\frac{r^2}{2}\varphi}{\pi R_{\text{disc}}^2} \tag{2-28}$$

$$P_{\text{disc}}(r,\varphi)=\frac{r^2\varphi}{2\pi R_{\text{disc}}^2} \tag{2-29}$$

The radial CDF is:

$$P_{\text{disc}}(r)=\frac{\int_0^{2\pi}\int_0^{r} u\,du\,dt}{\pi R_{\text{disc}}^2}=\frac{2\pi\frac{r^2}{2}}{\pi R_{\text{disc}}^2} \tag{2-30}$$

$$P_{\text{disc}}(r)=\frac{r^2}{R_{\text{disc}}^2} \tag{2-31}$$

The uniform random variate $\Re_r$ is equal to the radial CDF:

$$\Re_r=P_{\text{disc}}(r) \tag{2-32}$$

Using eq. 2-31 and 2-32:

$$r = R_{\text{disc}}\sqrt{\Re_r} \tag{2-33}$$

The angular CDF is:

$$P_{\text{disc}}(\varphi) = \frac{\int_0^{\varphi}\int_0^{R_{\text{disc}}} u\,du\,dt}{\pi R_{\text{disc}}^2} = \frac{\varphi\frac{R_{\text{disc}}^2}{2}}{\pi R_{\text{disc}}^2} \tag{2-34}$$

$$P_{\text{disc}}(\varphi) = \frac{\varphi}{2\pi} \tag{2-35}$$

The angular component as a function of a uniform random variate $\Re_\varphi$ is determined using:

$$\Re_\varphi = \int_0^{\varphi} P_{\text{disc}}(\varphi)\,d\varphi \tag{2-36}$$

Using eq. 2-35 and 2-36:

$$\varphi = 2\pi\Re_\varphi \tag{2-37}$$

The random uniformly distributed ray starting position on a disc source is:

$$\mathbf{r}_{\text{disc}} = R_{\text{disc}}\sqrt{\Re_r}\cos\left(2\pi\Re_\varphi\right)\hat{\mathbf{x}} + R_{\text{disc}}\sqrt{\Re_r}\sin\left(2\pi\Re_\varphi\right)\hat{\mathbf{y}} \tag{2-38}$$

2.1.3.4 Pillbox sunshape model for Monte-Carlo ray-tracing simulations

The pillbox sunshape describes a uniform intensity distribution over the solid angle subtended by the sun disc in the sky. In polar coordinates:

$$\begin{cases} x_{\text{d}} = \sin(\theta)\cos(\varphi) \\ y_{\text{d}} = \sin(\theta)\sin(\varphi) \\ z_{\text{d}} = \cos(\theta) \end{cases} \tag{2-39}$$

The uniform angular flux probability density function for an angular range of θ_{disk} is:

$$P_{\text{pillbox}}(\theta,\varphi) = \frac{\int_0^{\theta}\int_0^{\varphi} \hat{I}_{\text{pillbox}}(t,u)\cos(t)\sin(t)\,dt\,du}{\int_0^{2\pi}\int_0^{\theta_{\text{disc}}} \hat{I}_{\text{pillbox}}(\theta,\varphi)\cos(\theta)\sin(\theta)\,d\theta\,d\varphi} \tag{2-40}$$

$$P_{\text{pillbox}}(\theta,\varphi) = \frac{\sin^2(\theta)\varphi}{2\pi\sin^2(\theta_{\text{disc}})} \quad \text{for } \theta < 4.65 \text{ mrad} \tag{2-41}$$

The zenithal CDF is:

$$P_{\text{pillbox}}(\theta)=\frac{\int_0^{\theta}\int_0^{2\pi}\hat{I}_{\text{pillbox}}(t,u)\cos(t)\sin(t)\,dtdu}{\pi\sin^2(\theta_{\text{disc}})}=\frac{2\pi\dfrac{\sin^2(\theta)}{2}}{\pi\sin^2(\theta_{\text{disc}})} \tag{2-42}$$

$$P_{\text{pillbox}}(\theta)=\frac{\sin^2(\theta)}{\sin^2(\theta_{\text{disc}})} \tag{2-43}$$

The azimuthal CDF is:

$$P_{\text{pillbox}}(\varphi)=\frac{\varphi}{2\pi} \tag{2-44}$$

Similarly to eq. 2-32:

$$\Re_{\theta}=P_{\text{pillbox}}(\theta) \tag{2-45}$$

$$\Re_{\theta}=\frac{\sin^2(\theta)}{\sin^2(\theta_{\text{disc}})} \tag{2-46}$$

$$\theta=\sin^{-1}\left(\sqrt{\Re_{\theta}}\sin(\theta_{\text{disc}})\right) \tag{2-47}$$

For the azimuth angle:

$$\varphi=2\pi\Re_{\varphi} \tag{2-48}$$

The pillbox unit direction vectors are:

$$\hat{\mathbf{d}}_{\text{pillbox}}=\left(\sqrt{\Re_{\theta}}\sin(\theta_{\text{disc}})\right)\left(\cos(2\pi\Re_{\varphi})\hat{\mathbf{x}}+\sin(2\pi\Re_{\varphi})\hat{\mathbf{y}}\right)+\sqrt{1-\Re_{\theta}\sin^2(\theta_{\text{disc}})}\hat{\mathbf{z}} \tag{2-49}$$

2.1.3.5 Buie sunshape model for Monte-Carlo ray-tracing simulations

The following method to integrate the Buie sunshape was developed as part of the PhD research.

The angular flux CDF for the Buie sunshape in polar coordinates is:

$$P_{\text{Buie}}(\theta,\varphi)=\frac{\int_0^{\theta}\int_0^{\varphi}\hat{q}''_{\text{Buie}}(t,u)\sin(t)\,dtdu}{\int_0^{2\pi}\int_0^{\theta_{\text{aureole}}}\hat{q}''_{\text{Buie}}(\theta,\varphi)\sin(\theta)\,d\theta d\varphi} \tag{2-50}$$

The sunshape is axi-symmetrical therefore $\hat{q}''_{\text{Buie}}$ is independent of the azimuth angle. The Buie sunshape CDF is:

$$P_{\text{Buie}}(\theta,\varphi)=\frac{\varphi\int_0^{\theta}\hat{\hat{q}}''_{\text{Buie}}(t)\sin(t)dt}{2\pi\int_0^{\theta_{\text{aureole}}}\hat{\hat{q}}''_{\text{Buie}}(\theta)\sin(\theta)d\theta} \tag{2-51}$$

First, the denominator of 2-51 is integrated. As presented in eq. 2-13, the Buie sunshape is a piecewise-defined function and the integration can be split over the two components of the θ domain:

$$\int_0^{\theta_{\text{aureole}}}\hat{\hat{q}}''_{\text{Buie}}(\theta)\sin(\theta)d\theta=\int_0^{\theta_{\text{disc}}}\hat{\hat{q}}''_{\text{Buie}}(\theta)\sin(\theta)d\theta+\int_{\theta_{\text{disc}}}^{\theta_{\text{aureole}}}\hat{\hat{q}}''_{\text{Buie}}(\theta)\sin(\theta)d\theta \tag{2-52}$$

$$\hat{\hat{q}}''_{\text{Buie, disc}}=\int_0^{\theta_{\text{disc}}}\hat{\hat{q}}''_{\text{Buie}}(\theta)\sin(\theta)d\theta \tag{2-53}$$

$$\hat{\hat{q}}''_{\text{Buie, aureole}}=\int_{\theta_{\text{disc}}}^{\theta_{\text{aureole}}}\hat{\hat{q}}''_{\text{Buie}}(\theta)\sin(\theta)d\theta \tag{2-54}$$

The solar disc part of the function is challenging to integrate analytically and a numerical piecewise linear integration using the trapezoidal rule is preferred. The interval $\theta\in[0,\theta_{\text{disc}}[$ is discretised into $N_{\theta_{\text{disc}}}$ angular elements of $\Delta_\theta=\theta_{\text{disc}}/N_{\theta_{\text{disc}}}$ angular range to obtain the integrated solar disc region of the Buie sunshape. Buie gave his sunshape expression with angles declared in miliradians and a conversion factor of 10^3 is here introduced to use radians instead. The integrated normalised Buie intensity on each interval is:

$$\int_{i\Delta_\theta}^{(i+1)\Delta_\theta}\hat{\hat{q}}''_{\text{Buie}}(\theta)\sin(\theta)d\theta\simeq\frac{\Delta_\theta}{2}\left(\sin\left((i+1)\Delta_\theta\right)\hat{\hat{q}}''_{\text{Buie}}\left(10^3(i+1)\Delta_\theta\right)+\sin(i\Delta_\theta)\hat{\hat{q}}''_{\text{Buie}}\left(10^3 i\Delta_\theta\right)\right) \tag{2-55}$$

The overall solar disc region integration is:

$$\hat{\hat{q}}''_{\text{Buie, disc}}=\sum_{i=1}^{N_{\theta_{\text{disc}}}}\left[\frac{\Delta_\theta}{2}\left(\sin\left((i+1)\Delta_\theta\right)\hat{\hat{q}}''_{\text{Buie}}\left(10^3(i+1)\Delta_\theta\right)+\sin(i\Delta_\theta)\hat{\hat{q}}''_{\text{Buie}}\left(10^3 i\Delta_\theta\right)\right)\right] \tag{2-56}$$

To determine a suitable number of linear segments in the trapezoidal integration, the solar disc region was first integrated using $N_{\theta_{\text{disc}}}=1{,}000{,}000$ elements to obtain a virtually error free integration and then a sensitivity analysis on $N_{\theta_{\text{disc}}}$ was carried out, as shown in Figure 2-5. The integration error is defined here as the relative difference between the value obtained with $N_{\theta_{\text{disc}}}$ and the value obtained with $N_{\theta_{\text{disc}}}=1{,}000{,}000$.

$$\text{integration error}=\left|\frac{\hat{\hat{q}}''_{\text{Buie, disc, N}_{\theta_{\text{disc}}}}-\hat{\hat{q}}''_{\text{Buie, disc, N}_{\theta_{\text{disc}}}=1{,}000{,}000}}{\hat{\hat{q}}''_{\text{Buie, disc, N}_{\theta_{\text{disc}}}=1{,}000{,}000}}\right| \tag{2-57}$$

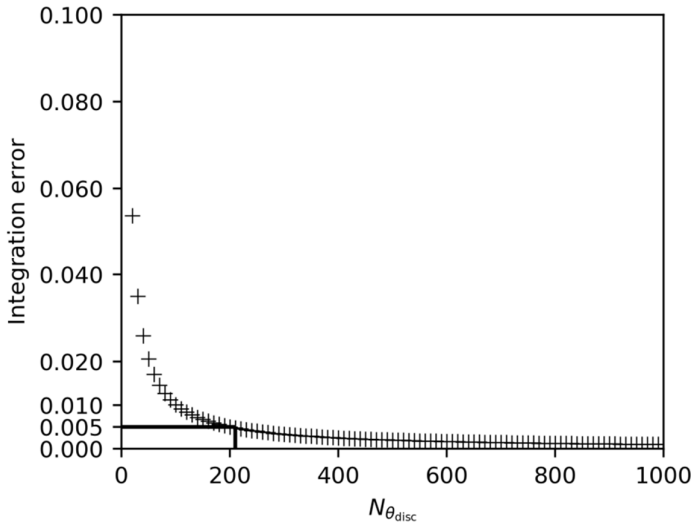

Figure 2-5: Sensitivity analysis on the trapezoidal integration of the solar disc region of the Buie sunshape.

$N_{\theta_{disc}}$ is set to 210 elements to obtain an integration error below 0.005 (0.5%).

The analytical integration for the aureole or circumsolar region of the Buie sunshape is:

$$\hat{\dot{q}}''_{\text{Buie, aureole}} = \int_{\theta_{disc}}^{\theta_{aureole}} e^{\kappa} \left(10^3 \theta\right)^{\gamma} \sin(\theta) d\theta \tag{2-58}$$

Using Buie's approximation, θ is small therefore $\sin(\theta) \simeq \theta$. The integration becomes:

$$\hat{\dot{q}}''_{\text{Buie, aureole}} = 10^{-6} \frac{e^{\kappa}}{\gamma+2} \left[\left(10^3 \theta_{\text{aureole}}\right)^{\gamma+2} - \left(10^3 \theta_{\text{disc}}\right)^{\gamma+2} \right] \tag{2-59}$$

The 10^3 and 10^{-6} factors added in the two previous equations are a direct consequence of the choice of units made by Buie in his study. In the original study, the choice is made to use miliradians as working units. The CDF approximation is:

$$P_{\text{Buie}}(\theta) \approx \frac{\int_0^{\theta} \hat{\dot{q}}''_{\text{Buie}}(t) \sin(t) dt}{\hat{\dot{q}}''_{\text{Buie, disc}} + \hat{\dot{q}}''_{\text{Buie, aureole}}} \tag{2-60}$$

The declaration of the Buie sunshape direction unit vectors as a function of a random variate $\Re_{\theta}$ is performed differently depending on the domain. For the solar disc region, the sunshape is numerically integrated using the trapezoidal integration. Using the previously mentioned angular interval:

$$j = \left\lfloor \frac{\theta}{\Delta_{\theta}} \right\rfloor \tag{2-61}$$

$$\theta_j = j\Delta_{\theta} \tag{2-62}$$

$$P_{\text{Buie}}\left(\theta_j\right) \approx \frac{\sum_{i=1}^{j}\left[\frac{\Delta_\theta}{2}\left(\sin\left((i+1)\Delta_\theta\right)\hat{q}''_{\text{Buie}}\left(10^3(i+1)\Delta_\theta\right)+\sin\left(i\Delta_\theta\right)\hat{q}''_{\text{Buie}}\left(10^3 i\Delta_\theta\right)\right)\right]}{\hat{q}''_{\text{Buie, disc}}+\hat{q}''_{\text{Buie, aureole}}} \quad (2\text{-}63)$$

The values of $P_{\text{Buie}}\left(\theta_j\right)$ are pre-calculated and stored to be compared with the random variate $\Re_\theta$. A new random variate $\Re^*_\theta$ is declared to determine a θ angle for each ray in this linearly approximated segment of the Buie sunshape:

$$\theta = \theta_j + \Re^*_\theta \Delta_\theta \text{ for } \Re_\theta \in \left[P_{\text{Buie}}\left(\theta_j\right), P_{\text{Buie}}\left(\theta_{j+1}\right)\right[\quad (2\text{-}64)$$

For the circumsolar region, using 2-59:

$$P_{\text{Buie}}\left(\theta\right) \approx \frac{\hat{q}''_{\text{Buie, disc}} + 10^{-6}\frac{e^\kappa}{\gamma+2}\left[\left(10^3\theta\right)^{\gamma+2}-\left(10^3\theta_{\text{disc}}\right)^{\gamma+2}\right]}{\hat{q}''_{\text{Buie, disc}}+\hat{q}''_{\text{Buie, aureole}}} \quad (2\text{-}65)$$

$$P_{\text{Buie, disc}} = P_{\text{Buie}}\left(\theta \,|\, \theta < \theta_{\text{disc}}\right) \quad (2\text{-}66)$$

$$P_{\text{Buie, aureole}} = P_{\text{Buie}}\left(\theta \,|\, \theta_{\text{disc}} \le \theta < \theta_{\text{aureole}}\right) \quad (2\text{-}67)$$

The following equation is used to sample θ from the probability distribution function:

$$\Re_\theta = P_{\text{Buie}}\left(\theta\right) \quad (2\text{-}68)$$

Using eqs. 2-68 and 2-65:

$$\theta = 10^{-3}\left(\left(10^3\theta_{\text{disc}}\right)^{\gamma+2} + 10^6\frac{\gamma+2}{e^\kappa}\left(\Re_\theta-1\right)\hat{q}''_{\text{Buie, disc}} + \Re_\theta\left[\left(10^3\theta_{\text{aureole}}\right)^{\gamma+2}-\left(10^3\theta_{\text{disc}}\right)^{\gamma+2}\right]\right)^{\frac{1}{\gamma+2}} \quad (2\text{-}69)$$
$$\text{for } \Re_\theta \in \left[P_{\text{Buie, disc}}, P_{\text{Buie, aureole}}=1\right[$$

Rearranging eq. 2-69:

$$\theta = \left(\left(\Re_\theta-1\right)\left(\frac{\gamma+2}{10^{3\gamma}e^\kappa}\hat{q}''_{\text{Buie, disc}}-\theta_{\text{disc}}{}^{\gamma+2}\right)+\Re_\theta\theta_{\text{aureole}}{}^{\gamma+2}\right)^{\frac{1}{\gamma+2}} \quad \text{for } \Re_\theta \in \left[P_{\text{Buie, disc}}, P_{\text{Buie, aureole}}=1\right[\quad (2\text{-}70)$$

The azimuthal CDF and uniform random sampling for the Buie sunshape is:

$$P_{\text{Buie}}\left(\varphi\right) = \frac{\varphi}{2\pi} \quad (2\text{-}71)$$

$$\varphi = 2\pi\Re_\varphi \quad (2\text{-}72)$$

The Buie sunshape direction unit vectors are:

$$\hat{\mathbf{d}}_{\text{Buie}} = \sin\left(\theta\right)\cos\left(2\pi\Re_\varphi\right)\hat{\mathbf{x}} + \sin\left(\theta\right)\sin\left(2\pi\Re_\varphi\right)\hat{\mathbf{y}} + \cos\left(\theta\right)\hat{\mathbf{z}} \quad (2\text{-}73)$$

with:

$$\begin{cases} \Re_\theta \in \left[P_{\text{Buie}}\left(\theta_j\right), P_{\text{Buie}}\left(\theta_{j+1}\right) \right[\rightarrow \theta_j \\ \theta = \theta_j + \Re_\theta^* \Delta_\theta \end{cases} \quad \text{for } \Re_\theta \in \left[0, P_{\text{Buie, disc}} \right[$$

$$\theta = \left(\left(\Re_\theta - 1\right) \left(\frac{\gamma+2}{10^{3\gamma} e^{\kappa}} \hat{q}''_{\text{Buie, disc}} - {\theta_{\text{disc}}}^{\gamma+2} \right) + \Re_\theta {\theta_{\text{aureole}}}^{\gamma+2} \right)^{\frac{1}{\gamma+2}} \quad \text{for } \Re_\theta \in \left[P_{\text{Buie, disc}}, P_{\text{Buie, aureole}} = 1 \right[\tag{2-74}$$

An integration of the Buie sunshape with 1,000,000 random samples is shown and compared with the analytical formulation by Buie for validation.

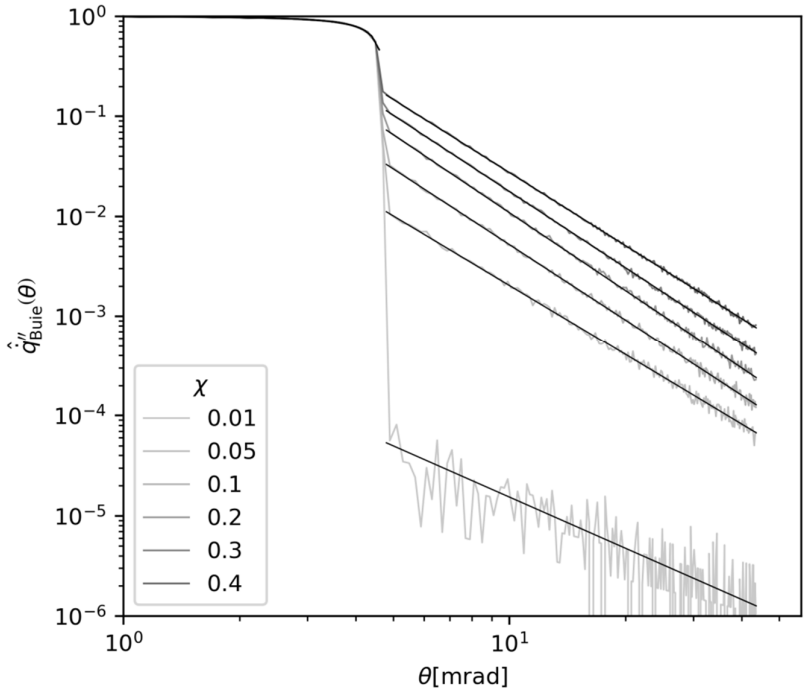

Figure 2-6: Buie sunshape integration validation. The analytical normalised angular flux values are in black and the corresponding integrated sunshapes in greyscales.

2.1.3.6 Comments on simulating solar radiation with the Buie sunshape.

As pointed-out in Rabl and Bendt [123] the CSR is hard to correlate with easily measured weather data and using the Buie Sunshape can be complicated for realistic models, to evaluate yearly performance of systems for example. Most sites suitable to CSP, however, would be located in sites with rather high quality irradiation and may expect low values of CSR. Figure 2-7 shows a comparison between the CSR input to the Buie sunshape model and and the modelled CSR obtained, evaluated through the integration of the sunshape distribution. A discrepancy between input and output of CSR values appears, especially in the lower range of CSR that matters for CSP, as shown in Figure 2-7 (b).

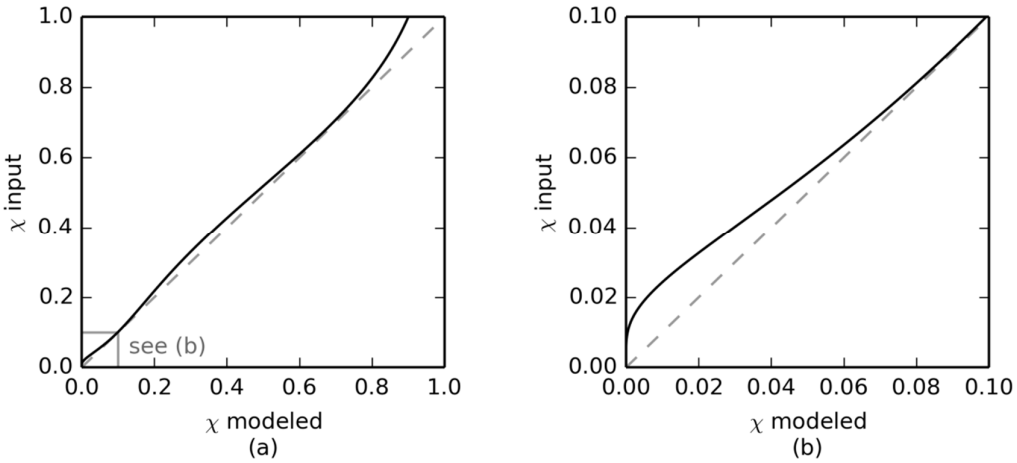

Figure 2-7: Comparison between the CSR input and the obtained CSR output using a Buie sunshape model.

Theoretically, the CSR input and output values should be identical. This discrepancy in lower CSR ranges can lead to an underestimation of the angular spread of solar intensity and consequently an overestimation of the incoming resource quality when simulating solar radiation. When the CSR reaches values higher than 0.8, the Buie sunshape model is not adapted to describe the solar intensity distribution as the sunshape model itself produces unrealistic profiles as shown in Figure 2-8.

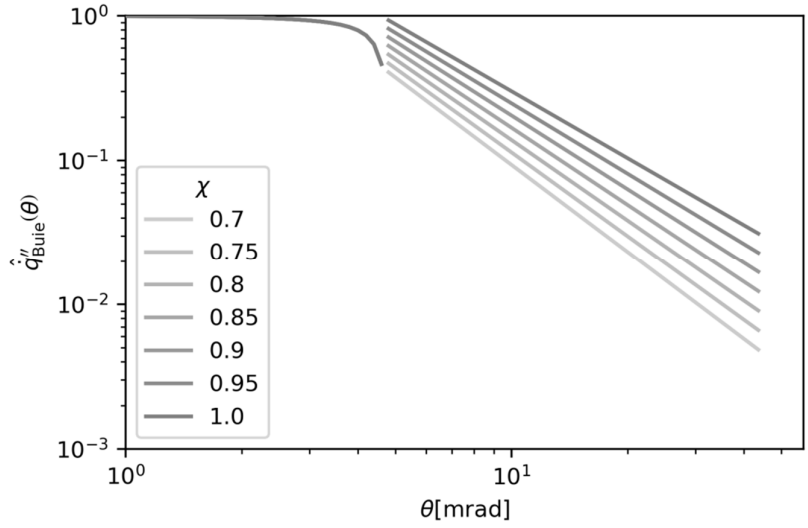

Figure 2-8: Unrealistic Buie sunshape profiles for CSR values over 0.7.

The accuracy of the sunshape at high CSR values is not a real concern for CSP modelling as CSP systems are unlikely to be installed and operate in regions subject to this type of solar radiation conditions. In order to obtain expected values of CSR output from the Buie Sunshape model without corrupting its validity, a corrected CSR input, χ_{cor}, is required. The following equation presents two quartic polynomial equations that were obtained by polynomial fitting and can be used to correct the input factor and obtain the adequate sunshape output from the model.

$$\begin{cases} \chi_{cor} = -2245\chi^4 + 520.7\chi^3 - 39.39\chi^2 + 1.891\chi + 0.008 & \text{for } \chi \in]0, 0.1] \\ \chi_{cor} = 1.973\chi^4 + 2.481\chi^3 + 0.607\chi^2 + 1.151\chi - 0.020 & \text{for } \chi > 0.1 \end{cases} \quad (2\text{-}75)$$

The modelled CSR values using the un-corrected and corrected CSR values are shown in Figure 2-9.

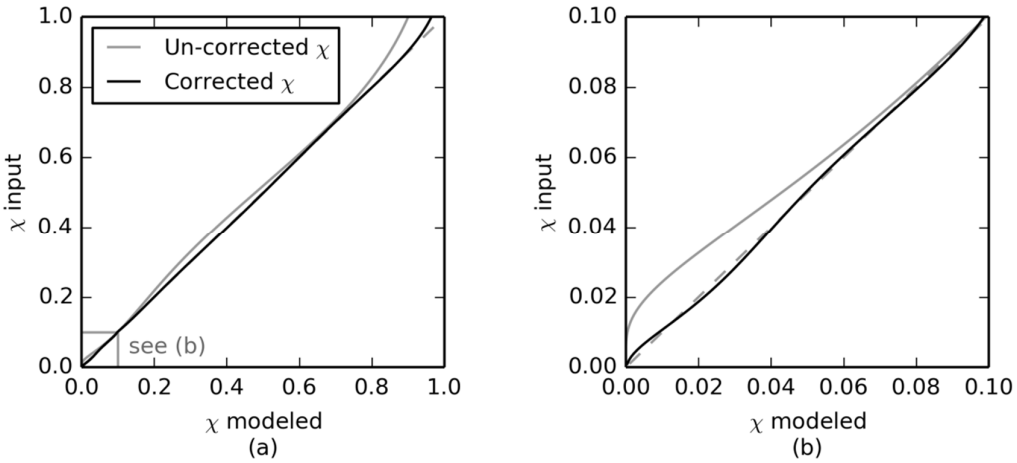

Figure 2-9: Corrected CSR input/modelled comparison.

With this corrected CSR, the sunshape modelled will have a CSR much closer to the desired value. In practice, once a CSR value is chosen for a simulation, the corrected CSR is calculated and used as the variable for the sunshape integration described earlier.

2.2 Concentrating optics

2.2.1 Point focus concentrator fundamentals

Notations and conventions on fundamental concepts are introduced here and will be referred to in the rest of this work.

2.2.1.1 Specular reflection on planes and parabolae

Solar concentration is obtained by optically re-directing the radiation coming to the aperture of the concentrator to a smaller region. The redirection of light follows the Snell-Descartes law of reflection and refraction.

$$n_1 \sin(\theta_1) = n_2 \sin(\theta_2) \quad (2\text{-}76)$$

With n_1 and n_2 the refraction indices of the media, θ_1 the incident angle to the surface normal and θ_2 the reflected angle to the surface normal (Figure 2-10).

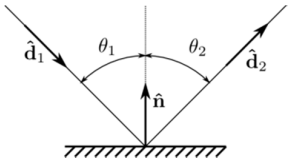

Figure 2-10: Illustration of the ideal specular reflection according to the Snell-Descartes law.

The direction unit vector of the specular reflection $\hat{\mathbf{d}}_2$ is obtained from the incident direction unit vector $\hat{\mathbf{d}}_1$ and the normal unit vector $\hat{\mathbf{n}}$ with:

$$\hat{\mathbf{d}}_2 = 2\left(\hat{\mathbf{n}}.\hat{\mathbf{d}}_1\right)\hat{\mathbf{n}} - \hat{\mathbf{d}}_1 \tag{2-77}$$

The normal unit vector depends on the surface geometry. A plane is described with the equation:

$$ax + by + cz + d = 0 \tag{2-78}$$

The normal unit vector at any point on this plane is obtained by taking the partial derivate of each position vector component, inverting the direction of the resulting vector and normalising it:

$$\hat{\mathbf{n}} = \frac{1}{\sqrt{a^2 + b^2 + c^2}}\left(-a\hat{\mathbf{x}} - b\hat{\mathbf{y}} - c\hat{\mathbf{z}}\right) \tag{2-79}$$

In most CSP systems, the light is reflected by mirror surfaces to a target and the aperture of the receiver placed at that location. The ideal concentrator shape used to perform this optical process is the parabola which focuses collimated incoming light to a single point as shown in Figure 2-11.

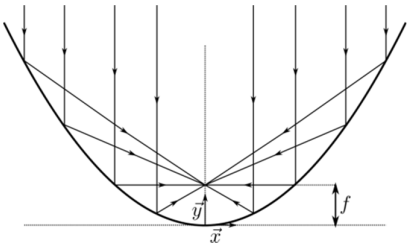

Figure 2-11: Illustration of the parabola reflection property.

The focal length f determines the position of the focus of the parabola. The equation of the parabola in two dimensions is:

$$y = \frac{x^2}{4f} \tag{2-80}$$

The normal unit vector at any point of a parabola in the two dimension case is:

$$\hat{\mathbf{n}} = \frac{1}{\sqrt{x^2 + 4f^2}}\left(-x\hat{\mathbf{x}} + 2f\hat{\mathbf{y}}\right) \tag{2-81}$$

Eq. 2-80 is extended in the three dimensional case to paraboloid surfaces in eq. 2-82:

$$z = \frac{x^2 + y^2}{4f} \tag{2-82}$$

In the three dimension situation, the normal to the surface is:

$$\hat{\mathbf{n}} = \frac{1}{\sqrt{x^2 + y^2 + 4f^2}} \left(-x\hat{\mathbf{x}} - y\hat{\mathbf{y}} + 2f\hat{\mathbf{z}} \right) \tag{2-83}$$

2.2.1.2 Point focus concentrators

The two most common point focus concentrators are the parabolic dish and the heliostat field. Dish concentrators are commonly defined using a combination of aperture plane radius and rim angle as presented in Figure 2-12.

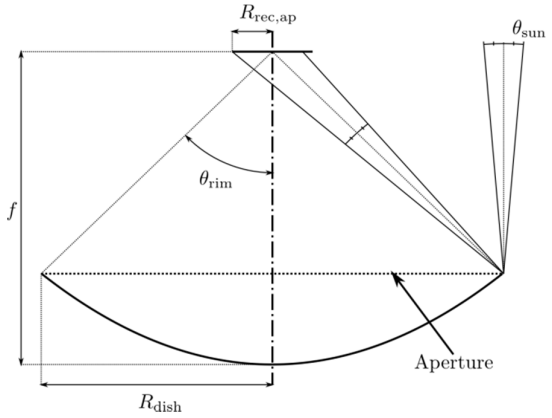

Figure 2-12: Parabolic dish profile definition using the concentrator radius and the rim angle.

The rim angle and the focal length of the concentrator are linked by the following relation:

$$\theta_{\mathrm{rim}} = \arctan\left(\frac{4 f R_{\mathrm{dish}}}{4f^2 - R_{\mathrm{dish}}^2} \right) \tag{2-84}$$

Heliostat fields are Fresnel discretisation versions of dish concentrators, as illustrated in Figure 2-13. The mirror surface of heliostat fields is composed of numerous heliostats focusing the radiation on a receiver situated at the top of a tower.

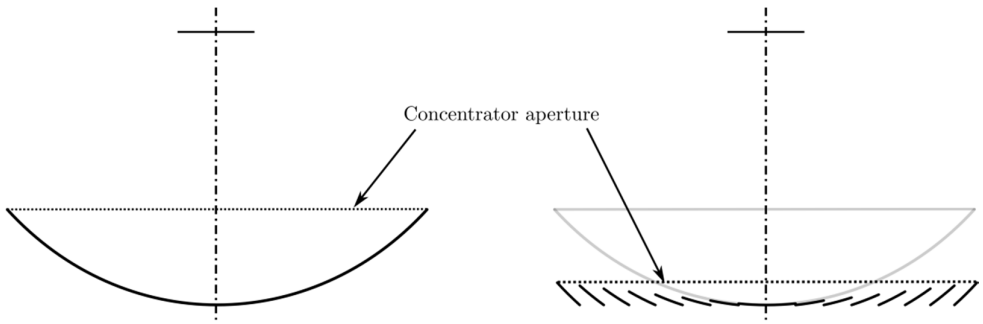

Figure 2-13: Heliostat field as Fresnel optics version of a parabolic dish.

Heliostat fields are commonly differentiated according to the general layout relatively to the tower. Heliostat fields that spread around the tower are labelled “surround fields” and heliostat fields that face only one side of the tower are labelled “polar fields”, as illustrated in Figure 2-14. The field layout has an influence on the spatial distribution of the concentrated radiation and consequently impacts receiver design.

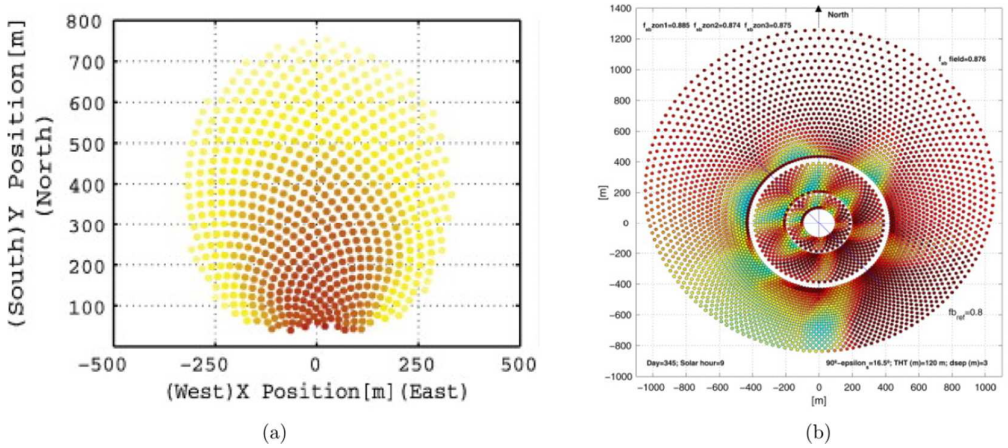

Figure 2-14: (a) Polar field using the biomimetic layout method [104] and (b) surround field using the Campo method [28].

A heliostat field is defined by a list of heliostat spatial coordinates and dimensions as well as a receiver position. Heliostats are generally composed mirror facets that do not follow exactly the parabolic curvature required and these facets are often “canted” to approach a parabolic behaviour and improve their accuracy. As a consequence, it is often more accurate to model heliostats as parabolic surfaces. It is common to give the heliostat coordinates relative to the tower base, placed at the centre of the referential and from the heliostat pivot point altitude.

2.2.1.3 Sun tracking

The sun position in the sky depends on the location on the surface of the earth and time. Opensource algorithms exist to describe the position of the sun in the sky precisely [16]. As the sun position in the sky changes during the day, the concentrators have to re-align, or “track” the sun, to continuously focus the incoming radiation to the right position. In parabolic dish concentrators it is done by positioning the axis of symmetry of the paraboloid collinear to the solar vector. In heliostat fields, each heliostat is aligned independently. Given a solar vector $\hat{\mathbf{d}}_{\text{sun}}(t)$, the heliostat position $\mathbf{r}$ and an aim point $\mathbf{r}_{\text{aim}}$ on the receiver, the aiming unit direction vector $\hat{\mathbf{d}}_{\text{aim}}(\mathbf{r})$ is:

$$\hat{\mathbf{d}}_{\text{aim}}(\mathbf{r}) = \frac{\mathbf{r}_{\text{aim}} - \mathbf{r}}{\left\| \mathbf{r}_{\text{aim}} - \mathbf{r} \right\|} \tag{2-85}$$

The heliostat normal unit direction vector $\hat{\mathbf{n}}(\mathbf{r},t)$ is positioned collinear to the bisectrix of the angle formed by the solar vector and the aiming vector, illustrated in Figure 2-15:

$$\hat{\mathbf{n}}(\mathbf{r},t) = \frac{\hat{\mathbf{d}}_{\text{sun}}(t) + \hat{\mathbf{d}}_{\text{aim}}(\mathbf{r})}{\left\| \hat{\mathbf{d}}_{\text{sun}}(t) + \hat{\mathbf{d}}_{\text{aim}}(\mathbf{r}) \right\|} \tag{2-86}$$

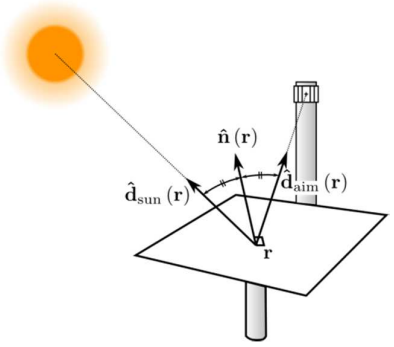

Figure 2-15: Heliostat tracking alignment illustration.

Several alternative actuation configurations exist to align the concentrator normal vectors on the desired direction. Among the existing tracking methods, the azimuth-elevation tracking is the most common one but alternative actuation mechanisms exist [26].

2.2.1.4 Concentration definitions

The geometrical concentration C_{g} of a concentrator is defined as the ratio of concentrator aperture to receiver aperture and gives an approximation of the overall radiative flux multiplication provided by the concentrator.

$$C_{\text{g}} = \frac{A_{\text{con,ap}}}{A_{\text{rec,ap}}} \tag{2-87}$$

The concentration level at the receiver aperture is non-uniform and the optical concentration $C_{\text{opt}}(\mathbf{r})$, ratio of the local radiative flux to the DNI, can be used to describe local concentration values.

$$C_{\text{opt}}(\mathbf{r}) = \frac{\dot{q}''(\mathbf{r})}{G} \tag{2-88}$$

There is a limit to the achievable geometrical concentration that can be obtained by CSP concentrators which is imposed by the angular distribution of the incoming radiation [92]. For dish concentrators with a 2D circular aperture, the geometrical concentration is expressed with:

$$C_{g,2D} = \frac{\sin^2(2\theta_{rim})}{4\sin^2(\theta_{sun})} \tag{2-89}$$

For dish concentrators with spherical receiver apertures, the geometrical concentration is:

$$C_{g,2D} = \frac{\sin^2(\theta_{rim})}{4\sin^2(\theta_{sun})} \tag{2-90}$$

$C_{g,2D}$ is maximised for rim angles of 45° for flat apertures and 90° for spherical apertures and reaches the same value for both configurations. Considering that all solar radiation is received in the $\theta_{sun} = 4.65$ mrad angle as in a pillbox sunshape distribution, the limit $C_{g,max,2D}$ is:

$$C_{g,2D,max} = \frac{1}{4\sin^2(\theta_{sun})} = 11,600 \tag{2-91}$$

This ideal limit of geometrical concentration is not an attainable value in real concentrator operations because of the non-uniformity of the angular solar irradiance and concentrator imperfections mentioned in the next section. The geometrical concentration limit represents the limit in average concentration over the receiver aperture and it can be locally exceeded. The non-uniformity of the optical concentration on the receiver aperture is analysed in more detail in further sections of this thesis.

2.2.2 Non-ideal concentration optics

2.2.2.1 Reflectance

In real surfaces, a fraction of the incident energy is absorbed by the concentrator surface and the reflectance, which is defined as the ratio of the reflected energy to the incident energy, is less than 1. The spectral bi-directional reflection function $\rho(T, \lambda, \hat{\mathbf{d}}_1, \hat{\mathbf{d}}_2)$ models the reflective behaviour of real surfaces. The reflectance of a material is a function of the temperature T of the material, $\hat{\mathbf{d}}_1$ the incident direction of the radiation considered, $\hat{\mathbf{d}}_2$ the reflected direction considered and λ the wavelength of the incident radiation [101] (Figure 2-16). In solar collector studies, the relatively low and steady temperature of the concentrator surface does not have a strong influence on the reflectance. In addition, the materials used, silver backed glass in most CSP collectors, are highly specular and can be approximated by fully specular materials. Finally, the spectral dependency of the reflectance is not usually considered in collectors studies and the total reflectance, integrated over the spectrum is used instead. The total specular reflectance of the material ρ_{con} will be used in the collector models presented in this dissertation.

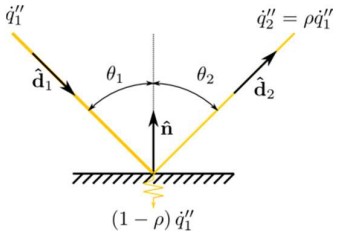

Figure 2-16: Illustration of the total specular reflectivity.

2.2.2.2 Geometric error

The orientation of the reflective surfaces of real world concentrators differs from ideal shapes and consequently limits the performances of concentrating optics by causing off-focus reflections. Four different factors influence this imperfection:

- The specularity error $\mathbf{e}_{\text{spec}}$ accounts for the microscopic errors arising form non-ideal specular behaviour of the materials used.
- The surface slope error $\mathbf{e}_{\text{slope}}$ accounts for local microscopic geometrical effects resulting from the manufacturing of the mirror facets.
- Concentrator shape error $\mathbf{e}_{\text{shape}}$ accounts for macroscopic effects related to the shape of the concentrator arising from fabrication errors, or deformations arising from thermal stress loads, gravity sag or wind loads for example.
- Tracking error $\mathbf{e}_{\text{track}}$ is associated with non-ideal tracking position of the optical concentrator.

All these error mechanisms affect the orientation of the surface met by the incoming radiation. An approximation to take these orientation errors into account is to artificially modify the direction of the normal unit vector of the surface when calculating the reflected radiation direction. The realistic normal unit vector is obtained by adding error components to the ideal normal and normalising:

$$\hat{\mathbf{n}}_{\text{real}}(\mathbf{r}) = \frac{\hat{\mathbf{n}}(\mathbf{r}) + \hat{\mathbf{e}}_{\text{spec}} + \hat{\mathbf{e}}_{\text{slope}} + \hat{\mathbf{e}}_{\text{shape}} + \hat{\mathbf{e}}_{\text{track}}}{\left\| \hat{\mathbf{n}}(\mathbf{r}) + \hat{\mathbf{e}}_{\text{spec}} + \hat{\mathbf{e}}_{\text{slope}} + \hat{\mathbf{e}}_{\text{shape}} + \hat{\mathbf{e}}_{\text{track}} \right\|} \tag{2-92}$$

It is common accepted practice to model components of these local error vectors as randomly distributed bi-variates following centred normal law distributions $N(\sigma)$ [152]. A consequence of this assumption is the possibility to regroup all geometrical surface errors into a single total surface normal error vector with a standard deviation $\sigma_{\hat{\mathbf{n}}}$ of [90]:

$$\sigma_{\hat{\mathbf{n}}} = \sqrt{\sigma_{\text{spec}}^2 + \sigma_{\text{slope}}^2 + \sigma_{\text{shape}}^2 + \sigma_{\text{track}}^2} \tag{2-93}$$

The resulting local surface error vector is:

$$\hat{\mathbf{e}}_{\hat{\mathbf{n}}} = e_x\hat{\mathbf{x}} + e_y\hat{\mathbf{y}} + \cos\left(\sin^{-1}\left(\sqrt{e_x^2 + e_y^2}\right)\right)\hat{\mathbf{z}} \tag{2-94}$$

With e_x and e_x determined using angles randomly sampled from normal law distribution algorithm samplings such as the Ziggurat algorithm used in NumPy and SciPy as well as in the GSL library [95].

$$\begin{cases} e_x = \sin\left(\theta_{e_x}\right) \text{ with } \theta_{e_x} = N^{-1}\left(\sigma_s, \Re_{e_x}\right) \\ e_y = \sin\left(\theta_{e_y}\right) \text{ with } \theta_{e_y} = N^{-1}\left(\sigma_s, \Re_{e_y}\right) \end{cases} \tag{2-95}$$

The real surface normal is obtained with eq. 2-96:

$$\hat{\mathbf{n}}_{\text{real}} = \hat{\mathbf{n}} + \hat{\mathbf{e}}_{\hat{\mathbf{n}}} \tag{2-96}$$

Figure 2-17 summarises the angular and vector conventions used to declare realistic normals.

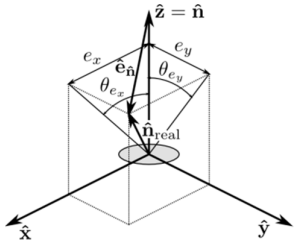

Figure 2-17: Modification of the surface normal vector to take into account geometrical errors.

These results are for the characterisation of the surface normal error and not the beam distribution error which is the result of interest for MCRT based models. When calculating the beam distribution error directly, the impact of any modification of the surface orientation is doubled because of reflections.

2.2.3 Concentrator energy loss

So far, the only energy loss mechanism mentioned was the absorption of a fraction of the incident solar radiative flux by the concentrator surface. The geometric errors are redirecting the radiation in non-ideal directions but the energy is not lost as it can still be used by the receiver, provided that the receiver is able to intercept it. Two other mechanisms affect concentrator operations: atmospheric attenuation and blocking. Depending on the efficiency definition associated with the concentrator, some additional cosine and shading loss mechanisms need to be considered.

2.2.3.1 Atmospheric attenuation

After reflection by the concentrator surface, radiation passes through the space between the reflection location and the receiver aperture. This space is usually filled with a mixture of air and particulate matter in suspension and is not perfectly transparent. A fraction of the reflected energy is consequently absorbed and constitutes a loss for the system, usually named atmospheric attenuation loss. Atmospheric attenuation is generally neglected in systems in which this distance travelled is small, such as parabolic dishes or troughs. In large heliostat fields, however, atmospheric attenuation can have a non-negligible impact and needs to be considered. Several models exist to describe atmospheric attenuation [9].

2.2.3.2 Shading

Shading is absorption of a fraction of the incident radiation on its way to the concentrator by a part of the system that does not participate in the concentration process. The intercepted solar radiation does not reach the concentrator and is therefore not redirected to the receiver aperture. Typically, shading is caused by the receiver and its support structure casting a shadow on the concentrator as illustrated in Figure 2-18 (a).

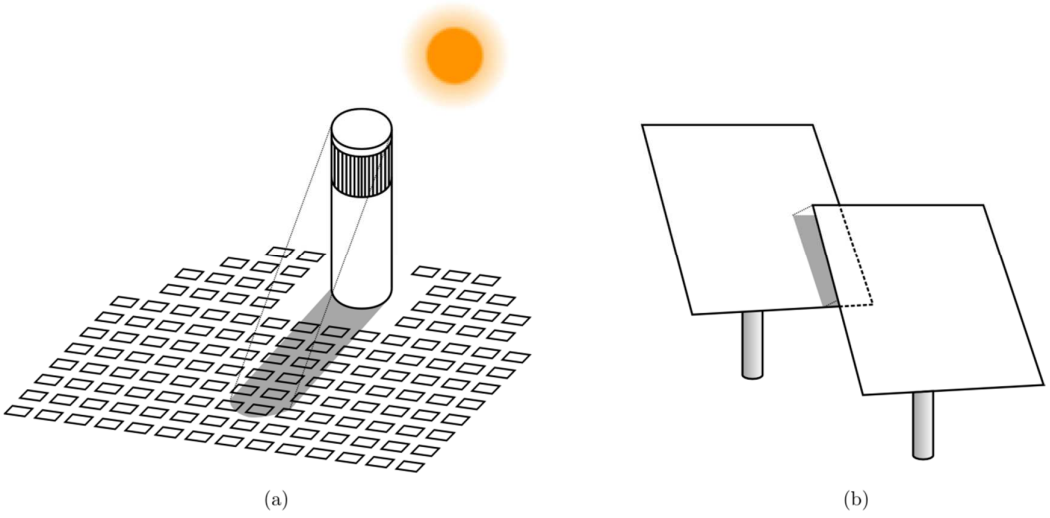

Figure 2-18: (a) Tower and receiver shading on a heliostat field and (b) heliostat field self-shading illustration.

Another aspect of shading is self-shading. In Fresnel type optics such as heliostat fields, the discretised structure of the concentrator causes some sections of the concentrator to cast a shadow on others depending on the sun position as illustrated in Figure 2-18 (b) with two heliostats. Shading is not technically a loss of energy as it affects radiation before it reaches the concentrator surface. Shading caused by the receiver is associated to the receiver design in the rest of this document. Self-shading is useful to characterise an inefficient usage of the concentrator surface in heliostat field layout studies. Shading is evaluated using spatial integrations methods such as MCRT or “cone optics”. Cone optics methods rely on analytical

spherical projection or convolution methods [78]. As mentioned earlier, all the optical simulations are using MCRT in this dissertation.

2.2.3.3 Blocking

Blocking occurs when a fraction of the reflected radiation is absorbed before reaching the receiver aperture. Blocking is generally non-inexistent in parabolic dishes, as the support structures of receivers are usually installed outside of the reflected rays path, but it has an impact on heliostat fields where some reflected radiation is intercepted by the back side of other heliostats as illustrated in Figure 2-19. Blocking loss is determined using the same type of simulation techniques as shading.

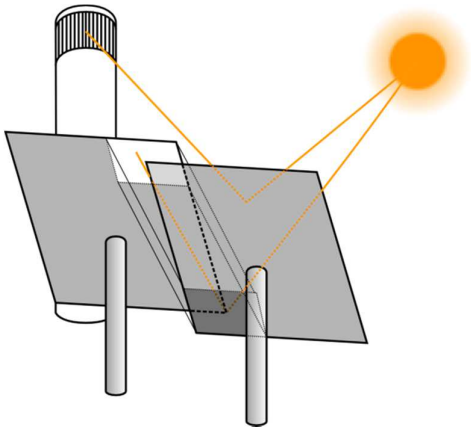

Figure 2-19: Illustration of blocking in a heliostat field.

2.2.4 Concentrator energy balance

The concentrator energy balance is summarised in the following equation and illustrated in Figure 2-20. The energy intercepted by the aperture of the concentrator $\dot{Q}_{con,ap}$ is equal to the sum of the energy reflected by the concentrator that is not intercepted before or attenuated $\dot{Q}_{con}$, the blocked energy $\dot{Q}_{bloc}$, the energy absorbed through atmospheric attenuation $\dot{Q}_{atm}$ and the energy absorbed at the concentrator surface due to non-ideal reflectance $\dot{Q}_{con,abs}$.

$$\dot{Q}_{con,ap} = \dot{Q}_{con} + \dot{Q}_{bloc} + \dot{Q}_{atm} + \dot{Q}_{con,abs} \quad (2\text{-}97)$$

With:

$$\dot{Q}_{con,ref} = \dot{Q}_{con,ap} - \dot{Q}_{con,abs} \quad (2\text{-}98)$$

$$\dot{Q}_{aim} = \dot{Q}_{con,ref} - \dot{Q}_{bloc} \quad (2\text{-}99)$$

$$\dot{Q}_{con} = \dot{Q}_{aim} - \dot{Q}_{atm} \quad (2\text{-}100)$$

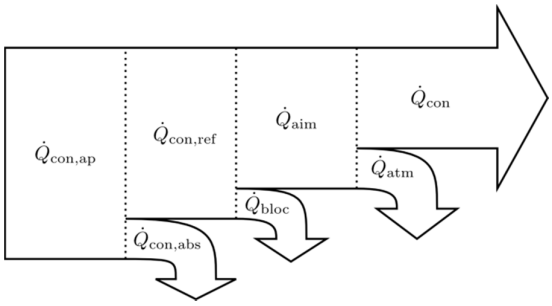

Figure 2-20: Concentrator energy balance from the collector aperture to the receiver aperture.

It can be convenient to use efficiency definitions for each of the processes involved in the concentration process. The following equation presents the efficiency of the concentrator.

$$\eta_{\text{con}} = \frac{\dot{Q}_{\text{con}}}{\dot{Q}_{\text{con,ap}}} \tag{2-101}$$

$$\eta_{\text{atm}} = \frac{\dot{Q}_{\text{con}}}{\dot{Q}_{\text{aim}}} \tag{2-102}$$

$$\eta_{\text{bloc}} = \frac{\dot{Q}_{\text{aim}}}{\dot{Q}_{\text{con,ref}}} \tag{2-103}$$

$$\eta_{\text{ref}} = \frac{\dot{Q}_{\text{con,ref}}}{\dot{Q}_{\text{con,ap}}} \tag{2-104}$$

$$\eta_{\text{con}} = \eta_{\text{atm}} \eta_{\text{bloc}} \eta_{\text{ref}} \tag{2-105}$$

In some situations, the denominator of the efficiency is not the flux incoming on the concentrator surface but the solar irradiance multiplied by the area of reflecting surface of the concentrator. This formulation is useful for heliostat field layout studies as it encompasses shading as well as the influence of the ground covering of the field, which is related to the real cost of the system. When this efficiency measure is chosen, some additional precautions have to be taken to account for all losses: shading needs to be explicitly declared in the efficiency computations and the “cosine” efficiency, accounting for the non-alignment of the concentrator aperture with the solar vector, has to be taken into account. Dish concentrators are not subject to cosine loss as their aperture is always orthogonal to the solar vector but heliostat fields do, depending on the sun position in the sky. The energy balance is presented in the following equation and illustrated in Figure 2-21:

$$GA_{\text{con}} = \dot{Q}_{\text{con}} + \dot{Q}_{\text{shad}} + \dot{Q}_{\text{cos}} + \dot{Q}_{\text{bloc}} + \dot{Q}_{\text{atm}} + \dot{Q}_{\text{con,abs}} \tag{2-106}$$

With:

$$\dot{Q}_{\text{con,inc}} = GA_{\text{con}} - \dot{Q}_{\text{shad}} \tag{2-107}$$

$$\dot{Q}_{\text{con,ap}} = \cos(\theta_{\text{in}})\dot{Q}_{\text{con,inc}} \tag{2-108}$$

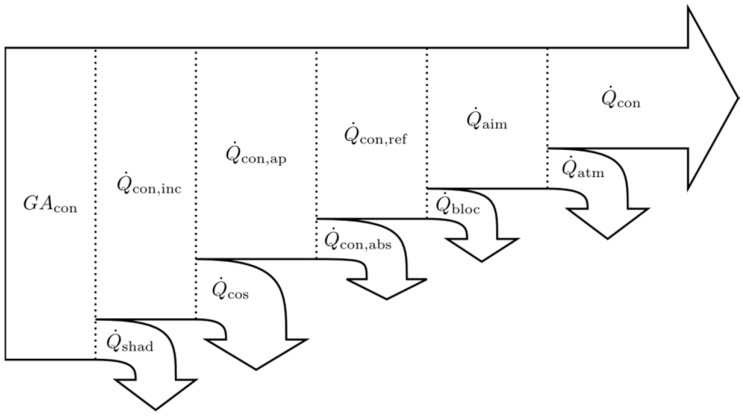

Figure 2-21: Concentrator energy balance using the overall reflective area and solar DNI as a reference.

The efficiencies in this situation are defined as follows:

$$\eta_{\text{con,tot}} = \frac{\dot{Q}_{\text{con}}}{GA_{\text{con}}} \tag{2-109}$$

$$\eta_{\text{cos}} = \frac{\dot{Q}_{\text{con,ap}}}{\dot{Q}_{\text{con,inc}}} \tag{2-110}$$

$$\eta_{\text{shad}} = \frac{\dot{Q}_{\text{con,inc}}}{GA_{\text{con}}} \tag{2-111}$$

$$\eta_{\text{con,tot}} = \eta_{\text{con}}\eta_{\text{cos}}\eta_{\text{shad}} = \eta_{\text{atm}}\eta_{\text{bloc}}\eta_{\text{ref}}\eta_{\text{cos}}\eta_{\text{shad}} \tag{2-112}$$

2.3 Receiver model

2.3.1 Receiver geometry nomenclature

An indirectly irradiated CSP receiver is a heat transfer device positioned at the focus of the concentrator to absorb radiation and transfer heat to a Heat Carrier (HC) also known as working fluid or heat transfer fluid, which transports heat outside the receiver volume. Figure 2-22 is an abstract representation of indirectly irradiated receivers.

The HC circulates in a heat exchanger, embedded in the receiver volume. The external surface of the receiver is decomposed into two categories:

- Absorber surfaces that contribute to the radiative heat transfer with the heat exchanger.
- Envelope surfaces that include support structure and the insulated surfaces that do not exchange radiatively with the heat exchanger.

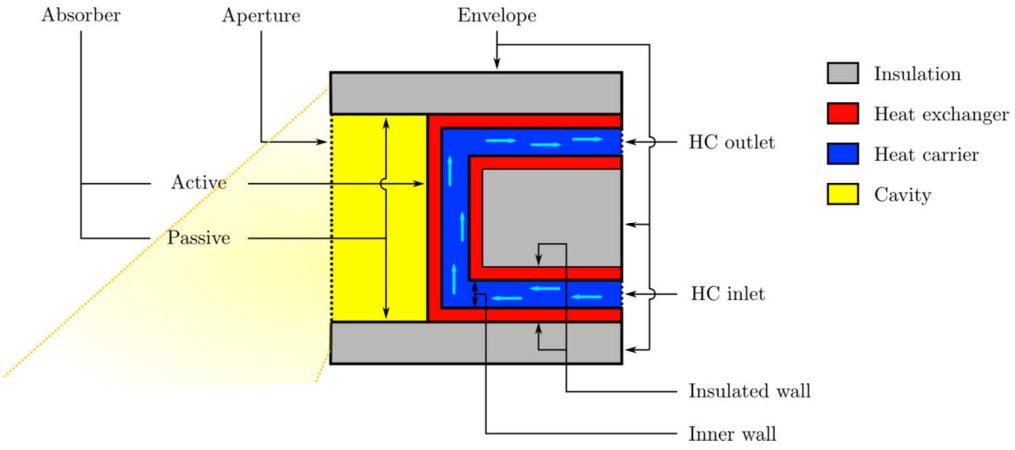

Figure 2-22: Schematic representation of surfaces and volumes in an indirectly irradiated receiver.

In addition to these surfaces, the aperture is defined as the smallest convex surface through which all radiation enters and leaves the receiver. With this definition, redistributive effects such as light-trapping and cavity-effect are more easily taken into account as will be shown in Section 2.3.5. If the aperture and the receiver surfaces are distinct, the volume formed in between is labelled cavity volume.

The absorber surfaces are subsequently divided into two regions:

- Active surfaces, through which heat is transferred to the HC via conduction.
- Passive surfaces, that radiatively exchange with the active surfaces.

The active surfaces of the receiver constitute the outer wall of the heat exchanger. The heat exchanger volume is the vessel in which the HC circulates and the HC flows through the HC volume. The surface marking the frontier between the two volumes is the inner wall surface of the heat exchanger. The surfaces of the heat exchanger that are not exposed to the concentrated radiative flux from the aperture are insulated and labelled insulated surfaces. The surfaces through which the HC flows in and out of the system are labelled HC inlet and HC outlet. The volume of the receiver that is not occupied by the heat exchanger is the insulation volume.

2.3.2 Radiative heat transfer on receiver surfaces

2.3.2.1 Opaque surfaces with isotropic properties

The surfaces of the receiver are considered opaque. This simplification is common for metals that generally absorb radiation over very small distances in the material [101]. Radiation incoming to an opaque surface from a direction $\hat{\mathbf{d}}$ is absorbed or reflected by the surface:

$$\alpha'\left(\lambda,T,\hat{\mathbf{d}}\right)+\rho'_{\text{hemi}}\left(\lambda,T,\hat{\mathbf{d}}\right)=1 \tag{2-113}$$

with $\alpha'\left(\lambda,T,\hat{\mathbf{d}}\right)$ the spectral direction absorptance of the surface defined as the ratio of the absorbed energy over the incoming energy and $\rho'_{\text{hemi}}\left(\lambda,T,\hat{\mathbf{d}}\right)$ the spectral directional-hemispherical reflectance of the surface [101]. The receiver surfaces considered have isotropic properties and are a function of the wavelength and temperature only. In the case of isotropic surface radiative properties or diffuse incoming radiation, the following equation is valid:

$$\alpha(\lambda,T)+\rho(\lambda,T)=1 \tag{2-114}$$

Where $\alpha(\lambda,T)$ is the spectral hemispherical absorptance and $\rho(\lambda,T)$ the spectral hemispherical reflectance.

2.3.2.2 Semigrey simplification

For non-black surfaces, the emitted flux is:

$$E(T)=\int_0^{+\infty} E_{b,\lambda}(\lambda,T)\varepsilon(\lambda,T)d\lambda \tag{2-115}$$

Assuming a DNI of $G=1000$ W.m^{-2}, the equivalent blackbody temperature of the sun, distinct from the real temperature of the extra-terrestrial solar radiation because it considers the several attenuation mechanisms presented earlier, is obtained from eq. (2-3) is $T_{\text{Sun}}(1000)=5345$ K. Hot receiver surfaces emit radiation at lower temperatures and over a different spectrum as shown in Figure 2-23.

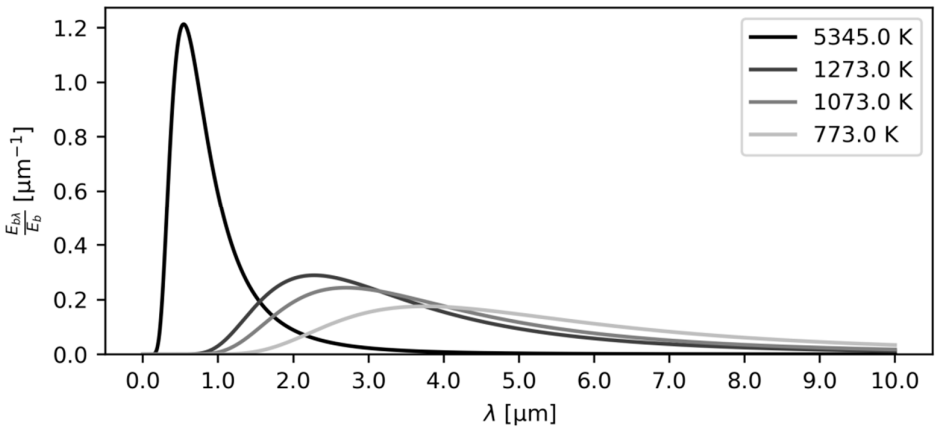

Figure 2-23: Black-body spectral emissive power normalised on the total black-body emissive power at four different temperatures.

The integration of Plank's distribution gives the fraction of radiation in distinct parts of the spectrum. This integration is complex and a good approximation of it is available in radiation textbooks using $f(n\lambda T)$ a tabulated density function [101].

$$\int_{\lambda_a}^{\lambda_b} E_{b,\lambda}(T,\lambda)d\lambda = \left[f(n\lambda_b T) - f(n\lambda_a T) \right] n^2 \sigma T^4 \quad (2\text{-}116)$$

In Table 2-1, the integrated values show that more than 90% of the solar radiative flux is contained in the 0 to 2 µm band of the spectrum while the thermal emissions from hot surfaces at the temperatures considered in Figure 2-23 are mostly emitted in wavelengths over 2 µm.

Table 2-1: Fraction of black-body power contained in the first portion of the spectrum for four temperature values and using linear interpolation from Modest (Modest 2003).

		λ			
	T	0-1.5 µm	0-2 µm	0-2.5 µm	0-3 µm
$\frac{\int_{\lambda_a}^{\lambda_b} E_{b,\lambda}(T,\lambda)d\lambda}{E_b}$	5762 K	0.856905	0.926894	0.95812	0.973906
	1273 K	0.053489	0.17136	0.314182	0.446978
	1073 K	0.020557	0.091252	0.201458	0.32227
	773 K	0.001636	0.01601	0.056852	0.123864

The relative partitioning of energy between distinct regions of the spectrum facilitates the treatment of radiative problems with materials having different properties in different regions of the spectrum.

Surfaces with radiative properties independent of the wavelength are called grey surfaces by analogy with black surfaces for black-body behaviour. It is assumed that the radiative properties of the materials used in the receiver can be approximated to grey surface properties with different values in different regions of the spectrum: this is the semigrey approximation. In the dual-band semigrey approach, one band is for the shorter wavelengths, characteristic of the concentrated solar irradiation in our case, and one for the longer wavelengths, for thermal emissions of hot surfaces.

The temperature of 1273 K (1000 °C) can be considered as an upper temperature boundary for receiver surfaces given that few materials can withstand such high temperature values and keep acceptable mechanical properties. The dual-band semigrey assumption is consequently a generally valid approximation to model indirectly heated receivers as the error it introduces in the calculation of radiative heat transfer is small thanks to the distinct regions of the spectrum occupied by solar radiation on one side (short wavelengths) and thermal emissions from hot surfaces on the other side (long wavelengths). Some factors will positively influence the accuracy of the method:

- The lower the temperatures of the hot surfaces, the better the accuracy as their spectrum of emission is located in the longer wavelengths and therefore little overlap exists with the solar spectrum.
- If the radiative properties of surfaces do not change a lot between the two bands, the results become less sensitive to the spectral effects.

Local thermodynamic equilibrium is assumed and Kirchhoff's law is applied. A dual-band semigrey approximation is assumed for all receiver surfaces with a step wavelength of $\lambda_{\text{step}} = 2$ μm and the radiative properties at each point of the receiver geometry are defined as follows:

$$\alpha(\mathbf{r}) = \varepsilon(\mathbf{r}) = \begin{cases} \alpha_{\lambda_0}(\mathbf{r}) = 1 - \rho_{\lambda_0}(\mathbf{r}) & \text{for } \lambda < \lambda_{\text{step}} = 2\ \mu\text{m} \\ \alpha_{\lambda_1}(\mathbf{r}) = 1 - \rho_{\lambda_1}(\mathbf{r}) & \text{for } \lambda \geq \lambda_{\text{step}} = 2\ \mu\text{m} \end{cases} \tag{2-117}$$

$$E(T) \approx \varepsilon_{\lambda_0} \int_0^{\lambda_{\text{step}}} E_{b,\lambda}(\lambda, T)\, d\lambda + \varepsilon_{\lambda_1} \int_{\lambda_{\text{step}}}^{+\infty} E_{b,\lambda}(\lambda, T)\, d\lambda \tag{2-118}$$

2.3.2.3 Diffuse directions

The receiver surfaces are assumed to be rough and exhibit diffuse reflection behaviour [101]. Diffuse reflections "spread" the incoming radiative flux in the open hemisphere centred on the normal unit vector to the surface. In Monte-Carlo ray-tracing, diffuse reflections are modelled by taking a random direction with a uniform probability distribution in the open hemisphere for each incoming reflected ray. Using a coordinate system with $\hat{\mathbf{z}}$ collinear to the surface normal as in previous sections, diffuse unit direction vectors $\hat{\mathbf{d}}_{\cap}$ are determined using eq. 2-49 and replacing θ_{disk} with $\theta_{\cap} = \pi/2$, the full extent of the hemisphere polar angle:

$$\hat{\mathbf{d}}_{\cap} = \left(\sqrt{\Re_\theta}\sin(\theta_{\cap})\right)\left(\cos(2\pi\Re_\varphi)\hat{\mathbf{x}} + \sin(2\pi\Re_\varphi)\hat{\mathbf{y}}\right) + \sqrt{1 - \Re_\theta \sin^2(\theta_{\cap})}\,\hat{\mathbf{z}} \tag{2-119}$$

2.3.2.4 View factors

The exchange of radiation between surfaces depends on the geometry. View factors are a convenient way of describing the geometrical relation between two surface elements and are presented extensively by Modest [101].

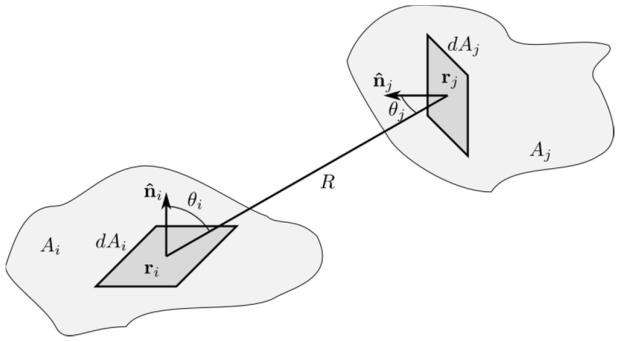

Figure 2-24: View factors between two surface elements.

The view factor between two elemental surface elements, presented in Figure 2-24, is:

$$dF_{dA_i \to dA_j} = \frac{\cos(\theta_i)\cos(\theta_j)}{\pi R^2} dA_j \tag{2-120}$$

When the intensity is constant on each of the surface elements considered, diffuse view factors are:

$$F_{A_i \to A_j} = \frac{1}{A_i} \int_{A_i} \int_{A_j} \frac{\cos(\theta_i)\cos(\theta_j)}{\pi R^2} dA_i dA_j \tag{2-121}$$

Specular view factors $F^s_{A_1 \to A_2}$ are the specular counterparts of diffuse view factors. Specular view factors are more complex to evaluate than diffuse view factors and generally require the use of numerical methods such as Monte-Carlo ray-tracing.

The summation and the reciprocity rules are important relations that apply to view factors. The summation rule states that the sum of the view factors from a surface to the rest of the system is 1.

$$\sum_{j=1}^{N} F_{A_i \to A_j} = 1 \tag{2-122}$$

The reciprocity rule states that view factors between two surfaces are “reversible” using the following relation:

$$A_i F_{A_i \to A_j} = A_j F_{A_j \to A_i} \tag{2-123}$$

2.3.3 Convective heat transfer

Convection is the movement of molecules of fluids within a fluid environment through diffusion and/or advection. Fluid molecules transport and exchange thermal energy, causing convective heat transfer, one of the three heat transfer modes. There are three distinct convection regimes:

- Natural convection is driven by buoyancy, the force created by density gradients. Density gradients in a fluid are created by temperature differences or gravitational effects. In receivers, natural convection is caused by the heating of the surrounding air by the hot surfaces of the absorber.
- Forced convection is driven by external forces bringing momentum to the fluid. In receivers, forced convection typically occurs when wind blows surrounding air on the receiver absorber surfaces and in the heat exchanger where the HC exchanges heat with the hot inner walls.
- Mixed convection is a combination of forced and natural convection where each regime can reinforce or mitigate the effects of the other one. Mixed convection occurs when no single regime is dominant.

Detailed calculation of convective heat transfer involves solving the Navier-Stokes equations, usually done via the finite volume method. The complexity of the solution usually involves using Computational Fluid Dynamics (CFD) software. The result of interest in receiver modelling is the convective heat transfer rate on the surfaces of the receiver which can be quantified via a convective heat transfer coefficient $u_{\text{conv}}(\mathbf{r})$.

$$\dot{q}''_{\text{conv}}(\mathbf{r}) = u_{\text{conv}}(\mathbf{r})\left(T_{\infty} - T_{\text{w}}(\mathbf{r})\right) \tag{2-124}$$

In most common situations such as forced flow in or around cylindrical pipes, correlations have been developed to estimate u_{conv} and therefore deduce the heat transfer coefficients without having to solve the full finite volume problem. These correlations generally involve the calculation of the Nusselt number which is defined as the ratio of convective heat transfer to the conductive heat transfer:

$$Nu = \frac{u_{\text{conv}} D_{\text{conv}}}{k} \tag{2-125}$$

with D_{conv} a characteristic length that depends on the geometry and correlation considered and k the thermal conductivity of the fluid. Nusselt number correlations generally involve the evaluation of the Reynolds and Prandtl numbers for forced convection and Rayleigh and Prandtl numbers for natural convection.

$$\text{Re} = \frac{\rho v D}{\mu} = \frac{v D}{\nu} \tag{2-126}$$

$$\text{Ra} = \frac{g\beta}{\nu\alpha_{\text{d}}}\left(T - T_{\text{amb}}\right) D^3 \tag{2-127}$$

$$\mathrm{Pr} = \frac{\nu}{\alpha_d} \tag{2-128}$$

$$\alpha_d = \frac{k}{\rho Cp} \tag{2-129}$$

where ρ is the density, β the thermal expansion coefficient, α_d the thermal diffusivity, Cp the heat capacity at constant pressure, v is the velocity, ν the kinematic viscosity, μ the dynamic viscosity and D a characteristic length.

The specific correlations used will be presented in the applications of the receiver model on a case by case basis.

2.3.4 Conductive heat transfer

Heat conduction is the transfer of thermal energy through the collision of molecules, erratic movement of electrons and phonon transport in a material. Heat conduction is the major heat transfer mechanism in opaque solids. Fourier's law describes heat conduction.

$$\dot{\mathbf{q}}''_{cond} = -k\nabla T \tag{2-130}$$

The conductivity of the material through which the heat flows is typically temperature dependent. Conduction problems are solved using numerical methods such as finite element, finite volume or finite difference methods.

2.3.5 Receiver energy loss

2.3.5.1 Receiver aperture definition

In optical systems, the aperture is generally defined as the surface through which radiation enters and leaves the system and the geometry of this surface is free to determine as long as this condition is respected.

The energetic aperture or receiver aperture is refined here as the smallest convex surface through which concentrated radiation enters and leaves the receiver volume. Figure 2-25 illustrates different possible definitions of the aperture. A ray of light enters the receiver volume crossing the aperture through A and reflects on the absorber to cross again the aperture in B. In Figure 2-25 (a) and (b), the aperture definition does not exclude reflections back to the absorber surface which complicates the expression of the radiative loss mechanisms. In Figure 2-25 (c) all the radiative energy crossing the aperture coming from the receiver volume is radiative loss. The definition suggested and illustrated in Figure 2-25 (c) simplifies the identification of radiative heat transfer dependent losses while keeping the general aperture definition valid.

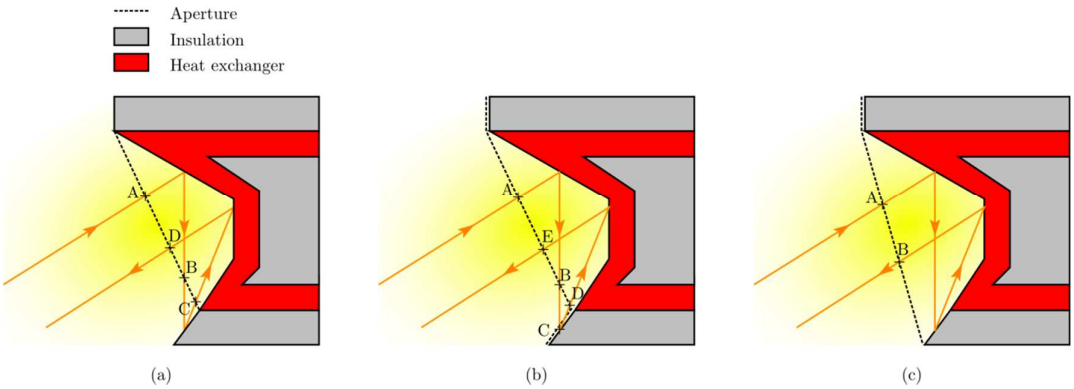

Figure 2-25: Receiver aperture definitions comparison: (a) the aperture covers the active region of the absorber only, (b) the aperture covers the total irradiated surface of the receiver and is not convex, (c) the aperture covers the irradiated surface of the receiver and is convex.

2.3.5.2 Optical loss

Two purely optical loss mechanisms impact receiver performance: the reflective loss and the spillage loss. Spillage is the fraction of the non-attenuated concentrated radiative energy that does not reach the absorber area of the receiver. Because the aperture definition chosen is delimiting the absorber surfaces, the spillage loss is expressed with:

$$\dot{Q}_{\text{spil}} = \dot{Q}_{\text{con}} - \int_{A_{\text{abs}}} H_{\lambda_0}(\mathbf{r})\, dA_{\text{abs}} \tag{2-131}$$

Reflective loss accounts for the fraction of the radiation incident on the absorber that is reflected to the surroundings.

$$\dot{Q}_{\text{ref}} = \int_{A_{\text{abs}}} \rho_{\lambda_0}(\mathbf{r}) H_{\lambda_0}(\mathbf{r}) F_{dA_{\text{abs}} \to A_{\text{ap}}}\, dA_{\text{abs}} \tag{2-132}$$

The definition of the reflective loss is simplified by the convex property of the aperture. If the aperture were not convex, it would not be used here in the view factor term as radiation reaching the aperture could cross it again and get back to the absorber.

2.3.5.3 Thermal loss

The two-temperature dependent energy losses are thermal emission and convective loss. Conduction through the insulation ultimately leads to the loss of energy to the surroundings in the form of thermal emissions or convective loss. It has been reported that conductive loss is usually negligible assuming that the receiver is properly insulated [144]. In the rest of this model, perfect insulation is assumed and conduction through the insulation volume neglected.

Hot surfaces of the receiver radiatively exchange with each other and with the surroundings through the aperture. Emissive losses account for the fraction of the thermal emissions from the envelope and the absorber that is lost to the environment.

$$\dot{Q}_{\text{emi}} = \int_{A_{\text{abs}}} \left(\varepsilon_{\lambda_1}(\mathbf{r}) E_b(T) + \rho_{\lambda_1}(\mathbf{r}) H_{\lambda_1}(\mathbf{r}) \right) F_{dA_{\text{abs}} \to A_{\text{ap}}} dA_{\text{abs}} \tag{2-133}$$

Convective loss to the environment is modelled using heat transfer coefficients determined using correlations in the literature.

$$\dot{Q}_{\text{conv}} = \int_{A_{\text{abs}}} u_{\text{conv}}(\mathbf{r}) \left(T(\mathbf{r}) - T_{\text{amb}} \right) dA_{\text{abs}} \tag{2-134}$$

2.3.6 Receiver energy balance

2.3.6.1 General steady-state receiver balance

From the heat loss mechanisms identified in the previous section, the energy balance of the receiver is:

$$\dot{Q}_{\text{HC}} = \dot{Q}_{\text{con}} - \dot{Q}_{\text{spil}} - \dot{Q}_{\text{ref}} - \dot{Q}_{\text{emi}} - \dot{Q}_{\text{conv}} \tag{2-135}$$

The energy balance is illustrated in Figure 2-26:

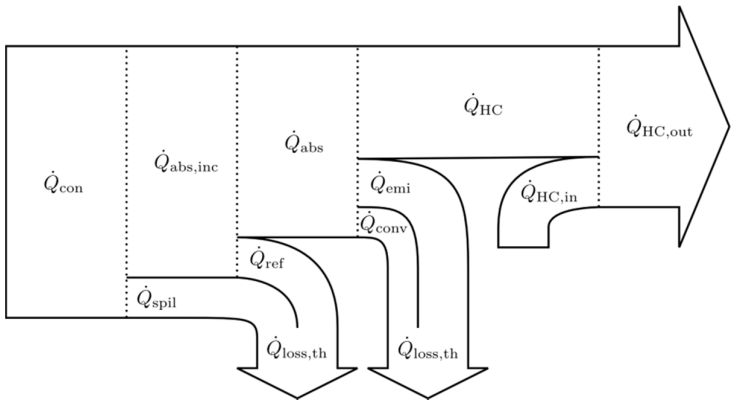

Figure 2-26: Receiver Sankey diagram.

$\dot{Q}_{\text{HC}}$ accounts for the net heat gain by the HC:

$$\dot{Q}_{\text{HC}} = \dot{Q}_{\text{HC,out}} - \dot{Q}_{\text{HC,in}} \tag{2-136}$$

The energy incident on the absorber is:

$$\dot{Q}_{\text{abs,inc}} = \dot{Q}_{\text{con}} - \dot{Q}_{\text{spil}} \tag{2-137}$$

The energy absorbed by the absorber is:

$$\dot{Q}_{\text{abs}} = \dot{Q}_{\text{abs,inc}} - \dot{Q}_{\text{ref}} \tag{2-138}$$

The "receiver efficiency" of the η_{rec} is:

$$\eta_{rec} = \frac{\dot{Q}_{HC}}{\dot{Q}_{con}} \tag{2-139}$$

The "intercept efficiency" η_{int} is defined as:

$$\eta_{int} = \frac{\dot{Q}_{abs,inc}}{\dot{Q}_{con}} \tag{2-140}$$

The "absorption efficiency" η_{abs} is defined as:

$$\eta_{abs} = \frac{\dot{Q}_{abs}}{\dot{Q}_{abs,inc}} \tag{2-141}$$

The "heat exchanger efficiency" η_{hx} is defined as:

$$\eta_{hx} = \frac{\dot{Q}_{HC}}{\dot{Q}_{abs}} \tag{2-142}$$

The "thermal efficiency" of the receiver is defined as:

$$\eta_{th} = \frac{\dot{Q}_{HC}}{\dot{Q}_{abs,inc}} \tag{2-143}$$

Overall the receiver efficiency is:

$$\eta_{rec} = \eta_{int}\eta_{abs}\eta_{hx} = \eta_{int}\eta_{th} = \eta_{opt}\eta_{hx} \tag{2-144}$$

Regrouping the optical heat loss mechanisms the optical efficiency is given:

$$\dot{Q}_{loss,opt} = \dot{Q}_{spil} + \dot{Q}_{ref} \tag{2-145}$$

$$\eta_{opt} = \eta_{int}\eta_{abs} = 1 - \frac{\dot{Q}_{spil} + \dot{Q}_{ref}}{\dot{Q}_{con}} \tag{2-146}$$

The thermal loss is:

$$\dot{Q}_{loss,th} = \dot{Q}_{conv} + \dot{Q}_{emi} \tag{2-147}$$

The heat exchanger efficiency can also be expressed as:

$$\eta_{hx} = 1 - \frac{\dot{Q}_{conv} + \dot{Q}_{emi}}{\dot{Q}_{abs}} \tag{2-148}$$

The local energy balance at each point of the absorber is a function of the local temperature and is coupled with the heat transfer to the HC through the heat exchanger wall. The study is restricted to steady-state modelling.

2.3.6.2 Local energy balance: absorber

The net locally absorbed heat by the absorber $\dot{q}''_{\text{abs}}(\mathbf{r},T_{\text{abs}})$ is:

$$\dot{q}''_{\text{abs}}(\mathbf{r},T_{\text{abs}})=\alpha_{\lambda_0}(\mathbf{r})H_{\lambda_0}(\mathbf{r})+\alpha_{\lambda_1}(\mathbf{r})H_{\lambda_1}(\mathbf{r})-\varepsilon_{\lambda_1}(\mathbf{r})E_b(T_{\text{abs}})-u_{\text{conv}}(\mathbf{r},T_{\text{abs}})(T_{\text{abs}}-T_{\text{amb}}) \quad (2\text{-}149)$$

With the short wavelengths band irradiance H_{λ_0} defined as the sum of the flux reflected by the concentrator and the radiation reflected by the absorber:

$$H_{\lambda_0}(\mathbf{r})=\int_{A_{\text{con}}}\rho_{\text{con}}(\mathbf{r}_{\text{con}})H_{\lambda_0}(\mathbf{r}_{\text{con}})F^{s}_{dA_{\text{con}}\to dA_{\text{abs}}}dA_{\text{con}}+\int_{A^*_{\text{abs}}}\rho_{\lambda_0}(\mathbf{r}^*)H_{\lambda_0}(\mathbf{r}^*)F_{dA^*_{\text{abs}}\to dA_{\text{abs}}}dA^*_{\text{abs}} \quad (2\text{-}150)$$

The longer wavelengths band irradiance H_{λ_1} is the sum of the thermal emissions from the rest of the absorber added to the emissions from the surroundings to the absorber through the aperture:

$$H_{\lambda_1}(\mathbf{r})=\int_{A^*_{\text{abs}}}\left[\rho_{\lambda_1}(\mathbf{r}^*)H_{\lambda_1}(\mathbf{r}^*)+\varepsilon_{\lambda_1}(\mathbf{r}^*)E_b\left(T_{\text{abs}}(\mathbf{r}^*)\right)\right]F_{dA^*_{\text{abs}}\to dA_{\text{abs}}}dA'_{\text{abs}}+E_b(T_{\text{abs}})A_{\text{ap}}F_{A_{\text{ap}}\to dA_{\text{abs}}} \quad (2\text{-}151)$$

2.3.6.3 Local energy balance: heat exchanger

The passive region of the absorber is adiabatic as per the perfect insulator assumption:

$$\dot{q}''_{\text{abs,passive}}(\mathbf{r})=0 \quad (2\text{-}152)$$

The net absorbed heat on the active region of the absorber is transferred through the heat exchanger wall via conduction:

$$\dot{\mathbf{q}}''(\mathbf{r})=-k(\mathbf{r})\nabla T \quad (2\text{-}153)$$

The heat-exchangers are restricted to cylindrical pipe geometries and mono-dimensional radial conduction is assumed. The heat conducted through the wall of the heat exchanger is:

$$\int_{r_{\text{HX,ext}}}^{r_{\text{HX,int}}}\frac{\dot{q}''_{\text{abs,active}}(\mathbf{r})}{r}dr=\int_{T_{\text{abs,active}}}^{T_{\text{HX,int}}}-k(\mathbf{r})dT \quad (2\text{-}154)$$

With homogeneous radial conductivity:

$$\dot{q}''_{\text{abs,active}}(\mathbf{r})=-k(\mathbf{r})\frac{(T_{\text{HX,int}}-T_{\text{abs,active}})}{\ln\left(\frac{r_{\text{HX,int}}}{r_{\text{HX,ext}}}\right)} \quad (2\text{-}155)$$

The temperature on the inner wall of the pipe is:

$$T_{\text{HX,int}}=T_{\text{abs,active}}-\dot{q}''_{\text{abs,active}}(\mathbf{r})\frac{\ln\left(r_{\text{HX,ext}}/r_{\text{HX,int}}\right)}{k(\mathbf{r})} \quad (2\text{-}156)$$

The heat conducted through the wall of the heat exchanger is transferred to the heat carrier by forced convection at the inner wall interface:

$$\dot{q}''_{\text{HC}}(\mathbf{r}) = u_{\text{conv,int}}(\mathbf{r})\left(T_{\text{HX,int}}(\mathbf{r}) - T_{\text{HC}}(\mathbf{r})\right) \tag{2-157}$$

All the absorbed energy is transferred to the HC:

$$\dot{q}''_{\text{abs,active}}(\mathbf{r}) = \dot{q}''_{\text{HC}}(\mathbf{r}) \tag{2-158}$$

Combining Eqs. 2-156, 2-157 and 2-158 and rearranging:

$$\dot{q}''_{\text{abs,active}}(\mathbf{r}) = \frac{T_{\text{abs,active}}(\mathbf{r}) - T_{\text{HC}}(\mathbf{r})}{\left(\frac{1}{u_{\text{conv,int}}\left(T_{\text{HC}}(\mathbf{r})\right)} + \frac{\ln\left(r_{\text{HX,ext}}/r_{\text{HX,int}}\right)}{k(\mathbf{r})}\right)} \tag{2-159}$$

The HC flows in the heat exchanger and progressively increases in enthalpy. The flow path $\ell \in [0, \ell_{\text{HC}}]$ is a curvilinear mono-dimensional axis describing the trajectory of the HC in the three-dimensional problem. The HC volume is simplified as a mono-dimensional problem following the curvilinear axis.

$$\mathbf{r} = f_{\text{flow-path}}(\ell) \tag{2-160}$$

The correspondence between the positions in the three-dimensional space of the receiver and the flow-path depends on the geometry and discretisation scheme and is addressed on a case-by-case basis in the model applications presented in the next chapter. The general expression for the change of variable is given in the following equation:

$$\dot{q}''_{\text{abs,active}}(\mathbf{r})\,dA_{\text{abs,active}} = \dot{q}'_{\text{abs,active}}\left(f_{\text{flow-path}}(\ell)\right) f'_{\text{flow-path}}(\ell)\,d\ell = \dot{q}'_{\text{abs,active}}(\ell)\,d\ell \tag{2-161}$$

Figure 2-27 summarises the temperature values considered in the heat carrier and heat exchanger model at a given position on the flow-path.

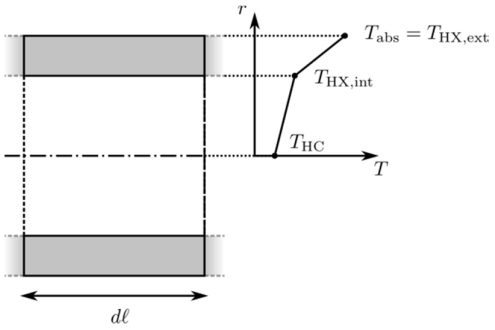

Figure 2-27: Temperature nomenclature over a differential flow path length of pipe.

2.3.6.4 Local energy balance: heat carrier

The local heat transfer coefficient in a pipe is a function of the local HC temperature, pressure and velocity as well as the geometry of the pipe.

$$u_{\text{conv,int}}(\ell) = f_{\text{HC,conv}}(T_{\text{HC}}, p_{\text{HC}}, v) \tag{2-162}$$

HC properties are usually defined as functions of the temperature and pressure of the HC and the velocity with the conservation of mass and momentum over the flow path.

The conservation of mass along the flow path is:

$$\frac{d\dot{m}_{\text{HC}}(\ell)}{d\ell} = 0 \tag{2-163}$$

As a consequence, $\dot{m}_{\text{HC}}$ is constant along the flow path and the mass flow at any point of ℓ is equal to the initial mass flow at $\ell = 0$:

$$\pi r_{\text{HX,int}}^2(\ell=0)\rho(T_{\text{HC,in}}, p_{\text{HC,in}})v(\ell=0) = \pi r_{\text{HX,int}}^2(\ell)\rho(T_{\text{HC}}, p_{\text{HC}})v(\ell) \tag{2-164}$$

The local conservation of momentum is given by the Navier-Stokes equation:

$$\frac{d\rho_{\text{HC}}\mathbf{v}}{dt} = -\nabla p_{\text{HC}} + \rho_{\text{HC}}\mathbf{g} + \mu\nabla^2\mathbf{v} \tag{2-165}$$

In steady state, the velocity can change along the flow path but is locally constant. Eq. 2-165 becomes:

$$\frac{d(\rho_{\text{HC}}\mathbf{v})}{d\ell}\frac{d\ell}{dt} = -\nabla p_{\text{HC}} + \rho_{\text{HC}}\mathbf{g} + \mu\nabla^2\mathbf{v} \tag{2-166}$$

Assuming that the flow-path constitutes a streamline of the HC flow:

$$\frac{d(\rho_{\text{HC}}(\ell)v(\ell))}{d\ell}v(\ell) = -\frac{dp_{\text{HC}}(\ell)}{d\ell} - \rho_{\text{HC}}(\ell)g + \mu(\ell)\frac{d^2v(\ell)}{d\ell^2} \tag{2-167}$$

$$\frac{d}{d\ell}\left(\frac{\rho_{\text{HC}}(\ell)v^2(\ell)}{2}\right) = -\frac{dp_{\text{HC}}(\ell)}{d\ell} - \rho_{\text{HC}}(\ell)g + \mu(\ell)\frac{d^2v\ (\ell)}{d\ell^2} \tag{2-168}$$

Integrating between $\ell = 0$ and any point on the flow-path:

$$p_{\text{HC,in}} + \rho(T_{\text{HC,in}}, p_{\text{HC,in}})\left(\frac{v(\ell=0)^2}{2} + gz_{\text{in}}\right) = p_{\text{HC}}(\ell) + \rho(T_{\text{HC}}, p_{\text{HC}})\left(\frac{v^2(\ell)}{2} + gz(\ell)\right) + F_{\Delta p} \tag{2-169}$$

With $F_{\Delta p}$ to account for momentum dissipation into heat, responsible for pressure drops for example and determined using methods specific to each case study (as shown in later sections).

The conservation of energy on the flow-path is:

$$\dot{m}_{\mathrm{HC}} h_{\mathrm{HC}}(\ell)\, d\ell = \dot{q}'_{\mathrm{abs,active}}(\ell)\, d\ell \tag{2-170}$$

The specific enthalpy of the HC increases as it gains heat:

$$h_{\mathrm{HC}}(\ell)\, d\ell = \frac{\dot{q}'_{\mathrm{abs,active}}(\ell)\, d\ell}{\dot{m}_{\mathrm{HC}}} \tag{2-171}$$

The specific enthalpy at a location ℓ on the flow path is (here ℓ^* is used as the integration variable along the flow-path):

$$h_{\mathrm{HC}}(\ell) = \int_0^{\ell} h_{\mathrm{HC}}(\ell^*)\, d\ell^* = \frac{1}{\dot{m}_{\mathrm{HC}}} \int_0^{\ell} \dot{q}'_{\mathrm{abs,active}}(\ell^*)\, d\ell^* \tag{2-172}$$

The temperature of the HC is determined from the local specific enthalpy of the HC material using physical properties correlations or implicit equations and is specific to every case-study:

$$T_{\mathrm{HC}}(\ell) = f_h\left(h_{\mathrm{HC}}(\ell)\right) \tag{2-173}$$

2.3.6.5 Local energy balance: coupled heat transfer model

The three layers of the model are coupled using the absorber surface temperature.

For the absorber passive region, the local energy balance is obtained from Eqs. 2-149 to 2-152:

$$\begin{cases} \alpha_{\lambda_0}(\mathbf{r}) H_{\lambda_0}(\mathbf{r}) + \alpha_{\lambda_1}(\mathbf{r}) H_{\lambda_1}(\mathbf{r}) - \varepsilon_{\lambda_1}(\mathbf{r}) E_b(T_{\mathrm{abs}}) - u_{\mathrm{conv}}(\mathbf{r}, T_{\mathrm{abs}})(T_{\mathrm{abs}} - T_{\mathrm{amb}}) = 0 \\ H_{\lambda_0}(\mathbf{r}) = \int_{A_{\mathrm{con}}} \rho_{\mathrm{con}}(\mathbf{r}_{\mathrm{con}}) H_{\lambda_0}(\mathbf{r}_{\mathrm{con}}) F^{s}_{dA_{\mathrm{con}} \to dA_{\mathrm{abs}}} dA_{\mathrm{con}} + \int_{A^*_{\mathrm{abs}}} \rho_{\lambda_0}(\mathbf{r}^*) H_{\lambda_0}(\mathbf{r}^*) F_{dA^*_{\mathrm{abs}} \to dA_{\mathrm{abs}}} dA^*_{\mathrm{abs}} \\ H_{\lambda_1}(\mathbf{r}) = \int_{A^*_{\mathrm{abs}}} \rho_{\lambda_1}(\mathbf{r}^*) H_{\lambda_1}(\mathbf{r}^*) F_{dA^*_{\mathrm{abs}} \to dA_{\mathrm{abs}}} dA^*_{\mathrm{abs}} + E_b(T_{\mathrm{abs}}) F_{A_{\mathrm{ap}} \to dA_{\mathrm{abs}}} \end{cases} \tag{2-174}$$

The ambient temperature, view factors and radiative properties being determined independently and prior to solution of the local energy balance, there are three unknowns $\left\{T_{\mathrm{abs}}(\mathbf{r}), H_{\lambda_0}(\mathbf{r}), H_{\lambda_1}(\mathbf{r})\right\}$ and three equations.

Combining eqs. 2-149 to 2-173, the absorber active region energy balance is obtained:

$$
\begin{cases}
\dot{q}''_{\text{abs,active}}\left(\mathbf{r},T_{\text{abs}}\right)=\alpha_{\lambda_0}\left(\mathbf{r}\right)H_{\lambda_0}\left(\mathbf{r}\right)+\alpha_{\lambda_1}\left(\mathbf{r}\right)H_{\lambda_1}\left(\mathbf{r}\right)-\varepsilon_{\lambda_1}\left(\mathbf{r}\right)E_b\left(T_{\text{abs}}\right)-u_{\text{conv}}\left(\mathbf{r},T_{\text{abs}}\right)\left(T_{\text{abs}}\left(\mathbf{r}\right)-T_{\text{amb}}\right)\\
H_{\lambda_0}\left(\mathbf{r}\right)=\int\limits_{A_{\text{con}}}\rho_{\text{con}}\left(\mathbf{r}_{\text{con}}\right)H_{\lambda_0}\left(\mathbf{r}_{\text{con}}\right)F^{s}_{dA_{\text{con}}\to dA_{\text{abs}}}dA_{\text{con}}+\int\limits_{A^*_{\text{abs}}}\rho_{\lambda_0}\left(\mathbf{r}^*\right)H_{\lambda_0}\left(\mathbf{r}^*\right)F_{dA^*_{\text{abs}}\to dA_{\text{abs}}}dA^*_{\text{abs}}\\
H_{\lambda_1}\left(\mathbf{r}\right)=\int\limits_{A^*_{\text{abs}}}\rho_{\lambda_1}\left(\mathbf{r}^*\right)H_{\lambda_1}\left(\mathbf{r}^*\right)+\varepsilon_{\lambda_1}\left(\mathbf{r}^*\right)E_b\left(T_{\text{abs}}\left(\mathbf{r}^*\right)\right)F_{dA^*_{\text{abs}}\to dA_{\text{abs}}}dA^*_{\text{abs}}+E_b\left(T_{\text{abs}}\right)A_{\text{ap}}F_{A_{\text{ap}}\to dA_{\text{abs}}}\\
\dot{q}''_{\text{abs,passive}}\left(\mathbf{r}\right)=0\\
\dot{q}''_{\text{abs,active}}\left(\mathbf{r}\right)=\dfrac{T_{\text{abs,active}}\left(\mathbf{r}\right)-T_{\text{HC}}\left(\mathbf{r}\right)}{\left(\dfrac{1}{u_{\text{conv,int}}\left(T_{\text{HC}}\left(\mathbf{r}\right)\right)}+\dfrac{\ln\left(r_{\text{HX,ext}}/r_{\text{HX,int}}\right)}{k\left(\mathbf{r}\right)}\right)}\\
\mathbf{r}=f_{\text{flow-path}}\left(\ell\right)\\
u_{\text{conv,int}}\left(\ell\right)=f_{\text{HC,conv}}\left(T_{\text{HC}},p_{\text{HC}},v\right)\\
v\left(\ell\right)=\dfrac{r^2_{\text{HX,int}}\left(\ell=0\right)\rho\left(T_{\text{HC,in}},p_{\text{HC,in}}\right)v\left(\ell=0\right)}{r^2_{\text{HX,int}}\left(\ell\right)\rho\left(T_{\text{HC}},p_{\text{HC}}\right)}\\
p_{\text{HC}}\left(\ell\right)=p_{\text{HC,in}}+\rho\left(T_{\text{HC,in}},p_{\text{HC,in}}\right)\left(\dfrac{v\left(\ell=0\right)^2}{2}+gz_{\text{in}}\right)-\rho\left(T_{\text{HC}},p_{\text{HC}}\right)\left(\dfrac{v^2\left(\ell\right)}{2}+gz\left(\ell\right)\right)+F_{\Delta p}\\
v_{\text{HC}}\left(\ell\right)=\dfrac{\dot{m}_{\text{HC}}}{\pi r^2_{\text{HX,int}}\rho_{\text{HC}}\left(T_{\text{HC}},p_{\text{HC}}\right)}\\
h_{\text{HC}}\left(\ell\right)=\dfrac{1}{\dot{m}_{\text{HC}}}\int\limits_0^{\ell}\dot{q}'_{\text{abs,active}}\left(\ell^*\right)d\ell^*\\
T_{\text{HC}}\left(\ell\right)=f_{hT}\left(h_{\text{HC}}\left(\ell\right)\right)
\end{cases}
\tag{2-175}
$$

Eq. 2-175 is a system of 11 equations with 11 unknown variables $\left\{\dot{q}''_{\text{abs,active}}\left(\mathbf{r}\right),T_{\text{abs}}\left(\mathbf{r}\right),H_{\lambda_0}\left(\mathbf{r}\right),H_{\lambda_1}\left(\mathbf{r}\right),\ell,T_{\text{HC}}\left(\ell\right),p_{\text{HC}}\left(\ell\right),v\left(\ell\right),u_{\text{conv,int}}\left(\ell\right),\dot{m}_{\text{HC}},h_{\text{HC}}\left(\ell\right)\right\}$.

2.4 Receiver Heat transfer simulation

In this section the simulation techniques and tools used to run the model are presented in more details. First, the overarching procedure is presented then the different simulation tools are introduced in more detail.

2.4.1 Simulation procedure

The surface of the receiver is discretised into $i=\{1,\ldots,N\}$ surface elements of constant temperature T_i and absorbed flux $\dot{q}''_{\text{abs,in},i}$ approximating the integration to the following sums:

$$\dot{Q}_{\text{spil}}=\dot{Q}_{\text{con}}-\int\limits_{A_{\text{abs}}}H_{\lambda_0}\left(\mathbf{r}\right)dA_{\text{abs}}\approx\dot{Q}_{\text{con}}-\sum_{i=1}^{N}H_{\lambda_0,i} \tag{2-176}$$

$$\dot{Q}_{\text{ref}}=\int\limits_{A_{\text{abs}}}\rho_{\lambda_0}\left(\mathbf{r}\right)H_{\lambda_0}\left(\mathbf{r}\right)F_{dA_{\text{abs}}\to A_{\text{ap}}}dA_{\text{abs}}\approx\sum_{i=1}^{N}\rho_{\lambda_0,i}H_{\lambda_0,i}F_{A_{\text{abs},i}\to A_{\text{ap}}} \tag{2-177}$$

$$\dot{Q}_{\text{emi}} = \int_{A_{\text{abs}}} \left(\varepsilon_{\lambda_1}(\mathbf{r})E_b(T) + \rho_{\lambda_1}(\mathbf{r})H_{\lambda_1}(\mathbf{r},T)\right)F_{dA_{\text{abs}}\to A_{\text{ap}}}dA_{\text{abs}} \approx \sum_{i=1}^{N}\left(\varepsilon_{\lambda_1,i}E_b(T_i) + \rho_{\lambda_1,i}H_{\lambda_1,i}\right)F_{A_{\text{abs},i}\to A_{\text{ap}}} \quad (2\text{-}178)$$

$$\dot{Q}_{\text{conv}} = \int_{A_{\text{abs}}} u_{\text{conv}}(\mathbf{r})(T - T_{\text{amb}})dA_{\text{abs}} \approx \sum_{i=1}^{N} u_{\text{conv},i}(T_i - T_{\text{amb}}) \quad (2\text{-}179)$$

$$\dot{Q}_{\text{HC}} = \int_{\ell_{\text{HC}}} \frac{\dot{q}'_{\text{abs,active}}(\ell)}{\dot{m}_{\text{HC}}} d\ell_{\text{HC}} \approx \sum_{i=1}^{N} \frac{(\ell_{i+1} - \ell_i)\dot{q}'_{\text{abs,active},i}}{\dot{m}_{\text{HC}}} \quad (2\text{-}180)$$

Evaluation of the flux absorbed by the absorber after reflection from the concentrator is independent of the temperature and can be solved directly using MCRT prior to solution of the temperature dependent expressions. The diffuse view factors needed to solve the long wavelength radiative heat transfer components are also determined using MCRT before starting the solution process. The evaluation of thermal emissions, convective loss and HC heat gain are coupled and they are solved simultaneously. The enthalpy gain by the HC is set to be equal to an assumed net heat input and the external temperature of the absorber determined from the heat transfer model. This absorber temperature is used to re-evaluate the net heat gain using the radiosity method. The assumed flux distribution is then iteratively updated until the discrepancy between both the assumed net absorbed flux and the one obtained from the HC energy balance falls below a convergence threshold σ_p. The algorithm is illustrated in the following flow chart:

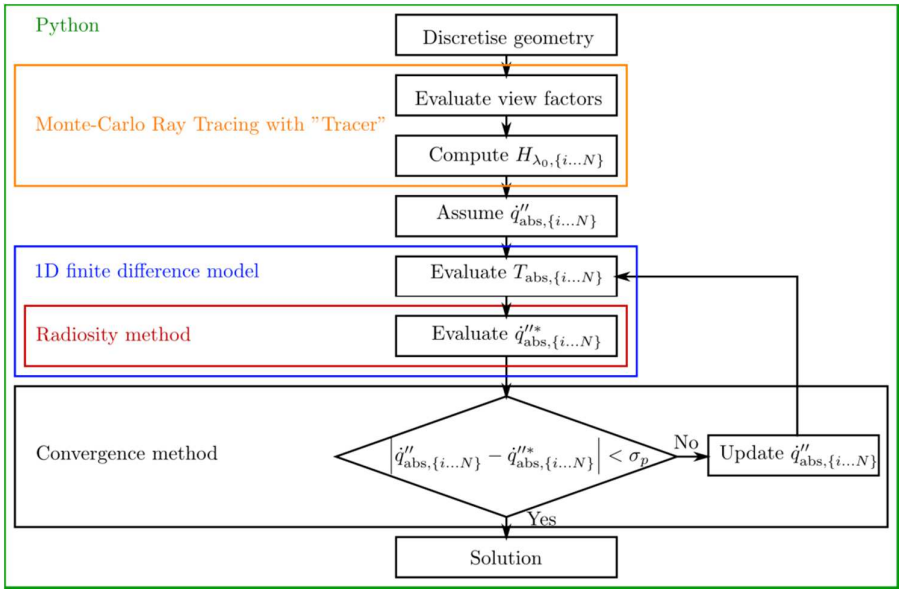

Figure 2-28: Receiver energy balance iterative solution algorithm using the absorber net heat flux as converging variable.

The method can be conducted by taking a guess on the temperature of the surfaces instead of the net absorbed flux and then use the resulting heat flux to the HC to estimate the temperature of the HC. In this second situation, the external temperature of the heat

exchanger needs to be evaluated again, from the HC temperature obtained, before being able to estimate the convergence.

The solution algorithm with the temperature as an iterative variable is:

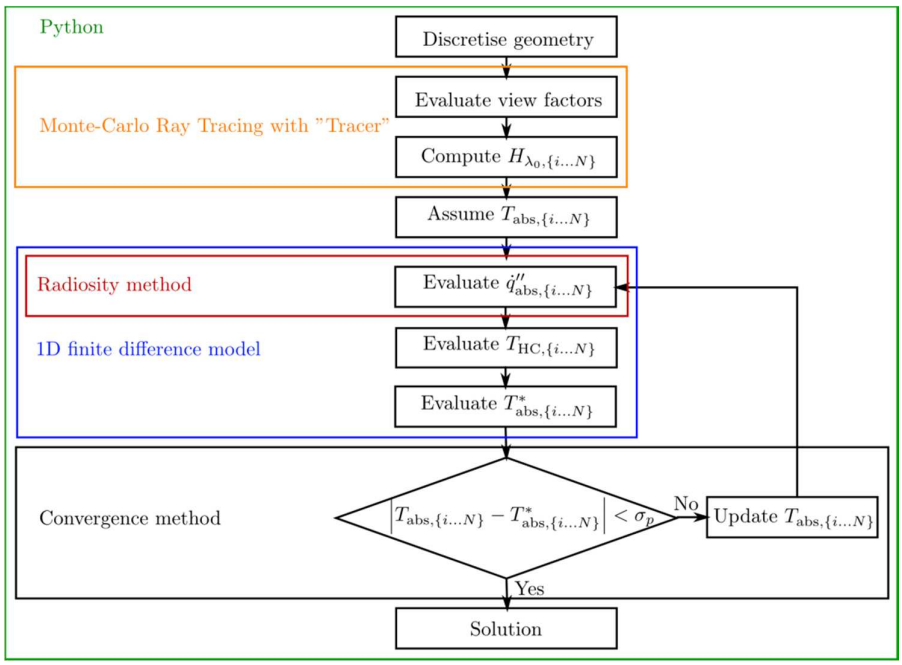

Figure 2-29: Receiver energy balance iterative solution algorithm using the absorber temperature as converging variable.

2.4.2 Monte Carlo-Ray Tracing with Tracer: open source library in Python

The ray tracing code used is “Tracer”, an object oriented library in Python language. Tracer makes extensive use of the array-oriented programming structure of NumPy, which provides an interface to fast and optimised array operation routines in lower-level complied programming languages such as C and Fortran. A consequence of that is that it is convenient and faster to use the Tracer with bundles of rays instead of single rays which is a difference compared with more traditional ray-by-ray MCRT codes. Tracer supports energy-partitioning ray-tracing. This method presents some advantages in terms of convergence rates as it imitates the real physics of the problem more closely and reduces the statistical noise associated with the Boolean approach.

In purely stochastic ray-tracing methods, rays accounting for photon bundles interact with surfaces in a purely stochastic manner. For reflection, as an example, a ray is totally absorbed or totally reflected and the decision made using a uniform random Boolean variate declaration at each interaction, also known as “Russian roulette” method. In the “energy-partitioning” method, a ray of light propagates through the geometry of the problem and progressively transfers the energy it carries to surfaces, following the physical phenomena

involved [101]. Once the energy carried by a ray becomes negligible, it is ignored and the simulation continues with new rays from the source of radiation.

The Tracer library being open-source and fully accessible online, only a short summary of the inner workings of the code is proposed in the following paragraphs and illustrated in Figure 2-30. A tracer simulation is composed of two elements:

- An assembly object locating and orienting the geometry of the system.
- A ray-bundle object describing the position, direction of propagation, energy carried and any other property borne by a group of rays.

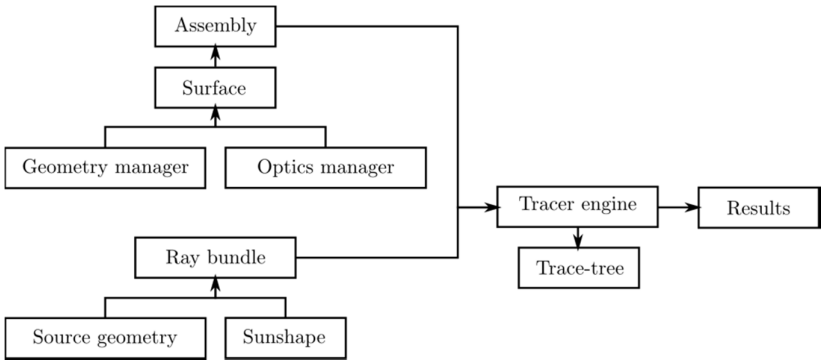

Figure 2-30: Simplified structure for the Tracer code.

The assembly object contains surface objects which are at the core of the geometrical and optical definition of the geometry. Surface objects include a geometrical manager instance bringing:

- A method to compute the intersection points of the surface with rays in the ray-bundle.
- A method to find the ideal normal to the surface at any intersection point.

Also included in the surface is the optical manager of the surface that describes the optical properties and how the ray intersections should be performed (eg. Specular reflection, slope error, refraction, etc.).

The assembly and ray bundle objects are used as arguments to create an instance of the Tracer engine class that will propagate the rays from the ray-bundle through the assembly, interrogate the surfaces for any potential intersection, find the first intersection event for each ray, re-create a new ray-bundle after all rays in the current bundle have been processed, iterate until the energy in the bundle depletes and store the history of each ray in a ray-tree object that can be interrogated once the simulation is complete. In addition, the Tracer contains numerous functions and methods to generate sunshape based sources of various geometries.

During the research presented in this dissertation Tracer was improved from a state where it could simulate ideal parabolas and flat surfaces with disc sources and pillbox sunshapes to a more complete ray-tracing tool while keeping the efficient architecture in place. Notable additions are:

- A modification of the ray-quadric intersection solver and normal vector computation with special attention paid to the numerical reliability of the intersection solution
- Gaussian bi-variate slope error optics
- Buie Sunshape integration and declaration
- Conical source positions and directions used in the estimation of view factors on axisymmetric geometries
- Multiprocessing engine using the Pathos framework [97]
- An interface with Common Inventor for efficient 3D visualization [79]

The most important asset brought by Tracer in this work is the complete access to the code through the easily accessible Python language that enabled the interaction of ray-tracing with external code for coupled heat transfer modelling, geometrical flexibility and optimisation.

2.4.3 Adaptive view factors calculation algorithm

The determination of the view factors is geometry dependent. For some generic and simple configurations, analytical view-factor expressions are available [65]. In situations where the geometry is complex, MCRT can be used to evaluate view factors. View factors are specific to the geometry and to the discretisation scheme considered; however, a general algorithm can be put in place to maximise the reusability of the view factor computation method.

Considering a geometry composed of N surface elements, diffuse rays are cast from each surface element for 1 intersection only. The sample view factor $F_{A_i \to A_j,k}$ from a surface element A_i to another surface element A_j is equal to the ratio of $n_{\text{rays},i\to j}$, the number of rays intercepted by A_j; to the total number of rays cast n_{rays}:

$$F_{A_i \to A_j,k} = \frac{n_{\text{rays},A_i \to A_j}}{n_{\text{rays}}} \tag{2-181}$$

At each iteration k, n_{rays} are cast from each surface element and the iteration view factors $F_{i\to j,k}$ estimated on all surfaces in the geometry to update the view factors estimation $\overline{F_{A_i\to A_j,k}}$:

$$\overline{F_{A_i\to A_j,k}}=\frac{1}{k}\sum_{l=1}^{k}F_{A_i\to A_j,l} \tag{2-182}$$

The sample standard deviation of the view factor estimator is:

$$s_{A_i\to A_j,k}=\sqrt{\frac{1}{k-1}\sum_{l=1}^{k}\left(F_{A_i\to A_j,l}-\overline{F_{A_i\to A_j,k}}\right)^2} \tag{2-183}$$

The expected value of the view factor $F_{A_i\to A_j}$ belongs to an interval centred around the view factor estimator $\overline{F_{A_i\to A_j,k}}$:

$$F_{A_i\to A_j}\in\left[\overline{F_{A_i\to A_j,k}}-CI_{A_i\to A_j,k},\overline{F_{A_i\to A_j,k}}+CI_{A_i\to A_j,k}\right] \tag{2-184}$$

Provided that the number of samples k is large enough ($k>100$), the central limit theorem states that the confidence interval for a 99.7 % confidence level is:

$$CI_{A_i\to A_j,k}=\frac{3s_{A_i\to A_j,k}}{\sqrt{k}} \tag{2-185}$$

To evaluate the reciprocity rule from the view-factors estimators, eq. 2-184 is introduced in the reciprocity rule:

$$A_iF_{A_i\to A_j}-A_jF_{A_j\to A_i}\approx A_i\left(\overline{F_{A_i\to A_j,k}}\pm CI_{A_i\to A_j,k}\right)-A_j\left(\overline{F_{A_j\to A_i,k}}\pm CI_{A_j\to A_i,k}\right) \tag{2-186}$$

$$A_i\left(\overline{F_{A_i\to A_j,k}}\pm CI_{A_i\to A_j,k}\right)-A_j\left(\overline{F_{A_j\to A_i,k}}\pm CI_{A_j\to A_i,k}\right)\approx 0 \tag{2-187}$$

The approximation comes from the fact that the confidence interval is an estimation of the real error to the expected value. Considering the worst-case scenario, the precision of the reciprocity rule applied to the view-factors estimators is given by:

$$\max\left(A_i\overline{F_{A_i\to A_j,k}}_{\,i}-A_j\overline{F_{A_j\to A_i,k}}\right)\approx A_jCI_{A_j\to A_i,k}+A_iCI_{A_i\to A_j,k} \tag{2-188}$$

The right hand side of this equation, which includes the uncertainty relative to the Monte-Carlo sampling, can then be compared with a precision criterion to monitor the precision of the result.

The results from Monte-Carlo sampling are by nature sample estimates of the ideal population of infinite k samples and consequently follow a Student's t distribution. At large number of samples (or degrees of freedom in statistical vocabulary), the Student's t

distribution approximates a Normal law. If k is small ($k<100$), the distribution of the results is further away from a normal law and the *t* variable needs to be considered when evaluating the confidence intervals.

Increasing the total number of rays used reduces the span of the interval, which is an improvement in the precision of the evaluation. The algorithm imposes the summation rule of view factors. The reciprocity rule is verified in combination with the precision of each single view factor. Once the interval widths of all the view factors and the reciprocity rule errors from a surface become smaller than a prescribed precision criterion $\sigma_{p,i,j}$, the estimation is precise enough and the surface does not need to be simulated anymore. In this original implementation of MCRT-based view factor computations, the casting of rays from a surface is decided based on the current level of precision of the ray-trace. This implementation is in fact similar to the importance sampling concept [36] but presents the advantage of being blind to the geometry of the problem as it only depends on the sampled results estimation and precision and does not require any operation on the ray sampling function.

Once the view factors from all surfaces reach the precision level, the view factors matrix is obtained.

Some precautions have to be taken when implementing the view factor algorithm in order to avoid numerical overflow. In iterative algorithms, the accumulation of data over time can lead to the saturation of the allowable memory, known as numerical overflow. Numerical overflow is likely to happen if the result of each iteration is kept in memory to compute the view factor estimators and sample standard deviations. To overcome this issue, running-sum versions of the sampled variables are adopted to reduce the set of sampled variables representing their history to a single variable. The view factor estimator is calculated with:

$$\begin{cases} \overline{F_{A_i\to A_j,k=0}}=0 \\ \overline{F_{A_i\to A_j,k}}=\dfrac{(k-1)\overline{F_{A_i\to A_j,k-1}}+F_{A_i\to A_j,k}}{k} \end{cases} \tag{2-189}$$

The running computation of the sample standard deviation is using an added intermediary variable $s^*_{A_i\to A_j,k}$ [149]:

$$\begin{cases} s^*_{A_i\to A_j,k=0}=0 \\ s^*_{A_i\to A_j,k}=S_{A_i\to A_j,k-1}+\dfrac{k-1}{k}\left(F_{A_i\to A_j,k}-\overline{F_{A_i\to A_j,k-1}}\right)^2 \\ s_{A_i\to A_j,k}=\sqrt{\dfrac{s^*_{A_i\to A_j,k}}{k-1}} \end{cases} \tag{2-190}$$

A set of binary variables, $progress_{\{1,\ldots,N\},\{1,\ldots,N\}}$ is introduced to keep track of the surfaces that need to be ray-traced. Originally set to 1 for every surface, the value of progress is changed to 0 when both the confidence interval and reciprocity law precision criteria are verified. The precision criterion $\sigma_{\mathrm{p},i,j}$ can be an absolute value or relative to the view-factor estimator values. If a relative precision criterion is chosen, the precision ratio $\sigma_{\%,i,j}$ is chosen first and then the precision criteria are estimated at each iteration of the algorithm using:

$$\sigma_{\mathrm{p},i,j,k} = \sigma_{\%,i,j}\overline{F_{A_i \to A_j,k}} \tag{2-191}$$

The use of MCRT to determine view-factors intrinsically enforces the summation or closure rule but is generally slow in converging to acceptable reciprocity rule values. This is a well known problem in view factors estimation which has been addressed by post-processing of the dataset using a series of analytical methods enforcing the reciprocity rule, then refining the result to respect the summation rule [65, 141]. The situation where very small $A_i F_{A_i \to A_j}$ quantities exist, due to grazing angles or very small surface area of elements, is still a problem for any MCRT based method. In this work, the intention is to use the adaptive view-factors method to compute view-factors in geometries randomly declared and a more robust, albeit less sophisticated method, is preferred to control the precision of the reciprocity rule evaluation.

When the value of a $A_i F_{A_i \to A_j}$ estimation is lower than the expected precision associated with the largest view-factor from the same surface to any other surface, then the relative influence of $A_i F_{A_i \to A_j}$ is considered negligible and the surface is automatically accepted for the reciprocity rule verification. The following equations summarise this reciprocity relevance test:

$$A_i\left(\overline{F_{A_i \to A_j,k}} + IC_{A_i \to A_j,k}\right) < \sigma_{\mathrm{p},i,\{1\ldots N\},k} \max\left(A_i \overline{F_{A_i \to \{A_1 \ldots A_N\},k}}\right) \tag{2-192}$$

$$\frac{\overline{F_{A_i \to A_j,k}} + IC_{A_i \to A_j,k}}{\max\left(\overline{F_{A_i \to \{A_1 \ldots A_N\},k}}\right)} < \sigma_{\mathrm{p},i,\{1\ldots N\},k} \tag{2-193}$$

The relative precision of the view factor estimator itself is still verified and used to determine the progess state. Figure 2-31 summarises the view factor calculation algorithm.

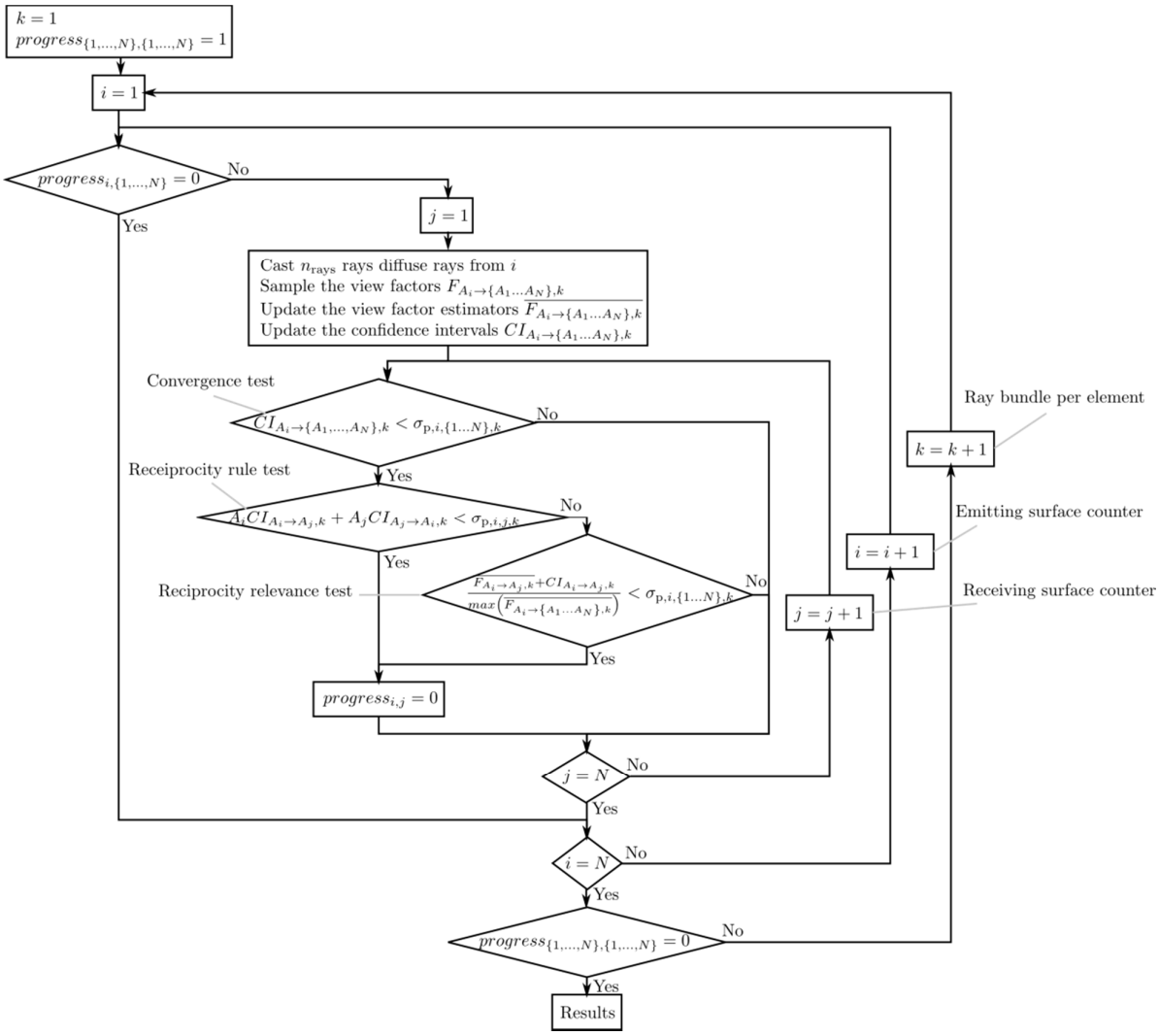

Figure 2-31: MCRT view factors algorithm. '*i*' is the iterator indicating the surface element from which rays are cast; '*j*' is the iterator indicating the surface elements intercepting the rays and '*k*' is the iterator indicating the number of ray bundles cast from each non-converged surface element.

2.4.4 The radiosity method

The radiosity method is used to compute the energy balance in radiative grey and diffuse enclosures. The sum of the emitted and reflected radiative energy is the radiosity J_i:

$$J_i = \varepsilon_{\lambda_1,i} E_b\left(T_i\right) + \rho_{\lambda_1,i} H_{\lambda_1,i} \tag{2-194}$$

The irradiance $H_{\lambda_1,i}$ is the combination of the radiosities of all the surfaces in the geometry that exchange with surface i:

$$A_i H_{\lambda_1,i} = \sum_{j=1}^{N} J_j A_j F_{j \to i} \tag{2-195}$$

Using the view factor reciprocity rule from eq. 2-123:

$$H_{\lambda_1,i} = \sum_{j=1}^{N} J_j \frac{A_j}{A_i} F_{j\to i} = \sum_{j=1}^{N} J_j F_{i\to j} \tag{2-196}$$

$$J_i = \rho_{\lambda_1,i} \sum_{j=1}^{N} J_j F_{i\to j} + \varepsilon_{\lambda_1,j} E_b\left(T_i\right) \tag{2-197}$$

This previous equation is useful when the surface boundary condition is a temperature. If the surface boundary condition is defined in terms of net flux, another form of the radiosity problem is needed. The energy balance on every surface element is expressed as a function of a fixed net heat flux absorbed at the surface taking into account the overall incident short and large wavelength radiation:

$$J_i = \rho_{\lambda_1,i} \sum_{j=1}^{N} J_j F_{i\to j} + \varepsilon_{\lambda_1,i} \left(\alpha_{\lambda_0,i} H_{\lambda_0,i} - \dot{q}''_{i,\text{net}}\right) \tag{2-198}$$

The overall system is linear and arranged into matrix form:

$$\mathbf{AJ} = \mathbf{B} \tag{2-199}$$

Where $\mathbf{A}$ is a $N \times N$ matrix of coefficients describing the problem, $\mathbf{J}$ the vector of radiosities and $\mathbf{B}$ the right hand side of the linear system. $\mathbf{A}$ is:

$$\begin{cases} \mathbf{A}_{ij} = 1 - \rho_{\lambda_1,i} F_{i\to j} & \text{if } i = j \\ \mathbf{A}_{ij} = -\rho_{\lambda_1,i} F_{i\to j} & \text{if } i \neq j \end{cases} \tag{2-200}$$

For surfaces defined with a temperature boundary condition, $\mathbf{B}$ is:

$$\mathbf{B}_i = \dot{q}''_{i,\text{rad}} = \varepsilon_{\lambda_1,i} E_b\left(T_i\right) \tag{2-201}$$

For surfaces defined with a net absorbed flux boundary condition, $\mathbf{B}$ is:

$$\mathbf{B}_i = \dot{q}''_{i,\text{rad}} = \varepsilon_{\lambda_1,i} \left(\alpha_{\lambda_0,i} H_{\lambda_0,i} - \dot{q}''_{i,\text{net}}\right) \tag{2-202}$$

The previous system of equations can be solved by inverting the coefficient matrix to obtain the vector of radiosities describing the system.

$$\mathbf{J} = \mathbf{A}^{-1}\mathbf{B} \tag{2-203}$$

From the result, the net radiative heat flux at the surfaces, if unknown, is given by:

$$\begin{cases} \dot{q}''_{i,\text{rad}} = \dfrac{\varepsilon_{\lambda_1,i}}{\rho_{\lambda_1,i}} \left(E_b\left(T_i\right) - J_i\right) & \text{if } \varepsilon_{\lambda_1,i} < 1 \\ \dot{q}''_{i,\text{rad}} = E_b\left(T_i\right) - \sum_{j=1}^{N} J_j F_{i\to j} & \text{if } \varepsilon_{\lambda_1,i} = 1 \end{cases} \tag{2-204}$$

If the temperatures are unknown, they are obtained from:

$$T_i = \sqrt[4]{\frac{1}{\sigma}\left(J_i + \frac{\rho_{\lambda_1,i}}{\varepsilon_{\lambda_1,i}} \dot{q}''_{i,\text{rad}} \right)} \tag{2-205}$$

The matrix inversion is conducted numerically with the Numpy function "Numpy.linalg.solve" which uses the LAPACK routine "gesv" [1].

2.4.5 1D staggered grid finite difference HC model

The inlet and outlet temperatures of the HC, $T_{\text{HC,in}} = T_{\text{HC}}(\ell = 0)$ and $T_{\text{HC,out}} = T_{\text{HC}}(\ell = \ell_{\text{HC}})$ are fixed boundary conditions of the problem. The mass flow of HC is evaluated using the following expression:

$$\dot{m}_{\text{HC}} = \frac{\sum_{i=1}^{N} \dot{q}_{\text{abs, active},i}}{h\left(T_{\text{HC,out}}\right) - h\left(T_{\text{HC,in}}\right)} \tag{2-206}$$

At every iteration o of the net heat flux value $\dot{q}_{\text{abs, active},i,o}$, the mass flow is updated accordingly. In the discretised model, each surface element of the active region of the absorber corresponds to a section of heat exchanger pipe. The temperature of the surface of the absorber is constant and the temperature of the HC varies over the corresponding element length of pipe. A staggered grid finite difference scheme is adopted to solve the bulk temperature of the HC as illustrated in Figure 2-32. With this scheme, the temperature of the HC in the pipe section $[\ell_i, \ell_{i+1}]$ is:

$$T_{\text{HC},i} = \frac{T_{\text{HC}}(\ell_i) + T_{\text{HC}}(\ell_{i+1})}{2} \tag{2-207}$$

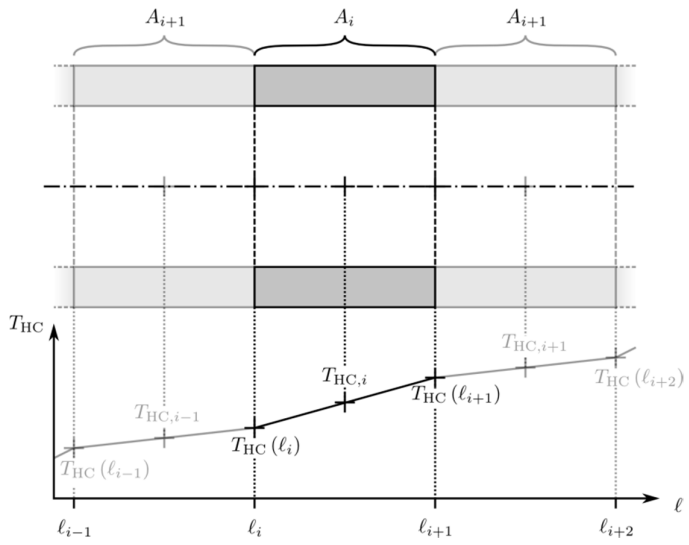

Figure 2-32: Staggered grid discretisation scheme used along the flow-path.

The enthalpy gain in the HC volume is determined using a local iterative method. First, a net HC heat gain is needed to evaluate the temperature profile in the HC. When using the absorber temperature as iteration variable in the receiver model, the net heat gain is obtained from the radiosity system solution. When using a heat flux iteration variable, it is directly used. A heat carrier temperature guess is set at the boundaries of each HC element using the following expression:

$$T_{\mathrm{HC,o=0}}\left(\ell_{i+1}\right)=T_{\mathrm{HC,o=0}}\left(\ell_{i}\right)+\sum_{m=1}^{i}\dot{q}_{\mathrm{abs,active},m}\frac{\left(T_{\mathrm{HC,out}}-T_{\mathrm{HC,in}}\right)}{\sum_{i=1}^{N}\dot{q}_{\mathrm{abs,active},i}} \tag{2-208}$$

The enthalpy gain for the iteration o in the element of HC is evaluated using:

$$\Delta H_{\mathrm{HC},i,o}=\dot{m}_{\mathrm{HC}}\left(h\left(T_{\mathrm{HC,o}}\left(\ell_{i+1}\right)\right)-h\left(T_{\mathrm{HC,o}}\left(\ell_{i}\right)\right)\right) \tag{2-209}$$

The outlet temperature of each HC element is then iteratively updated until the enthalpy gain in the HC element matches the heat input to the HC element using the following equation.

$$T_{\mathrm{HC},o+1}\left(\ell_{i+1}\right)=T_{\mathrm{HC},o}\left(\ell_{i}\right)+\left(T_{\mathrm{HC},o}\left(\ell_{i+1}\right)-T_{\mathrm{HC},o}\left(\ell_{i}\right)\right)\frac{\dot{q}_{\mathrm{abs,active},i}}{\Delta H_{\mathrm{HC},i,o}} \tag{2-210}$$

The converged temperature outlet value is used as the inlet temperature for the next element. Once the last HC element converges, the bulk temperature of the HC element is determined using eq. (2-207). Figure 2-33 summarises the iterative solution algorithm for the HC temperature.

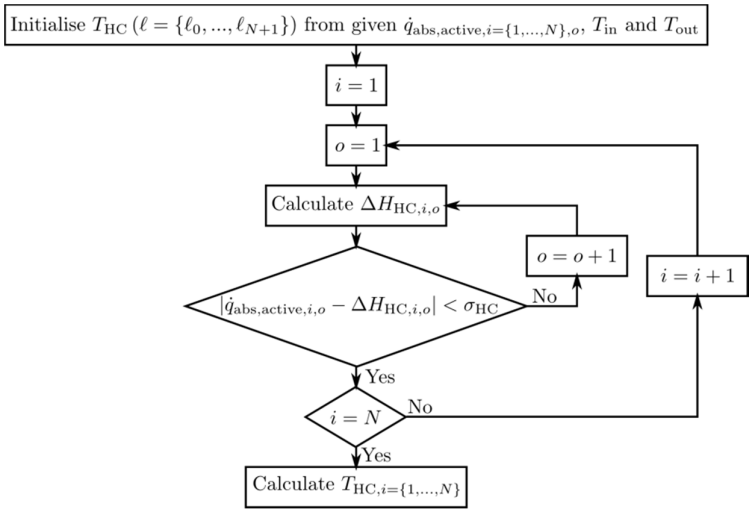

Figure 2-33: HC temperature iterative algorithm.

The absorber temperature is then determined using the following expression:

$$T^*_{\text{abs},i} = T_{\text{HC},i} + \dot{q}''_{\text{abs,active},i}\left(\frac{1}{u_{\text{conv,int}}\left(T_{\text{HC},i}, p_{\text{HC},i}\right)} + \frac{\ln\left(r_{\text{HX,int},i}/r_{\text{HX,ext},i}\right)}{k_i}\right) \tag{2-211}$$

If the absorber net heat input is used as the iteration variable, the radiosity system is solved with the absorber temperature as a boundary condition to obtain the radiative loss $\dot{q}''^*_{\text{rad,i,o}}$:

$$\begin{cases} \dot{q}''^*_{\text{abs}i,\text{rad}} = \dfrac{\varepsilon_{\lambda_1,i}}{\rho_{\lambda_1,i}}\left(E_b\left(T^*_{\text{abs},i}\right) - J_i\right) & \text{if } \varepsilon_{\lambda_1,i} < 1 \\ \dot{q}''^*_{i,\text{rad}} = E_b\left(T^*_{\text{abs},i}\right) - \sum_{j=1}^{N} J_j F_{i\to j} & \text{if } \varepsilon_{\lambda_1,i} = 1 \end{cases} \tag{2-212}$$

The convective heat loss is updated with $T^*_{\text{abs},i}$:

$$\dot{q}''^*_{\text{conv,i,o}} = -u_{\text{conv,i,o}}\left(T^*_{\text{abs},i}\right)\left(T^*_{\text{abs},i} - T_{\text{amb}}\right) \tag{2-213}$$

The new evaluation of the net heat flux is then obtained with:

$$\dot{q}''^*_{\text{abs,i,o}} = \alpha_{\lambda_0,i} H_{\lambda_0,i} - \dot{q}''^*_{\text{rad,i,o}} - \dot{q}''^*_{\text{conv,i,o}} \tag{2-214}$$

2.4.6 Simulation convergence method

When using the temperature of the absorber for convergence, the temperature guess on the absorber is updated for the next iteration $o+1$ using:

$$T_{\text{abs},i,o+1} = \sqrt[4]{\frac{T^4_{\text{abs},i,o} + T^{*4}_{\text{abs},i,o}}{2}} \tag{2-215}$$

If the net heat flux is used for convergence, the net heat flux for the next iteration $o+1$ is determined using:

$$\dot{q}''_{\text{abs},i,o+1} = \frac{\dot{q}''_{\text{abs},i,o} + \dot{q}''^*_{\text{abs},i,o}}{2} \tag{2-216}$$

3 Receiver model applications

In this chapter, the simulation of two examples of point focus concentrator and receiver systems is presented in order to establish and prove the reasonableness of the model presented in the previous chapter for dish and tower receivers. This step is important as the model is then used for the optimisation of receivers, which is the core contribution of this work. A second objective is to illustrate some of the trade-offs involved in receiver design for both systems and give examples of reference systems.

The first system modelled is a parabolic dish concentrator system coupled with a cavity receiver that is installed at the ANU facilities. Parabolic dish receivers received a lot of focus during the first half of the PhD research as the author contributed to a grant-funded USA-Australia project on modelling and reduction of cavity receiver losses for dish concentrator applications. The development of the project led to the design, construction and testing of a new cavity receiver with improved performance and will be commented on in Chapter 4. Publications (d) and (o) of the initial publication list (p. ix) include an earlier version of the flow-boiling heat transfer model used.

After the dish receiver project, the receiver research at the ANU was oriented towards heliostat field concentrator based systems, in line with the goals of the Australian Solar Thermal Research Initiative (ASTRI). The second model is a surround field and cylindrical tower receiver which will serve as a base case scenario comparison for the rest of the work developed. The heliostat field model in publication (n) in the list of publications (p. ix) was based on the Sandia NSTTF heliostat field presented.

3.1 Dish and cavity receiver model

3.1.1 SG4 dish model

The SG4 (Solar Generation 4) is a parabolic dish concentrator of approximately 500 m^2 aperture with 13.4 m focal length and altitude–azimuth tracking. It uses 380 identical spherically curved 1.17 m × 1.17 m mirror panels, which incorporate glass-on-metal laminate mirrors [93]. Technical characteristics of the SG4 dish are summarised in Table 3-1 and illustrated in Figure 3-1.

The effective mirror aperture area of the concentrator is 489 m^2 taking into account the absence of a mirror panel at the centre of the concentrator, the shading of the supporting structures, and gaps between mirrors. The reflectance of the SG4 dish model is modified to

take into account the difference between the aperture area and effective mirror aperture area. The effective reflectance is given by:

$$\rho_{SG4,eff} = \rho_{SG4}\left(\frac{A_{eff}}{A_{ap}}\right) \tag{3-1}$$

Table 3-1: SG4 Dish characteristics summary.

Total panel aperture area	494 m^2
Total mirror aperture area	489 m^2
Focal length	13.4 m
Average diameter	25.1 m
Average rim angle	50.2°
Mirror reflectivity	93.5%
Number of mirrors	380
Mirror glass size	1165 mm × 1165 mm
Total mass of dish	19.1 t
Total mass of base and supports	7.3 t

Figure 3-1: The SG4 parabolic dish concentrator at the ANU.

As the SG4 dish is an assembly of spherically curved mirrors on a parabolic frame, the flux distribution of the reflected sunlight differs from an ideal parabolic dish concentrator of the same dimensions. Figure 3-2 shows the comparison of the Normalised Capture Ratio (NCR) and flux distribution for an ideal dish concentrator with the previously mentioned properties and the reflected flux distribution measured on the 4th of September of 2009 using the full moon as a source to get reasonable flux levels and avoid damaging the target [70]. The target used was a flat square aluminium plate painted white and considered Lambertian with dimensions 2.4 m by 2.4 m positioned at the focal plane of the concentrator [93]. The flux distribution is integrated from the centroid of the flux image and over a radius r_t and expressed as a Normalised Capture ratio (NCR) (see Eq. 3-2).

$$NCR(r) = \frac{\int_0^r \dot{q}'_t(r^*)dr^*}{\int_0^{r_t} \dot{q}'_t(r^*)dr^*} \tag{3-2}$$

The slope error of the mirrors were unknown at that time due to the lack of flux-mapping measurement, therefore three iterations of the model, each with a different slope error value, are presented. The moon is a convenient source of light to realise this type of measurement and extrapolate it to solar radiation because it subtends a half angle between 4.26 and 4.96 mrad at full moon which is in the same order of magnitude as the sun half-angle range, usually taken as 4.65 mrad. The moon also displays a relatively uniform diffuse reflective behaviour, similar to the sun emissive behaviour.

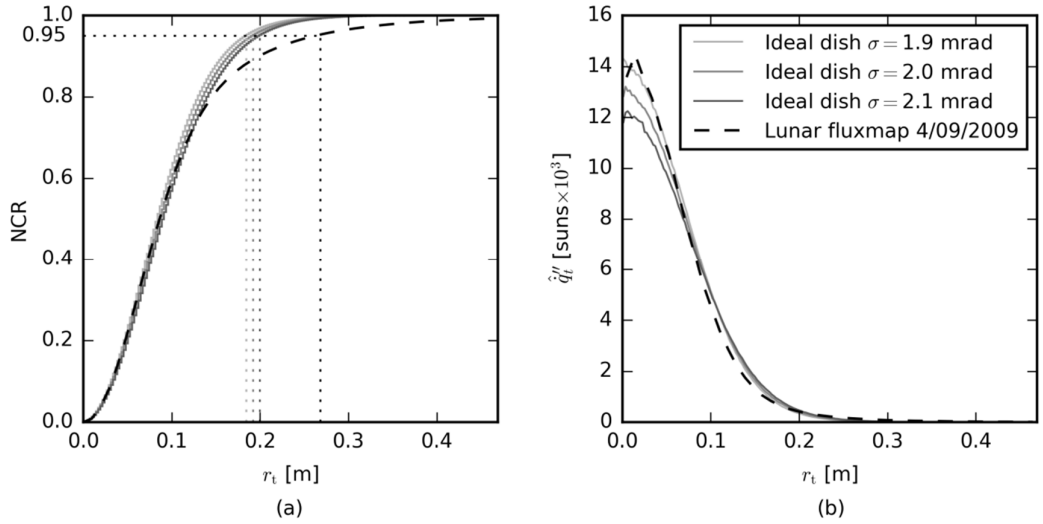

Figure 3-2: Comparison of three ideal dish models with different mirror slope errors and an experimental lunar fluxmap measurement with (a) the Normalised Capture Ratios (NCR) with the 95% capture radii for each dish model highlighted with the vertical dotted lines and (b) the normalised flux based on the ray-trace result considering 1sun DNI. Simulations are performed with 10^7 rays.

The experimental measurements were obtained from the post-processing of CCD camera images and are consequently relative measurements. In Figure 3-2 (a), the NCR distributions show good agreement between the experimental and ideal dish models close to centre of the target ($r_t < 0.1$ m) but deviate from each other at larger radii. Using the ideal dish model would overestimate the radial extent of the distribution of NCR as shown with the 95% capture radius lines: in the experimental measurements, the radius of capture of 95% of the energy is much larger than with the ideal dish models. The normalised flux distributions in Figure 3-2 (b) are obtained by scaling the experimental measurement values with the overall energy captured by the target in the ray-trace simulations. In addition to the focal plane measurements, the 90% and 95% NCRs were determined from a series of fluxmap images taken at different positions on the axis of symmetry of the concentrator. These results are

compared with simulations of the same positions with an ideal dish with 1 slope error of 1.9 mrad (the clearer curve in Figure 3-2) in Figure 3-3.

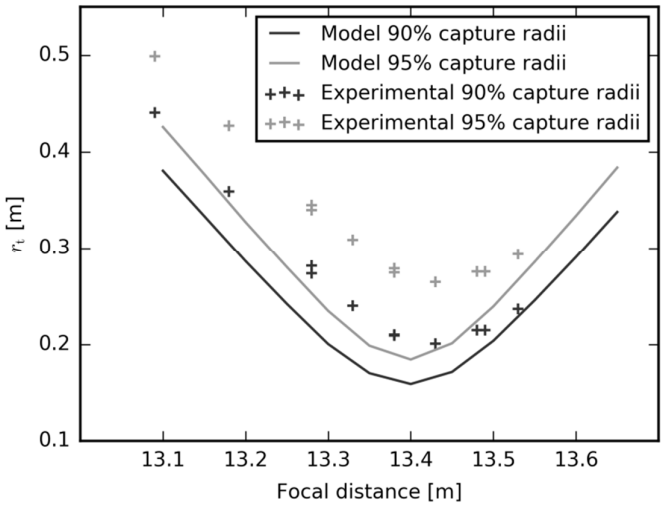

Figure 3-3: Comparison of the 90% and 95% capture ratios obtained from simulation of an ideal dish with 1.9 mrad of slope error with the lunar fluxmap experimental measurements at different focal distances.

The capture ratios from the ideal dish are smaller at the focal plane and generally smaller and closer together which corroborates the previous observations. The experimental values [70] reveal that the real focal distance of the SG4 dish is 13.4 m as designed but closer to 13.43 m. In the rest of the SG4 modelling work, this new value is taken as the real focal distance of the SG4 concentrator.

A modelling technique based on the use of surface slope error is used to approximate the behaviour of the SG4 dish in the numerical model. The idea developed here is to use an ideal parabolic dish shape and apply surface slope error deviations able to take into account the usual mirrors imperfections as well as the combined effects of misalignment and spherical curvature of the mirror panels. The concentrator is divided into two concentric sections that have different slope error values. This model is suggested because it was impossible to get a good agreement between the simulation and experimental results, particularly at large NCR values. To explain this discrepancy, it was suggested that the dish has a different behaviour close to the centre than close to the edge. There is a technical justification for this: when the SG4 dish was build, the choice was made to install mirrors measured with larger focal distances, due to manufacturing imperfections, close to the edge of the concentrator, and the ones with shorter ones closer to the centre. Three variables are considered in this dual-region model and illustrated in Figure 3-4:

- The partition diameter D_{part} which separates the two sections with different slope error values.
- The slope error of the inner section $\sigma_{\text{SG4,in}}$

- The slope error of the outer section $\sigma_{SG4,out}$

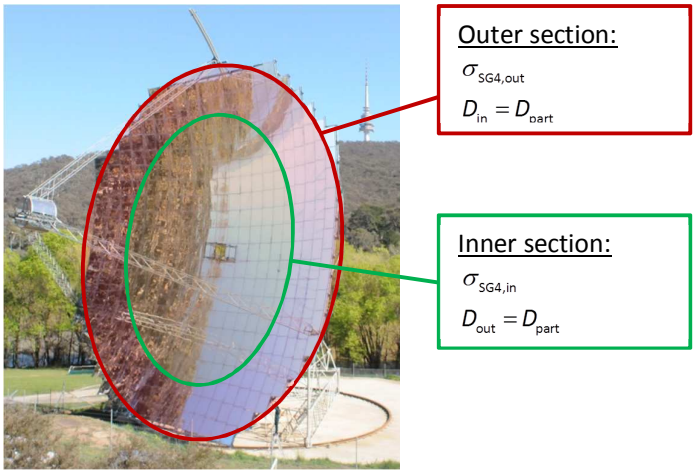

Figure 3-4: SG4 dish slope error based model illustration.

The model is manually adjusted to match the simulation results to the experimental measurements of flux distribution and cumulative radial power. The following figure presents a comparison of a fitted slope error based SG4 with the ideal one and the experimental result.

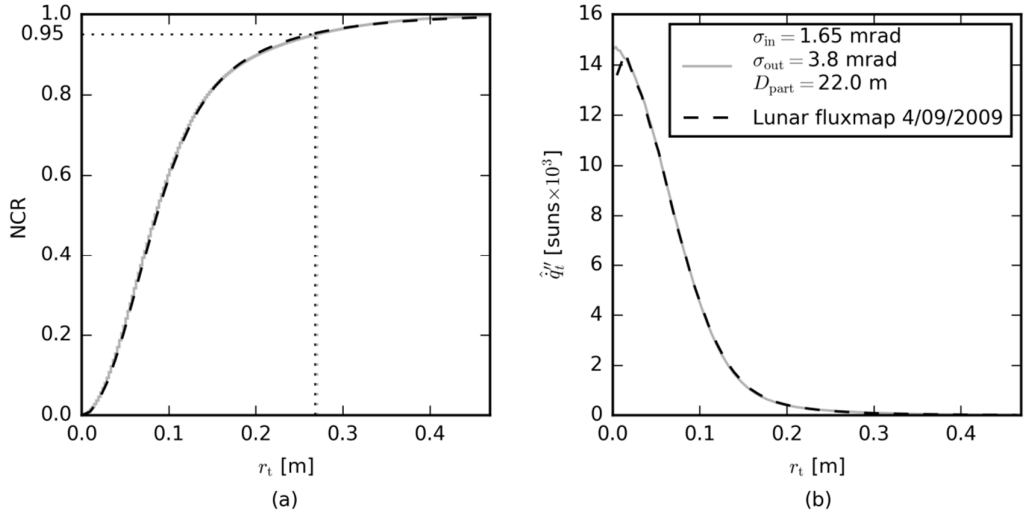

Figure 3-5: Comparison of a dual-region modelled dish and experimental measurements for (a) the Normalised capture ratio and (b) the normalised flux distribution at the focal plane target. Simulation is performed with 5.10^7 rays.

The agreement between the dual-region model and the fluxmap measurements is good at the focal plane location. In order to bring more confidence into the model, the variation of 90% and 95% capture radii outside of the focal plane is compared with experimental results in Figure 3-6. The results show a much better agreement between the modelling and experimental results and the dual region dish model with the parameters presented in Figure 3-6 (D_{part}=22 m, σ_{in}=1.65 mrad, σ_{out}=3.8 mrad) is adopted for the rest of the model.

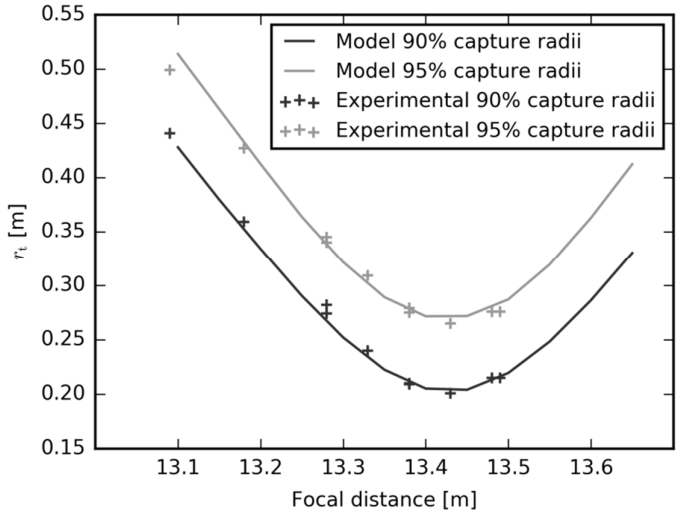

Figure 3-6: Comparison of the 90% and 95% capture ratios obtained from simulation of a fitted dual-region dish model with the lunar fluxmap experimental measurements at different focal distances.

3.1.2 SG3 receiver model

The receiver used in this model is the SG3 receiver that was originally designed and installed at the focus of the SG3 concentrator, the previous iteration of large aperture dish works at the ANU [70]. This receiver was installed on the SG4 dish after the SG3 dish was decommissioned and the SG4 dish built.

Figure 3-7: The SG3 dish concentrator and receiver in operation at the STG facilities prior to de-commissioning.

The design concept behind the SG3 receiver is to use a “cold” pre-heater section with a generally large view factor to the surroundings to capture the off-focus light without suffering strong emissive loss penalties and then transition to a cavity-type receiver able to mitigate thermal emission loss from the hotter regions. Figure 3-8 presents the SG3 receiver diagram. The SG3 receiver is a once-through direct steam generation receiver. Water in liquid state enters the receiver on the external edge of the preheater section and flows in a single pipe,

helically arranged, towards the inside of the receiver. After ~28 loops on the frustum (conical section) of the preheater section, the tube winding transitions to a cylindrical coil for ~15 loops before changing to a larger tube diameter. At this stage, water is reaching boiling conditions. The pipe then cylindrically coils towards the back wall of the cavity for ~37 loops and then covers it in a spiral pattern for ~9 loops. The pipe then exits the receiver and the central region of the back wall is covered with a ceramic piece (not showed on the picture) to protect the structures lying behind. The receiver is designed to operate for superheated steam output at 500 °C and 45 bar.

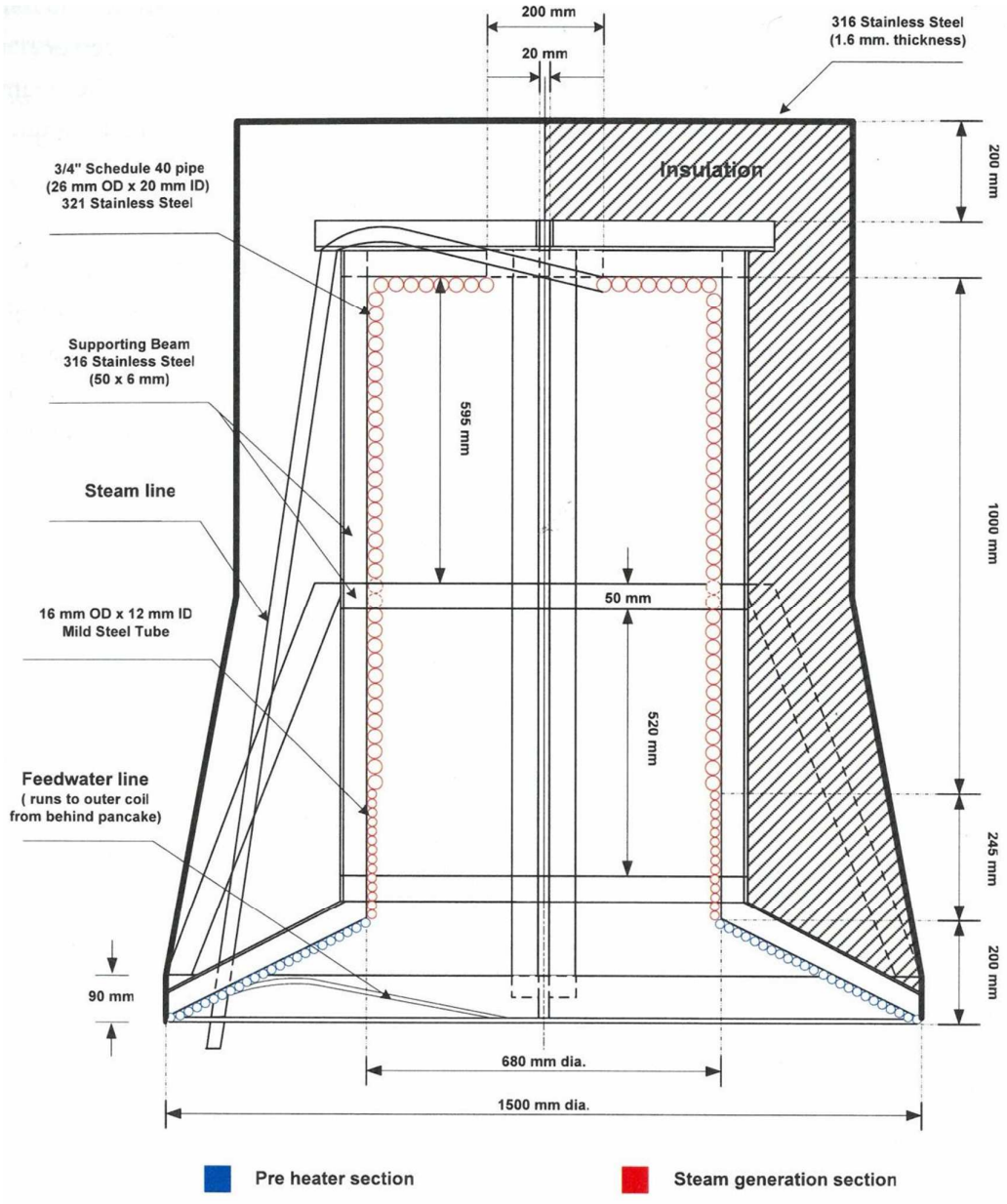

Figure 3-8: SG3 receiver diagram from L. Siangsukone's PhD thesis [137].

The receiver pipes are made of two different types of steel. The preheater section uses mild steel with relatively good thermal conductivity and lower cost. Larger diameter 321

stainless steel tubes are used in the cavity to counteract corrosion. The pipes are larger in the boiling and superheating regions than in the pre-heating region to mitigate the pressure drops caused by the higher velocity of the flow of steam. The pipes' external surfaces are oxidised from previous high-temperature operations and the emissivity is assumed to be 0.87 at all wavelengths [137]. The thermal conductivity of the mild steel section and 321 stainless steel sections are set to 40 $W.m^{-1}.K^{-1}$ and 20 $W.m^{-1}.K^{-1}$ respectively[6]. Constant thermal conductivities are an approximation, in reality, the thermal conductivities vary with temperature and a more refined approach would consider this variation. The pipes are assumed to be optically rough and therefore to show diffuse reflective properties.

Figure 3-9 presents the allocation of the SG3 receiver surfaces and volumes as per the model presented in Chapter 2.

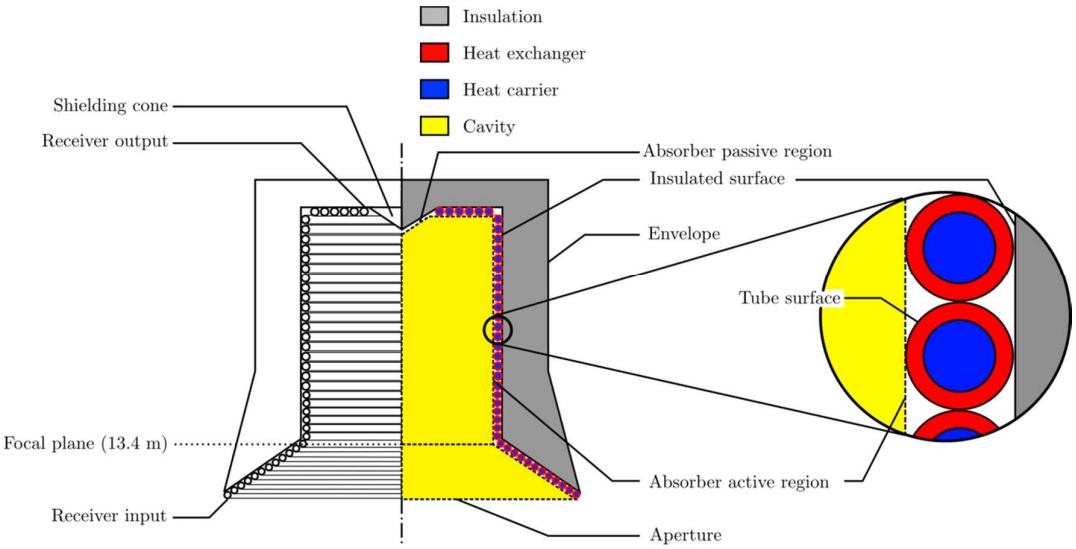

Figure 3-9: Receiver model surfaces and volumes allocation.

The receiver model is considered axi-symmetrical. The absorber surface is approximated with surfaces tangent to the pipes. This simplification enables the use of far fewer geometrical surfaces than for the full coil in the ray-tracing; which speeds up and simplifies the simulation. The model is composed of 7 surfaces or receiver sections as shown in Figure 3-10:

1. A conical frustum for the pre-heater discretised into 28 sections of equal slant height.
2. A first cylinder for the second part of the pre-heater discretised into 15 cylindrical sections of equal heights.
3. A second cylinder for the second part of the cavity side wall, discretised into 37 cylindrical sections of equal heights.

[6]Source : Steel retailer: http://www.azom.com/

4. An annulus for the back wall of the cavity with 9 annular sections of equal width.
5. A cone to model the ceramic shielding cone at the back of the receiver.
6. A cylinder to approximate the envelope side.
7. A disc for the envelope region situated at the back of the receiver.

The pipe windings are approximated by horizontal loops and each loop is associated with a frustum or cylindrical section on the absorber surface as presented in Figure 3-10.

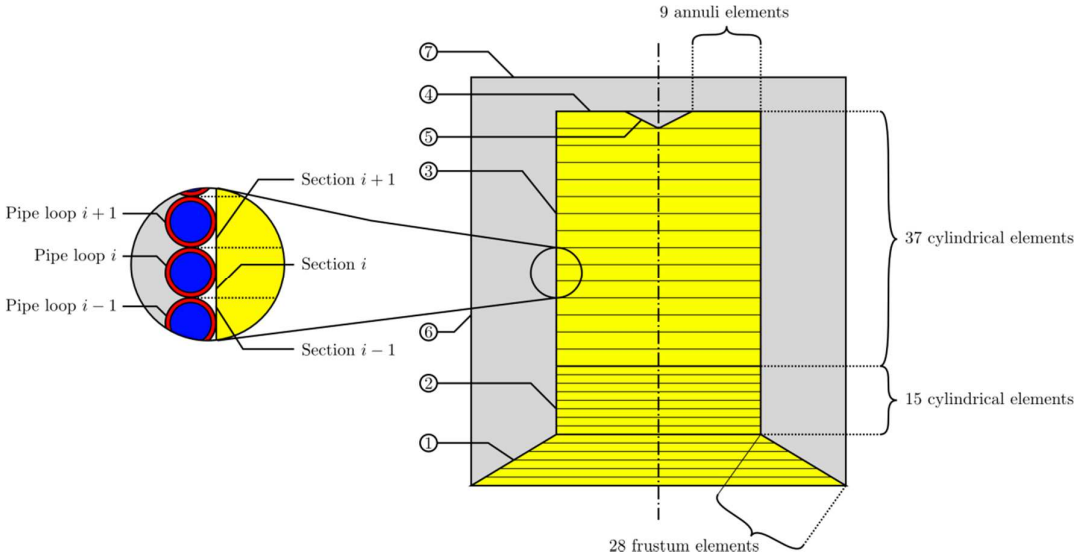

Figure 3-10: SG3 model discretisation schematic diagram with the 8 geometrical sections highlighted.

The approximation of the real surfaces of the receiver with simpler axi-symmetrical shapes requires the grooves formed by the pipes on the receiver surface to be explicitly taken into account. Radiation intercepted by the walls of the simplified receiver and reflected back is in reality partially reflected to the neighbouring tube sections, artificially increasing the effective absorptivity of the simplified surface. As the pipe surfaces have diffuse behaviour, the determination of the radiative effective properties is a purely geometrical problem [63]. Neglecting the impact of the potential gaps between the tubes, the effective absorptivity is:

$$\alpha_{\mathrm{i}} = \frac{\alpha_{\mathrm{pipe}}}{\frac{2}{\pi}\left(1-\alpha_{\mathrm{pipe}}\right)+\alpha_{\mathrm{pipe}}} \tag{3-3}$$

The effective emissivity in the longer wavelengths is established identically. The surfaces of the absorber are numbered into $N=84$ elements starting from the first frustum element close to the aperture to the annulus element at the back of the cavity following the profile of the receiver. The HC flow path follows the same order: liquid water enters the receiver going through the first pipe loop element which corresponds to the first surface, then flows through

the second one and progressively follows the profile to exit the receiver after having been through the last pipe loop at the bottom of the cavity.

The fluid properties of the water-steam mixture are determined using Freesteam [118] which is based on the IAPWS-IF97 steam tables.

Neglecting the hydrostatic static pressure contribution the momentum balance (eq. 2-169) and applying it to the discretised flow-path of the HC gives:

$$p_{\mathrm{HC}}\left(\ell_{i+1}\right)=p_{\mathrm{HC}}\left(\ell_{i}\right)+\rho\left(T_{\mathrm{HC}}\left(\ell_{i}\right),p_{\mathrm{HC}}\left(\ell_{i}\right)\right)\left(\frac{v\left(\ell_{i}\right)^{2}}{2}\right)-\rho\left(T_{\mathrm{HC}}\left(\ell_{i+1}\right),p_{\mathrm{HC}}\left(\ell_{i+1}\right)\right)\left(\frac{v\left(\ell_{i+1}\right)^{2}}{2}\right)-F_{\Delta p,i} \quad (3\text{-}4)$$

The heat transfer coefficient u_{conv} is determined using different Nusselt number correlations depending on the flow structure and quality of the water steam mixture [73] (Table 3-2). The following flow boiling model is an updated version of a published study [161].

$$u_{\mathrm{conv,i}}=\frac{k\left(\ell_{i}\right)Nu\left(\ell_{i}\right)}{D\left(\ell_{i}\right)} \quad (3\text{-}5)$$

The steam equilibrium quality, also known as dryness fraction, ξ, is defined as the ratio of the mixture enthalpy to the saturation enthalpy of the liquid at the same pressure and divided by the latent heat of vaporisation.

$$\xi\left(\ell\right)=\frac{h_{\mathrm{HC}}\left(\ell\right)-h_{\mathrm{HC}}\left(p_{\mathrm{sat}}\left(\ell\right)\right)}{L_{\mathrm{vap}}} \quad (3\text{-}6)$$

Table 3-2: Heat transfer coefficient correlations for turbulent flow of water-steam mixtures in a cylindrical pipe.

		$\mathrm{Re}<10^4$	$\mathrm{Re}\geq10^4$
ξ	$\xi<0$	Gnielinski [46]	Petukhov & Popov [115]
	$0<\xi<0.8$	Kandlikar [74]	
	$0.8\leq\xi<0.9$	Groeneveld [51]	
	$\xi>0.9$	Gnielinski [46]	Petukhov & Popov [115]

The Gnielinski and the Petukhov and Popov correlations have similar validity regions but Kandlikar, used here for the flow boiling region, bases his boiling coefficients on the Gnielinski correlation for Reynolds numbers below 10,000 and on the Pethukov and Popov correlation for Reynolds numbers over 10,000. We consequently keep the same arrangement for single phase flows in the model.

The Gnielinski correlation is:

$$Nu = \frac{\left(\mathrm{Re}-1000\right)\mathrm{Pr}\frac{f_F}{2}}{1+12.7\left(\mathrm{Pr}^{\frac{2}{3}}-1\right)\sqrt{\frac{f_F}{2}}} \tag{3-7}$$

The Petukhov and Popov correlation is:

$$Nu = \frac{\mathrm{RePr}\frac{f_F}{2}}{1.07+12.7\left(\mathrm{Pr}^{\frac{2}{3}}-1\right)\sqrt{\frac{f_F}{2}}} \tag{3-8}$$

With f_F the Fanning friction factor. The Darcy-Weisbach friction factor, f_{DW}, is given by the solution proposed by Brkić for the Colebrook-White correlation [19]:

$$f_{DW} = \left(-2\log_{10}\left(\frac{\varepsilon_r}{3.71D}+\frac{2.18S}{\mathrm{Re}}\right)\right)^{-2} \tag{3-9}$$

With ε_r the roughness of the pipe, usually (~0.045 mm for standard steel pipes), D the diameter of the pipe and S:

$$S = \ln\left(\frac{\mathrm{Re}}{1.816\ln\left(\frac{1.1\mathrm{Re}}{\ln\left(1+1.1\mathrm{Re}\right)}\right)}\right) \tag{3-10}$$

The Fanning friction factor is obtained from the Darcy-Weisbach friction factor with:

$$f_F = \frac{1}{4} f_{DW} \tag{3-11}$$

The Kandlikar correlation evaluates a modified heat transfer coefficient based on the heat transfer coefficient obtained with the previous correlations for a saturated liquid only phase. Two flow boiling regimes are distinguished, convective boiling (CB) and nucleation boiling (NB). For non-horizontal tubes:

$$u_{\mathrm{conv,\,CB}} = u_{\mathrm{conv,liquid}}\left(1-\xi\right)^{0.8}\left(1.136Co^{-0.9}+667.2Bo^{0.7}\right) \tag{3-12}$$

$$u_{\mathrm{conv,\,NB}} = u_{\mathrm{conv,liquid}}\left(1-\xi\right)^{0.8}\left(0.6683Co^{-0.2}+1058Bo^{0.7}\right) \tag{3-13}$$

With Co the convection number:

$$Co = \left(\frac{\rho_{\mathrm{gas}}}{\rho_{\mathrm{liquid}}}\right)^{0.5}\left(\frac{\left(1-\xi\right)}{\xi}\right)^{0.8} \tag{3-14}$$

And the boiling number, Bo :

$$Bo = \frac{\dot{q}''_{\mathrm{HC}}}{\rho_{\mathrm{HC}} v_{\mathrm{HC}} h_{\mathrm{HC}}} \tag{3-15}$$

ρ_{liquid} and ρ_{gas} refer to the density of the saturated liquid and saturated vapour steam at the pressure and saturated temperature considered.

The heat transfer coefficient adopted is the higher of the two values obtained:

$$u_{\mathrm{conv}} = \max\left(u_{\mathrm{conv,\,CB}}, u_{\mathrm{conv,\,NB}}\right) \tag{3-16}$$

The Groeneveld correlation is:

$$Nu = a\left(\mathrm{Re}_{\mathrm{gas}}\left(\xi + \frac{\rho_{\mathrm{gas}}}{\rho_{\mathrm{liquid}}}(1-\xi)\right)\right)^{b} \mathrm{Pr}^{c}\,\mathrm{Y}^{d} \tag{3-17}$$

$\mathrm{Re}_{\mathrm{gas}}$ is the Reynolds number for the equivalent saturated vapour flow in the pipe (considering saturated vapour in the pipe element). For tubes: $a = 1.09\times10^{-3}$, $b = 0.989$, $c = 1.41$, and $d = -1.15$. Y is given by:

$$\mathrm{Y} = 1 - 0.1\left(\frac{\rho_{\mathrm{liquid}}}{\rho_{\mathrm{gas}}} - 1\right)^{0.4}(1-\xi)^{0.4} \tag{3-18}$$

The pressure drop due to friction $F_{\Delta p,i}$ is given by the following relation in which ρ_i is determined from equations of state with the pressure and enthalpy:

$$F_{\Delta p,i} = f_{\mathrm{DW}} \frac{\left(\ell_{i+1} - \ell_i\right)}{D_i} \rho_i \frac{v^2}{2} \tag{3-19}$$

3.1.3 SG4 dish with SG3 receiver simulation

The precision of the view factors is set to 0.1 % following the methodology presented in 2.4.3. The convergence criterion for the energy balance is 0.001%.

Parallel work in the same project on modelling and experimental measurement of natural convection heat transfer loss from cavity receivers established an approximate heat-transfer coefficients map using an approximated Direct Navier-Stokes (DNS) CFD method and a more conventional turbulence model based approach [120]. The results from the resulting simulations, presented in Figure 3-11, are used as external heat transfer coefficients in the cavity receiver model.

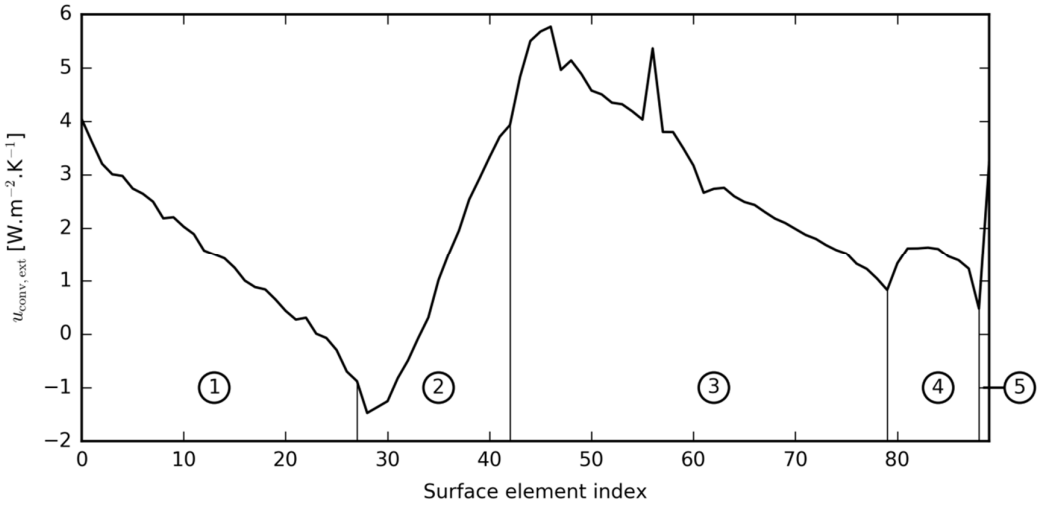

Figure 3-11: Natural convection heat transfer coefficient for the external convective heat loss on each axisymmetric element of the receiver from internal data at the Solar Thermal Group. The numbers in circles indicate the receiver region concerned as per the previous diagram.

The heat transfer coefficient is negative on some of the surface elements, denoting a recovery of convective heat. In the negative heat transfer coefficient elements, air heated by convective heat loss from hot regions comes into contact with colder regions and exchanges heat back to the absorber.

The following results (Figure 3-12) were obtained for a simulation with a liquid water input at 60 °C and 50 bar, and setting the outlet temperature at 500 °C. The ray-tracing was performed using 5,000,000 rays and the source model used a Buie sunshape with 1 % CSR and 1000 W/m^2 DNI.

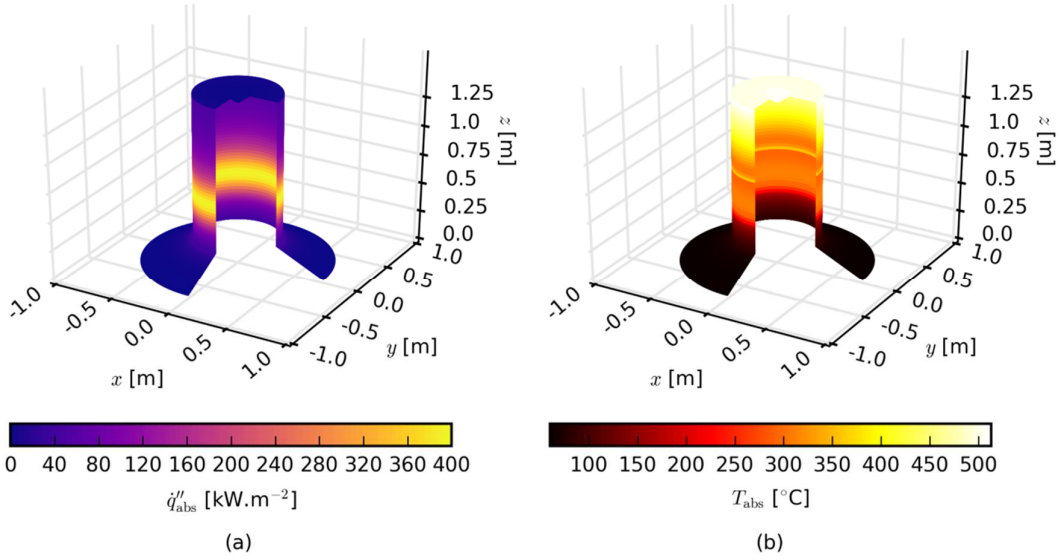

Figure 3-12: SG3 absorber (a) net heat flux and (b) temperature distributions.

The net heat flux on the virtual, non-grooved, absorber surface is presented in Figure 3-12 (a). Figure 3-13 displays the variation of temperature, pressure specific enthalpy,

convective heat transfer coefficient, steam dryness fraction and flux along the flow path. The radiative flux is relatively low on the region number 1 of the receiver which is fairly exposed to the surroundings. In that region the tube surface temperature is relatively cold and the receiver suffers little emissive loss. The flux gradually increases on the first cylindrical section of the receiver (section 2) and then sharply increases to reach the peak flux value of ~400 $kW.m^{-2}$ on section 3. Similarly, the temperature increases on section 2 and the reaches a stable value on section 3, revealing the boiling region. The flux then gradually decreases down to values below 50 $kW.m^{-2}$ and the receiver profile transitions to the flat disc, section 4 where the flux instantly increases, the flux being more intense on the surface due to cosine effects. In these regions, the steam is in superheated stage and the temperature gradually increases again. Finally, the passive cone section at the back is adiabatic and has no net heat flux, however, the incident flux being still significant (60.5 $kW.m^{-2}$ without considering the thermal emissions from the rest of the cavity), the temperature of the passive cone is very high to release the energy in the form of convective and radiative loss.

The temperature profile at the top of Figure 3-13 clearly shows the position of the boiling region. The inner and outer wall temperatures show some localised variations related to the change in heat transfer coefficient along the flow path. The first significant drop in heat transfer coefficient occurs with the change in diameter between section 2 and section 3 which causes the velocity of the HC to drop. This change in diameter has a positive impact on the pressure drops as can be seen with the change in the slope of the pressure curve just after the transition to section 2. With the start of the sub-cooled flow boiling region, the heat transfer coefficient starts to increase significantly thanks first to nucleate boiling then to the convective boiling driven regimes between steam dryness fractions of 0 and 0.8. At the dryness fraction of 0.8 the steam flow reaches the dry-out region, liquid water is isolated from the tube internal walls by dry steam and the heat transfer coefficient drops and the temperature of the pipes increases sharply as can be seen clearly in Figure 3-12 (b). At this stage, the pressure drops start to become significant with most of the HC being in gas phase. The difference between the temperature of the fluid and the inner wall of the tube increases post dry-out. The reduction in flux at the end of section 3 causes a reduction in the difference of temperature between the fluid and the wall of the heat exchanger. The two different flux lines represented in the bottom graph of Figure 3-13 show the value relative to the tube surface, considering a uniform distribution on the semi-cylindrical section of each coil loop, and the value relative to the equivalent absorber surface previously presented. The absorber averaged surface value is significantly higher because of the smaller area involved. In reality, however, the peak flux seen by the tube surface could reach much higher values as some of the tube surfaces faces the incoming flux more perpendicularly.

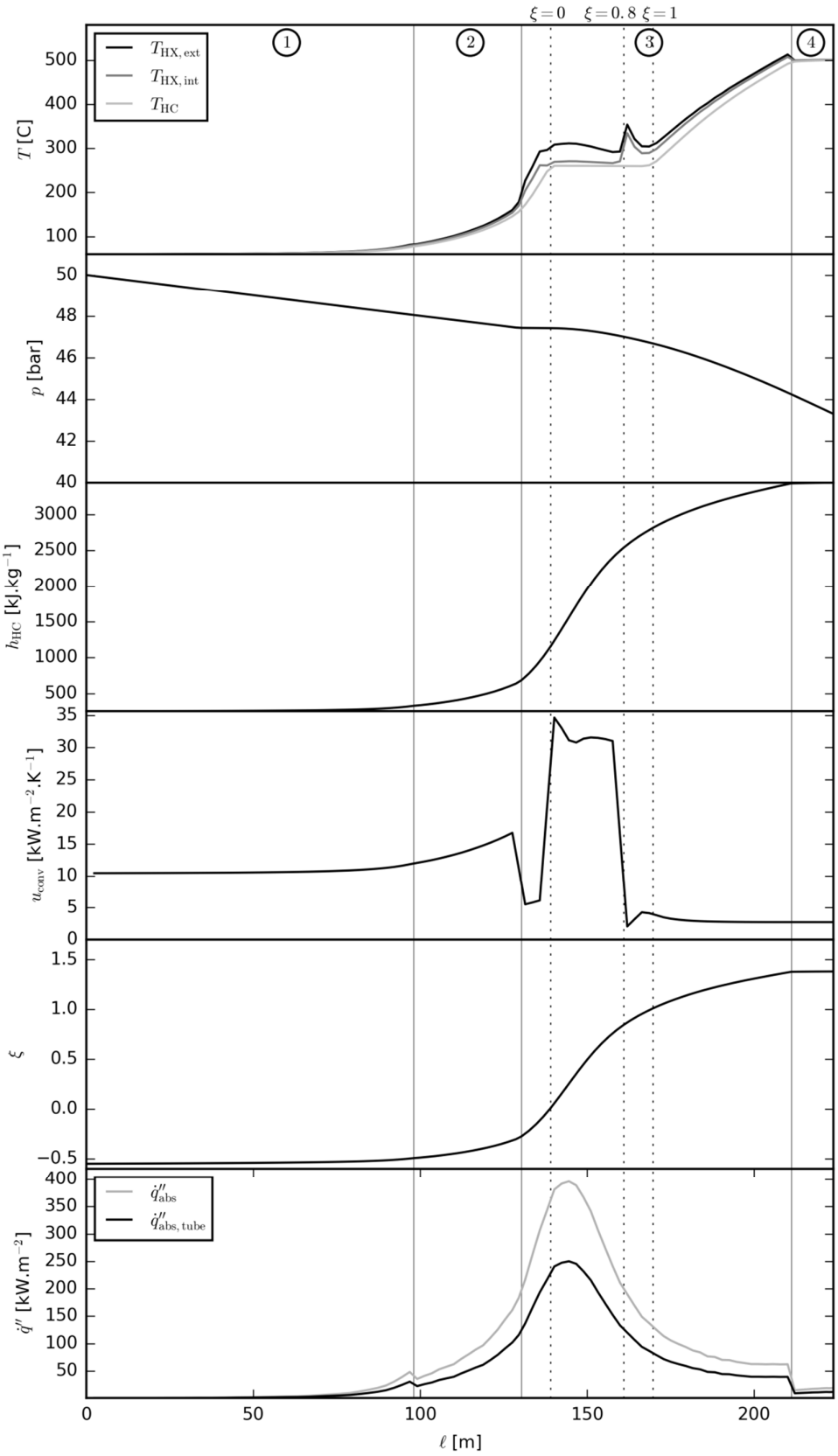

Figure 3-13: SG3 receiver flow path simulation results. The surfaces of the receiver that the flow path covers are separated with solid vertical lines and the surfaces indices identified with the circled number in the top plot. The vertical dashed lines identify the quality of the saturated mixture.

The energy balance of the system is displayed in Figure 3-14.

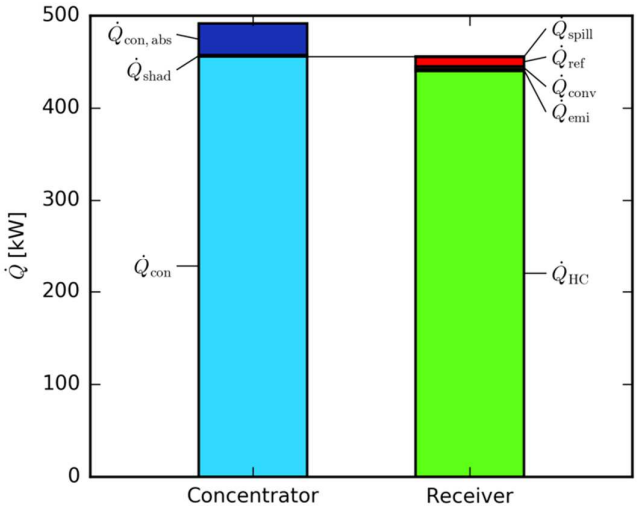

Figure 3-14: Concentrator and receiver energy balance breakdown.

The largest contributors to the energy loss of the system are the absorption loss from the concentrator and the convective loss from the receiver. A closer look at the receiver losses breakdown is shown in Figure 3-15. Spillage losses amount to about 200 W and are negligible.

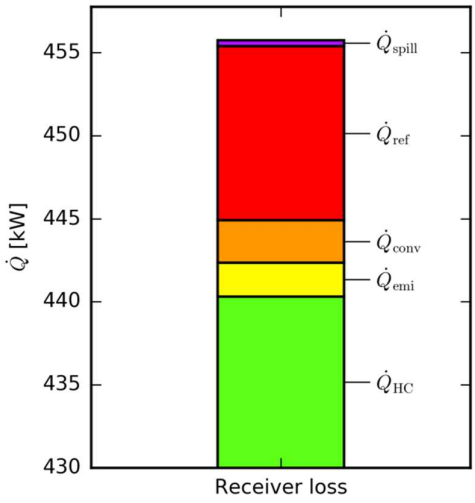

Figure 3-15: Receiver energy balance breakdown highlighting heat losses.

The largest heat loss contribution is from reflective loss with 5.1 kW, followed by convective losses with 2.4 kW of energy loss, then 1.9 kW of emissive loss and finally 214 W of spillage loss. The efficiencies breakdown is given in Table 3-3.

The two major areas of uncertainty on the results of this model concern the convective loss, due to the difficulty in validating natural convection loss simulations, and the pressure drops in which a standard and non-validated pipe roughness of 0.045 mm was arbitrarily chosen, which could influence the heat transfer coefficient in the tube. In the absence of

experimental measurements, these results cannot be validated for the SG3 receiver. The design of a new receiver for the SG4 dish will be presented in the last chapter of this thesis and experimental results used to validate the model.

Table 3-3: SG3 concentrator and cavity receiver efficiency summary.

<table>
<tr><td colspan="4">System efficiency:
$\eta_{sys} = \eta_{con}\eta_{rec} = 89.6\ \%$</td></tr>
<tr><td>Concentrator efficiency:
$\eta_{con} = 92.7\ \%$</td><td colspan="3">Receiver efficiency:
$\eta_{rec} = 96.6\ \%$</td></tr>
<tr><td></td><td colspan="2">Optical efficiency:
$\eta_{opt} = 97.6\ \%$</td><td>Thermal efficiency:
$\eta_{th} = 96.7\ \%$</td></tr>
<tr><td></td><td>Intercept efficiency:
$\eta_{intercept} = 99.9\ \%$</td><td>Absorption efficiency
$\eta_{abs} = 97.7\ \%$</td><td>Heat exchanger efficiency:
$\eta_{hx} = 99.0\ \%$</td></tr>
</table>

3.2 Central receiver system model

3.2.1 Comments on heliostat field modelling

The optics of central receiver systems are challenging to model accurately due to the added complexity brought by the Fresnel discretisation of the reflective surface. While a single quadratic surface can be used to evaluate reflected ray intersections and reflection directions for a dish concentrator, for a CRS each heliostat has to be modelled. The number of different surfaces that have to be considered for intersections is greatly increased and sometimes leads to impractical computation times. Approaches exist to mitigate the computation time on such large scenes and the computer graphics field is rich with algorithms able to greatly speed-up heliostat field computations: pseudo-MCRT, voxel partition and other bounding volumes approaches, backward MCRT [66]. Most of these approaches are not standard in scientific ray-tracing codes and require significant code development and validation. The programming language and efficiency of the routines used can have an impact on the computations as well.

Tracer, used in this work, is not a code optimised for the ray-tracing of large number of surfaces and is relatively slow with scenes involving large number of heliostats, despite the high performance of the numerical computations routines coded in Fortran and C that Numpy and Scipy use. The present work focuses on receiver optimisation and improvements to heliostat field simulation performance will not be detailed. Without any specific algorithmic approach, simulation of heliostat fields with relatively small number of heliostats (<500) is less challenging and can be undertaken with *Tracer* without modification of the general approach to ray-tracing. The first example of heliostat field considered in this section is a small scale

heliostat field modelled with *Tracer*. Finally a method to couple results of a different code and Tracer is proposed for improved performance in receiver optimisation problems.

3.2.2 Small scale heliostat field: Sandia National Laboratories NSTTF

The National Solar Thermal Test Facility is a laboratory operated by Sandia National Laboratories in Albuquerque in the United States of America and dedicated to the study of prototype and pilot scale solar technologies. The NSTTF includes a heliostat field and a tower with 3 testing bays for receivers.

The NSTTF heliostat field is composed of 218 square heliostats of 37 m^2 (6.1m by 6.1 m) of reflective surface and the tower is 61 m high. The mirror reflectivity has been measured at 0.96 however; some gaps between the 25 mirror facets composing each single heliostat reduce the effective mirror area to 97 % of the heliostat ideal surface. The slope error of the mirror facets is assumed to be 1 mrad.

Figure 3-16: On-site picture of the NSTTF tower and heliostat field at Sandia National Laboratories, Albuquerque (NM) (personal photograph).

The model proposed here evaluates the heliostat field total efficiency as defined in the previous chapter and repeated in the following equation:

$$\eta_{\text{con,tot}} = \eta_{\text{atm}}\eta_{\text{bloc}}\eta_{\text{ref}}\eta_{\cos}\eta_{\text{shad}} \tag{3-20}$$

Shading is evaluated with the difference between the ideal intercepted radiative power coming from the source $\dot{q}_{h,\text{in, ideal}}$ and the actual simulated value $\dot{q}_{h,\text{in}}$ for each heliostat. $\dot{q}_{h,\text{in}}$ is determined in the simulation using the known absorptivity of the heliostats and the amount of radiative energy they absorb in the first reflection. Using the conventions from chapter 2:

$$\dot{q}_{h,\text{in}} = \frac{1}{\alpha_h}\dot{q}_{h,\text{abs}} \tag{3-21}$$

$$\dot{q}_{h,\text{in, ideal}} = A_h G \hat{\mathbf{n}}_h . \hat{\mathbf{d}}_h \tag{3-22}$$

$$\dot{q}_{h,\text{shad}} = \dot{q}_{h,\text{in, ideal}} - \dot{q}_{h,\text{in}} \tag{3-23}$$

The cosine loss is implicit in the ray-tracing as it arises from the angle at which rays are incident on the heliostats and target. Cosine loss can be explicitly determined using:

$$\dot{q}_{h,\cos} = \dot{q}_{h,\text{in}} \hat{\mathbf{n}}_h . \hat{\mathbf{d}}_h \tag{3-24}$$

The reflected radiative power is identified using the incident radiative power at each heliostat location and their known reflectivity.

$$\dot{q}_{h,\text{ref}} = \dot{q}_{h,\text{in}} \rho_h \tag{3-25}$$

Blocking can be identified in the ray-trace by detecting which rays have been reflected one time from the heliostat reflective surfaces and intercepted again by a heliostat surface. Tracer treats the ray-tracing on a bundle-by-bundle basis. The first ray-bundle is cast from the source and all potential interactions are determined; then the second bundle is cast from the first intersection locations, etc. The information of each of these sequential ray-bundles can be stored in a "ray-tree", an object listing the successive ray-bundle objects, while the simulation is running. The ray-tree can be accessed for post-processing to obtain information about any ray cast. A very useful feature of the ray-tree object is the possibility to automatically store the indices of the rays that are related in successive bundles and consequently be able to recall the full history of every ray. Blocked rays identification is illustrated in Figure 3-17 and summarised here:

1. Detecting rays whose starting position in the third bundle is within the heliostat field dimensions; these are the end-points of the blocked rays.
2. Find the starting position of the blocked rays by detecting the starting location of their parent rays in the second bundle.
3. Assign the blocked rays to each heliostat by comparing their origin location with the heliostat coordinates.
4. Sum the energies borne by the blocked rays on each heliostat.

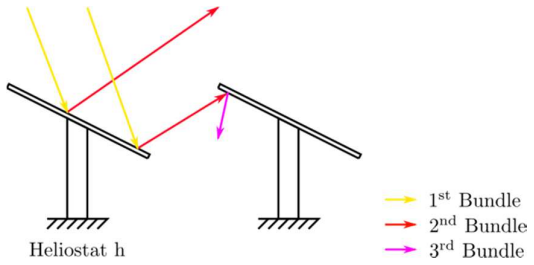

Figure 3-17: Sequential decomposition of blocking loss events in the ray-trace.

The heliostat field is relatively small and atmospheric attenuation losses are neglected. For the following simulation, the heliostats are assumed flat (an approximation adopted for comparison with relevant literature as shown later in this section) and the source extent is a

disc positioned above the heliostat filled with a radius large enough to cover the whole field and receiver, considering the maximum angular extent of the sunshape. The sunshape model is the Buie sunshape with a CSR of 1 %. This simple source model is very inefficient: a lot of the generated rays miss the heliostats in the field in the first iteration which causes the convergence of the simulation results to be relatively slower than it could be. The purpose of this model, however, is to present an example of a heliostat field simulation with Tracer and validate the results, and modifications to improve the efficiency of the model were not considered at this stage. The ray-tracing model is rendered in Figure 3-18.

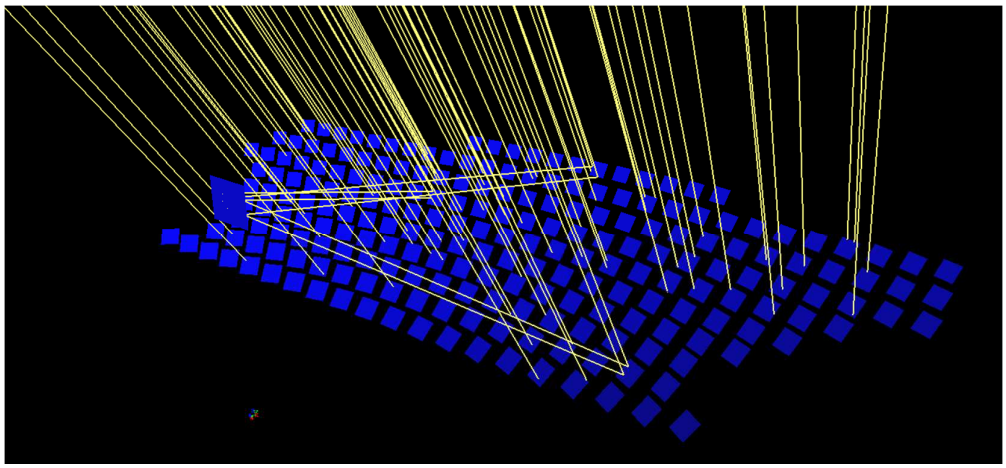

Figure 3-18: 3D rendering of the ray-trace of the NSTTF heliostat field with Tracer.

The following results were obtained after 200,000,000 rays cast from the source.

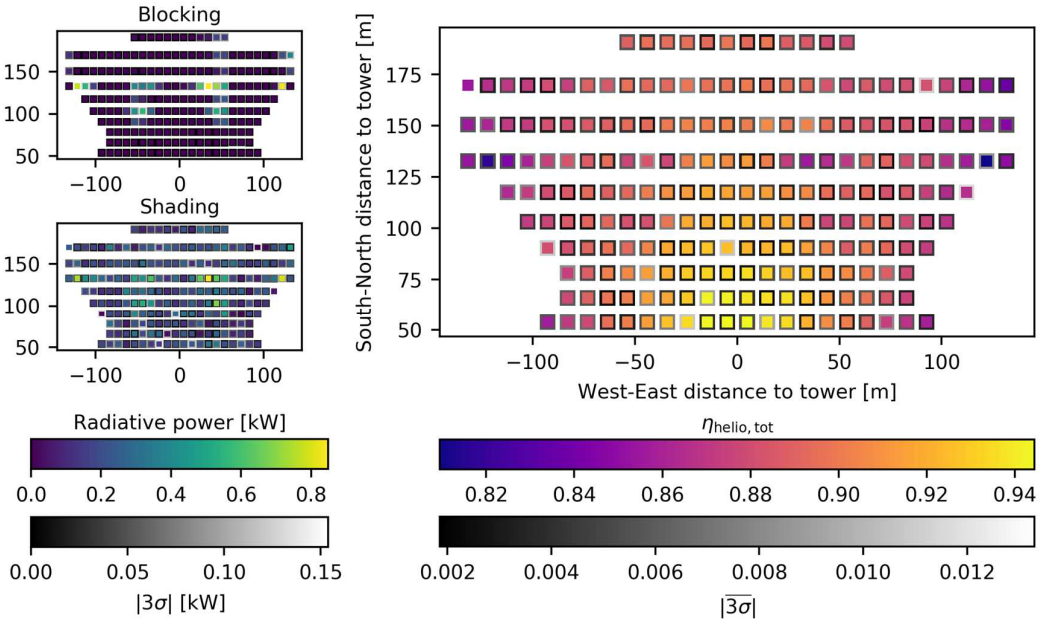

Figure 3-19: Optical simulation results for the Sandia NSTTF field for the spring equinox ($\theta_{az} = 0,\ \theta_{ze} = 34.96$). The inner colour in each square is for the performance of the heliostat while the grey shade in the outer frame indicates the precision of the evaluation, arising from Monte-Carlo sampling.

An existing study compared the simulation of the same field example with a range of optical simulation tools and concluded that SolTrace was an acceptable choice for their use [159]. The resulting fluxmaps of the NSSTF field on flat targets are presented in Figure 3-20.

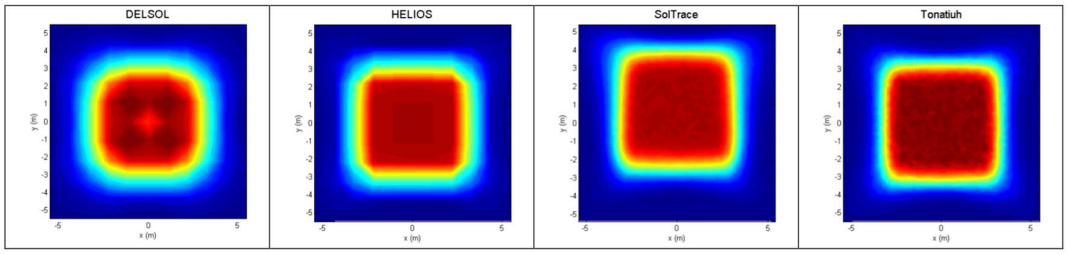

Figure 3-20: Fluxmap images from four optical tools from [159]. The flux from the NSTTF field is incident on a flat plate of size 11 m x 11 m. All four plots have the same x, y, (local coordinates of the receiver) and colorbar scales. Colorbar scale is from 0 to 170 kW.m^{-2}.

Some discrepancy was found when comparing the results from the Tracer with the proposed results from SolTrace, as can be observed by comparing Figure 3-21 with Figure 3-20, and a new simulation with the SolTrace package was set-up to validate the tracer.

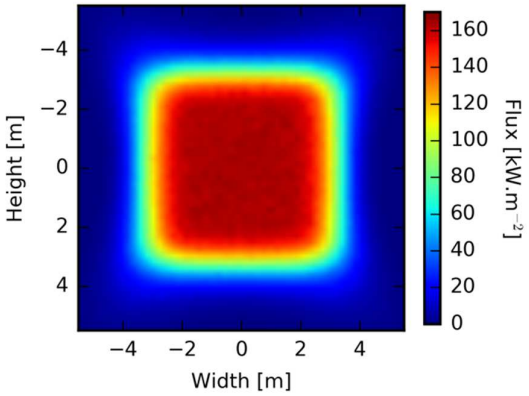

Figure 3-21: Tracer fluxmap of the NSTTF field on a flat target with flat heliostats [148].

The in-house simulation using SolTrace shows a very good agreement with Tracer results, as shown in Figure 3-22.

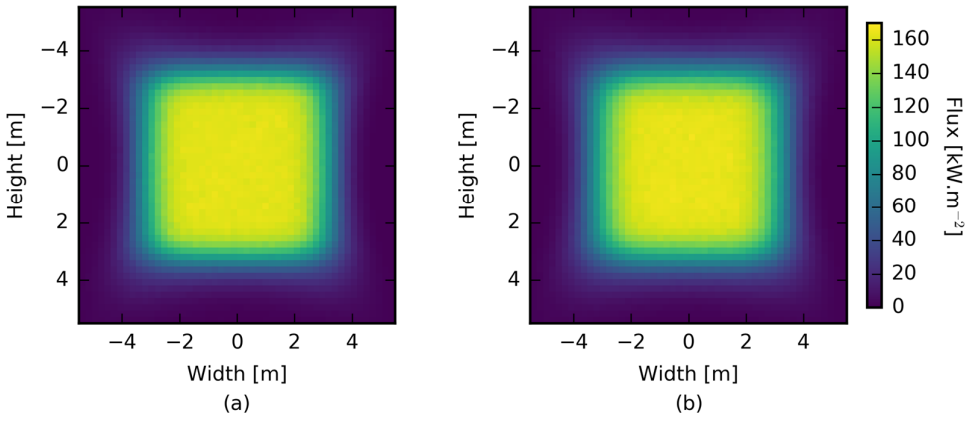

Figure 3-22: NSTTF flat target fluxmap with (a) Tracer and (b) SolTrace.

These fluxmaps were obtained using a square target located at the top front of the tower and 20,000,000 effective rays (rays reaching the heliostat field in the first place). The following table illustrates the good agreement between the results from the previous study and the new data presented here:

Table 3-4: Heliostat field model validation using target fluxmap data.

	[159]				This work	
	DELSOL	HELIOS	SolTrace	Tonatiuh	SolTrace	Tracer
Peak flux [kW.m^{-2}]	178	164	168	176	168	166
Average flux [kW.m^{-2}]	53.4	49.3	62.4	61.2	60.6	60.2
Total power [MW]	7.17	7.24	7.34	7.37	7.33	7.28

Despite the good agreement, a small discrepancy subsists between the results obtained in this work. The source of this discrepancy is most probably found in three differences between the Tracer model and the SolTrace model:

- The Buie sunshape in Tracer is using a modified input, presented in the previous chapter, to accurately model the right circumsolar ratio while SolTrace uses the non-modified model.
- There can be discrepancies in the treatment of the surface slope error on the heliostat surface which can lead to slightly different reflected ray directions.
- The convergence rate of both programs is expected to be different considering the ray-tracing strategies considered. Without detailed information about the inner workings of SolTrace or the standard deviation of the results, it is hard to evaluate how this impacts the results.

3.2.3 Large scale heliostat field: ASTRI test field

The reference case configuration developed by the ASTRI consortium is a surround field configuration aimed at providing enough concentrated solar radiation to run a 25 MWe power plant. The heliostat field is composed of 6177 square heliostats of 6.1 m x 6.1 m in a specific layout presented in Figure 3-23. The reflectance of the heliostat mirrors is 0.9 and the slope error of the heliostats is assumed to be following a Gaussian bi-variate distribution of 1.53 mrad of standard deviation. In this modelling work, the heliostats are considered flat.

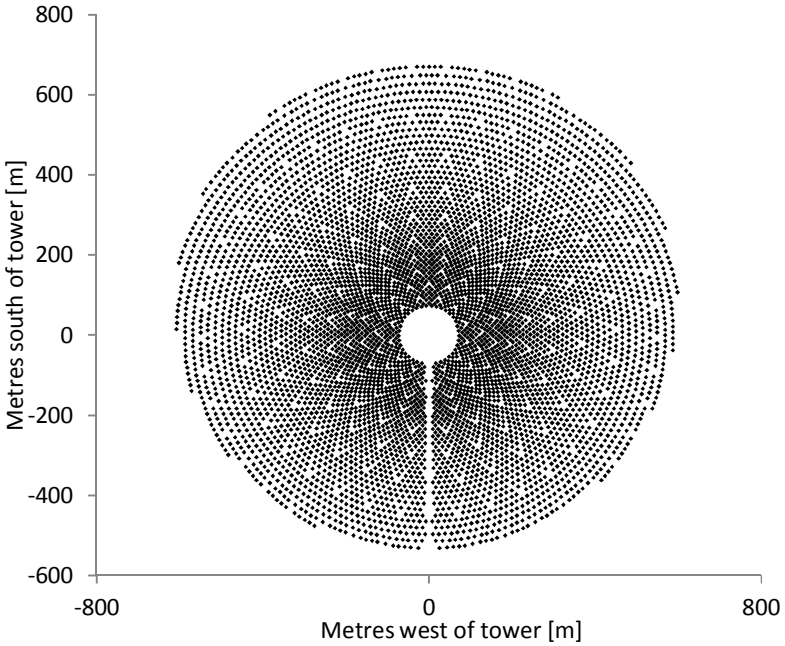

Figure 3-23: The ASTRI test field layout.

The larger number of heliostats leads to unpractical simulation times with the Tracer. The P11 group responsible for the development of improved heliostat field layouts in ASTRI has the capacity to produce detailed ray-traces of the reference case heliostat field with Tonatiuh[7], a further advanced statistical open-source ray-tracing code in c++ able to handle heliostat fields simulations. The focus of the work developed in this thesis is the optimisation of receiver geometries and therefore a method was developed to interface ray-tracing results from other softwares with the Tracer library. In addition to the flexibility provided, the capacity to store and re-use concentrator MCRT results is valuable in an optimisation perspective: the most computationally expensive stage of the simulation is generally the simulation of the heliostat field in concentrated receiver systems and re-using a given result for different receiver concepts can provide significant time gains.

3.2.4 Intermediate Receiver Enclosing Source (IRES) method

The method's objective is to re-use expensive ray-tracing results for any geometry or receiver put at the focal point of a concentrator. The rays, generated using random variates, are intercepted by a virtual bounding surface able to contain all the receiver concepts that are going to be simulated on that field. The rays positions, directions and energy content are then stored in a data file that can be called back as a source of rays for any upcoming ray-trace. Figure 3-24 illustrates the method set-up with a spherical surface positioned around a

[7] Source code: http://iat-cener.github.io/tonatiuh/

cylindrical receiver, itself at the focal point of a fraction of the ASTRI reference case heliostat field.

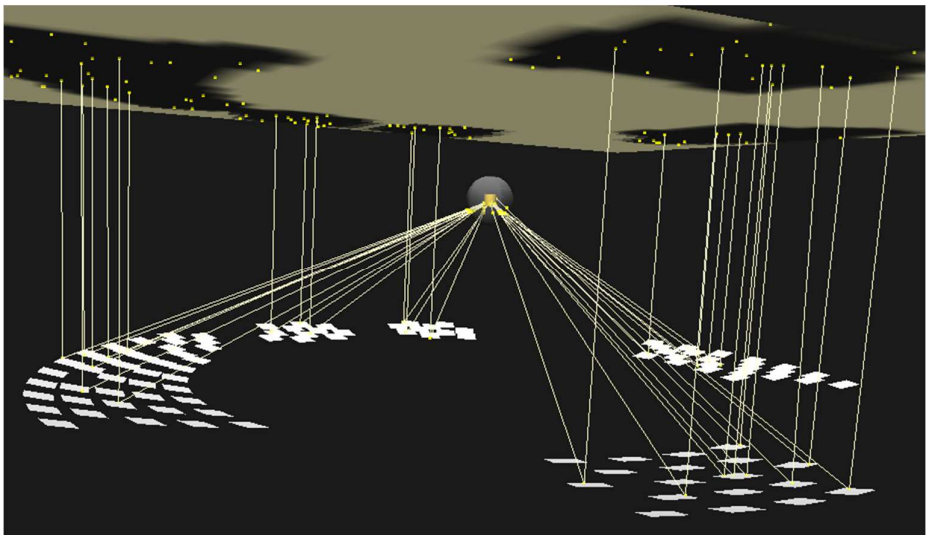

Figure 3-24: Tonatiuh rendering of a fraction of the ASTRI test field used to validate the IRES method (courtesy of C. Corsi).

The arrays describing the position of the intersections (3 float numbers) and unit direction vectors (3 float numbers between 0 and 1) of each ray with the intermediate surface are converted into binary ".dat" files to minimise the storage volume needed. Knowing the number of rays contained in a certain file and the format of the binary numbers, the information necessary to describe a full bundle of rays can be interpreted from the binary file and used as a source by Tracer. A validation of the IRES method was carried out using a test bundle of 100,000 rays and the fraction of the field shown in Figure 3-24. The ray-trace of a test cylindrical receiver was performed and the ray directions and intersection positions on the intermediate sphere recorded simultaneously. The IRES data are illustrated in Figure 3-25 and the corresponding 3D fluxmap on a cylindrical target inside the IRES shown in Figure 3-26.

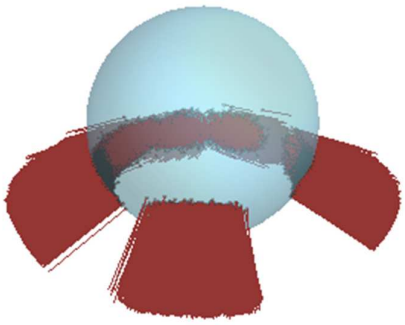

Figure 3-25: Rendering of the directions and locations of the rays from the test bundle of 100,000 rays on the IRES sphere (courtesy of C. Corsi).

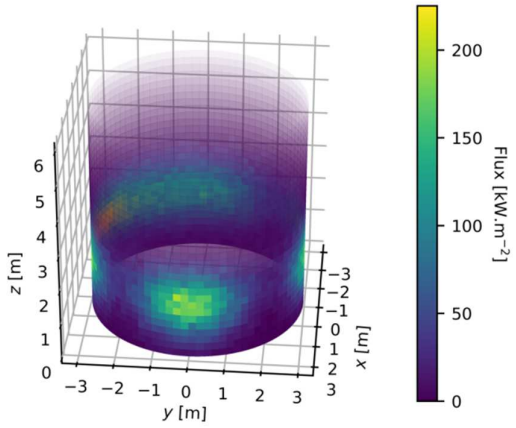

Figure 3-26: Fluxmap of the test bundle from the sphere to the test cylindrical receiver using Tracer.

To validate the results, the ray-trace was then performed using the IRES with Tracer and compared with the Tonatiuh result. Both results are exactly identical as shown in Figure 3-27.

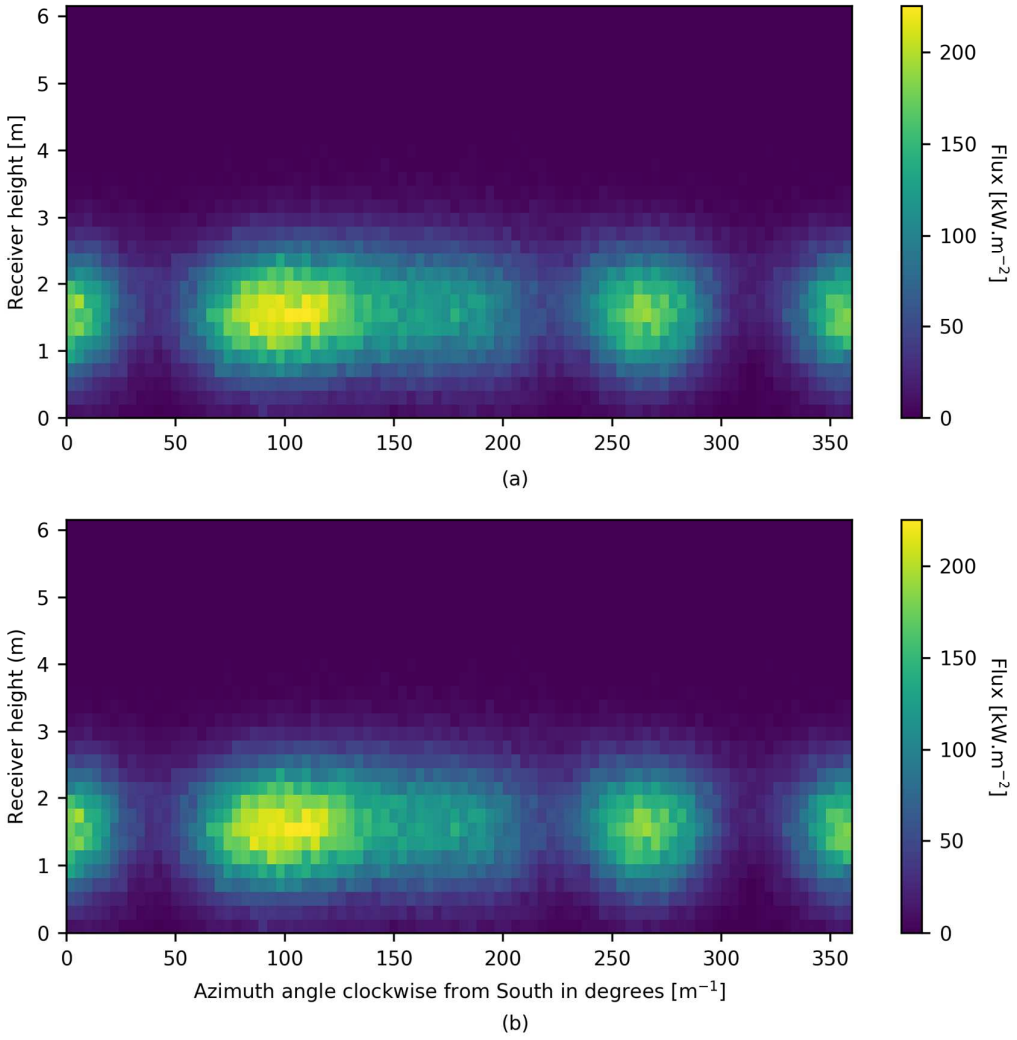

Figure 3-27: Fluxmaps from (a) Tracer and (b) Tonatiuh ray-traced data showing the exact agreement between the result data simulated with the two codes.

The IRES method is very convenient, particularly in a receiver geometry optimisation problem as it will be explained in chapter 4. The only limitation of the method concerns shading from the receiver to the Heliostat field. If the intermediate surface is chosen too large, it could artificially increase the shading provoked by the receiver on the heliostat field. This is however a secondary loss mechanism in most CSP systems and has little influence on the general performance of the full system. In order to mitigate the error, the size of the boundary surface must be chosen carefully and as small as possible. Receiver spillage issues, however, are not an issue as the ray-tracing of the receiver will still consider spillage correctly.

3.2.5 Receiver model

The objective of this section is to present a simplified central receiver model illustrative of the state-of-the-art using the model framework presented in the previous chapter. The receiver example is not an optimised system but rather a realistic configuration.

The ASTRI reference field was determined considering a cylindrical receiver of diameter $D_r = 6$ m and height $H_r = 6.33$ m positioned at the origin of the referential in Figure 3-23. The optical height of the receiver (from the elevation pivot point of the heliostats to the mid-height of the receiver) was set to $H_T = 91.1$ m. The absorber of the cylindrical receiver is split into 14 vertical sections of equal surface area, each of them accounting for a vertical bank of N_{tubes} parallel tubes as illustrated in Figure 3-28.

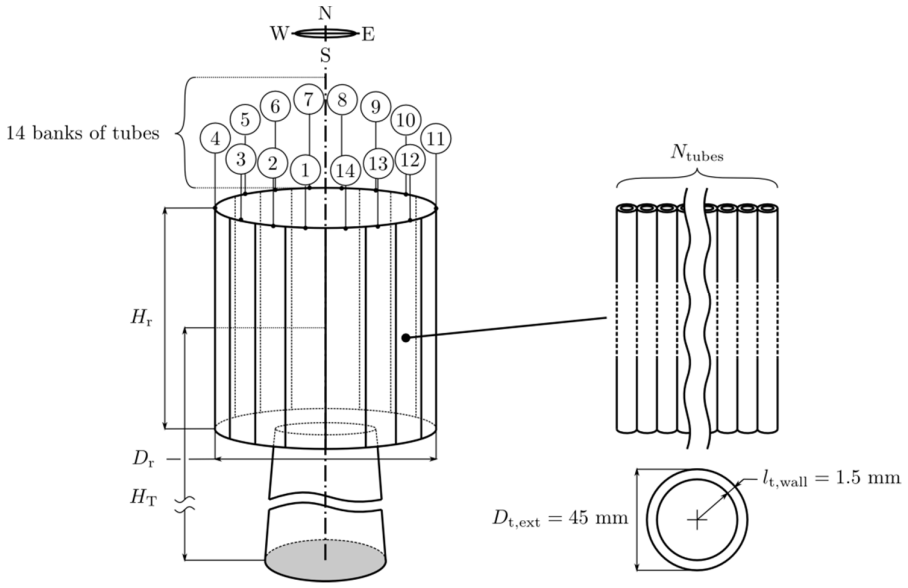

Figure 3-28: Cylindrical tower receiver geometrical model.

The number of tubes is determined using a floor rounded value of the bank surface divided by the tube diameter:

$$N_{\text{tubes}} = \left\lfloor \frac{A_{\text{bank}}}{D_{\text{t,ext}}} \right\rfloor \tag{3-26}$$

Two HC flows are considered in this model to illustrate some important concepts impacting receiver design. The first flow-path, in Figure 3-29 (a), is single pass and counter-clockwise in which the HC enters at the top of the receiver in the South-facing side and circulates in alternating downward and upward flows until reaching the last bank facing South again. In the second strategy two symmetrical hemi-cylindrical flow-paths enter the receiver at the top on the South-facing panels and circulate downward and upward until reaching the northmost panels as shown in Figure 3-29 (b). To avoid confusion, the ASTRI field is located in the southern hemisphere (Alice Springs, Australia) and therefore the highest flux is expected to reach the south-facing panels. The inlet temperature of the solar salt is set to 290°C and the outlet temperature to 565°C.

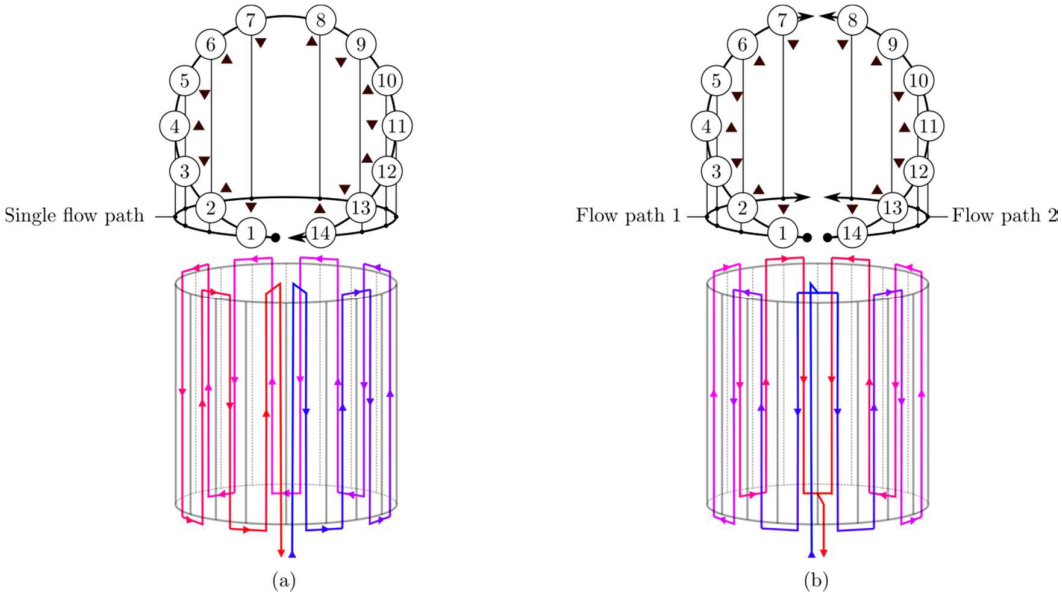

Figure 3-29: (a) Single counter-clockwise flow-path and (b) dual hemi-cylindrical flow-path arrangement. Upward and downward triangles indicate the vertical direction of the flow in the bank of tubes.

Literature values are used for the receiver tubes parameters as summarised in Table 3-5. The receiver tubes are coated with Pyromark 2500 a spectrally selective coating and the absorptance and emittance values at 700 °C are taken as reference and assumed constant over the overall receiver. The receiver tubes are considered to be made of Inconel 625 and the thermal conductivity at 500 °C taken as reference and assumed constant over the whole receiver. The tubes are considered perfectly insulated at the back half, and only exchange to the environment through the front irradiated half.

Table 3-5: Reference tower receiver's tube properties.

Tube property	Symbol	Value	Source
Tube outer diameter	$D_{t,o}$	45 mm	[129]
Tube wall thickness	t_t	1.5 mm	[129]
Inconel 625 thermal conductivity	k_t	19.6 W.m^{-1}.K^{-1}	Manufacturer data[8]
Pyromark 2500 coating thickness	t_c	45 µm	[131]
Pyromark 2500 absorptance	α_c	0.95	[62]
Pyromark 2500 emittance	ε_c	0.88	[62]
Pyromark 2500 thermal conductivity	k_c	0.6 W.m^{-1}.K^{-1}	[130]

Considering no gap between the tubes, each tube bank is composed of 30 tubes. The mass flow of HC is considered to be evenly split between the tubes in the bank so that a 30th of the mass flow in each flow path flows in each tube.

The HC chosen is solar salt (60 wt% $NaNO_3$, 40 wt% KNO_3) and incompressible physical properties correlations are used [14] (temperatures in Kelvin). The density is:

$$\rho_{HC} = 2090 - 0.636\left(T - 273.15\right) \quad [\text{kg.m}^{-3}] \tag{3-27}$$

The dynamic viscosity is:

$$\begin{aligned}\mu_{HC} = {} & 2.2714\times10^{-2} - 1.2\times10^{-4}\left(T-273.15\right) + 2.281\times10^{-7}\left(T-273.15\right)^2 \\ & - 1.474\times10^{-10}\left(T-273.15\right)^3 \quad [\text{kg.m}^{-1}.\text{s}^{-1}]\end{aligned} \tag{3-28}$$

The thermal conductivity is:

$$k_{HC} = 0.443 + 1.9\times10^{-4}\left(T - 273.15\right) \quad [\text{W.m}^{-1}.\text{K}^{-1}] \tag{3-29}$$

The heat capacity is:

$$Cp_{HC} = 1443 + 0.172\left(T - 273.15\right) \quad [\text{J.kg}^{-1}.\text{K}^{-1}] \tag{3-30}$$

The vertical tube banks are treated with the 1D model previously introduced in which each tube bank is discretised into 50 elements in the vertical direction. The heat transfer conditions and HC properties are identical in each of the 30 tubes contained in each of the 50 discretised elements. The internal heat transfer coefficient is obtained from correlations, depending on the fluid flow conditions as presented in Table 3-6.

[8]Source : Retailer website: http://www.hightempmetals.com

Table 3-6: Central receiver system internal pipe flow Nusselt number correlations for molten salts.

		Re		
	Pr	$2300 < Re < 10^4$	$10^4 < Re < 4{,}3x10^4$	$4{,}3x10^4 < Re < 5x10^6$
Nu	$0.5 < Pr < 1.6$			Gnielinski [47]
	$1.6 < Pr < 23.9$	Wu et al. [157] transition flow	Wu et al. [157] turbulent flow	
	$23.9 < Pr < 2{,}000$			

The transition flow correlation from Wu et al. is:

$$Nu = 0.00154\,\mathrm{Re}^{1.1}\,\mathrm{Pr}^{1/3} \tag{3-31}$$

The turbulent flow correlation from Wu et al. is:

$$Nu = 0.02948\,\mathrm{Re}^{0.787}\,\mathrm{Pr}^{1/3} \tag{3-32}$$

The Gnielinski correlation for molten salts is:

$$Nu = \frac{\left(\mathrm{Re}-1000\right)\mathrm{Pr}\,\frac{f_{DW}}{8}K}{1+12.7\left(\mathrm{Pr}^{2/3}-1\right)\sqrt{\frac{f_{DW}}{8}}} \tag{3-33}$$

with:

$$K = \left(\frac{\mathrm{Pr}}{\mathrm{Pr}_{wall}}\right)^{0.11} \tag{3-34}$$

And the Pr_{wall} number determined according to the wall temperature. The Darcy Weissbach friction factor is determined using the Brkić solution to the Colebrook-White equations as presented in eqs. 3-9 and 3-10 earlier in this chapter.

The solution of the problem is obtained using the wall temperatures convergence strategy, presented in the previous chapter.

The simple cylindrical geometry of the absorber enables the use of a fast, albeit approximate, cone optics integration method. The specific code used is SolarPILOT [106] from the US National Renewable Energy Laboratory (NREL) which is an improved version of DELSOL 3 [78], a long standing cone optics code based on Hermite polynomials expansion from Sandia National Laboratories. As mentioned in the introduction, the advantage of using convolution based codes is to result in much faster simulation times.

3.2.6 Results

The system is simulated at the equinox ($\theta_{az} = 0°, \theta_{el} = 66.2°$) under 1,000 W.m^{-2} of DNI. First the concentrated flux incident on the receiver was determined using SolarPILOT and a simple aim-point strategy in which each heliostat points at the centre of the closest bank of tubes. The results, in Figure 3-30 (a) show a peak flux of 2,975 kW.m^{-2} and an average flux of 1,170 kW.m^{-2}. Solar salt decomposition temperature, material corrosion and themo-mechanical cycling limits require fluxes on solar salt receivers lower than 1.2 MW.m^{-2} [129]. In order to obtain a lower receiver incident flux, a new aiming strategy, "image size priority" option in SolarPILOT, is used to produce a lower and more homogeneous flux distribution on the receiver. More information on these aiming strategies can be found in the SolarPILOT manual online [106]. Because of the high average flux obtained originally, the receiver size had to be changed to allow for more space to distribute the concentrated flux and the receiver height was changed from 6.33 m to 10 m to increase the receiver surface area. The result of this new configuration is shown in Figure 3-30 (b) and show an average flux of 764 kW.m^{-2} and a peak flux of 1,180 kW.m^{-2}. This last configuration is chosen for the rest of the case study.

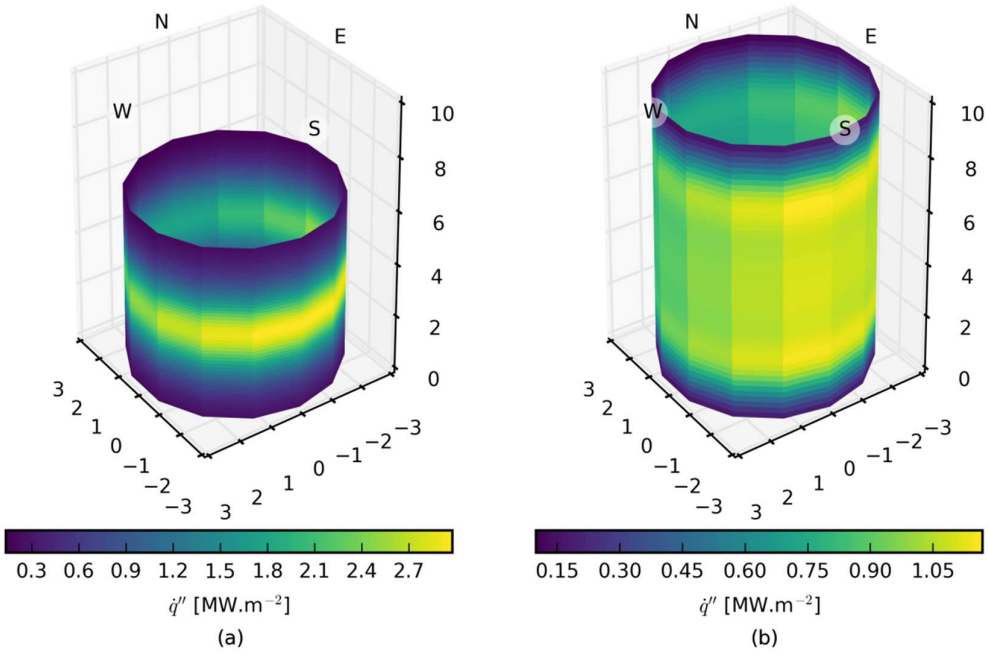

Figure 3-30: Flux distributions on the receiver surface for (a) a "simple aim points" strategy and a receiver height of 6.33 m; and (b) "image size priority" aiming strategy and a receiver height of 10 m.

The heliostat field efficiency breakdown is shown in Table 3-7.

Table 3-7: ASTRI heliostat field efficiencies for both the simple aim points and image size priority aiming strategies at equinox noon.

η_{cos}	80.3%
η_{atm}	95.7%
η_{shad}	100%
η_{ref}	90%
η_{bloc}	99.2%
$\eta_{con} = \eta_{atm}\eta_{bloc}\eta_{ref}$	85.4%
$\eta_{con,tot} = \eta_{atm}\eta_{bloc}\eta_{ref}\eta_{cos}\eta_{shad}$	68.6%

The receiver operation details are presented for the single flow path configuration first and the dual flow-path after that.

3.2.6.1 Single pass counter-clockwise flow-path.

The net heat flux and absorber temperature distributions in Figure 3-31 show the progressive heating of the outer wall of the tubes as the heat gets transferred to the HC flowing in the tubes. The net heat flux to the HC is higher where the flux is higher.

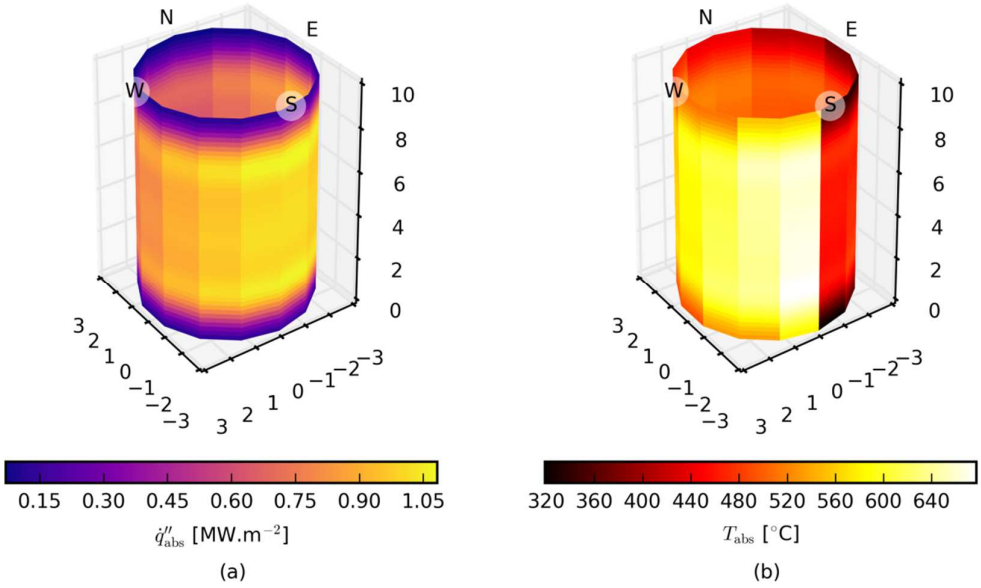

Figure 3-31: (a) Net heat flux and (b) temperature distribution on the reference receiver using a single counter-clockwise flow-path.

In Figure 3-32, the incident flux and net heat flux are compared along the flow path. The uneven flux distribution on each bank of tubes is clearly revealed by the wave pattern along the flow-path: the flux is much lower at the inlet and outlet of each bank. The effect of the flow-path strategy on the flux distributions is also highlighted here: the flux, more intense on

the South facing side of the receiver, is on average higher at the start and at the end of the flow path and lowest in the middle of the flow-path where the tubes face North. The aiming strategy used is not able to produce perfectly even flux along the tube banks and some oscillations can be seen on each of the tube bank.

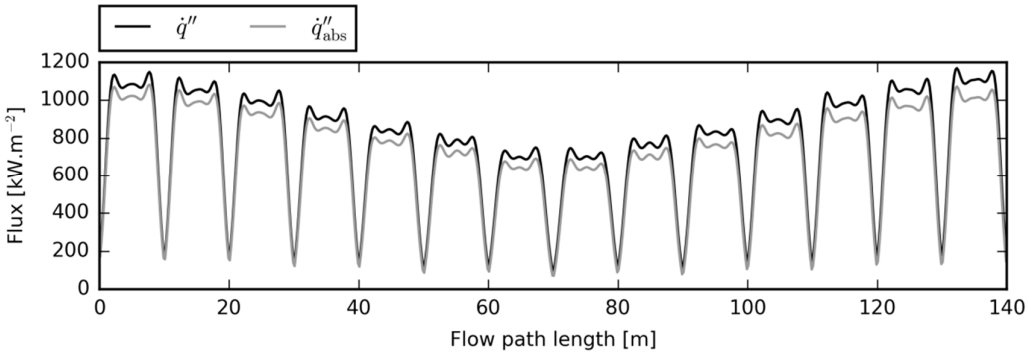

Figure 3-32: Incident and net heat flux along the single flow-path of the reference receiver.

The difference between the incident flux and the net heat flux is higher at the end of the flow-path than at the start because of the higher losses presented in more detail in Figure 3-33. Reflective losses dominate at the start of the flow-path and show an evolution directly proportional to the incident flux on the receiver. Convective loss slowly increases, proportionally with the increase of the temperature of the outer wall of the receiver. Radiative loss is a function of this same temperature to the power four and is the highest heat loss mechanism at the end of the flow path.

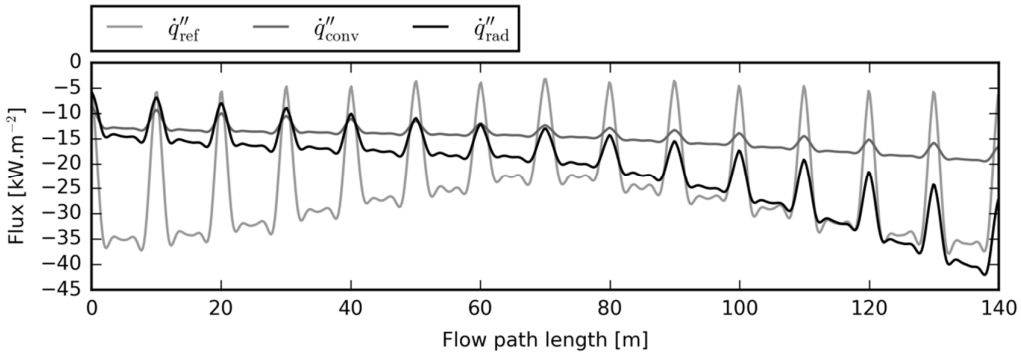

Figure 3-33: Heat losses flux along the along the single flow-path of the reference receiver.

The integrated absolute heat loss breakdown is given in Table 3-8 and highlights the larger contribution of the reflective loss followed by the radiative emission loss and the convective loss.

Table 3-8: Integrated heat losses over the central receiver.

$\dot{Q}_{\mathrm{ref}}$ [MW$_{\mathrm{th}}$]	$\dot{Q}_{\mathrm{conv,ext}}$ [MW$_{\mathrm{th}}$]	$\dot{Q}_{\mathrm{rad}}$ [MW$_{\mathrm{th}}$]
4.659	2.764	3.935

The evolution of the temperatures along the flow path, presented in Figure 3-34 show the progressive heating of the HC and the large temperature differences between the bulk HC, the inner wall of the tubes and the outer wall. The conduction resistance through the tube imposes a large difference of temperature across the tube wall, as a function of the net heat transfer through it. The temperature difference between the inner wall of the tube and the HC is lower at the end of the flow-path than at the start. This is mostly due to the improved convective heat transfer, as shown in Figure 3-35, due to the larger velocities and favourable change in heat transfer properties of the solar salt at higher temperatures. The heat transfer coefficient at the end of the flow-path is close to double the initial one, from 9,109 $W.m^{-2}.K^{-1}$ to 17,773 $W.m^{-2}.K^{-1}$.

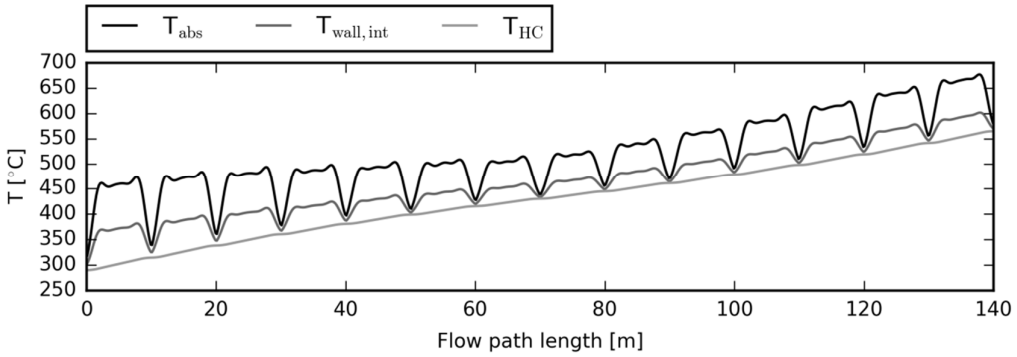

Figure 3-34: Temperature distributions along the single flow-path of the reference receiver.

The flow velocity is shown in parallel with the pressure drop along the flow path in Figure 3-35. The flow accelerates due to thermal expansion and the acceleration is higher when the HC circulates in the highly irradiated region and the net heat flux gain is higher.

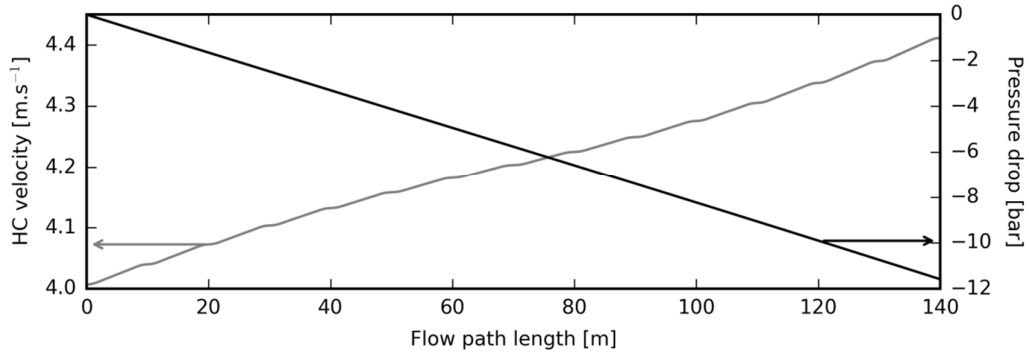

Figure 3-35: HC velocity and pressure drops along the single flow-path of the reference receiver.

3.2.6.2 Dual hemi-cylindrical flow-path.

The net heat flux and temperature distributions for the dual hemi-cylindrical flow-path in Figure 3-36 are symmetrical and the hottest region is at the back of the receiver where the flux is the lowest. The absorber temperature range is similar to the previous case.

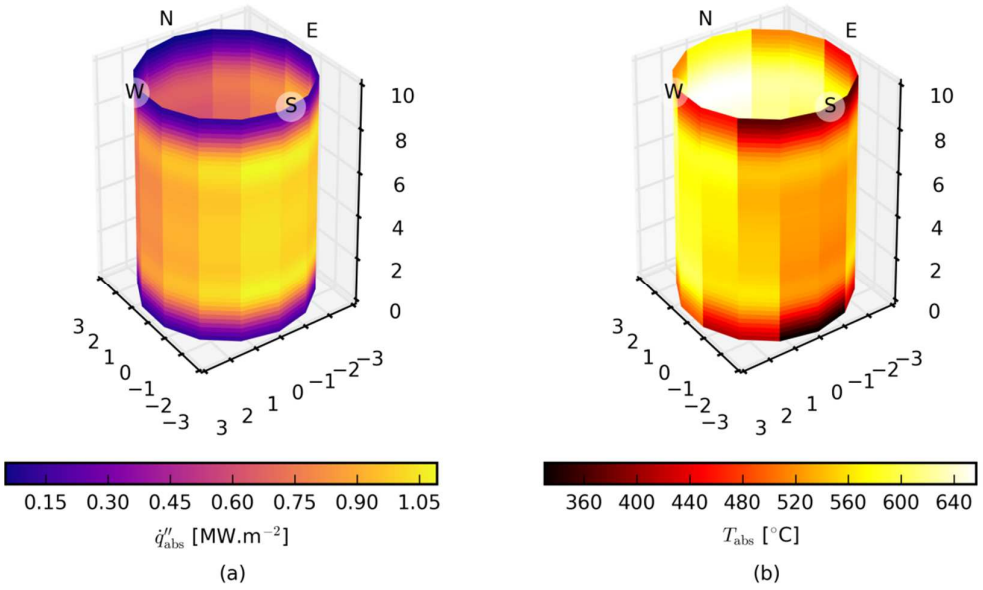

Figure 3-36: (a) Net heat flux and (b) temperature distribution on the reference receiver using a dual hemi-cylindrical flow-path.

The evolution of the incident and net heat flux on each flow path in Figure 3-37 shows the decreasing trend in average flux as the flow path progresses towards the north side of the receiver.

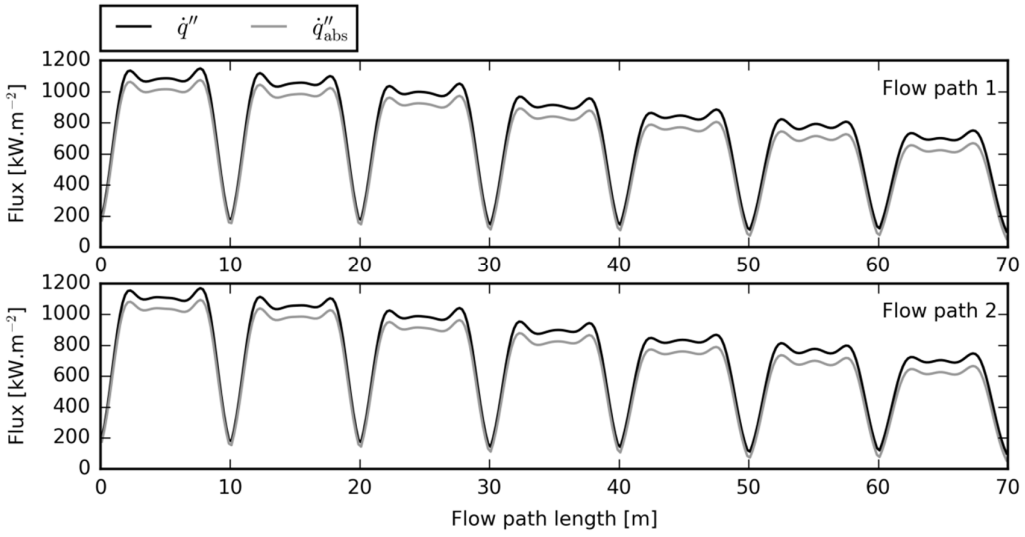

Figure 3-37: Incident and neat heat flux along the flow-paths of the reference receiver using a dual hemi-cylindrical flow-path.

In Figure 3-38, the heat losses follow the same trend as presented earlier but the radiative and convective heat loss are higher than in Case A as shown in Figure 3-38.

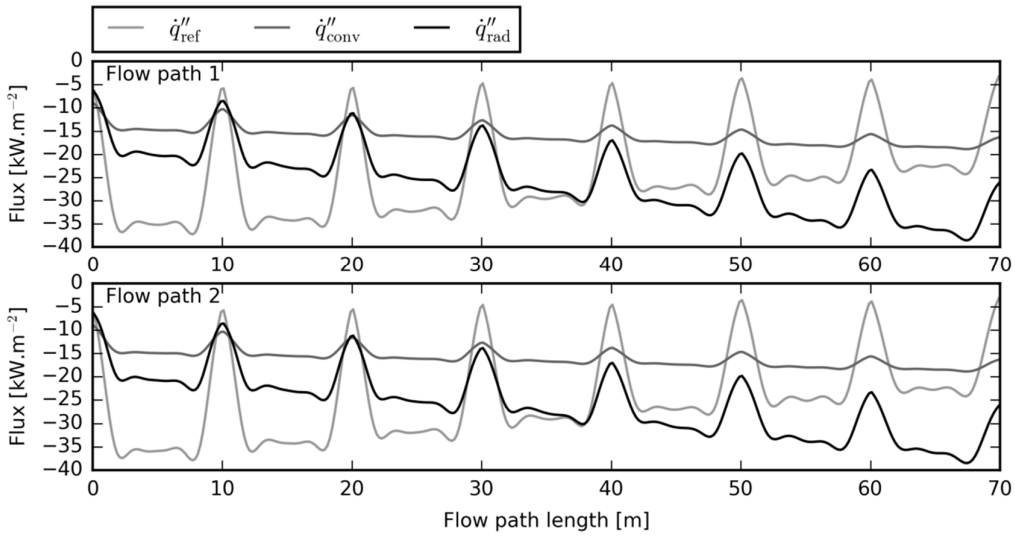

Figure 3-38: Heat losses flux along the flow-paths of the reference receiver using a dual hemi-cylindrical flow-path.

Table 3-9: Integrated heat losses over the central receiver using a dual hemi-cylindrical flow-path.

$\dot{Q}_{ref}$ [MW_{th}]	$\dot{Q}_{conv,ext}$ [MW_{th}]	$\dot{Q}_{rad}$ [MW_{th}]
4.659	3.013	4.807

The cause of the higher radiative and convective losses is the higher wall temperatures which are mostly caused by higher resistance to the heat transfer between the HC and the inner tube wall as can be seen when comparing Figure 3-39 and Figure 3-34.

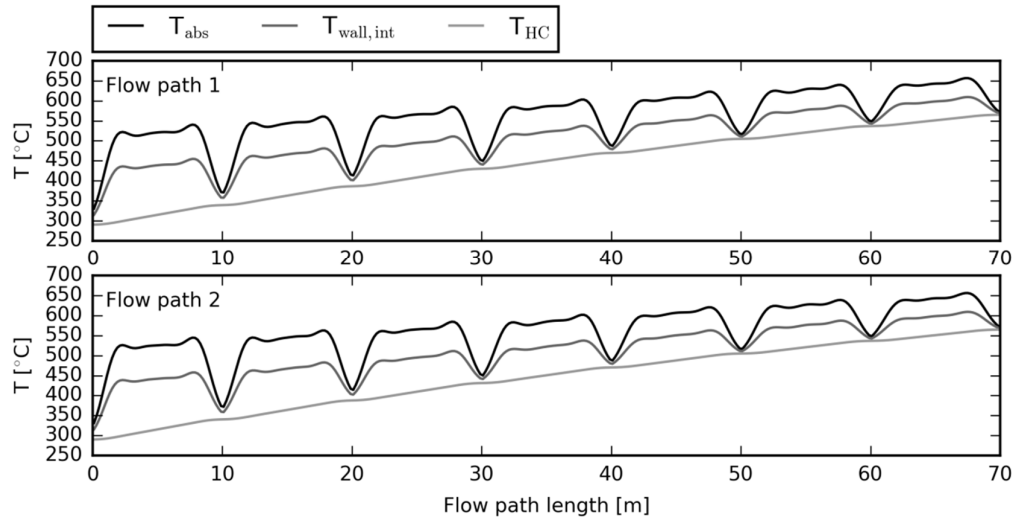

Figure 3-39: Temperature distributions along the flow-paths of the reference receiver using a dual hemi-cylindrical flow-path.

Having divided the HC flow in two distinct flow-paths, the velocity in the tubes (Figure 3-40) is accordingly reduced and causes a reduction in the internal convective heat transfer coefficient which is now 4,745 $W.m^{-2}.K^{-1}$ at the start of the flow-paths and 9,130 $W.m^{-2}.K^{-1}$ at

the end. The benefit of the reduction of the velocity in the pipes is a significant reduction of the pressure drop in the pipes as shown in Figure 3-40.

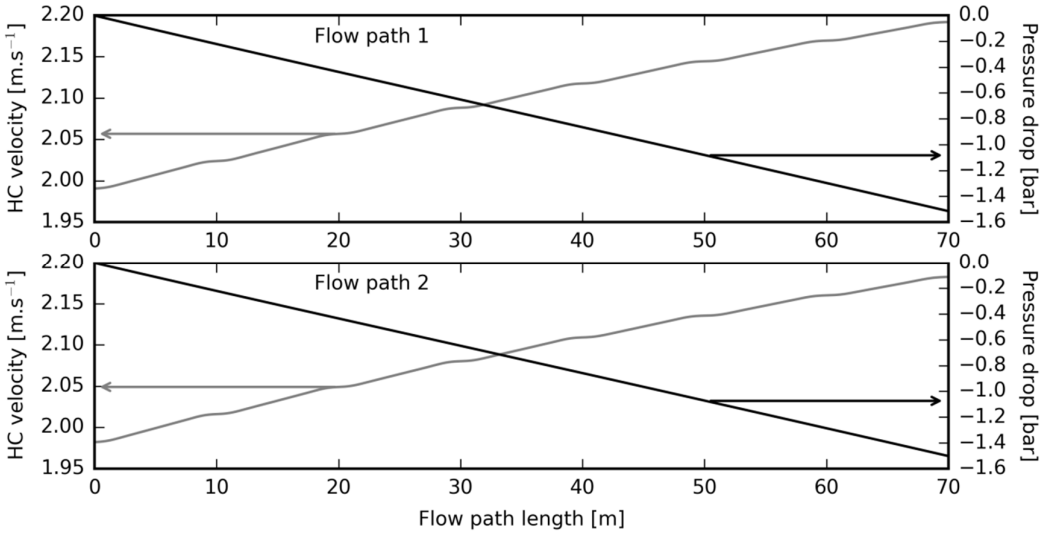

Figure 3-40: HC velocity and pressure drops along the flow-path of the reference receiver using a dual hemi-cylindrical flow-path.

With these results a general comparison of the two cases is carried out in the next section.

3.2.6.3 Central receiver reference model summary

A summary of the receiver efficiency is presented in Table 3-9.

Table 3-10: Summary of the efficiency metrics for the four receiver configurations evaluated.

	Flow-path	
	Single counter-clockwise	Dual hemi-cylindrical
η_{int}	93.9%	
η_{abs}	96.8%	
η_{hx}	95.2%	94.4%
$\eta_{th} = \eta_{abs}\eta_{hx}$	92.1%	91.3%
$\eta_{rec} = \eta_{intercept}\eta_{abs}\eta_{hx}$	86.5%	85.7%

The change in flow path affects the thermal efficiency of the receiver. For the dual flow path, the HC circulates more slowly in the tubes, lowering the heat transfer coefficient and causing an increase in the inner and outer tube wall temperature, ultimately leading to increased thermal losses to the environment. The area averaged absorber wall temperature changes from 789 K for the single flow-path to 833 K for the dual flow-paths. The efficiency values cannot be exactly validated with literature data because the heliostat field and receiver

dimensions being unique; however, they are in the right order of magnitude compared with systems of similar size or technology [18, 125].

These results do not consider the cost of the pressure drops in the system performance. To do so a simple approximation can be made by evaluating the work produced by the system and subtract the work necessary to compensate for the pressure drops from this value. The work available from the receiver HC outlet can be evaluated using the Carnot efficiency:

$$\dot{W}_{\text{rec}} = \dot{Q}_{\text{abs,net}} \left(1 - \frac{T_{\text{amb}}}{T_{\text{HC,out}}} \right) \tag{3-35}$$

Assuming a pump efficiency of $\eta_{\text{pump}} = 0.8$, the power consumption cause by the pressure drops is approximated by:

$$\dot{W}_{\Delta\text{p}} = \frac{2\dot{m}_{\text{HC}} \Delta p}{\eta_{\text{pump}} \left(\rho_{\text{HC,out}} + \rho_{\text{HC,in}} \right)} \tag{3-36}$$

Table 3-11: Receiver efficiency comparison including the pressure drop loss.

	Flow-path	
	Single counter-clockwise	Dual hemi-cylindrical
$\dot{W}_{\text{rec}}$ [MW]	79.10	78.34
$\dot{W}_{\Delta\text{p}}$ [MW]	-0.253	-0.033
$\dot{W}_{\text{tot}} = \dot{W}_{\text{rec}} + \dot{W}_{\Delta\text{p}}$ [MW]	78.85	78.3
$\dot{W}_{\text{tot}} / \dot{Q}_{\text{con}}$	0.548	0.546

The single flow-path case loses most of the advantage shown against the dual flow paths case. Considering the pipe headers or degraded pumping efficiencies could quickly make the dual flow-path the best option from this very basic design perspective. In relative terms however, the work involved in compensating the pressure drops represents ~0.3% of the total work extracted by the receiver which does not look like an excessive value. Optimising the diameter of the pipes in each case could lower the pressure drops or improve the receiver efficiency; however, this goes beyond the scope of the work developed in this section which is to apply the model to reference cases and highlight design parameters impact and trade-offs.

Detailed design of an external receiver of the type simulated here would involve consideration of the thermo-mechanical limits of the materials and the HC, control and flexibility of operations, costing, etc. These criteria are not solely energy related and are

difficult to compare on a fair basis and require optimisation and the use of multiple performance metrics.

3.3 Receiver modelling conclusions

The receiver model presented in Chapter 2 is used in this chapter to provide performance evaluations and relative comparison between different design options. The overall largest receiver heat loss mechanisms are reflections and thermo-radiative emissions.

The role of the geometry in the reduction of thermo-radiative and reflective loss has been highlighted in Chapter 1 and illustrated in this Chapter with the SG3 cavity receiver model. In the tower receiver example, the geometry was also shown to directly impact the receiver performance: a larger aperture enables the spread of the concentrated flux, allowing values feasible for an indirect tubular receiver design. The role of the optics in receiver performance is investigated in more detail in the next chapter.

In the tower receivers simulated, increasing the temperature of operations would confirm the predominant role of the thermo-radiative emissions as the major contributor in the receiver performance while the SG3 cavity receiver would benefit from the cavity effect and mitigate the increased loss. The flow-path on the receiver is shown to be part of the design parameters that need to be considered, having a strong impact on pressure drops and internal heat transfer in the pipes.

4 Optimisation of Receiver Design

Methods to optimise receivers based on coupled heat transfer models are presented in this chapter. To undertake this task, two major difficulties are addressed:

- The simulation of complex receiver geometries through MCRT with confidence is computationally intensive and hinders the capabilities of existing optimisation methods by limiting the number of alternatives that can be evaluated in a timely manner.
- The optimisation method needed to be able to progress using stochastic approximations of the results only.

A new method to tackle these two issues called “Progressive Monte-Carlo Evaluation (PMCE)”, is presented in the first section of this chapter. A practical example of the method application is provided in the second section of the chapter where a new design for the SG4 Dish receiver is established. The idea of PMCE emerged after the publication of (b) of the initial list (p. ix) and was exposed in (c). The optimisation work for the new design is in (d), (j) and (l) and the experimental results in (m) (p. ix).

Receiver design asks for multiple objective metrics to be considered in parallel to obtain useful optimisation results. As a consequence, PMCE needs to be included in an optimisation algorithm able to progress using multiple stochastic optimisation metrics without introducing any bias. A multi-objective optimisation technique including PMCE called “Multi-Objective and Evolutionary PMCE Optimisation (MOE-PMCE-O)” is introduced in the third section.

Section four of this chapter is an application of this method to the optimisation of the design of a sodium based central receiver system. Publications (e), (f) and (g) (p. ix) include some aspects of the design and optimisation work for the ASTRI sodium receiver. Publications (h), (i) and (k) (p. ix) motivated the selection of the objective metrics for this work.

4.1 PMCE, an MCRT-integrated stochastic and comparative evaluation

This section introduces a method to undertake single objective optimisation of a problem where the optimisation metric is evaluated using a stochastic method, and therefore shows uncertainty. The optimisation algorithm is derivative-free in the sense that it only uses estimation results and no derivatives, in order to avoid confining the method to specific classes of problems and improve its re-usability.

4.1.1 Progressive Monte-Carlo Evaluation (PMCE)

The objective of the optimisation method presented here is to progressively screen the best-performing scenes in a population, according to an optimisation metric M, by discarding under-performing candidates as soon as they can be identified. By doing so, MCRT simulations are only performed on potentially interesting candidate scenes, and computational time is saved. The initial population p_0 is populated with $i \in \{0...N\}$ randomly generated candidates.

The stochastic nature of the scene declaration makes it similar to a random search method and enables a comprehensive exploration of the parameter space, provided that the initial population p_0 is large enough to cover this parameter space, to perform meaningful statistics and avoids statistical biases.

MCRT runs are performed step-by-step with a small ray counts (~10,000 rays). A ray-tracing index j records the number of ray-traces performed and increases for each new ray-trace. A metric $M_{j,i}$ is used to assess the performance of each scene i in the current population p_j, at each step j. After each MCRT step j and for every scene i of the population p_j, the stochastic algorithm evaluates the weighted average of the optimisation metric from all previous ray tracing steps $\bar{M}_{j,i}$ as an unbiased estimator of the expected result, its sample standard deviation $S_{j,i}$ and confidence interval $CI_{j,i}$, presented in Eq. 4-1. The central limit theorem applied to large number of independent events, applicable in MCRT, states that the distribution of the results follows a normal distribution and consequently the three sigma rule can be used to estimate the 99.7% probability confidence interval $CI_{j,i}$ associated with the each estimations of the metric value $\bar{M}_{j,i}$.

$$\bar{M}_{j,i} = \frac{(j-1)\bar{M}_{j-1,i} + M_{j,i}}{j}; \quad S_{j,i} = \sqrt{\frac{\sum_{k=1}^{j}\left(M_{k,i} - \bar{M}_{k,i}\right)^2}{j-1}}; \quad CI_{j,i} = \frac{3S_{j,i}}{\sqrt{j}\bar{M}_{j,i}} \tag{4-1}$$

It is possible to use the values of the optimisation metric estimators and confidence intervals to decide which candidate to keep for the next population evaluation p_{j+1} and which ones to discard because they are highly unlikely to be optimal solutions of the problem, as illustrated in Figure 4-1 in a metric maximisation optimisation. At each ray-tracing step, the best performing candidate $i = \text{best}$ is identified and the worst-case scenario performance computed $\bar{M}_{j,\text{best}}\left(1 - CI_{j,\text{best}}\right)$. The best-case scenario performance of all the other candidates in the population $\bar{M}_{j,i}\left(1 + CI_{j,i}\right)$ is then compared to the worst-case scenario performance of the best candidate. The candidates kept for the next population are the ones with the best possible results higher than the lowest possible one of the best candidate. As more ray

bundles are cast, the confidence interval of the results from MCRT method decreases with a $1/\sqrt{j}$ ratio and the precision of the calculation increases for potential optimal candidates still present in the population p_j [101]. The method stops when all candidates in the last population evaluated have their confidence interval below a precision threshold σ_T established as an acceptable precision for the study considered.

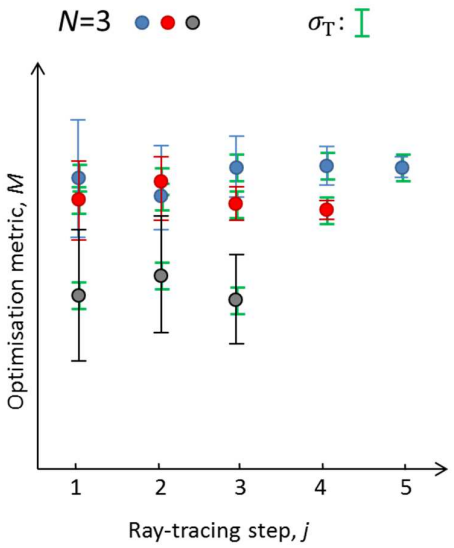

Figure 4-1: Illustration of the progression of the PMCE method with a population of three candidates (blue, red and black). The precision stopping criterion interval is in green. Blue is best at j=1, red becomes best at j=2 then blue remains best for the remaining steps. At j=4 candidate blue is the only remaining one in the population, having dominated black at j=3 and red at j=4, however, the uncertainty associated with the evaluation of its optimisation metric is larger than the termination criterion illustrated with the green interval. The metric evaluation of blue gets below the threshold σ_T at j=5 and the method ends.

The algorithm used is summarised in the following flow-chart.

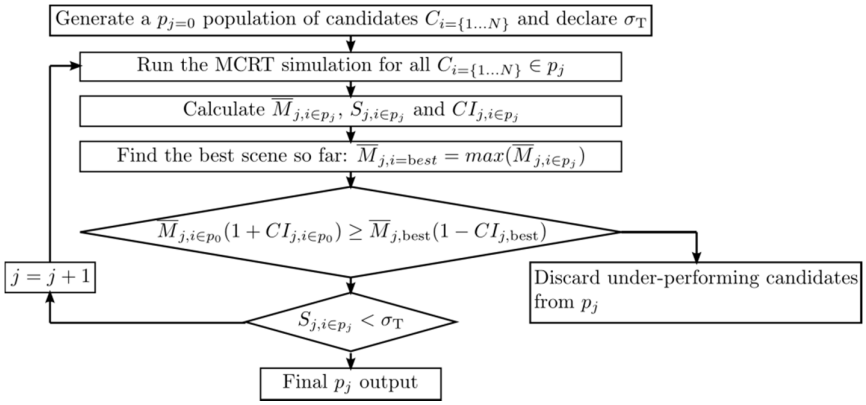

Figure 4-2: Flowchart of the PMCE algorithm.

In the standard implementation of the method, the number of rays cast at each step j is constant and the index j is increased by one. This algorithm only depends on the estimations of the metric and the standard deviations at each step and is independent of the inner nature of the problem considered. As a consequence, MCRT can be coupled with other physical and

chemical models to take into account more phenomena and still converge, as shown in the following case study.

4.1.2 PMCE case study

4.1.2.1 Receiver model

This case study focuses on axisymmetric water/steam tubular receivers located at the focal plane of the ANU SG4 dish [93].

The geometry of the candidate receivers is composed of N-1 stacked frusta (truncated cones) and a cone to close the geometry at the back, as shown in Figure 4-3 (b).

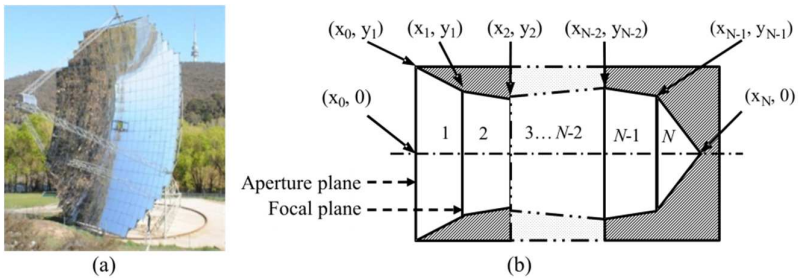

Figure 4-3: (a) The SG4 dish at the ANU STG facilities, and (b) cross-section of the parametric open cavity receiver model considered in this case study.

Each point on the geometry is described by a pair of axi-symmetrical coordinates (x,y) and the full profile of the geometry described using 2*N*+2 geometrical parameters. The axial position of the start of the second frustum section is always positioned at the focal point of the dish reducing the parameter space to 2*N*+1. By assigning random values within a cylindrical parameter space to each of the remaining parameters (except the cone where specific rules apply as shown in Figure 4-4) random shapes can be generated. After the profile is generated, a cylindrical envelope ensuring a minimum insulation thickness around the absorber is determined, according to an insulation thickness parameter.

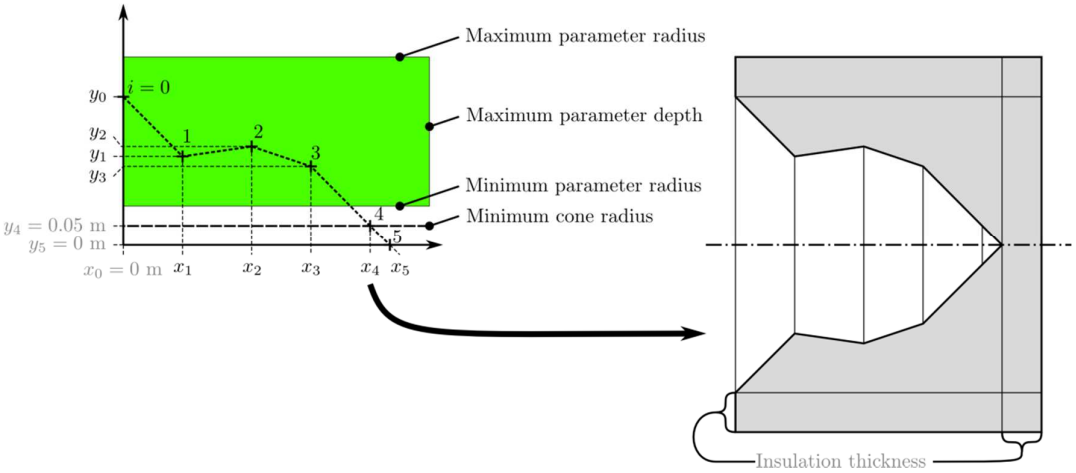

Figure 4-4: Geometry generation illustration for *N*=5. In black are the randomly declared variable parameters, in grey the fixed parameters. In green is the variable parameters declaration region.

The values of *x* for the frustum sections are only allowed to increase ($x_{k+1} > x_k$), creating shapes that progress towards the bottom of the cavity until the cone. The final cone can point inwards and collisions between any of the frusta profile lines and the cone have to be avoided. This is done by performing a test after generation of the full set of parameters and verifying that the *y* position on the cone at each *x* position of the profile is lower than the *y* position of all the frusta elements. The cone profile line equation is:

$$y_{\text{cone}}\left(x_{\text{cone}}\right) = a x_{\text{cone}} + b \tag{4-2}$$

With:

$$\begin{cases} a = \dfrac{-y_{N-1}}{x_N - x_{N-1}} \\ b = \dfrac{x_N y_{N-1}}{x_N - x_{N-1}} \end{cases} \tag{4-3}$$

To verify that the geometry is a valid one, the following test is performed using the full set of parameters in an array comparison:

$$y_{\text{cone}}\left(x_k\right) < y_k \quad \forall k \in \{1...N\} \tag{4-4}$$

If these inequalities are not respected, the geometry is cancelled and a new random geometry is generated. In addition, a small adiabatic region is placed at the bottom of the cavity where the tube curvature would have exceeded manufacturability limits, assumed to be a radius of 5 cm.

The tube surfaces are considered diffuse at all wavelengths and coated with a Pyromark 2500® selective coating for an absorptivity of 0.95 and an emissivity of 0.85 [62]. Effective emissivity and absorptivity of tube covered surfaces are considered to take into account the self-viewing grooved absorbing/emitting surface arising from the curved surface formed by adjacent tubes [63].

The cavity receiver is positioned to have one frustum element in front of the focal plane of the SG4 dish concentrator. The SG4 parabolic dish is modelled under a steady-state operating regime using the SG4 dish model presented in Chapter 3. The incoming solar radiation is modelled using a Buie sunshape with the model presented in Chapter 2 and a corrected CSR of 0.01.

While the optimisation coming next is focusing on the receiver geometry, the full system, including the concentrator, is simulated for every receiver candidate.

The receiver parameter values used in this case study are summarized in Table 4-1.

Table 4-1: PMCE case study receiver parameters.

Geometry generation parameters	Numer of receiver sections *N*	15 + 1 adiabatic cone tip
	Minimum parameter radius	0.15 m
	Maximum parameter radius	0.65 m
	Maximum depth	1.4 m
Receiver parameters	Insulation thickness	0.1 m
	Inner tube diameter	15.8 mm
	Outer tube diameter	21.34 mm
	Tube conductivity	20 $W.m^{-1}.K^{-1}$
	Pyromark2500 absorptivity	0.95
	Pyromark2500 emissivity	0.85
	Temperature inlet	50 °C (323.15 K)
	Temperature outlet	500 °C (773.15 K)
	Ambient temperature	26.85 °C (300 K)
	Pressure inlet	50 bar

The heat transfer model adopts a simpler version of the SG3 receiver model presented in Chapter 3:

- No convective heat loss is considered
- The internal convective heat transfer resistance in the tubes is ignored.
- No effort is made to fit the frustum sections dimensions to integer pipe loop numbers and the pipe lengths account for this approximation allowing partial loops.

The optimisation metric chosen here is the system efficiency η_{sys}, ratio of the rate of thermal energy harvested $\dot{Q}_{abs,net}$ to the incoming solar radiation input $\dot{Q}_{sun}$:

$$\eta_{sys} = \eta_{con}\eta_{rec} = \frac{\dot{Q}_{abs,net}}{\dot{Q}_{sun}} \tag{4-5}$$

View factor matrices, required to solve the radiosity balance, are calculated at the beginning of the optimisation using MCRT with a precision threshold of 0.005 absolute using the definition presented in Chapter 2.

4.1.2.2 SG4 receiver optimisation

This case study optimisation ran with a starting population $p_{j=0}$ of 1000 candidate receivers and a termination threshold $\sigma_T = 0.001$. The population count varies as the number

of ray cast per scene increases as shown in Figure 4-5 (a). The fluctuations in the population count are caused by re-evaluation of previously discarded scenes: the routine evaluates every simulated scene at each step and is consequently able to "recoup" previously discarded scenes if their efficiency has become acceptable. This occurs when a new best candidate appears and its sample standard deviation evaluation is larger than the previous best candidate, thus increasing the confidence interval used to select potential optima or due to statistical variations in the evaluation of the objective function itself.

The computational effort spent by the optimisation, shown in Figure 4-5 (b), highlights the efficiency of the algorithm when compared with a brute force random search evaluation. The presented optimisation obtains its results in 7.8% of the time it would have taken to obtain them using a brute-force random search approach where no candidates are eliminated along the way.

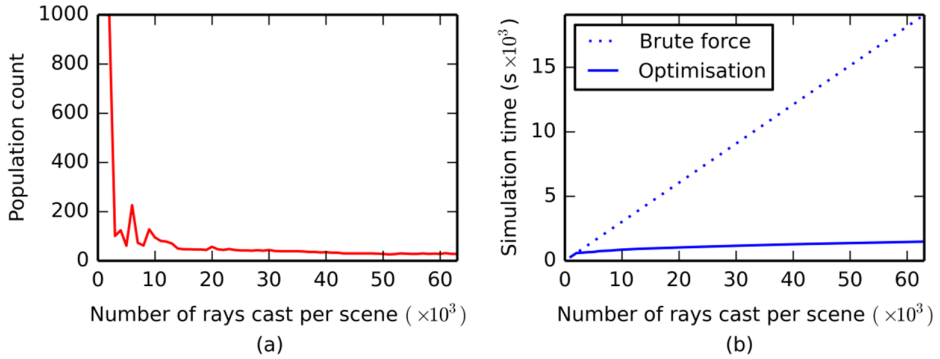

Figure 4-5: (a) Evolution of population count during optimisation and (b) computational effort spent on the optimisation case study as a function of the number of rays cast for each scene. The brute force simulation time was estimated by multiplying the number of MCRT passes by the average time spent per MCRT pass in the actual optimisation.

Figure 4-6 illustrates the convergence of the algorithm. The maximum potential thermal efficiency for each candidate scene is shown at each MCRT step. The grey area highlights the efficiency cutoff: red-marked scenes are the ones that get discarded for the next iteration of the routine while black ones are kept as potential optima. The convergence observed in Figure 4-6 shows that the optimisation is successfully eliminating under-performing scenes and finding an adequate optimum. All the remaining candidates at the last step are evaluated with a confidence interval smaller than 0.001 and are consequently regrouped in an interval of $2\sigma_T = 0.002$.

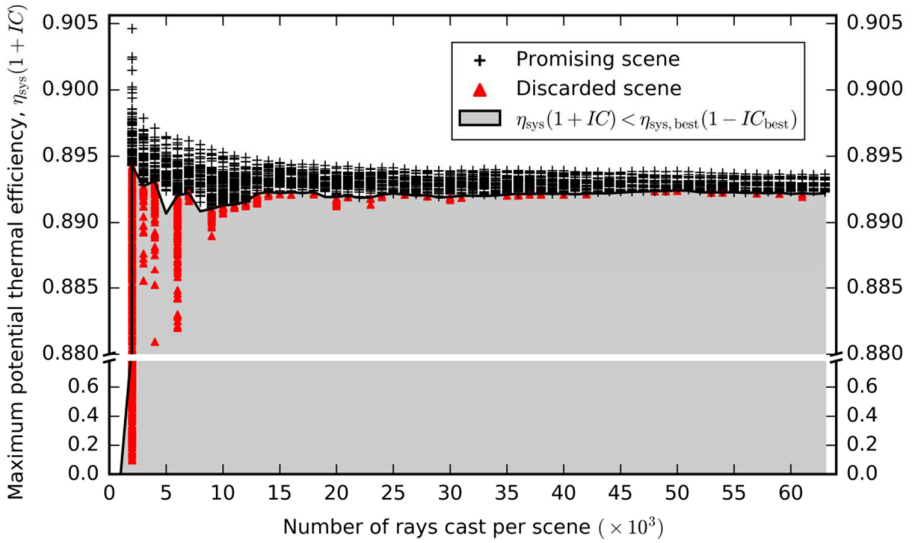

Figure 4-6: Convergence of the optimisation in the cavity receiver case study.

Analysing the information stored during the optimisation offers useful insights for the design problem of interest. To illustrate this, thermal efficiencies are shown in Figure 4-7 (a) as function of the general aperture and the focal plane aperture for each candidate scene. The correlation between the aperture of the receiver and thermal efficiency appears on the left figure: smaller apertures limit radiative energy rate input in the receiver. This behaviour is due to the low temperature HC input at the front of the cavity that tends to cause very low radiative loss in the first sections of the receiver as shown with the SG3 receiver in Chapter 2.

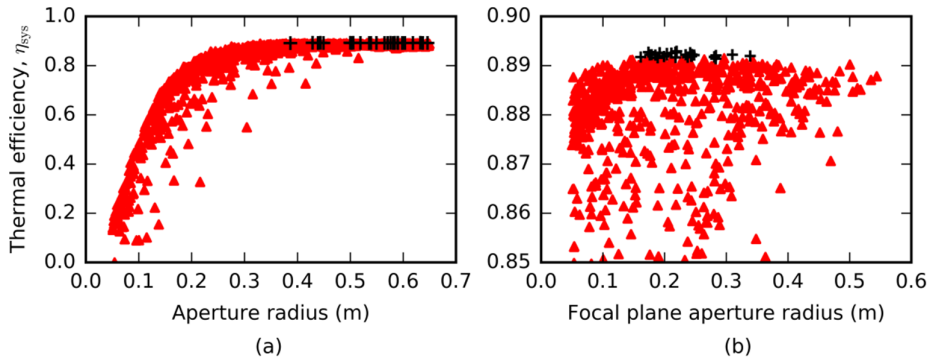

Figure 4-7: Sensitivity of simulated thermal efficiencies to (a) the aperture radius and (b) the focal plane aperture radius. Black crosses are the optimal candidates remaining in the last population and red ones are discarded candidates.

Figure 4-7 (b) illustrates the trade-off between concentrated solar flux input and thermal emission losses: if the radius on the focal plane is too large, the hot regions in the cavity tend to have a higher view factor to the surroundings and lose more energy; however, if this radius is too small, a higher portion of the incoming solar flux is reflected outside and does not enter the cavity.

4.1.2.3 Improvements of the PMCE method

Using 15 frustum sections per cavity geometry and using continuous random numbers for the parameter declaration causes the pool of potential candidate receivers to be infinite, however, "only" 1000 geometries are considered in this optimisation. As a consequence, PMCE is not a global optimisation method and is able to find local optima at best.

In addition, the single objective function based on the energy efficiency of the system does not capture all the trade-offs involved in receiver design. To illustrate this point, the axisymmetric profiles of two of the optimum geometries present in the final population are shown in Figure 4-8.

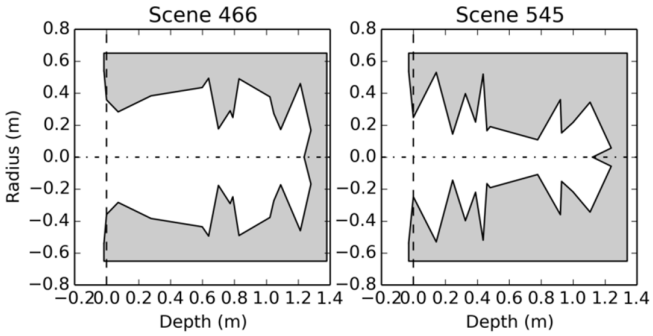

Figure 4-8: Example of two successful candidates or "scenes" with unrealistic geometries.

While these two geometries have statistically identical system efficiencies, their manufacturability could be an issue and some additional objective function on the simplicity of the shape could be introduced if the method was able to tackle multiple objectives in parallel.

Finally, another drawback of this method is the inefficiency of the population generation and initialisation. While 92.2% saving in computation runtime is obtained during the optimisation compared to a brute force approach was shown in Figure 4-5, most of the underperforming scenes are discarded at the very start of the routine. In addition, the view-factor matrix calculation for each of these geometries takes a significant amount of time, approximately 10 times the duration of the optimisation run for 1000 geometries.

4.1.3 Conclusion on PMCE

The PMCE method is able to improve the efficiency of a very basic stochastic optimisation method in finding optimal candidates according to a single optimisation metric without gradient estimations. Any metric of interest can be considered as PMCE does not require gradient estimations, which enables artificially constrained parameter and result spaces. Optimising receivers according to a single objective metric seems unlikely and a multi-objective version of PMCE method needs to be developed. Evaluating several metrics at each step for each candidate is straightforward but the algorithm needs to be adapted to take into

account the dominance relationship between metrics, necessary to undertake multi-objective optimisation.

PMCE alone is optimising the computational effort of an optimisation method by improving the evaluation step. The optimisation method considered in the case study is inherently inefficient at declaring interesting candidates and significant time is lost in the initialisation stage, mostly due to the view-factors calculation. A way forward to mitigate this issue is to use much smaller populations and introduce an evolutionary behaviour to introduce new candidates throughout the method. The new candidates are generated using information learnt from previous ones in order to improve their quality, the quality of the overall population (which influences the selection pressure) and potentially mitigate the time lost in initialisation by spending it on better candidates.

These improvements based on knowledge gained from the use of PMCE form the basis of the work presented in sections 3 and 4 of this chapter. However, as PMCE was extensively used for the design of a new 400 kW receiver for the SG4 dish, the following section describes the author's contribution to this work before moving to a more advanced optimisation method [120].

4.2 PMCE application: Optimisation of a new receiver for the SG4 Dish.

4.2.1 Optimisation objectives

Despite its limitations, the PMCE method was intensively used as part of the USASEC cavity receiver project at the ANU STG where it proved very helpful in geometrical design exploration. The USASEC project aimed at designing, building and testing an improved cavity receiver for the SG4 dish with a receiver efficiency improvement of at least 2.2% absolute compared with the SG3 receiver on the SG3 dish.

While a significant part of the project focused on understanding, modelling and validating natural convection heat loss from cavity receivers, it was found that natural convection was not the major heat loss contribution to the existing SG3 receiver. Three options were considered to improve the efficiency of the design:

- To use a selective coating on the tubes in the absorber.
- To change the geometry of the cavity.
- To change the tube sizes used in the cavity.

PMCE was used in the geometry determination of the new cavity receiver.

4.2.2 Two-step optimisation method

The method adopted to generate the geometry of the new receiver was a two step method. In the first step, PMCE ran in combination with the same type of random search method presented in the previous section, considering a large number of geometries and using a simplified receiver model similar to the one presented in the previous section with only 5 subdivisions in the receiver geometry. The objective metric was the system efficiency. In the second stage, the full heat transfer problem (as presented in Chapter 3) was used to refine the efficiency calculation results. The separation of these steps occurred because of the different stages of development and integration of the simulation tools at the time of the receiver design. The simulation tools were created while the receiver design was progressing. 22 iterations of geometry generation occurred during the project and each time refinements were added to the model and different assumptions were tested. PMCE can therefore be considered as a reliable design tool via its extensive usage and critical examination by the USASEC design team during the project. Figure 4-9 is an example of the type of results generated at each design iteration by the whole modelling framework of the project group.

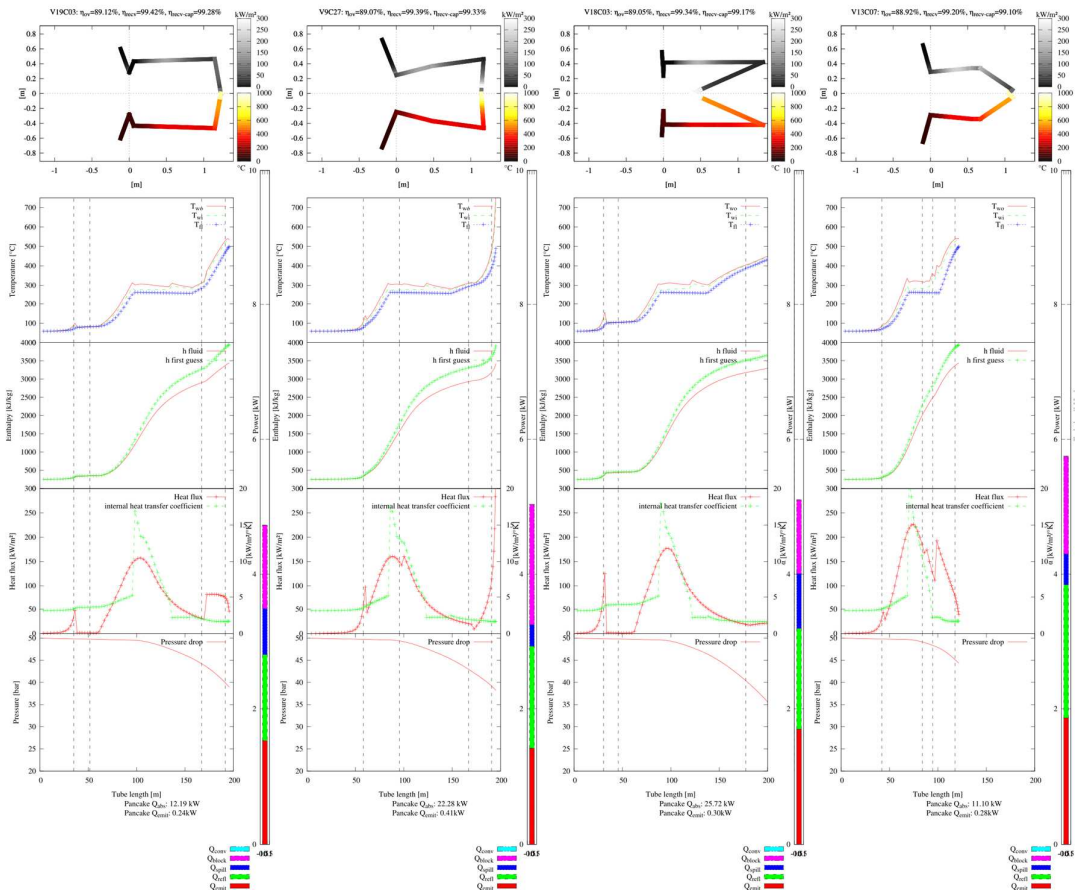

Figure 4-9: (from the USASEC project archives) Illustration of the results obtained after one of the PMCE-based optimisation runs. Each geometry is associated with flow-path plots of flux and temperature distributions, pressure drops and heat transfer coefficients as well as a breakdown of the heat loss . In this specific example, the nuber of frustum sections is 4 and 1 element is used for the adiabatic cone at the back of the geometry.

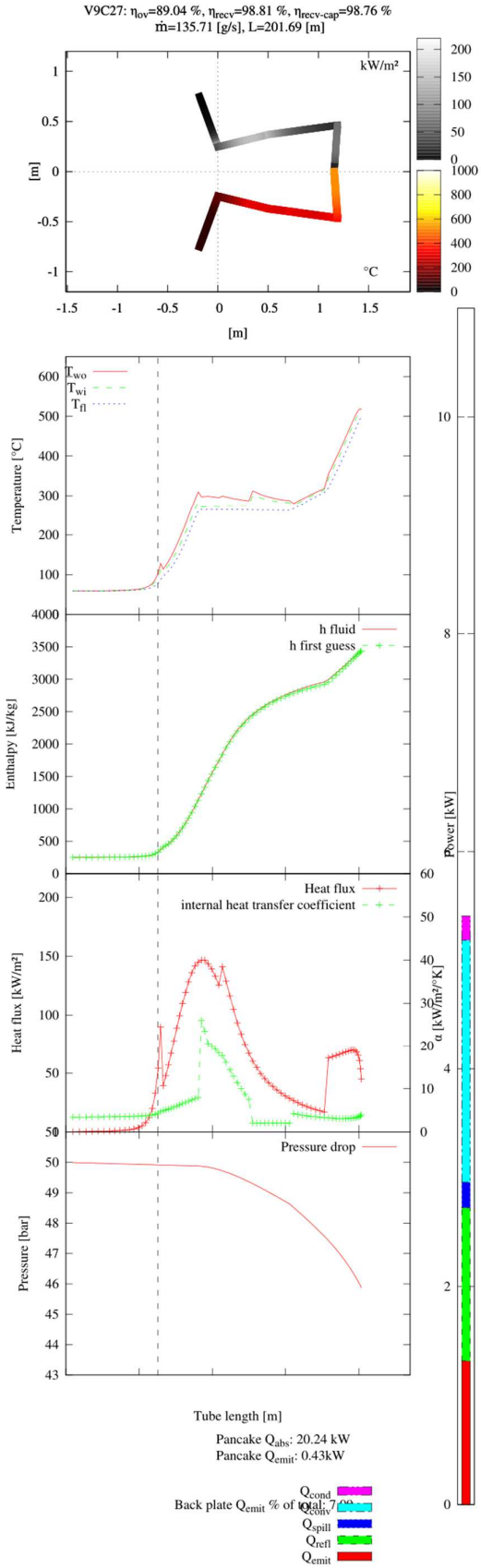

Figure 4-10: (from the USASEC project archives) Selected V9C27 geometry from the 2 stage optimisation involving PMCE.

From the hundreds of geometries obtained a promising candidate "V9C27", in Figure 4-10, was chosen:

- It has an overall good system efficiency.
- It has a relatively smooth transition between the flux values in different sections and a very low peak flux (≈150 kW.m^{-2}).
- It has a relatively simple shape from a manufacturing perspective.

4.2.3 Receiver design refinement

After the project team selected the V9C27 geometry, the design was refined through 32 sensitivity studies. The following non-exhaustive list illustrates this process with some of the design iterations variations:

- The diameter of the adiabatic section at the back and the slope of the ceramic cone placed to protect it.
- The influence of Pyromark on the geometry performance.
- The diameter of the pipes used and their thermal conductivity.
- Changes on optical properties of the SG4 dish after new fluxmap measurements (3 times) and corresponding aperture diameter changes.
- Peak operation conditions.
- Smooth flux transitions between receiver regions.

Overall the sensitivity studies led by the team determined the following modification of the V9C27 shape (exact dimensions are part of an intellectual property agreement and cannot be communicated here):

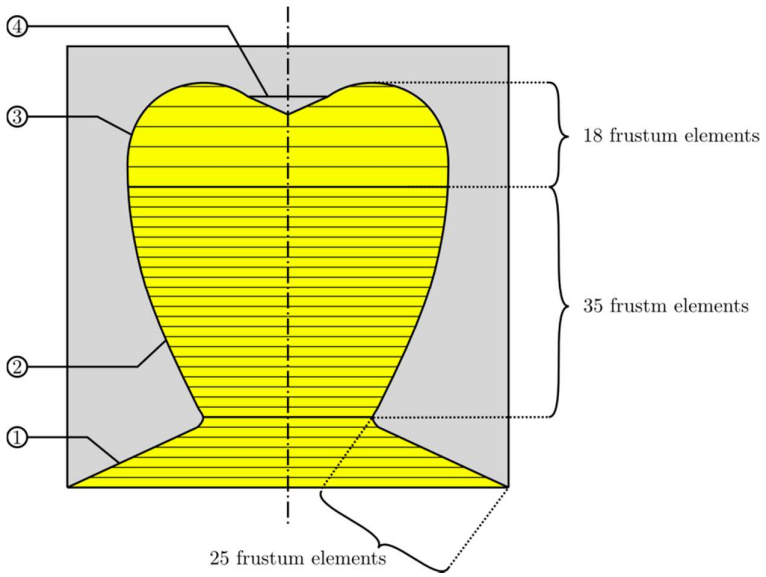

Figure 4-11: SG4 receiver discretisation scheme and schematic view of the improved geometry. The section reference numbers are given in the circled labels and used throughout the rest of this chapter.

With a final shape in mind, the full heat transfer model was solved in conjunction with CFD modelled convective heat loss coefficients. Because natural convection heat loss is dependent on the temperature profile in the receiver, the heat-transfer model was "soft-coupled" with the CFD model: the heat transfer model solved the problem with a set of heat transfer coefficients, then the resulting temperature profile was given to the CFD model to re-evaluate convective heat loss and the convective heat loss coefficients subsequently updated in the heat transfer model. Less than four iterations were needed to get good convergence. Figure 4-12 presents the resulting heat transfer coefficients.

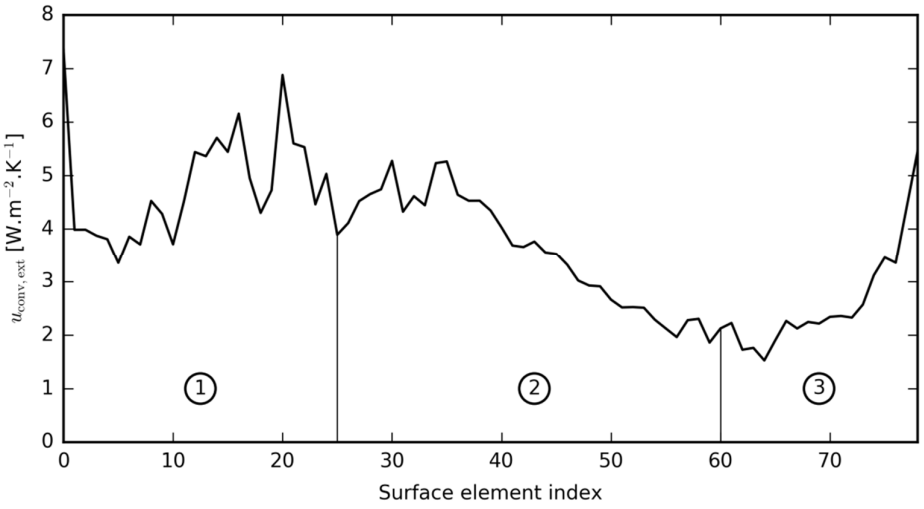

Figure 4-12: Natural convection heat transfer coefficients for each element in the axi-symmetrical model of the SG4 receiver.

4.2.4 Testing and model validation of SG3 receiver on SG4 dish

An accurate model of the optical concentrator was needed to be able to evaluate the experimental performance of the receiver and validate it with the model. Updated dish optics from new lunar fluxmap measurements were carried out as part of the project to design and optimise the new receiver shape. The SG4 dish optical quality changed significantly during the project. At the start of the project, the dish mirrors had degraded significantly and it was decided that a large fraction of the dish mirrored surface would be replaced. The faulty mirrors were replaced with new more reliable facets that subsequently improved the quality of the mirror surfaces. The new facets, though more robust, are less precise than the original ones and produced a dish with a lower optical quality than the original SG3 optics presented in Chapter 3. The following graphs present the last iteration of the SG4 dish optics modelling which was established using lunar fluxmap results obtained a few months before testing of the receiver.

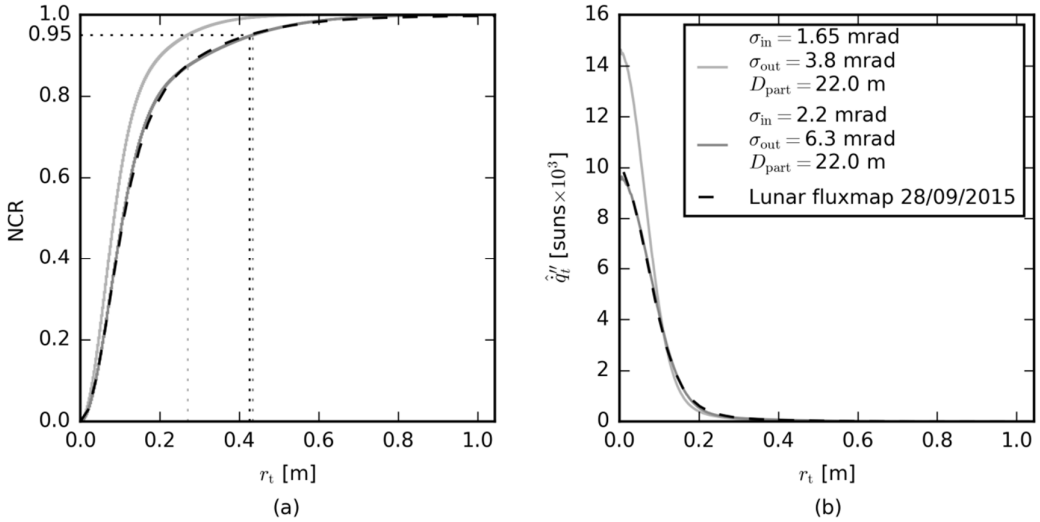

Figure 4-13: Old (4/09/2009, in light grey) and new (28/09/2015, in dark grey) models for the SG4 dish. (a) Normalised Capture Ratio (NCR) and (b) normalised flux distribution at a focal distance of 13.406 m.

The flux distribution in Figure 4-13 (b) shows a lower peak flux (9,633 kW.m^{-2}) and a wider base, compared to the older model (14,658 kW.m^{-2}) that described the newly built SG4 dish in 2009. In Figure 4-14, the 95% and 90% capture ratios are presented as a function of the focal plane distance and compared with experimental measurements. The fit between the model and results is relatively good although less compelling than in the previous dish model presented in Figure 3-6.

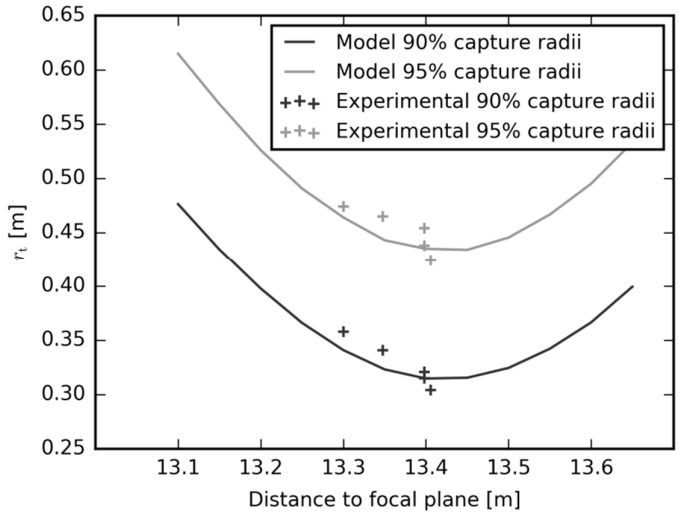

Figure 4-14: Comparison of the 90% and 95% capture ratios obtained from the new SG4 dish model and the lunar fluxmap experimental measurements at different focal distances.

The results of the simulation of the SG4 receiver with these new SG4 dish optics are presented in Figure 4-15 and Figure 4-16 using experimental parameters in order to compare them to actual experimental measurements. Table 4-2 Summarises the specific parameters used for the simulation which correspond to an experimental run. The data are averaged from

0.2 s data logging periods over a steady-state period of 50 minutes the 24th of November 2015 from 14:20:00 to 15:20:00.

Table 4-2: Averaged experimental parameters for the SG4 receiver testing on the 24th of November 2015 from 14:30:00 to 15:20:00 and corresponding model outputs for mass flow and outlet pressure. The SG4 dish mirror reflectivity was measured prior to the experimental run with handheld reflectometers.

	Experimental data	Model results
Model input	G [W.m^{-2}] 1037	
	ρ_{SG4} 0.921	
	$\rho_{SG4,eff}$ 0.917	
	$T_{HC,in}$ [°C] 36.3	
	$T_{HC,out}$ [°C] 509.5	
	T_{amb} [°C] 26.8	
	p_{in} [bar] 57.2	
	p_{out} [bar] 47.4	49.1
	$\dot{m}_{HC}$ [kg.s^{-1}] 0.1354	0.1379

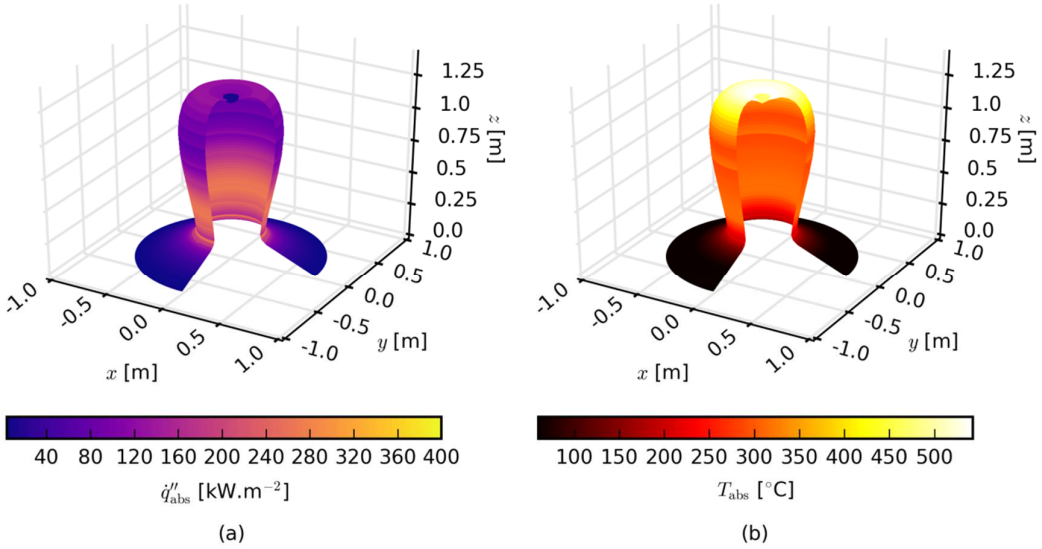

Figure 4-15: (a) Net heat flux and (b) temperature distribution on the SG4 receiver.

The SG4 receiver operation is similar to the SG3 receiver presented in Chapter 3 with the water progressively heating as it progresses from the front of the aperture to the back of the cavity. The simulated mass flow is 0.1379 kg.s^{-1} slightly higher than the experimental one (0.1354 kg.s^{-1}) and the pressure drops lower, with an output pressure of 49.1 bar, instead of the experimental one of 47.4 bar.

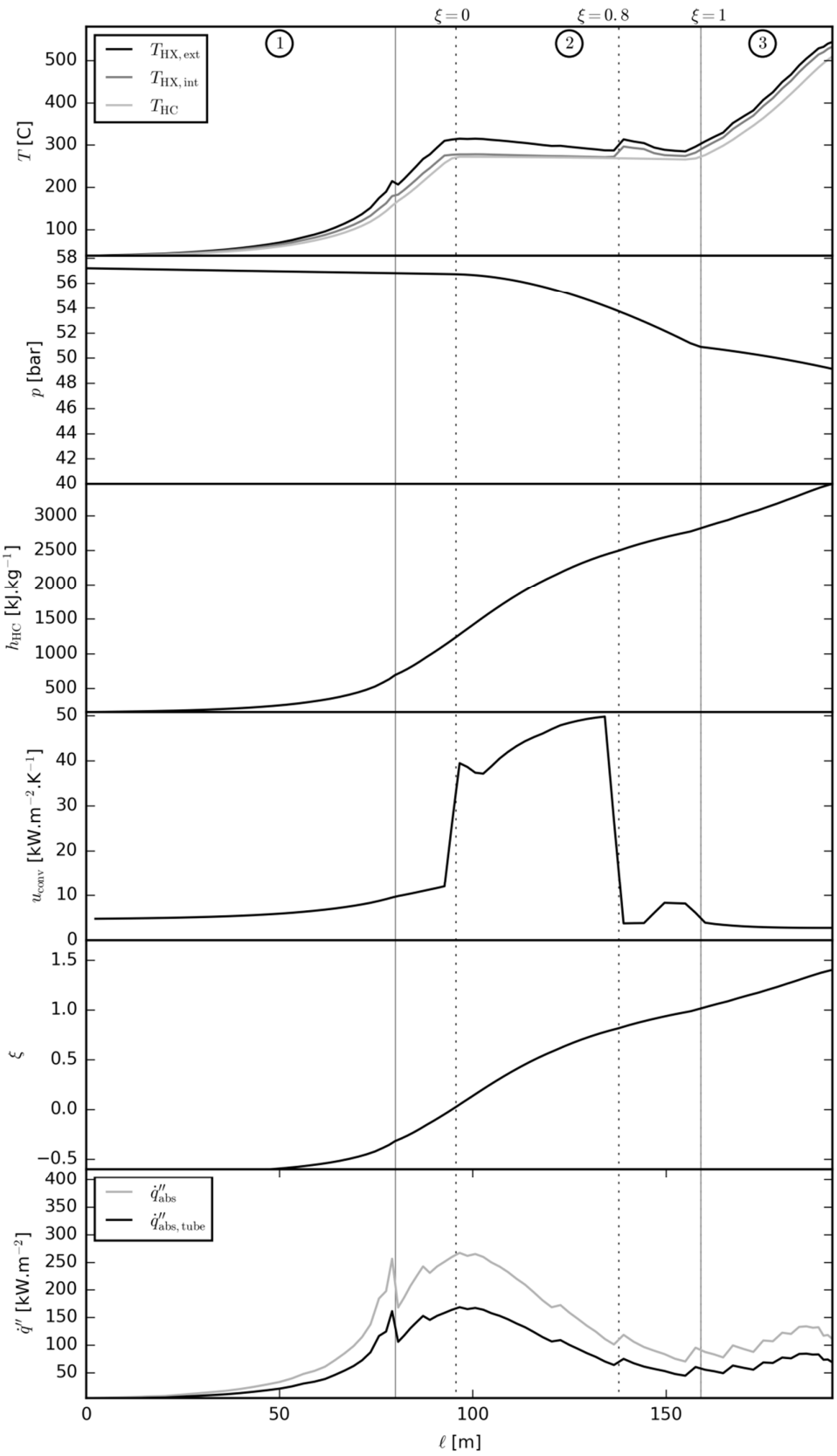

Figure 4-16: SG4 receiver absorber flow path simulation results.

The change of pipe diameter between section 2 and 3 of the receiver has a significant influence in pressure drops as shown in the second plot of Figure 4-16 with the change in slope of the pressure curve at the start of the third region. The jagged flux profiles in the bottom plot of Figure 4-16 are due to the geometry of the cavity, composed of linear profile segments: at the joint between each segment, the flux changes due to the change in angle between the wall and the incoming radiation as described by Lambert's law. One change to be highlighted is the material used to build the coil of the receiver: in this new receiver the whole coil is made of Inconel 601H alloy.

The main means of comparison between experimental results and the model simulations is the series of 22 thermocouples installed at the back of the tube along the flow-path as well as five in-line thermocouples measuring the HC temperature in the tube. Figure 4-17 compares the simulated and experimental temperature profiles along the flow path.

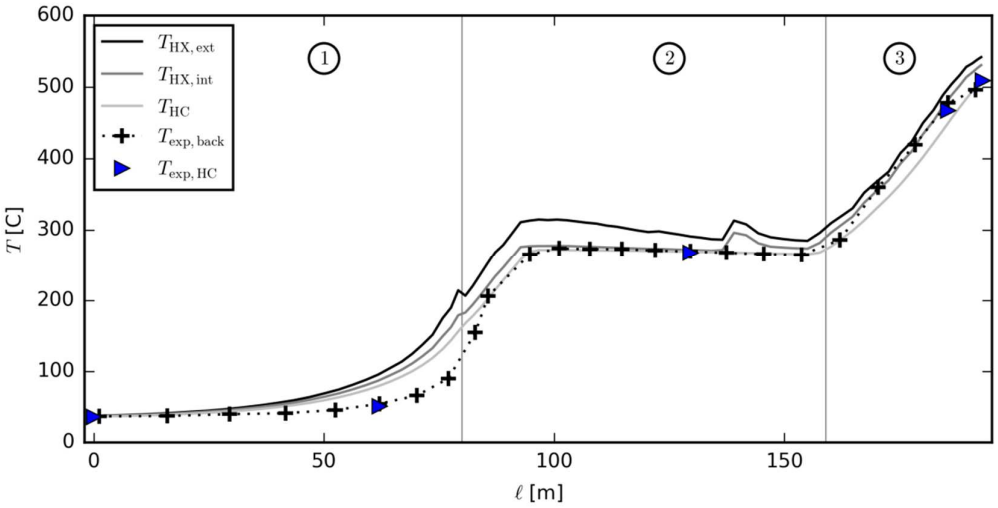

Figure 4-17: Comparison between the experimental and modelled temperature profiles for the SG4 receiver.

Overall the model and the experiment agree relatively well. In the first region of the receiver, the open frustum exposed to the environment, the model over-predicts temperatures. The model and experiment agree very well in region 2 of the receiver. In the third region, the model tends to under-predict the temperature values.

In the experiment, the in-line temperature measurements are very close to the ones taken at the back of the tubes; a tube temperature gradient effect due to conduction resistance seems unlikely to explain the discrepancies observed.

The heat flux per heat transfer mechanism, normalised with the absorbed radiative flux from the concentrator, is proposed in Figure 4-18. The relative influence of convective loss and long wave radiative heat transfer remains below 5% of the incident concentrated radiation for most of the flow-path. This suggests that the discrepancy between the experimental and

simulated temperatures is due to an inadequate evaluation of the incoming radiative flux in regions 1 and 3. The source of this discrepancy is expected to be due to the approximated model of the dish optics leading to an over-estimation of the flux on region 1 and under estimation of the flux on region 3. The potential role of forced convection loss, not considered in this model, is expected to be of minor impact, particularly considering the low wind speeds (average of 3.18 $m.s^{-1}$ at the receiver position) during this experimental run.

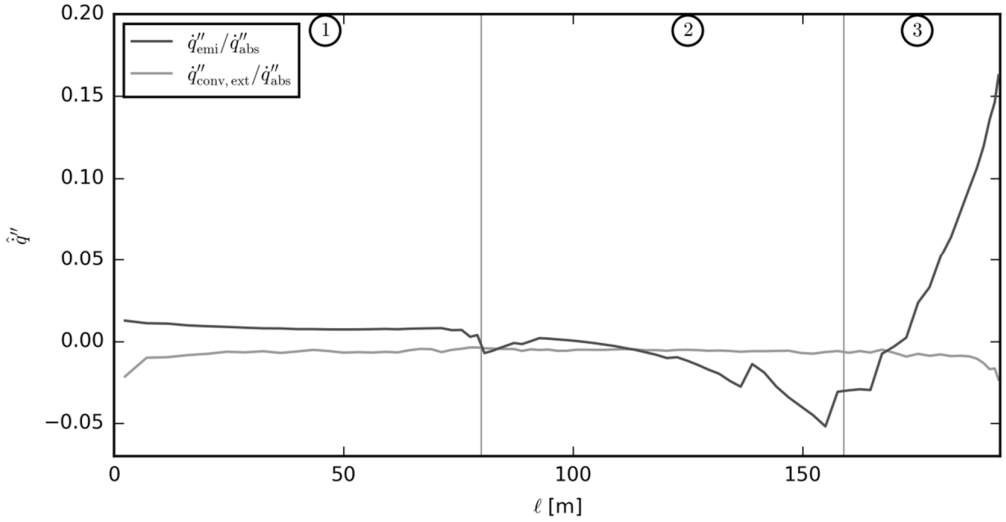

Figure 4-18: Comparison between the different heat transfer mechanisms along the flow path. The radiative input from the dish strongly dominates the heat balance along the whole flow path and the convective losses and radiative emissions only represent up to ~17% of the local heat flux. Negative values indicate a local loss of energy while positive values an added energy flux to the surface.

Further investigations in the role of the dish optics in the simulated discrepancies would require a different model based on accurate measurements of the dish surface properties and geometry. Photogrammetry has been used at the ANU STG for this purpose in the past [135], however, undertaking these measurements is outside the scope of this work and would require further experimental and modelling work (currently unfunded).

Table 4-3: System and estimated receiver efficiency comparison between the simulation and the experimental run.

	Model	Experiment	
$\eta_{\mathrm{sys}} = \frac{\dot{Q}_{\mathrm{abs,net}}}{\dot{Q}_{\mathrm{sun}}}$	89.3%	87.8%	
$\eta_{\mathrm{rec}} = \frac{\dot{Q}_{\mathrm{abs,net}}}{\dot{Q}_{\mathrm{con}}}$	97.7%	96.2%	Considering identical concentrator efficiency

The discrepancy in system efficiencies of the model and the experimental results is 1.5%. If the concentrator is assumed to be performing equally in the model and in the experiment, it leads to a 1.6% discrepancy between the model and the experiment. The uncertainty

associated with the measurement of the system efficiency was 2.2% [121] and that therefore the discrepancy between the model and the experimental results is lower than the actual precision of the measurements.

4.2.5 SG3 receiver on SG3 dish

In order to compare the performance gains of obtained by the SG4 dish and receiver system with the SG3 dish and receiver system, the SG3 system is simulated. The SG3 dish is modelled as an ideal paraboloid according with the solar flux map measurements from Johnston (1995) [70]. The SG3 dish model parameters are given in Table 4-4 and the validation of the model given in Figure 4-19.

Table 4-4: SG3 dish properties used to determine a suitable model using data from [70].

Dish diameter [m]	22.5
Dish area [m^2]	397.4
Dish effective area [m^2]	384.4
Focal length [m]	13.1
Surface slope error [mrad]	6.3
Effective reflectivity	0.72

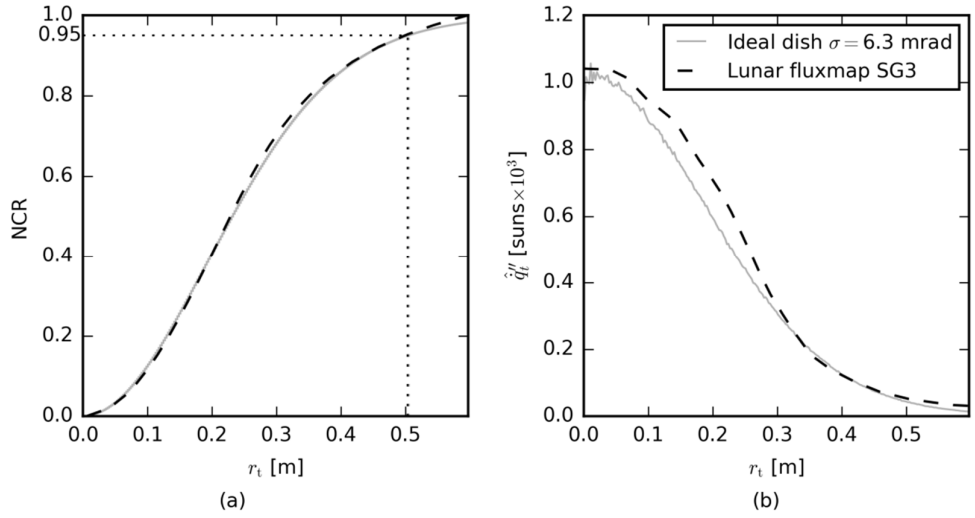

Figure 4-19: SG3 dish model validation. (a) Normalised capture ratio (NCR) and (b) radial flux distribution. The measurements were obtained with a water-cooled Lambertian target under 875 $W.m^{-2}$ of DNI.

The SG3 system is simulated using this SG3 dish model, the SG3 receiver model presented in Chapter 3 and the experimental parameters used in the previous subsection. The net heat flux and temperature distributions are presented in Figure 4-21 and the flow-path plots in Figure 4-20.

The impact of the lower quality of the SG3 optics is fully apparent here with lower net heat flux values obtained. The HC mass flow obtained in this simulation is 0.1261 $kg.s^{-1}$.

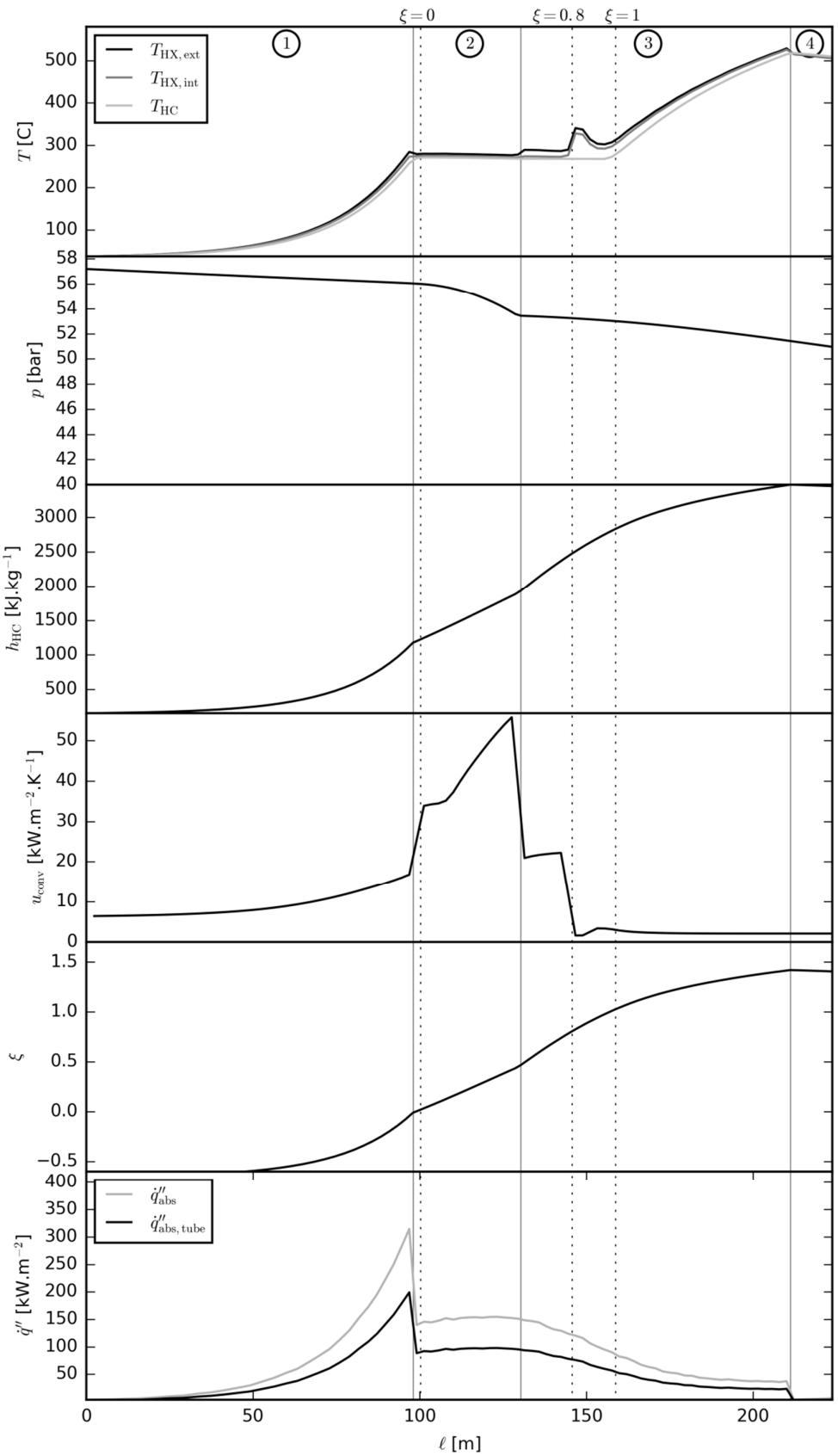

Figure 4-20: Flow path results for SG3 receiver on SG3 dish using experimental parameters in Table 4-2.

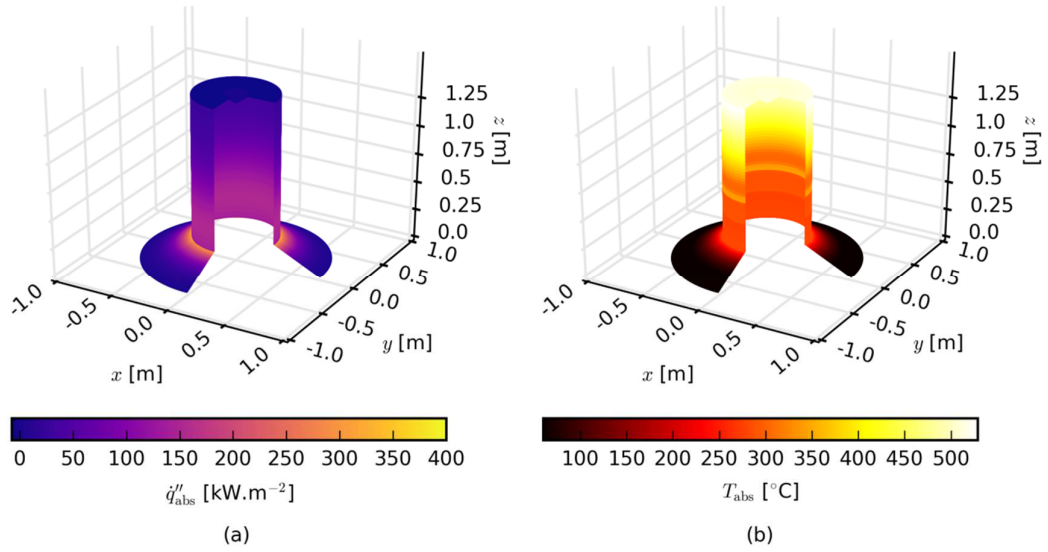

Figure 4-21: (a) Net heat flux and (b) temperature distributions on the SG3 receiver installed at the focus of the SG3 dish and using the experimental parameters in Table 4-2.

4.2.6 SG3 receiver on SG4 dish

In order to evaluate the performance gains brought by the optimised design of the SG4 receiver, the SG3 receiver is simulated on the SG4 dish using the experimental parameters. Here again, the net heat flux and temperature distributions are given in Figure 4-22 and the flow-path results in Figure 4-23.

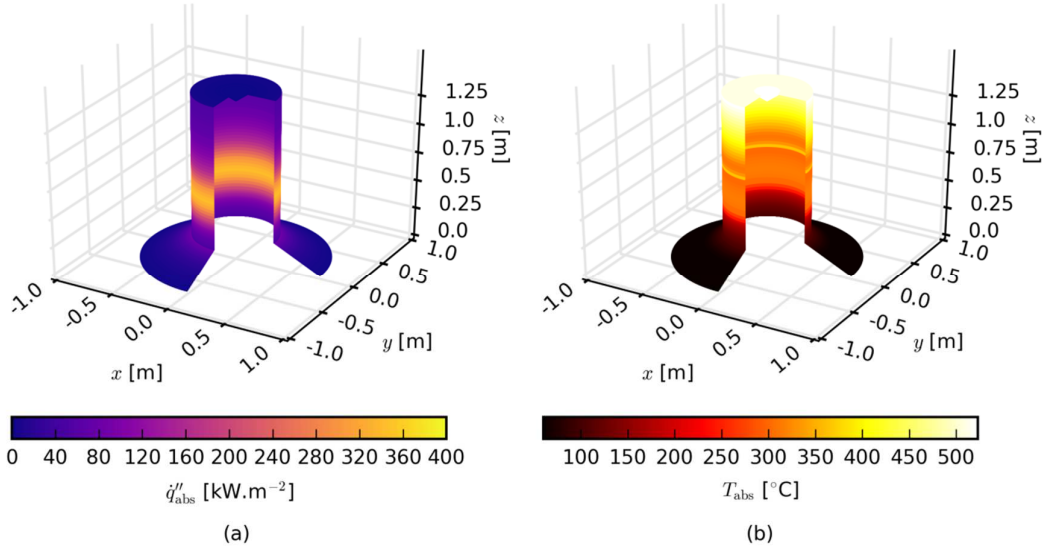

Figure 4-22: (a) Net heat flux and (b) temperature distributions on the SG3 receiver installed at the focus of the SG4 dish and using the experimental parameters in Table 4-2.

The peak flux is higher than with the SG3 dish and moved to the cylindrical section of the receiver. The mass flow is 0.1346 kg.s^{-1}.

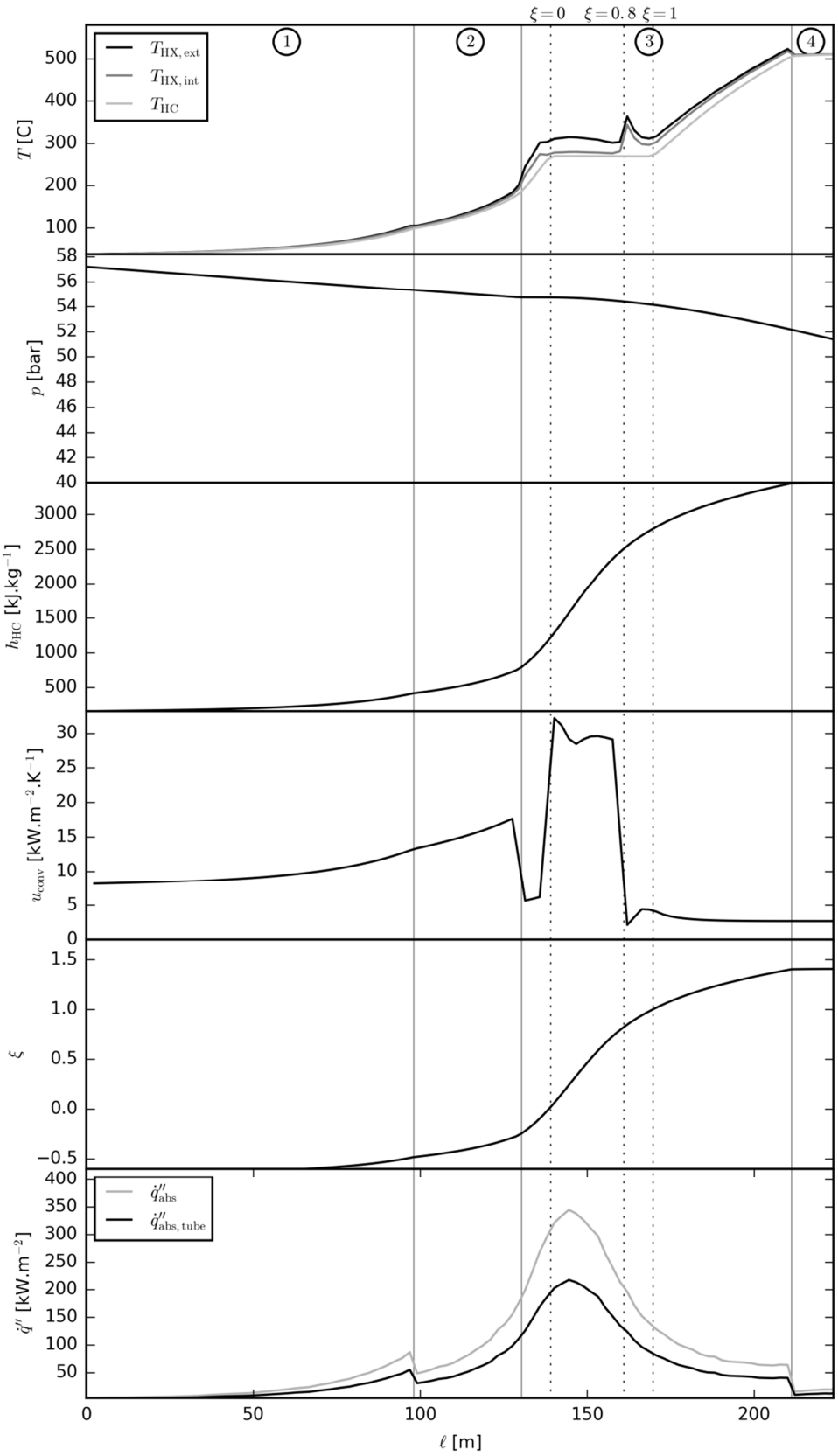

Figure 4-23: Flow path results for SG3 receiver on SG4 dish using experimental parameters in Table 4-2.

4.2.7 SG4 receiver geometry on SG4 dish

For completeness, a last simulation is performed using the SG4 receiver geometry with the SG3 receiver optical properties and pipe thermal conductivity. This simulation is therefore focusing on the performance changes associated with the geometry and independent of the spectrally selective coating and change in material made in the final SG4 receiver design.

The net heat flux and pipe outer wall temperature distributions show a qualitatively comparable distribution to the SG4 final design presented in Figure 4-15.

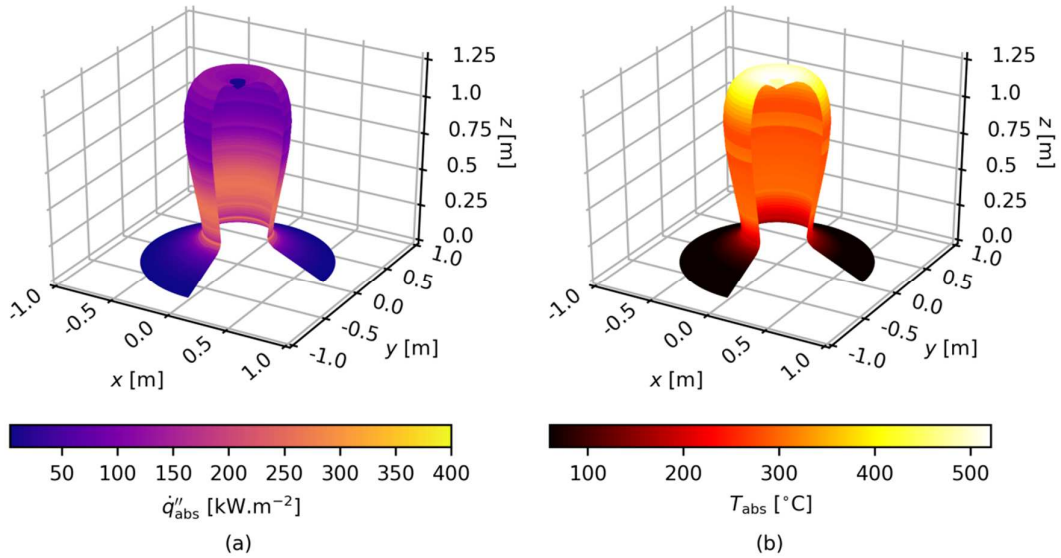

Figure 4-24: (a) Net heat flux and (b) temperature distributions on the SG4 receiver geometry with SG3 optical properties and thermal conductivity installed at the focus of the SG4 dish and using the experimental parameters in Table 4-2.

Similarly, the flow path results presented in Figure 4-25 for this configuration are comparable to the ones presented in Figure 4-16.

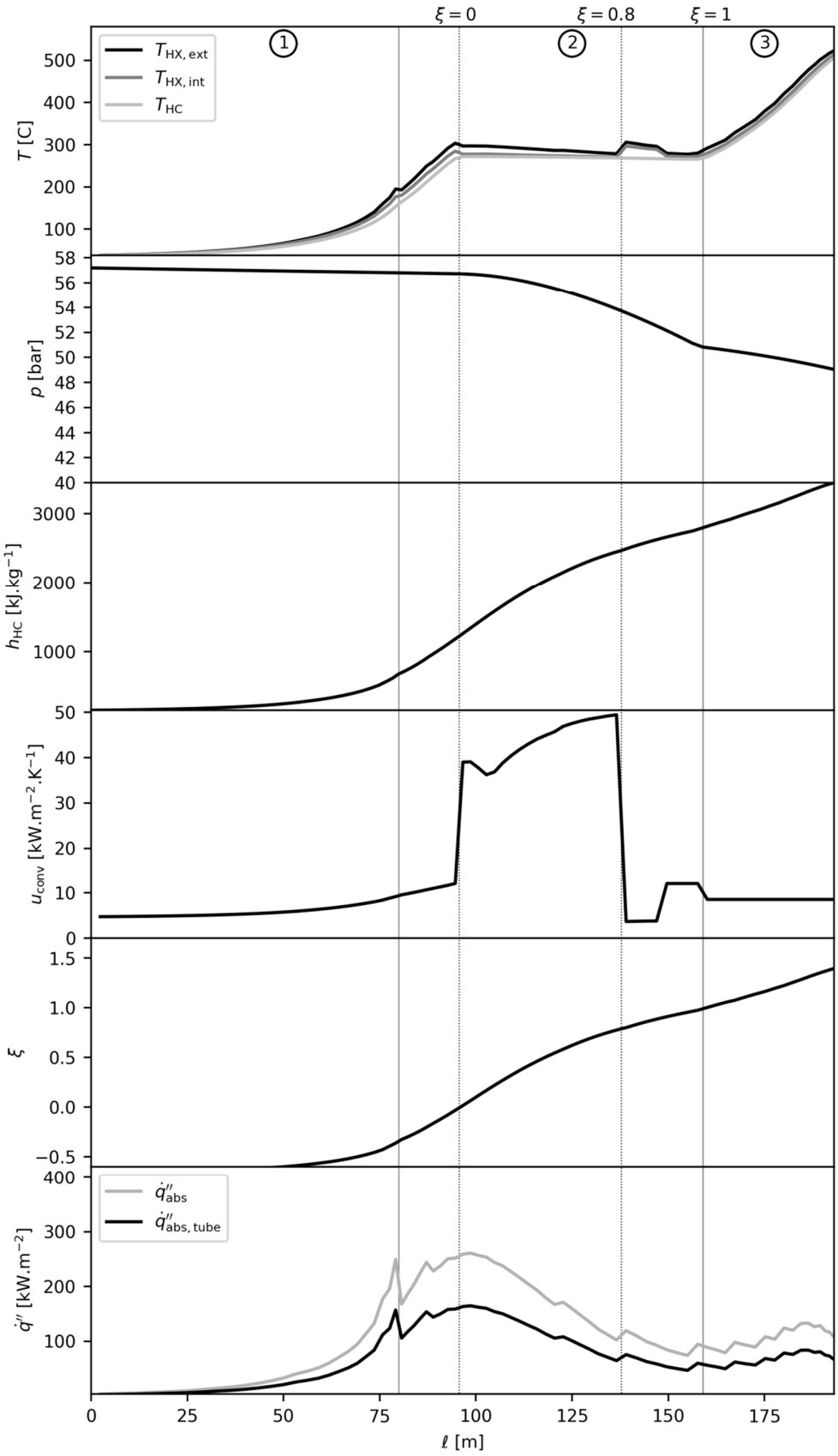

Figure 4-25: Flow path results for the SG4 receiver geometry with the SG3 receiver optical properties and pipe thermal conductivity on SG4 dish using experimental parameters in Table 4 2.

4.2.8 Conclusions

Figure 4-26 presents the normalised energy rate breakdown of the concentrator and receiver for the four case studies mentioned in this section.

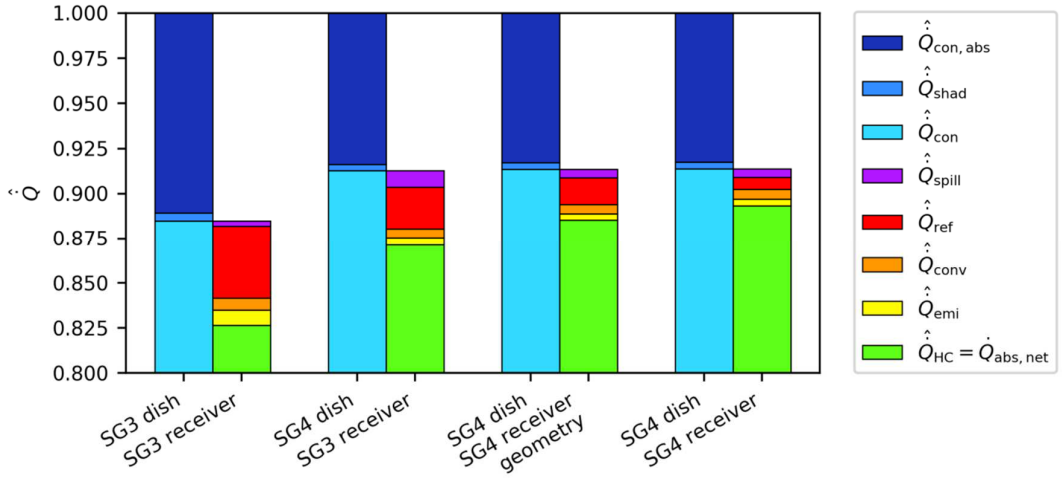

Figure 4-26: Efficiency comparison using normalised energy rate breakdown between the three models considered in this section: SG3 receive installed on SG3 dish, SG3 receiver installed on SG4 dish and SG4 receiver installed on SG4 dish.

The lower optical performance of the SG3 dish limits the performance of the whole system; not all efficiency gains are attributable to the design of a new receiver. The SG3 receiver is more efficient when placed at the focus of the SG4 concentrator, despite a slightly increased spillage loss. This spillage increase is due to the non-optimal geometry of the first frustum section of SG3 receiver (originally designed for the SG3 dish) regarding the radiation spatial distribution coming from the SG4 dish. When the SG4 receiver geometry with SG3 optical properties and thermal conductivity is placed on the SG4 dish, the losses are halved, mostly thanks to a greatly improved light trapping behaviour, as shown by the significant reduction in reflective loss; and a reduction in spillage loss. A small decrease in thermal emission loss occurs but is hardly noticeable as the emissive losses are quite low. The light trapping behaviour and thermal emission reduction are directly related to the change in the internal geometry of the receiver which offers less view factor to the environment and intercepts radiation deeper in the cavity. Changing now to the final SG4 receiver design on the SG4 dish, the use of the Pyromark spectrally selective coating further improves the light-trapping of the receiver. Thermal emissions, expected to be further reduced due to a decrease of 5% in emissivity of the surfaces in the longer wavelengths, are actually marginally increasing. This increase is caused by the change in pipe material of the receiver to an Inconel that has a lower thermal conductivity than the steels used in the original SG3 receiver; consequently causing an increase in outer wall temperatures. Table 4-5 summarises the

receiver efficiencies obtained from modelling. The objectives of the project are completed as the targeted improvement was an improvement of 2.2% of the SG4 receiver on SG4 dish compared to SG3 receiver on SG3 dish. In addition, the new receiver also outperforms SG3 receiver when it is positioned on the SG4 dish.

In the absence of reliable historical experimental data for SG3 receiver on SG3 dish, the modelling is the only available tool to compare the performance of these systems, however, the relative good agreement between the model and the presented experimental results, supports the validation of the model and therefore the success of the project.

Table 4-5: Absolute efficiency gains and relative energy loss reduction between the three case studies.

	SG3 receiver on SG3 dish	SG3 receiver on SG4 dish	SG4 receiver geometry on SG4 dish	SG4 receiver on SG4 dish
η_{rec}	93.4%	95.4%	96.9%	97.7%
$\Delta\eta_{rec}$	-	+ 2%	+ 3.5%	+ 4.3%
Loss reduction	-	- 30.3%	- 47.0%	- 65.2%

In addition to the project objectives, the new receiver presents interesting characteristics:

- The overall pipe length is shorter by 30.1 m, meaning that the receiver is lighter and potentially cheaper to manufacture and install. This was not the case for the prototype due to its one-off nature and because an Inconel alloy was chosen to avoid any thermo-mechanical issues.
- The flux distribution in the coil is generally more homogeneous which has potential added benefits in thermo-mechanical strength and ultimately receiver lifetime.

The benefits of a non-isothermal receiver profile tuned to the flux distribution using geometrical optimisation is illustrated with the results of this project and constitutes an encouraging way forward to improving multi-constrained and multi-objective receiver design.

Finally, PMCE was used to determine the general geometry of the receiver which was then fine tuned “manually” through successive parametric studies. While this method proved useful in designing, building and testing an efficient receiver for the SG4 dish, its reusability and versatility is limited. In the next section the method is extended to multi-objective and evolutionary optimisation problems to address its shortcomings.

4.3 MOE-PMCE-O: Multi-objective, evolutionary, MCRT-integrated stochastic optimisation

In this section the improvement of the PMCE for multi-objective problems and subsequent introduction in a new optimisation method, MOE-PMCE-O is described in more detail. The subsequent section will illustrate the method on a receiver example. To address the previously identified limitations of PMCE, the following changes are implemented:

- The method is converted to a multi-objective optimisation method which involves the use of a method to evaluate Pareto fronts composed of candidates evaluated with uncertainty.
- The method is changed from a single large population evaluation to an evolutionary optimisation algorithm where a smaller population is needed at the start and new candidates are added during the process, as information is learned about the problem to solve.

The method developed here evaluates populations of candidates successively to find a final population, p_{final}, in which all candidates are Pareto-optimal candidates and their objective function is evaluated with known precision. Progressing step-by-step, each candidate in the active population, p_{active} is evaluated for N_{obj} objectives and the decision to keep it or not in the active population is made based on a stochastic Pareto front evaluation. If a candidate is kept in the active population, it will be simulated again in the next iteration and the precision of the evaluation will increase. Contrarily to the previous optimisation algorithm, if a candidate is discarded, a new candidate is introduced in the active population to replace it. The overall population regrouping all the generated candidates is labelled total population p_{total}. The overarching algorithm of the optimisation is described in Figure 4-27.

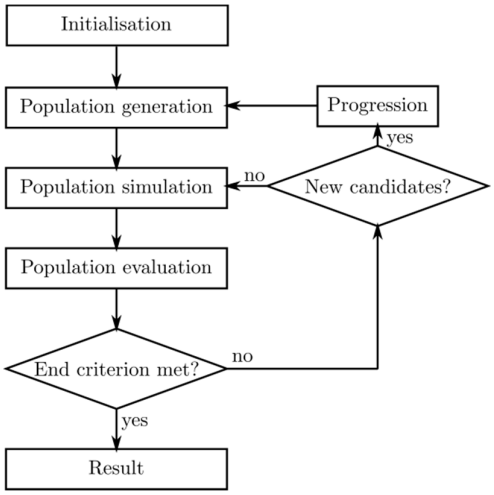

Figure 4-27: MOE-PMCE-O algorithm flowchart.

In this section and the rest of this work the objective metrics are maximised. The algorithm could easily be re-written for minimisation.

Each block of the algorithm is described in more details in the following sub-sections.

4.3.1 Initialisation

In this first step, the optimisation parameters and initial parameter space are set.

The optimisation parameters are:

- The size of the active population being simulated at each step $N_{\text{pop,active}}$
- The size of the final population desired $N_{\text{pop,final}}$
- The absolute precision of the evaluation desired for the N_{obj} objectives in the final population $\sigma_{\text{obj}} = \left\{\sigma_1, ..., \sigma_{\text{N}_{\text{obj}}}\right\}$.
- As an optional parameter, a minimum threshold on the objective values can be set $\sigma_{\text{t}} = \left\{\sigma_{\text{t},1}, ..., \sigma_{\text{t,N}_{\text{obj}}}\right\}$
- An exploration threshold $\tau \in [0,1]$ used to make the decision between exploration of the parameter space and refinement of the results by exploitation of the current results, explained in the "progression" step of the routine.

The initial parameter space PS_{ini} is established here to allow the population generation step to create the first population of candidates. As this work focuses on geometry, the parameters of interest are scalar distances and their parameter space defined by a maximum and a minimum value that form an interval. Each geometric variable $x \in \left\{x_1 ... x_{N_{\text{P}}}\right\}$ has its own interval $P_x = \left[x_{\min}, x_{\max}\right]$ and the combination of those form the parameter intervals set of the optimisation problem $PS = \left\{P_{x_1} ... P_{x_{N_{\text{P}}}}\right\}$.

4.3.2 Population generation

In the population generation step (Figure 4-28), parameter space information is used to generate $N_{\text{pop,new}}$ candidates in order to maintain an active population count of $N_{\text{pop,active}}$. For the first iteration of geometry generation, $N_{\text{pop,new}} = N_{\text{pop,active}}$.

For each geometry *g* generated, a specific parameter space information PS_g is given. The geometry generator uses information from the parameter space to build a candidate's parameter set as described in the following expression:

$$C_g = \left\{x_1 ... x_{N_{\text{P}}}\right\} = generate\left(PS_g\right) \tag{4-6}$$

The parameter set can then be used in the simulation stage to obtain evaluations of the optimisation metrics.

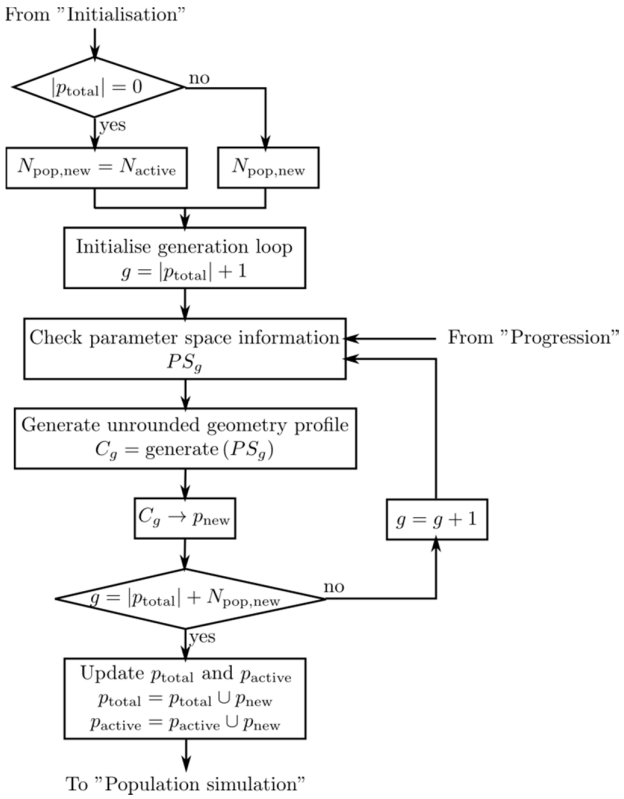

Figure 4-28: Population generation algorithm in charge of adding $N_{\text{pop,new}}$ new geometries to the total population.

4.3.3 Population simulation

At this step, the simulation of each candidate C_g in p_{active} is performed to obtain the set of N_{obj} objective metrics for each of them (Figure 4-29). The simulation result involves Monte-Carlo sampling and the previous estimate of the objective metrics, as well as the number of rays already cast on this candidate, are needed as an input in the simulation. The number of rays per bundle N_{bundle} is kept constant throughout the algorithm in this implementation of MOE-PMCE-O and the number of rays cast per geometry $N_{\text{rays},g}$ recorded throughout the optimisation process.

$$\left\{\bar{M}_1 \ldots \bar{M}_{N_{\text{obj}}}\right\}_{g,N_{\text{rays},g}} = simulate\left(C_g, \left\{\bar{M}_1 \ldots \bar{M}_{N_{\text{obj}}}\right\}_{g,N_{\text{rays},g}-N_{\text{bundle}}}, N_{\text{rays},g}\right) \tag{4-7}$$

The simulate function contains the problem-specific receiver model.

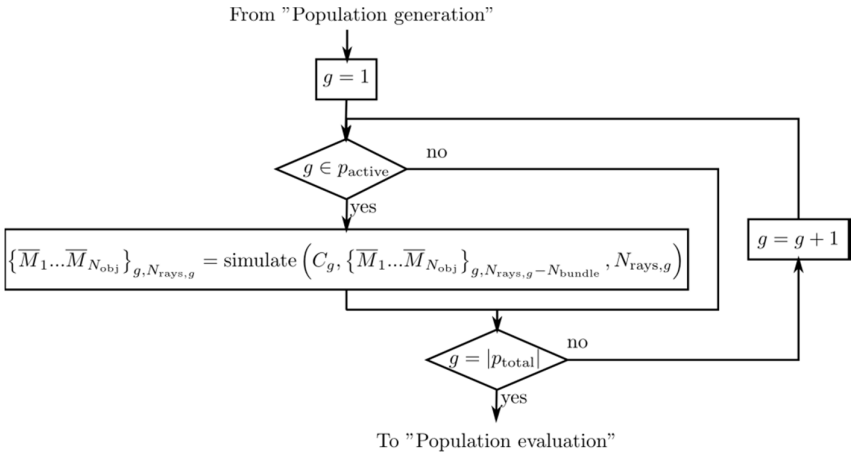

Figure 4-29: MOE-PMCE-O simulation loop selecting only the active population members to simulate among the total population.

4.3.4 Population evaluation.

At this step, the overall population is evaluated to identify fit candidates. This operation involves statistical work to identify the dominance relationship between the candidates in the total population (Figure 4-30).

The following equations are used to compute and store the data necessary to compute the sample standard deviation s for each candidate C_g and each objective metric m without risking numerical overflow [149].

$$\begin{cases} Q_{g,m,0} = 0 \\ Q_{g,m,N_{\text{rays}}} = Q_{g,m,N_{\text{rays},g}-N_{\text{bundle}}} + \dfrac{N_{\text{rays},g} - N_{\text{bundle}}}{N_{\text{rays},g}} \left(\overline{M}_{g,m,N_{\text{rays},g}} - \overline{M}_{g,m,N_{\text{rays},g}-N_{\text{bundle}}}\right)^2 \end{cases} \tag{4-8}$$

$$s_{g,m,N_{\text{rays},g}} = \sqrt{Q_{g,m,N_{\text{rays},g}} \frac{N_{\text{bundle}}}{N_{\text{rays},g} - N_{\text{bundle}}}} \tag{4-9}$$

Similarly to PMCE (Section 4.1), the MCRT sampling allows the evaluation of the confidence interval for each candidate and each objective metric:

$$CI_{g,m,N_{\text{rays},g}} = \frac{3 s_{g,m,N_{\text{rays},g}}}{\overline{M}_{g,m,N_{\text{rays},g}} \sqrt{\dfrac{N_{\text{rays},g}}{N_{\text{bundle}}}}} \tag{4-10}$$

$$M_{g,m} \in \left[\overline{M}_{g,m,N_{\text{rays},g}}\left(1 - CI_{g,m,N_{\text{rays},g}}\right), \overline{M}_{g,m,N_{\text{rays},g}}\left(1 + CI_{g,m,N_{\text{rays},g}}\right)\right] \tag{4-11}$$

The next step is to evaluate which of these candidates are promising candidates, and which are statistically unfit and need to be discarded from the active population. First, if objective thresholds have been defined at the start of the optimisation, the best-case scenario objective evaluations are compared with the minimum thresholds and unfit candidates are

discarded. If the best-case scenario objectives are below there respective minimum thresholds, the candidates are discarded.

The rest of this section describes stochastic non-dominated sorting, leading to the evaluation of the stochastic and multi-objective Pareto front. The stochastic multi-objective non-dominated sorting described here is supported by Figure 4-31 which illustrates the method in a simple two-objective case with seven candidates in the total population.

A stochastic multi-objective Pareto front is built in the results space to evaluate which candidates are promising or not. The result space is a hyperspace of N_{obj} dimensions in which each orthogonal axis accounts for one of the optimisation objectives. Each candidate in the total population holds a position in this space according with its current performance in each objective.

In the current version of the algorithm, the Pareto front is approximated to a convex surface using "Qhull", a fast and reliable convex hull algorithm [10]. The first thing to do is to verify that enough good candidates are available to evaluate the stochastic Pareto dominance relationships. The minimum number of candidates is equal to the number of dimensions of the problem which is the number of objectives. If there are not enough candidates, the Pareto dominance evaluation is bypassed and the method continues.

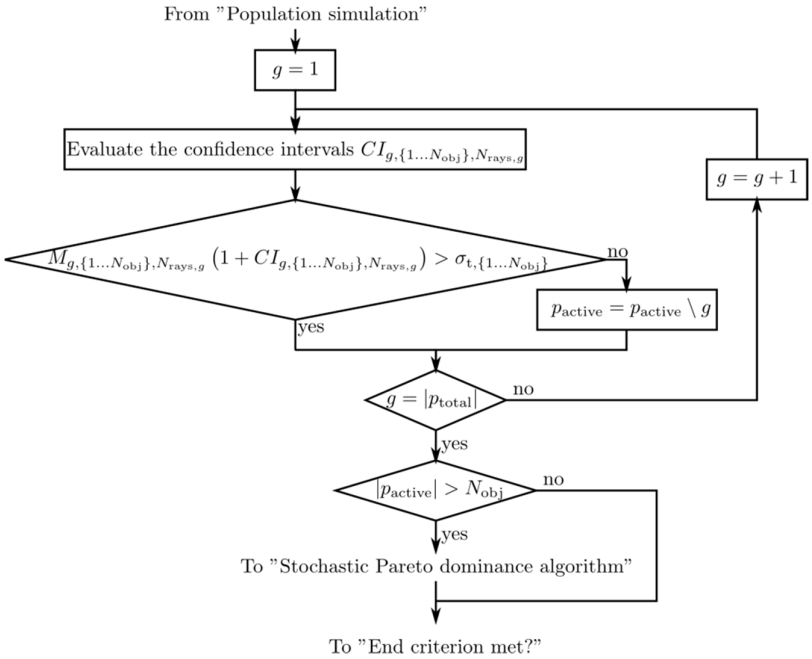

Figure 4-30: Population evaluation step of the algorithm

A first evaluation of the Pareto front is done using the current metric estimators $\bar{M}_{g,m,N_{\text{rays},g}}$ to obtain p_{Pareto}, a subset of the current population p_{active}. The candidates that belong to this Pareto front are kept in the active population for the next iteration.

The uncertainty of the objectives estimation is then taken into account to consider which of the remaining candidates are still statistically fit and which are the ones that are statistically unfit and need to be discarded. To do so, the first step is to quickly find obvious situations where the uncertainty of the estimation makes the decision of candidate fitness clear using Euclidian distances to the origin of the referential. The worst-case scenario $D_{\mathrm{wc},g}$ and best-case scenario $D_{\mathrm{bc},g}$ distances to the origin of the result space are computed for each candidate in the total population.

$$D_{\mathrm{wc},g} = \sqrt{\sum_{m=1}^{N_{\mathrm{obj}}} \left(\bar{M}_{g,m,N_{\mathrm{rays},g},\mathrm{E}} \left(1 - CI_{g,m,N_{\mathrm{rays},g},\mathrm{E}} \right) \right)^2} \tag{4-12}$$

$$D_{\mathrm{bc},g} = \sqrt{\sum_{m=1}^{N_{\mathrm{obj}}} \left(\bar{M}_{g,m,N_{\mathrm{rays},g}} \left(1 + CI_{g,m,N_{\mathrm{rays},g}} \right) \right)^2} \tag{4-13}$$

These distances are then compared with the minimum distance to the origin of the Pareto-optimal candidates $D_{\mathrm{threshold}}$ and the maximum one D_{ceil} defined as:

$$D_{\mathrm{threshold}} = \min\left(D_{\mathrm{wc},g \in p_{\mathrm{Pareto}}} \right) \tag{4-14}$$

$$D_{\mathrm{ceil}} = \max\left(D_{\mathrm{wc},g \in p_{\mathrm{Pareto}}} \right) \tag{4-15}$$

Candidates with a best case distance to the origin smaller than the distance $D_{\mathrm{threshold}}$ are statistically unfit and are not assigned the active population. Candidates with a best case distance to the origin greater than the distance D_{ceil} are statistically fit and are assigned to the active population.

The second step screens through the remaining candidates and evaluates the fitness of each candidate using iterative non-dominated sorting evaluations.

A temporary population p_{temp} is built with the worst-case scenario estimates of the candidates in p_{Pareto}, the original Pareto-optimal candidates, and the best-case scenario estimates of the candidates that remain to be screened. Knowing the indices of the Pareto-optimal candidates, it is possible to iteratively determine which uncertain candidates are still statistically competing. The Pareto front of the temporary population $p_{\mathrm{temp,Pareto}}$ is determined and the indices of its members in p_{total} compared with the known indices of Pareto-optimal candidates in p_{total}. If any candidate appearing in the Pareto front of the temporary population $p_{\mathrm{temp,Pareto}}$ is different to the original set of Pareto-optimal candidates, it is removed from the temporary population and kept in the active population. The process is repeated until the set of Pareto-optimal candidates of the temporary population has exactly the same indices as the

original one. At that point all the candidates that remain in p_{temp} and do not figure in $p_{\text{temp,Pareto}}$ are discarded from the active population: their best-case scenario estimate does not outperform the worst-case scenario estimate of the Pareto-optimal candidates.

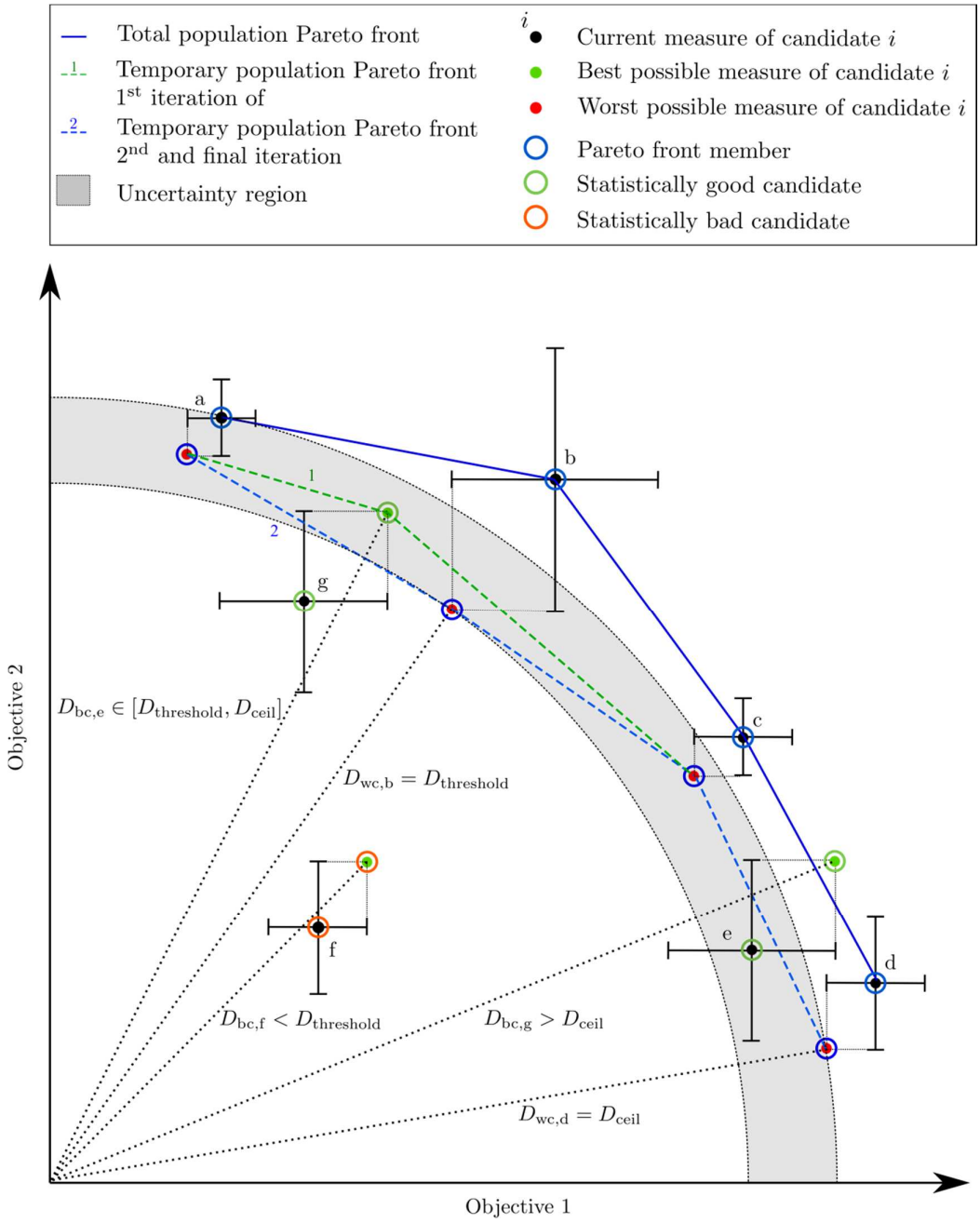

Figure 4-31: Illustration of the stochastic multi-objective Pareto front sorting algorithm with two objectives.

Figure 4-31 shows an example of the application of the stochastic multi-objective Pareto front sorting. Candidates a, b, c and d are Pareto-optimal candidates of the total population. Candidate b has the smallest worst-case scenario distance to the origin and candidate d the largest one, defining $D_{\text{threshold}}$ and D_{ceil}. Candidate e is statistically good and kept in the active population as its best-case scenario distance is larger than D_{ceil}. Candidate f is statistically bad

as its best-case scenario distance is smaller than $D_{\text{threshold}}$. Candidate g is the last candidate that needs to be screened as its best-case scenario distance lies in between $D_{\text{threshold}}$ and D_{ceil}. The temporary population is built with the worst-case scenario positions for the Pareto-optimal candidates a, b, c and d and the best-case scenario position for g. A first iteration of Pareto front detection finds a, g, c and d as Pareto-optimal candidates of the temporary population. g not being a member of the original total population Pareto-optimal candidates set (a, b, c and d), is discarded from the temporary population and kept into the active population. A second iteration of Pareto front detection finds a, b, c and d which is identical to the original total population Pareto-optimal candidates set which completes the algorithm (Figure 4-32).

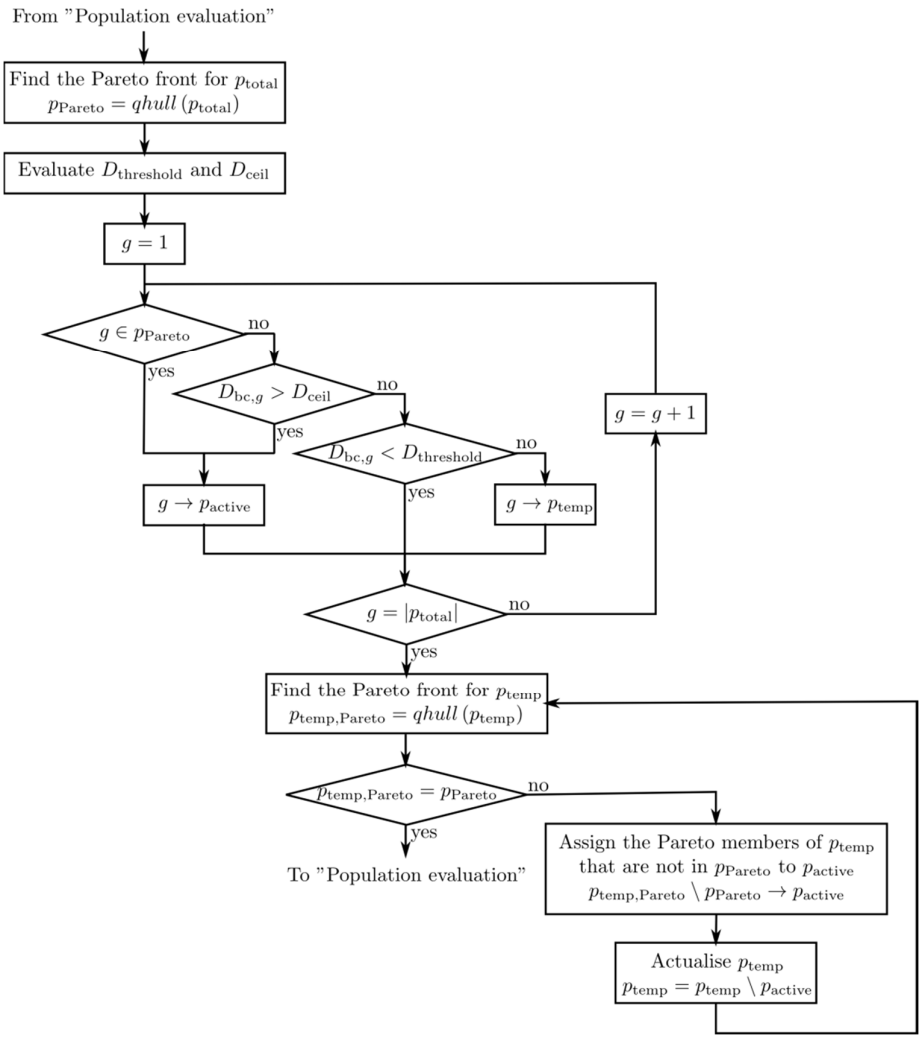

Figure 4-32: N-Dimensional stochastic Pareto dominance algorithm.

4.3.5 End criterion met?

Pareto-optimal candidates with confidence intervals smaller than the precision termination criteria $\left\{\sigma_1,\ldots,\sigma_{N_{obj}}\right\}$ declared at the start of the optimisation are moved from the

active population to the final population. When the final population count reaches $N_{pop,final}$ the optimisation is complete (Figure 4-33).

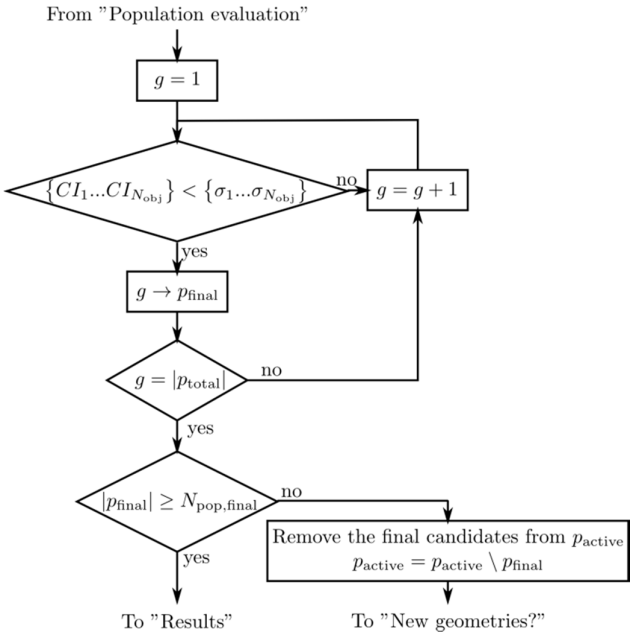

Figure 4-33: Algorithm used to determine if the MOE-PMCE-O is finished.

4.3.6 New candidates?

If the active population contains less candidates than $N_{pop,active}$, $N_{pop,new}$ new candidates have to be generated and the required number of new geometries is passed to the progression step.

$$N_{pop,new} = N_{pop,active} - |p_{active}| \tag{4-16}$$

The active population is directly sent to the simulation step when no new geometry generation is required (Figure 4-34).

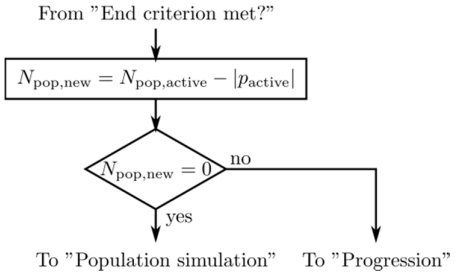

Figure 4-34: Algorithm bloc to determine if new candidates are needed and orient the optimisation consequently.

4.3.7 Progression

The optimisation progresses by generating new candidate receiver geometries. The receiver geometries are generated using parameter space information as exposed in the population generation step. The object of the progression step is to determine parameter

spaces and provide them to the population generation step in order to drive the generation of new geometries in a way that promotes the progression of the optimisation.

As is generally the case in optimisation, two options are offered at this stage to drive the progression of the method: exploration or exploitation. Exploration of the parameter space ensures that the method does not fall into local minima. Exploitation of the results will tend to refine the results by using information gathered during the optimisation to determine a suitable parameter space for new candidates. In this study, the decision between exploration and exploitation is performed for each new candidate generated using a random selector. For each new candidate, a random number is uniformly drawn between in the [0, 1] interval and compared with the exploration threshold τ. If the random number is lower than τ, the exploration behaviour is chosen, if its value is superior to it, the exploitation behaviour is chosen.

If the exploration behaviour is required for a new geometry, the initial parameter space information is sent to the population generation (Figure 4-35).

If the exploitation behaviour is required for a new geometry, new parameter space information PS_{new} is determined by analysing the currently successful candidates $\left(p_{\text{active}} \cup p_{\text{final}}\right)$.

$$P_x = \left[\min\left(x_{g\in p_{\text{active}}\cup p_{\text{final}}}\right), \max\left(x_{g\in p_{\text{active}}\cup p_{\text{final}}}\right)\right] \tag{4-17}$$

$$PS_{\text{new}} = \left\{P_{x_1} \ldots P_{N_p}\right\} \tag{4-18}$$

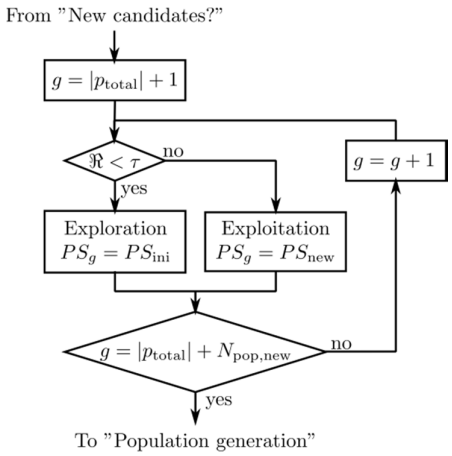

Figure 4-35: Progression algorithm used to decide between exploration and exploitation for each new geometry and determine the parameter space needed to do so.

4.3.8 Results

When $N_{pop,final}$ candidates have been found, the optimisation finishes and results can be interpreted. All the information gathered through the optimisation process is stored and available for analysis.

4.4 Optimisation of a liquid sodium receiver for a surrounding heliostat field

In this section we present an application of MOE-PMCE-O to the optimisation of the geometry of a tower receiver placed at the focus of a surrounding heliostat field. The optimisation targets three general objectives, defined in more detail later:

- The maximisation of the efficiency of the receiver.
- The maximisation of the reliability of the receiver.
- The minimisation of the cost of the receiver.

4.4.1 System model

4.4.1.1 Concentrator model

The heliostat field used in this study is the ASTRI test field (Section 3.2). An annular aiming strategy, where all the heliostats point towards the closest point to an aiming annulus, is adopted for both simplicity and potential reduction in optimal receiver aperture, all the heliostats in the field point at the closest point on a ring of radius $R_{aim} = 3\,\text{m}$ and height $L_{aim} = 91.1\,\text{m}$ from the pivot height of the heliostats (Figure 4-36 b). The optimisation will be conducted on a set of sun positions to approximate an annual performance. The determination of the 9 sun positions used in this study was done externally as part of ASTRI activities by Dr. Victor Grigoriev, using a method based on Gaussian quadrature. The heliostats considered are flat square surfaces of 6.1 m side length with 1.53 mrad of slope error. Flat heliostats are an approximation of the real behaviour that lowers local peak flux values but accurately describes the general distribution of flux from the heliostat field. The result of the method is a set of sun positions and their associated integration weights, given in Table 4-6.

To speed-up the computation of the incident flux on the receiver, the intermediate receiver enclosing source (IRES) method is used. Prior to this optimisation, a database of spherical IRESs with a radius of 15 m was created by simulating the heliostat field at each of the nine sun positions and for 100,000,000 rays. This task was performed by Clothilde Corsi in the ASTRI project using Tonatiuh. The database files were then shared on a cloud sever and locally re-formatted into IRESs containing 10,000 rays each in order to be able to perform

progressive ray tracing. These sources are the ones called by the optimisation routine. Using this method greatly speeds up the process as the simulation of the heliostat field is reduced to the emission of rays from the IRESs.

Table 4-6: Sun positions considered in the optimisation and their associated integration weights.

	t	θ_{el} [°]	θ_{az} [°]	$\dot{Q}_{con}$ [MW]	$w(t)$
Winter Solstice	1	14.894	59.359	100	363.244
	2	45.900	0.0	138	581.191
	3	14.894	-59.359	99.8	363.244
Equinox	4	18.495	81.516	109	405.556
	5	66.2	0.0	142	648.889
	6	18.495	-81.516	108	405.556
Summer Solstice	7	19.465	104.257	109	447.867
	8	86.5	0.0	144	716.587
	9	19.465	-104.257	109	447.867

4.4.1.2 Receiver model

The receiver geometry is axi-symmetrical and composed of 4 stacked frustum sections as shown in Figure 4-36. Receiver geometries are positioned in the general referential so that the vertical axis of symmetry of the geometry passes through the centre of the aiming annulus and the mid-height of the receiver profile is co-planar with the aiming annulus.

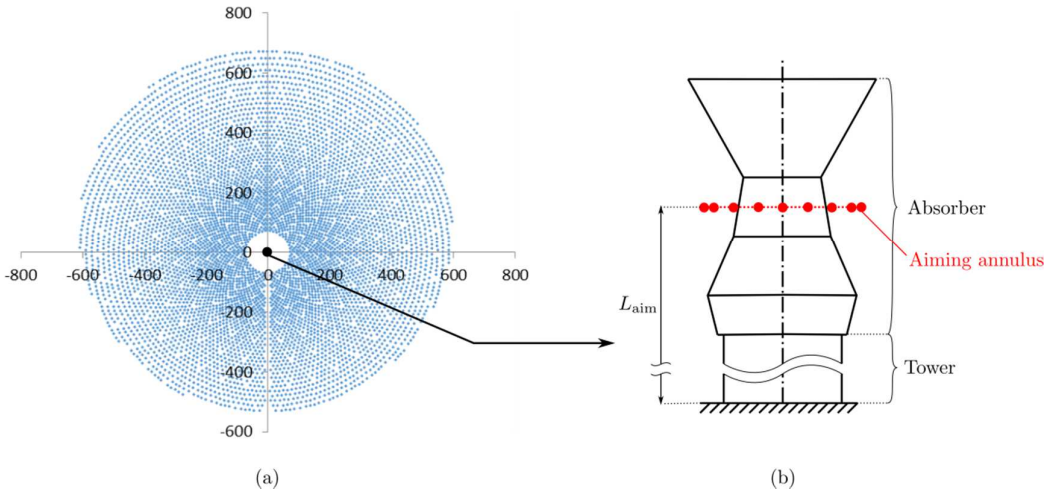

Figure 4-36: Concentrator (a) and 4 sections receiver (tower and absorber) (b) system diagram.

A set of geometrical constraints are applied on the receiver profile generation (Figure 4-37):

(1) The initial parameter space is the same for every point defining the geometry profile, except the first that always has a local height of 0 m.

(2) No point within the receiver profile can reach a vertical position higher than the top end of the profile, which is the receiver inlet. No point within the receiver profile can reach a vertical position lower than the bottom end of the profile, which is the receiver outlet.

(3) The receiver profile cannot intersect itself in cross-section.

(4) The axi-symmetrical sections lengths are integer multiples of the width of the bank of tubes, determined based on the tube diameters and number of tubes per bank.

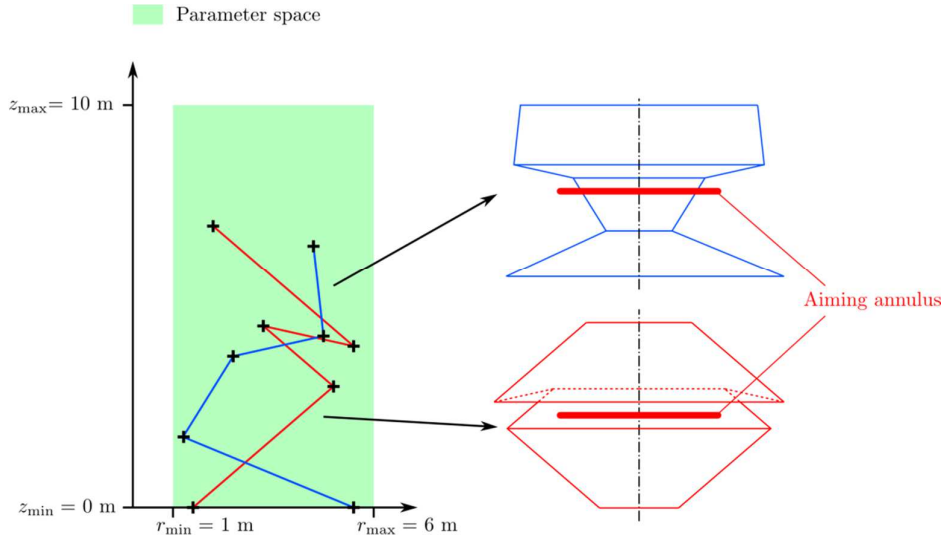

Figure 4-37: Geometry profile generation diagram and corresponding generated geometries with the aiming annulus position at mid height of the receiver.

The receiver profiles are created by loops of pipe arranged in annular banks. The receiver considered is a liquid sodium receiver. The liquid sodium enters the receiver at 480 °C and exits at 640 °C. The incompressible liquid sodium properties from [38] are given in eqs. 4-19 to 4-23 (temperatures are in Kelvin):

$$\rho_{Na}(T) = 219 + 275.32\left(1 - \frac{T}{2503.7}\right) + 511.58\sqrt{1 - \frac{T}{2503.7}} \quad (4\text{-}19)$$

$$\mu_{Na}(T) = \exp\left(-6.4406 - 0.3958\ln(T) + \frac{556.835}{T}\right) \quad (4\text{-}20)$$

$$k_{Na}(T) = 124.67 - 0.11382T + 5.5226\times10^{-5}T^2 - 1.1842\times10^{-8}T^3 \quad (4\text{-}21)$$

$$C_{p,Na}(T) = \left(1.6582 - 8.4790\times10^{-4}T + 4.4541\times10^{-7}T^2 - 2992.6T^{-2}\right)\times10^3 \quad (4\text{-}22)$$

$$h_{Na}(T) = \left(-365.77 + 1.6582T - 4.2395\times10^{-4}T^2 + 1.4847\times10^{-7}T^3 - 2992.6T^{-1}\right)\times10^3 \quad (4\text{-}23)$$

The receiver outlet is assumed to be at atmospheric pressure. The mass flow is assumed to be evenly distributed between the pipes. The pipes themselves are chosen within the

Nominal Pipe Sizes standard Schedule 5s. The pipe size selected keeps the pipe wall thickness at the lowest possible value (to limit the conduction barrier), and has the maximum available outer diameter (to minimise the mass of pipe). The tube outside diameter is 17.15 mm and the wall thickness is 1.245 mm. Each tube bank is composed of 100 tubes of Haynes 230® alloy. A correlation for the thermal conductivity of the Haynes 230® alloy was determined using manufacturer data[9] (Figure 4-38).

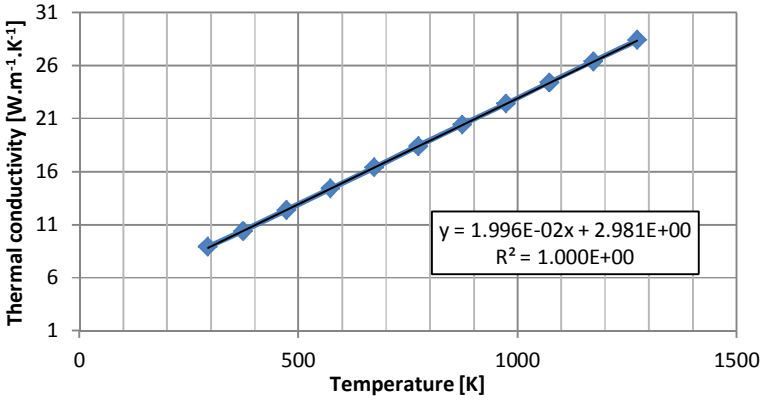

Figure 4-38: Thermal conductivity of Haynes 230® as a function of the temperature.

As seen in Chapter 3, the mass flow of HC should be divided in several flow-paths to keep the velocity of the fluid within a suitable range. The number of flow-paths needed for the geometries generated in this case is common to all of them and is constrained by using a maximum acceptable velocity of the liquid sodium in the pipes. The overall energy available to any geometry generated is the sum of the power reflected from the concentrator $\dot{Q}_{con}$. To find an upper bound on the flow velocity needed, it is assumed that all the energy from the concentrator is absorbed by the HC:

$$\dot{Q}_{con} = \dot{m}_{HC,ideal}\left(h_{HC,out} - h_{HC,in}\right) \tag{4-24}$$

The mass flow is itself a function of the flow velocity, HC density, number of flow-paths, number of tubes per flow-path and internal diameter of the tubes:

$$\dot{m}_{HC,ideal} = v_{HC} N_{fp} N_{tubes} \rho_{HC}\left(T_{HC}\right) \pi r_{HX,int}^2 \tag{4-25}$$

Assuming a maximum acceptable velocity of the fluid flow in the pipes $v_{HC,\,max}$, the number of flow paths required is given by:

$$N_{fp} = \left\lceil \frac{\dot{m}_{HC,ideal}}{v_{HC,max} N_{tubes} \rho_{HC}\left(T_{HC}\right) \pi r_{HX,int}^2} \right\rceil \tag{4-26}$$

[9] Manufacturer data: http://www.haynesintl.com

$\dot{Q}_{con}$ is maximum at the summer solstice ($t=8$) and the density is the lowest for the highest fluid temperature, which is found at the outlet of the receiver, the number of flow paths needed is therefore:

$$N_{fp} = \left\lceil \frac{\dot{Q}_{con,t=5}}{v_{HC,max} N_{tubes} \rho_{HC}\left(T_{HC,out}\right) \pi r_{HX,int}^2 \left(h_{HC,out} - h_{HC,in}\right)} \right\rceil \quad (4\text{-}27)$$

$N_{fp} = 8$ using the previously mentioned parameters. The flow-paths are directed on the receiver surface in a sequence of horizontal curved tube banks segments. The tube banks are horizontal so that the surface tangent to the tubes follows the geometry profile determined previously. The general direction of the flow is from the top to the bottom of the receiver as illustrated in Figure 4-39.

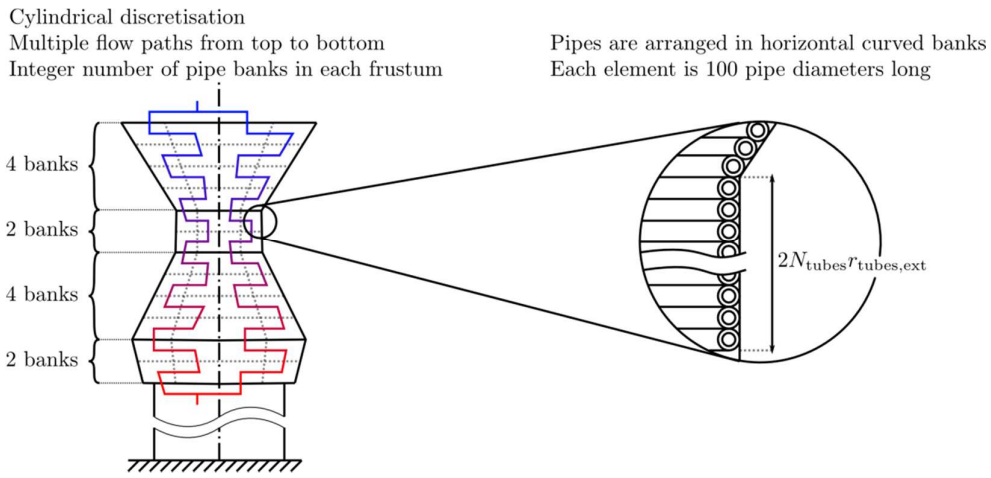

Figure 4-39: Illustration of the receiver discretisation, flow-path and tube banks layout.

The surface of the receiver is discretised into N_{banks} elements vertically and $2N_{fp}$ elements angularly. The view factors are calculated and stored each time a new candidate is generated and based on this discretisation scheme. The relative precision parameter given to the view factor computation algorithm is 5%.

4.4.2 Optimisation implementation

4.4.2.1 Objective metrics and thresholds

The objective metrics are evaluated on the nine sun positions presented in Table 4-6. The first objective metric (M_1), evaluates the quantity of useful work produced by the receiver. This useful work, similarly to Chapter 3, is calculated by applying the Carnot efficiency to the net heat gain in the receiver and subtracting the work lost by pressure drops. This value is then normalised using the radiative input from the concentrator. At each sun position the total pressure drop is calculated using:

$$\dot{W}_{\Delta p,t} = \sum_{f=1}^{N_{fp}} \left[\dot{m}_{HC,t,f} \sum_{i=1}^{N_{HC,t,f}} \frac{\Delta p_{t,f,i}}{\rho_{HC,t,f,i}} \right] \quad (4\text{-}28)$$

where $N_{HC,f}$ is the number of HC elements in the flow-path f. $M_{1,t}$ is then evaluated using:

$$M_{1,t} = \frac{\dot{Q}_{abs,net,t}\left(1 - T_{amb}/T_{HC,out}\right) - \dot{W}_{\Delta p,t}}{\dot{Q}_{con,t}} \quad (4\text{-}29)$$

The overall M_1 objective metric is finally evaluated using the Gaussian quadrature weights:

$$M_1 = \frac{\sum_{t=1}^{9} w(t) M_{1,t}}{\sum_{t=1}^{9} w(t)} \quad (4\text{-}30)$$

If any receiver candidate is estimated to convert less than 50% of the incoming radiative power into work on an annual basis, considering the uncertainty of the evaluation: $M_1\left(1 + IC_1\right) < 0.5$, the receiver candidate is discarded from the active population.

The second objective metric is related to the reliability of the receiver. Thermo-mechanical stresses in receiver tubes are related to the incident flux received by the absorber. Researchers from the General Electric company [116] evaluated that a peak flux of 1.8 MW.m^{-2} was acceptable for a tubular receiver using liquid sodium built from Incoloy 800 alloy and assuming a thirty-year design life (11,000 diurnal and ~40,000 cloud transient cycles). In their model, they estimated that the north-facing panels, most exposed to high fluxes, would need to be checked and probably changed every ten years. The Haynes 230 alloy considered here is a stronger alloy that did not exist at the time and is expected to behave at least equally in the context of a liquid sodium receiver. The second objective metric indirectly approximates the reliability of the receiver candidates by estimating the peak absorber incident flux, responsible for the peak tube stress. Using the following equation, the peak flux is transformed into a normalised objective metric to maximise in the optimisation:

$$M_2 = \frac{1}{1 + \max\left(\dot{q}''_{in,i=\{1..N\},t=\{1...9\}}\right) / 10^6} \quad (4\text{-}31)$$

If at any element the flux exceeds the flux limit of 1.8 MW.m^{-2}, considering here again the uncertainty relative to the estimation of the metric, $M_2\left(1 + IC_2\right) < 1/\left(1 + 1.8\right) \approx 0.357$ and the candidate is discarded from the active population.

The third objective metric considered evaluates the mass of tubes used in the receiver design using the overall length of the flow-paths ℓ_{HX} to determine the volume and then the

mass. This mass of tube is an indicator of the cost of the materials needed to build each receiver candidate.

$$m_{HX} = \ell_{HX}\pi\left(r_{HX,ext}^2 - r_{HX,int}^2\right)\rho_{HX} \tag{4-32}$$

The mass of tubes is normalised and converted into an objective to maximise using the following equation:

$$M_3 = \frac{1}{1 + m_{HX}/10,000} \tag{4-33}$$

The receiver mass is divided by 10,000 to provide objective functions with larger variations on the [0,1] interval. In addition to the threshold mentioned, an additional filter was added to avoid numerical errors in the optimisation. This filter identifies when a receiver candidate is unable to operate at the design conditions and consequently the energy balance on it does not compute properly and returns an abnormal negative value in mass flow or error value output from the matrix inversion in the radiosity method. These candidates are immediately discarded it from the overall optimisation routine without going through the whole routine.

4.4.2.2 Geometry evolution

The initial parameter space for the 2D profiles is defined between two radial coordinates and two vertical coordinates to form an annulus of rectangular section. The reduction of the parameter space occurs when new geometries are declared using the data learnt during the optimisation. The modification of the parameter space is illustrated in Figure 4-40. In Figure 4-40 (a), the three geometries declared on the initial parameter space have been evaluated and one of them has been identified as statistically unfit (the red profile) and is discarded. In Figure 4-40 (b), the maximum and minimum coordinates for each of the nodes of the active population geometries are identified. In Figure 4-40 (c), a new parameter space is determined according with the boundaries identified in Figure 4-40 (b). Finally in Figure 4-40 (d), a new geometry is generated. The new geometry is following the exploitation behaviour as defined in the “progression” step of the MOE-PMCE-O algorithm and the new parameter space is therefore used to generate this new profile.

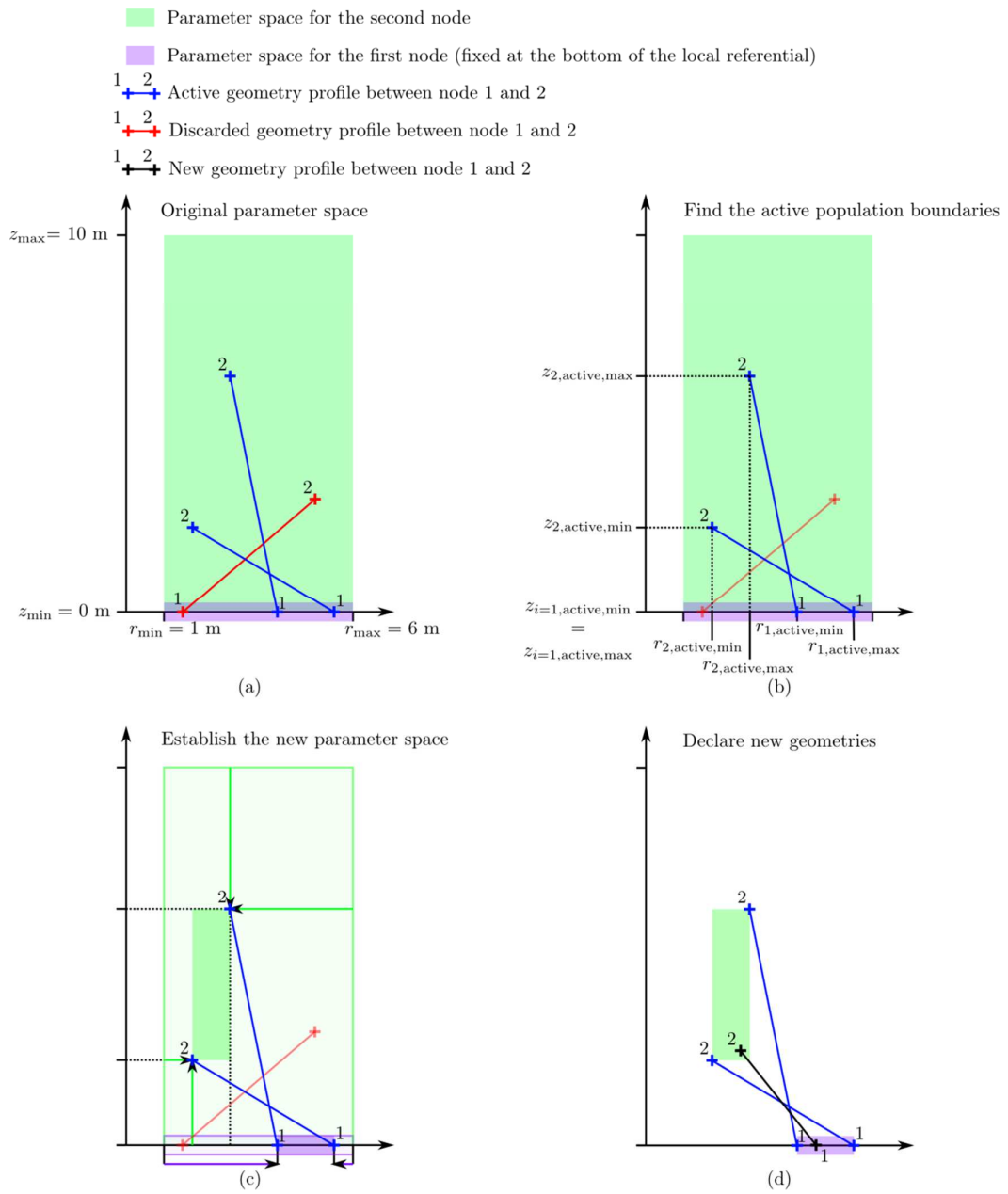

Figure 4-40: Illustration of the geometry evolution heuristic for a population of 3 and geometries composed of 1 section linking two nodes.

4.4.2.3 MOE-PMCE-O parameters

The example presented in this section is a demonstration of the technique and is run on a desktop computer. As a consequence, and in order to keep computational times manageable, the size of the active and final populations is small and the objective precision termination criteria are set relatively high. The optimisation parameters used in this example are summarised in Table 4-7.

Table 4-7: MOE-PMCE-O parameters for the case study.

Active population	Final population	Objectives precision criteria	Objectives thresholds	Exploration threshold
$N_{pop,active}=10$	$N_{pop,final}=10$	$\sigma_{obj}=\{0.01,0.01,0\}$	$\sigma_{t}=\{0.5,0.357,0\}$	$\tau=0.5$

4.4.3 MOE-PMCE-O results

The optimisation run took ~12 hours to complete and evaluated 181 geometries. Each view-factor matrix estimation via MCRT took approximately 2-6 minutes, depending mostly on the number of surface elements in the geometry, making it the overwhelmingly largest contributor in the computational effort.

The final state of the total population is shown in Figure 4-41. The ten blue dots are the receiver members of the final population, the red dots represent candidates that have been evaluated and discarded and the two green dots are candidates that are still statistically good at the end of the optimisation but are not evaluated with enough precision to potentially be in the final population. The threshold limits on the metrics M_1 and M_2 are represented as red planes in 3D and red lines in 2D.

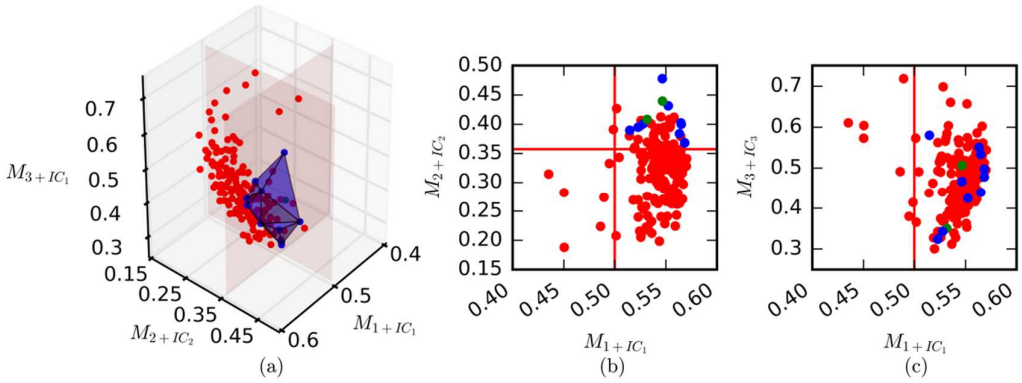

Figure 4-41: Total population best-case scenario performance for the three objective metrics: (a) 3-dimensional representation, (b) projection on the (M_1, M_2) plane and (c) projection on the (M_1, M_3) plane. The values for each candidate are the best-case scenario performance to be able to compare the values with the objective thresholds as these thresholds apply to the best-case scenario evaluation of the objective metrics as presented in the previous section.

From Figure 4-41(b), the selection pressure imposed by the peak flux threshold (metric M_2) becomes clear as a large number of candidates generated can be found below the horizontal red line.

Table 4-8 shows the performance of the final population on the three objective metrics. The incident flux and temperature distributions on the receivers from the final population at Spring equinox noon (t=5) are presented in Figure 4-43 to 4-45.

The geometries being generated using a random parameters, some unexpected "folds" appear in the final population receivers. The reason why these geometrical artefacts appear in the final population is because they do not cause the geometries found to underperform under the set of objective metrics and precision criteria selected for this optimisation run: the radiative heat is mostly recuperated and convective loss is not large enough to disqualify them on the first metric, it is not affecting the second metric M_2 that looks at peak fluxes and, while it does affect the third one (mass of pipes), no other candidate generated was able to displace them from the final population. The influence of the division in 8 flow paths from top to bottom and the low level of discretisation of the geometry (Figure 4-39) explain the "chessboard" pattern observed on the surface of the receivers.

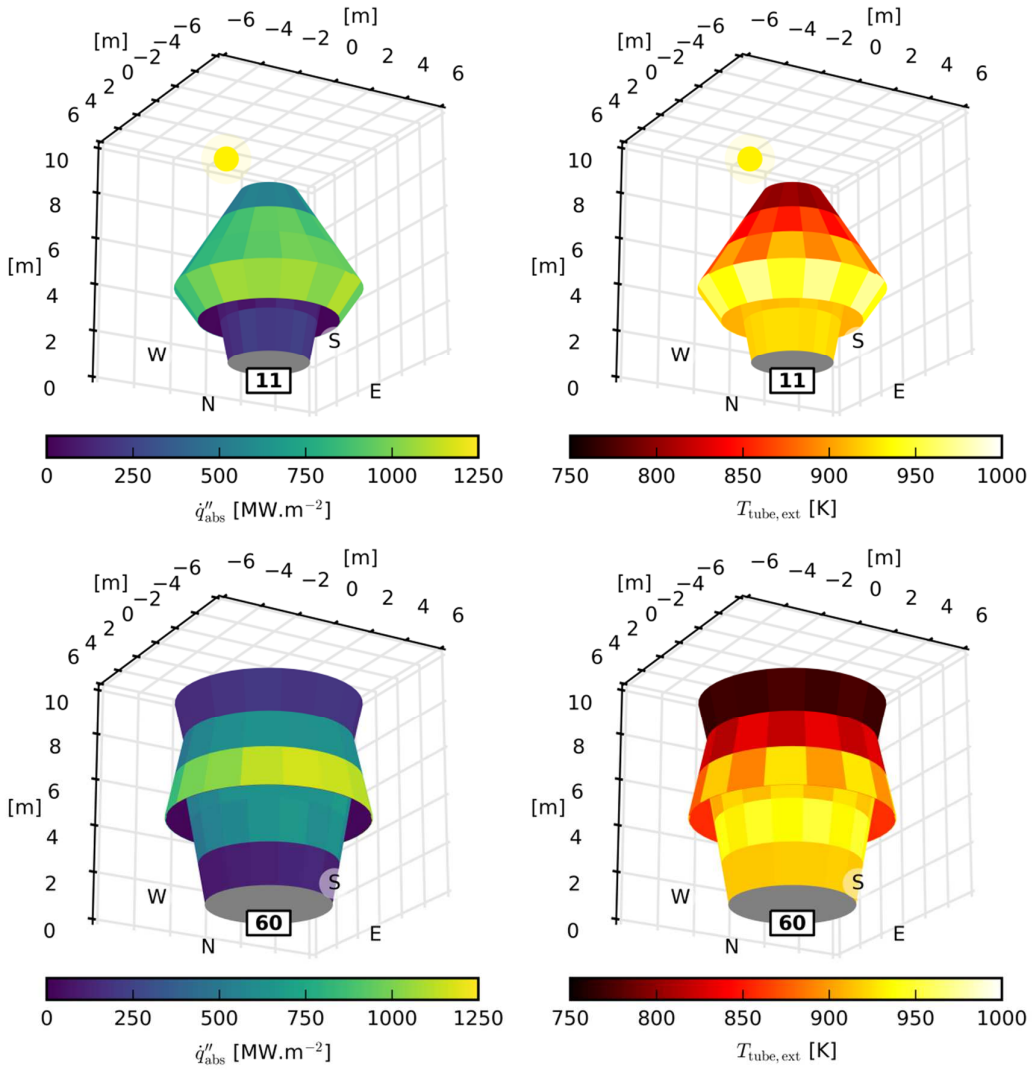

Figure 4-42: Incident flux (left) and temperature (right) distributions for the 10 final candidates at spring equinox noon (t=5)

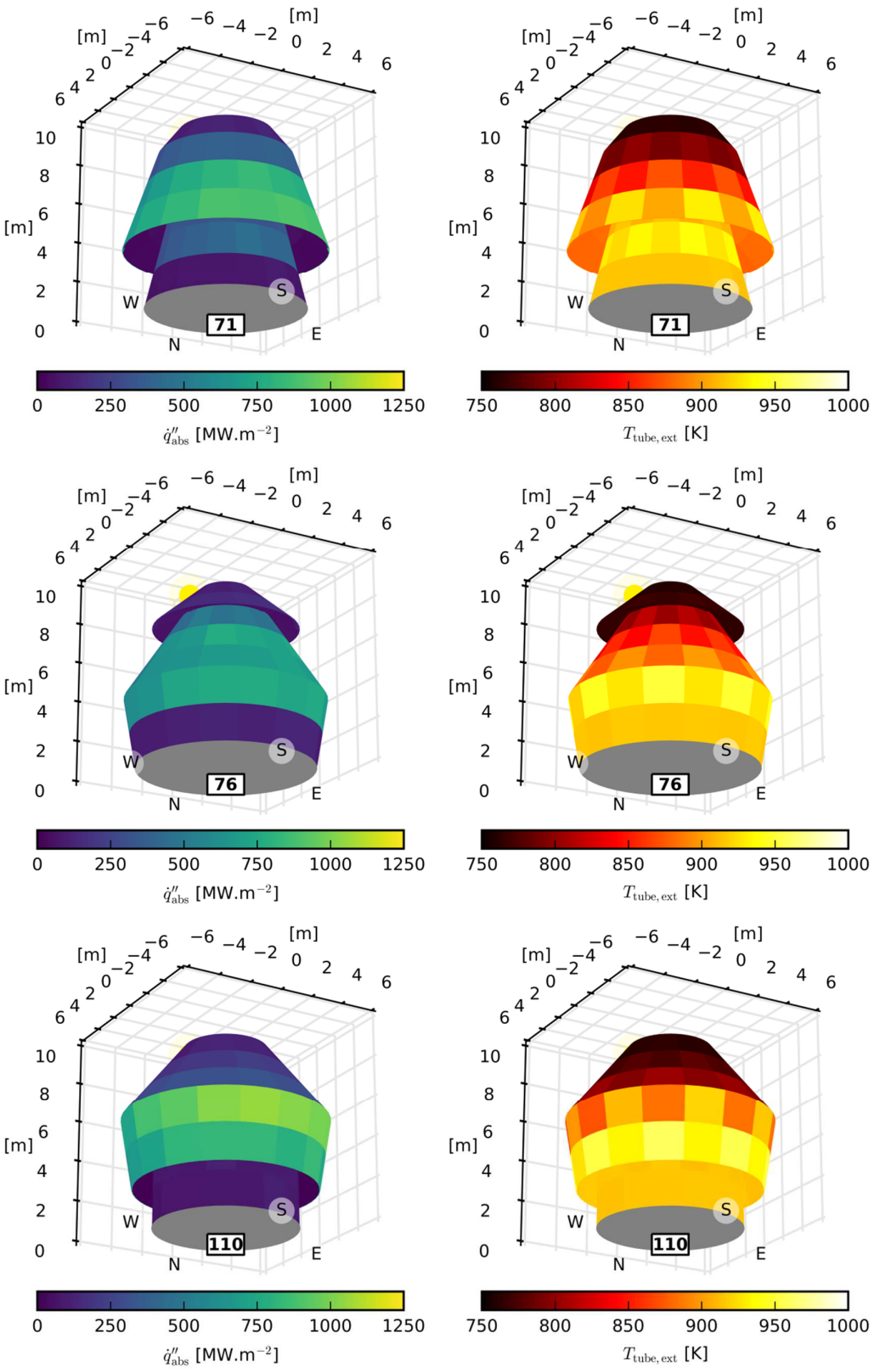

Figure 4-43: Incident flux (left) and temperature (right) distributions for the 10 final candidates at spring equinox noon (*t*=5) (continued)

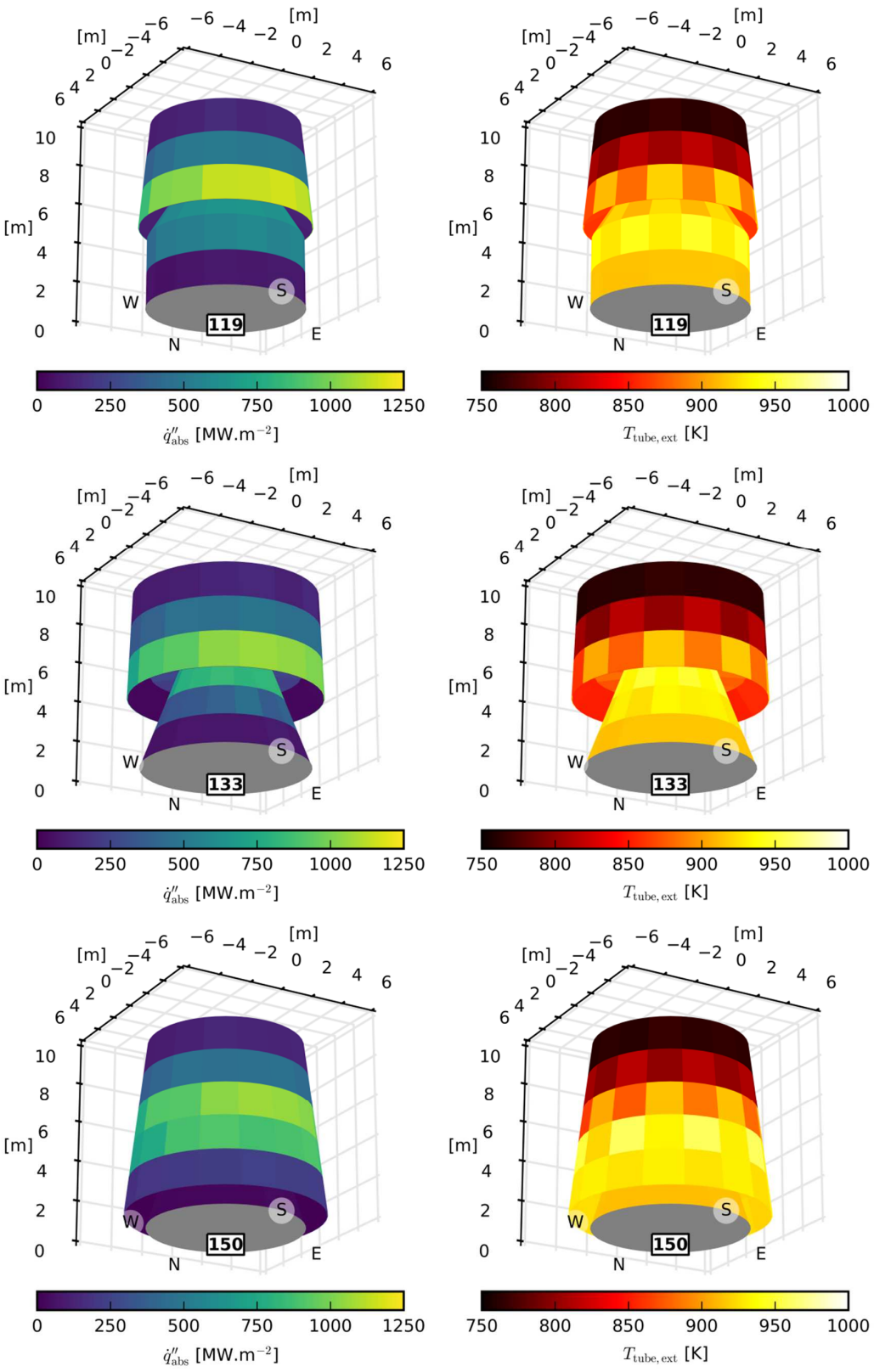

Figure 4-44: Incident flux (left) and temperature (right) distributions for the 10 final candidates at spring equinox noon (*t*=5) (continued)

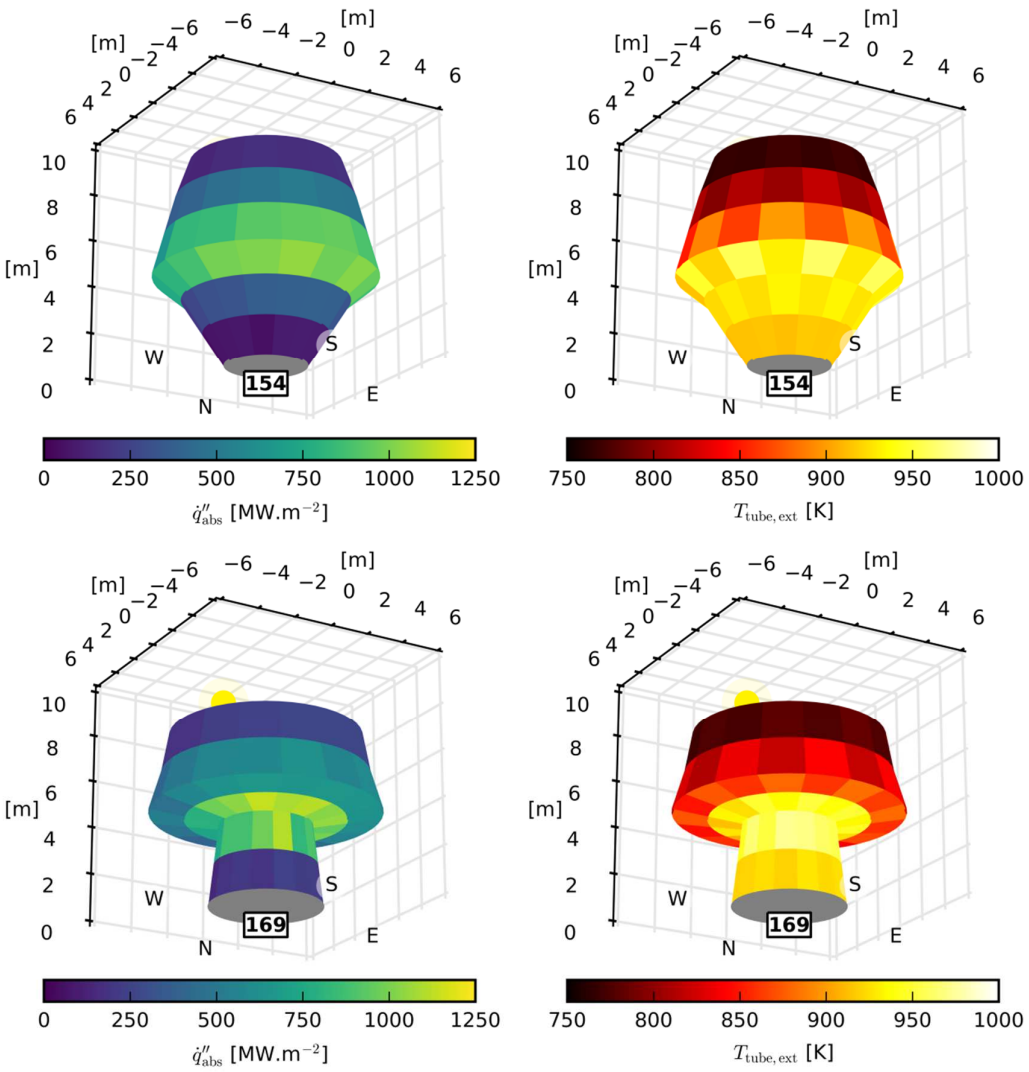

Figure 4-45: Incident flux (left) and temperature (right) distributions for the 10 final candidates at spring equinox noon (t=5) (continued)

The peak fluxes in Table 4-8 are higher than the ones shown in Figure 4-43 to 4-45 because the peak flux occurs at the winter solstice noon sun position (t=2) for all of these geometries due to the specific tower height and heliostat field layout considered.

Table 4-8: Final population performance summary.

Receiver index	M_1	M_2	M_3	Peak flux [MW.m^{-2}]	Mass of tubes [kg]
11	0.515	0.386	0.580	1.592	7,245
60	0.568	0.364	0.497	1.745	10,112
71	0.552	0.428	0.425	1.337	13,542
76	0.546	0.474	0.467	1.112	11,416
110	0.527	0.396	0.343	1.522	19,139
119	0.568	0.365	0.478	1.743	10,934
133	0.565	0.396	0.439	1.524	12,760
150	0.523	0.391	0.324	1.556	20,866
154	0.565	0.399	0.533	1.504	8,749
169	0.563	0.382	0.551	1.619	8,162

From these figures, a few interpretations can be made about the emergence of some specific characteristics in the final population receivers. Two strategies to manage the high incident flux from the heliostat field prevail in the final population:

- The first strategy is to mitigate the incident flux by tilting the receiver surface away from the orientation that maximises the flux. This "spreads" the radiation over a larger surface area which lowers the flux value. Receivers 11, 60, 71, 76, 150 and 154 use this technique by generally tilting the top of the geometry to face upwards. Receivers 154 and 169 do so by tilting the lower part of the geometry to face downwards. This effect is also happening at the centre of the geometry in receivers 71, 119 and 133.
- Alternatively, some receivers intercept radiation at larger radii hence further away from the aiming annulus, which reduces the values of the intercepted flux. Receivers 71, 76, 110, 133, 150 and 154 use this strategy.

A few concepts are present in both categories and use a combination of these strategies. The flux mitigation of the first strategy could still lead to high local peak fluxes on the pipes surfaces as there could be situations where a portion of the cylindrical profile of the pipes faces the incident radiation perpendicularly. This effect is not captured in this model as the pipe bank model is a 1D model that does not consider specific flux distributions around each pipe. The receivers that show the lowest peak flux are 71 and 76 which are the receivers that show are the most tilted upwards of this final population. The first strategy seems to be very efficient at reducing peak flux if used on all the high-flux region of the receiver.

The second strategy seems less effective than the upward tilting and more efficient than downward tilting at reducing the peak flux as in receivers 110, 133, 150 and 154 that have maximum radius similar of higher than 71 and 76 but not as much tilt. In addition, the mass of tubes required for the receivers using this second strategy also tends to be larger than other candidates as their dimensions are larger. On the positive side however, receiver 150 shows a general geometry that is close to the existing state of the art (cylindrical receivers) and a large radius cylindrical receiver would probably, if well dimensioned, perform similarly and present potentially less engineering difficulties than the more complex shapes using the first strategy.

The efficiencies of these receivers at the Spring equinox are presented in Table 4-9. The definitions of these efficiencies are presented in Chapter 2. The final population geometries show a range of performance variations in optical and thermal efficiency, depending on their geometry. The absorption efficiency of the different geometries changes according to the light-trapping performance of the receivers, quantified with the following ratio:

$$\Lambda = \frac{\eta_{abs} - \alpha_{eff}}{1 - \alpha_{eff}} \tag{4-34}$$

that represents the gain in added absorption compared to the purely convex geometry case.

Table 4-9: Efficiencies for the final population candidates at Spring equinox noon (*t*=5).

Receiver index	11	60	71	76	110	119	133	150	154	169
Intercept efficiency, η_{int}	0.904	0.991	0.989	0.974	0.988	0.996	0.994	0.997	0.992	0.966
Absorption efficiency, η_{abs}	0.941	0.947	0.949	0.946	0.941	0.950	0.954	0.940	0.940	0.949
Heat-exchanger efficiency, η_{hx}	0.913	0.901	0.876	0.883	0.842	0.893	0.886	0.827	0.899	0.914
Optical efficiency, η_{opt}	0.850	0.939	0.938	0.922	0.930	0.946	0.948	0.937	0.933	0.917
Thermal efficiency, η_{th}	0.859	0.853	0.831	0.835	0.793	0.848	0.846	0.778	0.845	0.867
Receiver efficiency, η_{rec}	0.777	0.846	0.822	0.814	0.783	0.845	0.840	0.776	0.839	0.838
Light trapping, Λ	0.018	0.118	0.150	0.104	0.023	0.159	0.236	0.006	0.003	0.143

The intercept efficiency varies significantly between the final receivers; as shown by the spillage values in Figure 4-46. Receiver 11 shows a large amount of spillage but has the smallest mass of tubes.

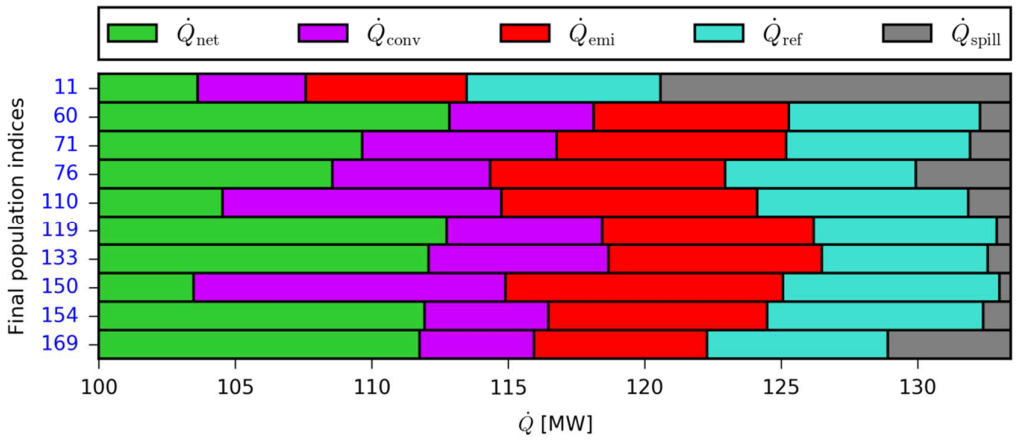

Figure 4-46: Energy Balance for the receiver candidates evaluated in the final population at Spring equinox (*t*=5).

Receivers 11, 110, 150 and 154 have a very low level of light trapping and their absorption efficiency is very close to the effective absorptivity of coated bank of tubes, $\alpha_{eff} = 0.94$.

The rest of the receivers show some level of light trapping caused by non-convex geometrical features in the region hit by the incoming radiation. This effect is particularly pronounced in receiver 133 that geometrically captures 23.6% of the light reflected after the

first bounce on the surface, thanks to a geometry that “wraps around” the incoming flux direction. In receiver 119, a small rift in the surface of the receiver, positioned right on the region of highest intensity, acts both as a peak flux mitigation and significant contributor to light trapping with 15.9% of light trapping.

The heat exchanger efficiency summarises how well the absorbed energy is transferred to the liquid sodium. The worst performing receivers in that regard are 110 and 150, due to very large convective losses as shown in Figure 4-46. These losses, however, are caused by the very large surface areas added to the receiver by the section that are folded inside as shown in Figure 4-47.

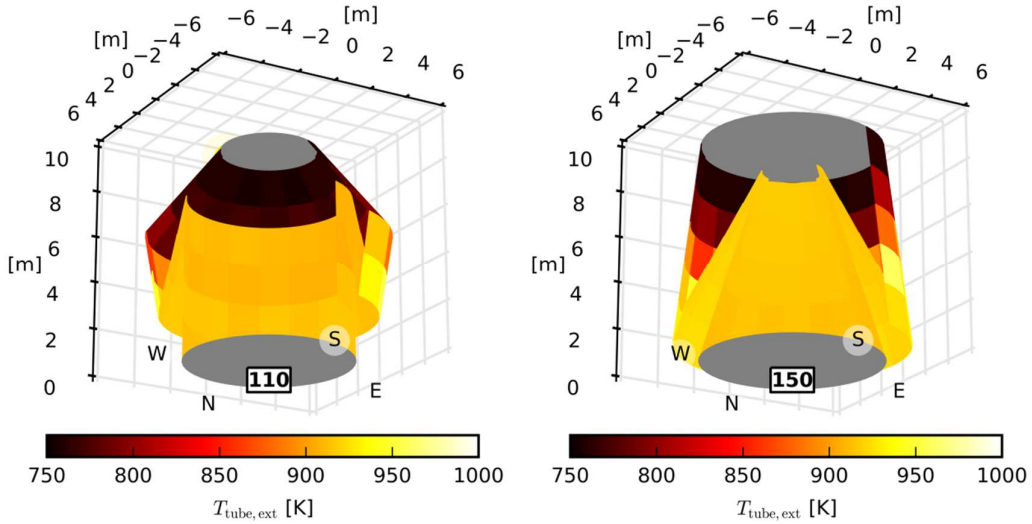

Figure 4-47: Cross section of receiver 110 and 150 showing the large "folded-in" hot sections responsible for large convective heat losses.

For the rest of the receivers, the convective heat loss is the smallest heat loss mechanism. It is important to note that the convective heat loss model in this study is very simple and most probably overestimates the losses, particularly in geometries that have geometrical features that would disturb upward buoyant flows and where, in the light of the work developed for the SG4 receiver development, natural convection should be mitigated and heat recuperation can occur through the appearance of stratification and stagnation zones. This convective loss mitigation should particularly occur for receivers 60, 71, 119, 133 and 169.

The geometry of the receivers influences the location of the distribution of the absorbed flux and the temperature distribution. Receiver 169 seems to have more intense incident flux on hotter regions than receiver 119 for example. The match between the absorbed flux distribution and the temperature is found to be related to the heat-exchanger efficiency. To quantify this aspect, the temperature-averaged absorbed flux is introduced:

$$\dot{q}''_{\text{abs},\hat{T}} = \frac{\sum_{i=1}^{N} T_{\text{tube,ext},i}\dot{q}_{\text{abs},i}}{\sum_{i=1}^{N} T_{\text{tube,ext},i}A_i} \tag{4-35}$$

This temperature-averaged flux assigns higher weight to flux values for surface elements with higher absorber temperature, a higher average therefore indicates receivers where the flux is generally absorbed at higher temperatures. $\dot{q}''_{\text{abs},\hat{T}}$ is plotted against the heat exchanger efficiencies in Figure 4-48 and reveals a clear trend on the final population receivers: the heat exchanger efficiency is higher when more energy is absorbed on the hotter regions of the receiver.

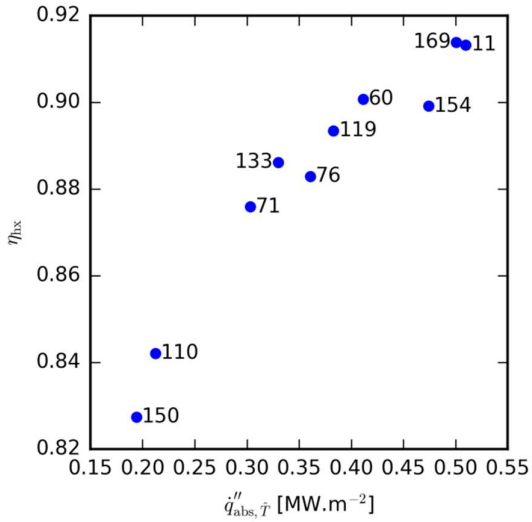

Figure 4-48: Heat exchanger efficiency as a function of the temperature averaged absorbed flux on the final candidate receivers.

Added to this general trend, the heat exchanger efficiency is influenced by the geometry via the thermal emissions behaviour. The fraction of the absorbed flux that is lost via thermal emissions is given in Table 4-10 and illustrates the performance differences between the receivers.

Table 4-10: Thermal emissions fraction of the absorbed energy for the final population.

Receiver index	11	60	71	76	110	119	133	150	154	169
Surface area [m^2]	223	310	416	350	587	335	391	640	268	250
$\dot{Q}_{\text{emi}}/\dot{Q}_{\text{abs}}$	5.2%	5.7%	6.7%	7.0%	7.5%	6.1%	6.2%	8.1%	6.4%	5.2%

The first effect that can be observed is that a smaller surface area tends to encourage lower thermal emission losses; at the expense of significant added spillage in receiver 11. The second effect that influences the emission loss is the cavity effect: the absorption of thermal emission from each receiver surface element by other receiver surfaces. Figure 4-49 and Figure

4-50 illustrate the differences between the geometries in the final population in terms of local thermal emission.

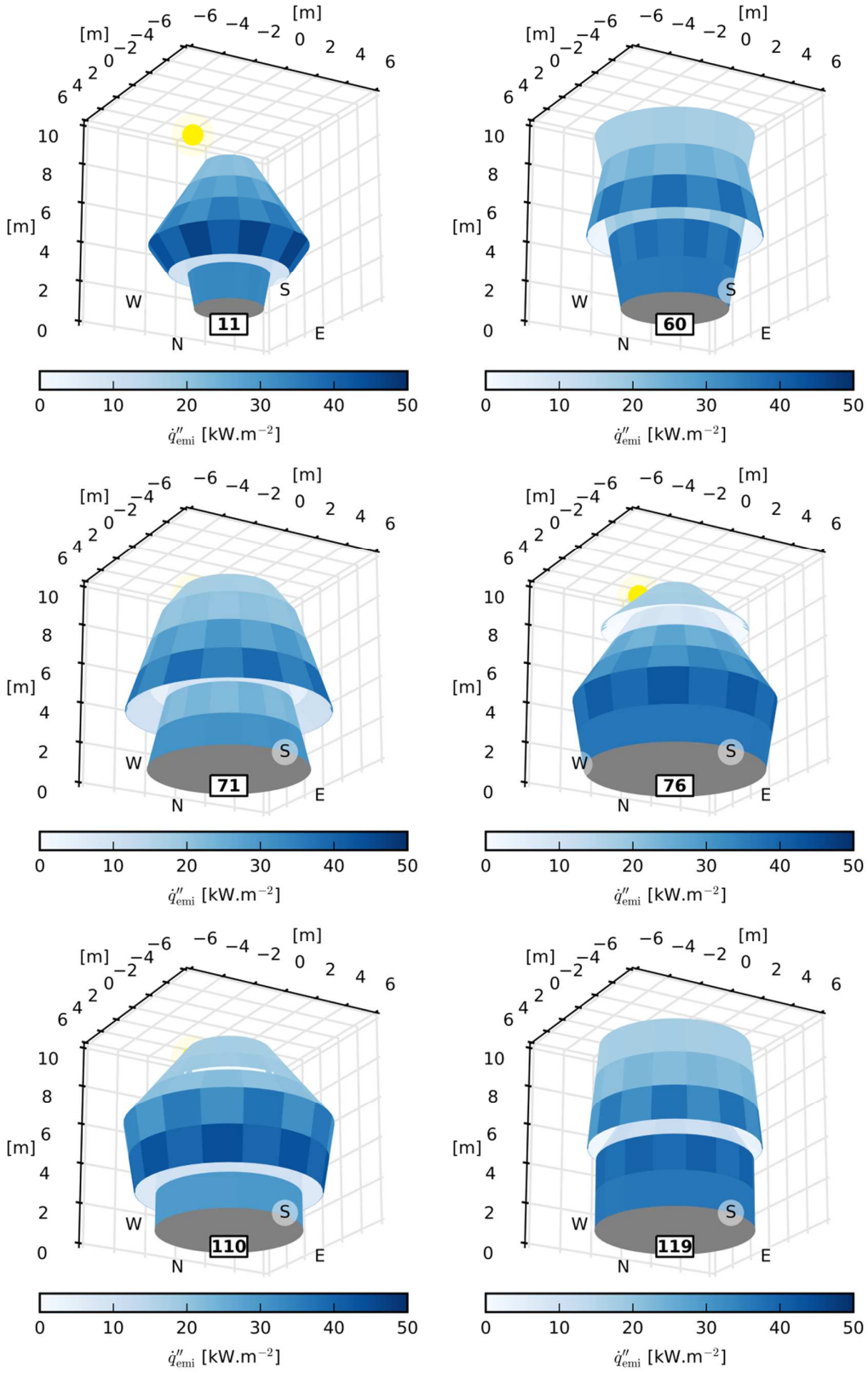

Figure 4-49: Net thermal emission flux from the final population.

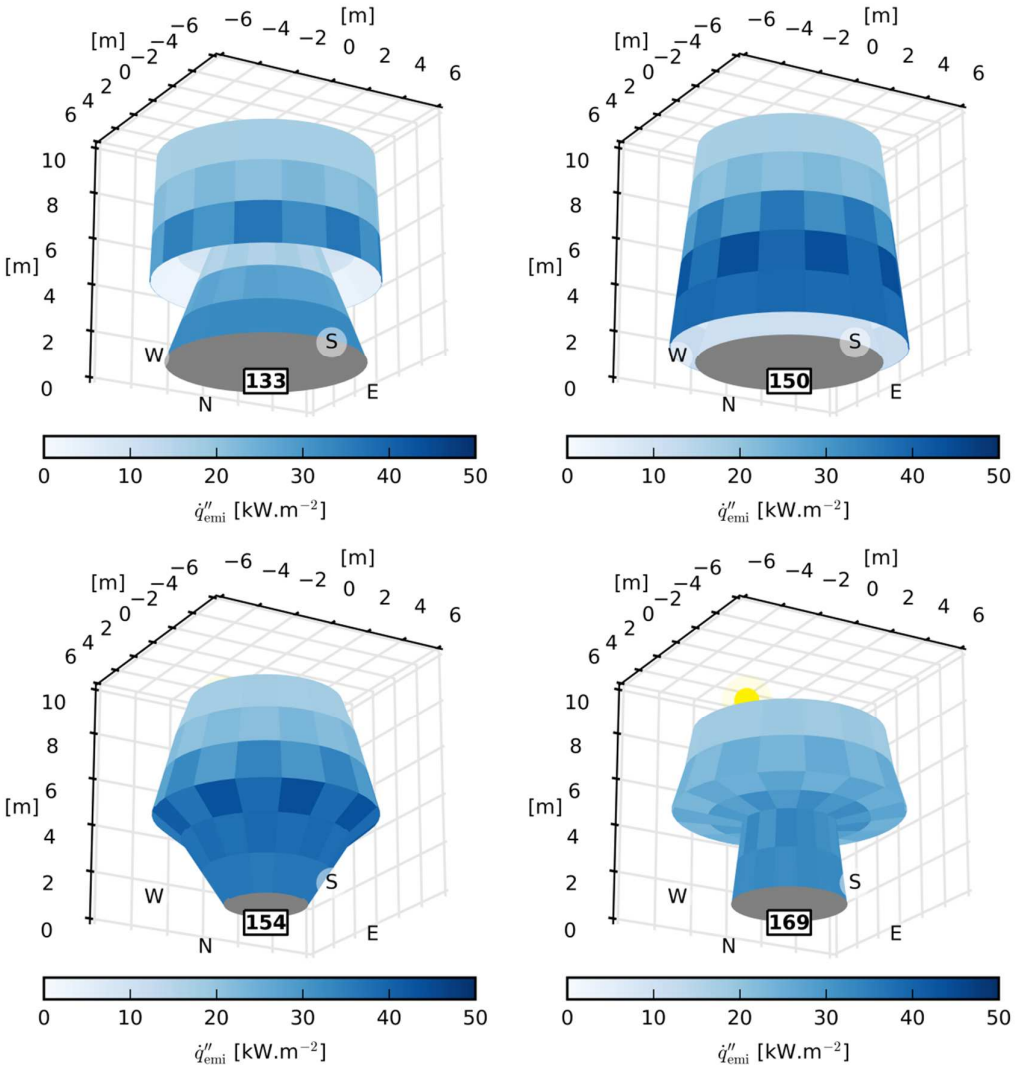

Figure 4-50: Net thermal emission flux from the final population (continued).

When the hot regions of the receivers have some view factors to the rest of the geometry, the local flux thermal emission flux is lower. Thanks to a strong cavity effect, receiver 169 has comparable emission losses with receiver 11, while having about one third of the spillage of the latter. Similarly, 60, 119 and 133 also have a good management of thermal emission losses. Receiver 154, with very little cavity effect, still performs well in overall efficiency due to a relatively small size combined with good intercept efficiency.

Overall, receiver 60, 119, 133, 154 and 169 are the most efficient of this final population. 133 and 154 have lower peak flux than the rest of these efficient receivers however, 133 uses 4 more tonnes of steel (+46% of mass) which would impact the decision on a final receiver geometry. Receiver 169 has a higher spillage than the rest of the efficient receivers, but has the highest thermal efficiency and a refined design of this concept could be interesting. The analysis of these optimised receivers gives a good insight into the important trade-offs in high-

temperature receivers and a final design would include aspects from all of the identified candidates. These unrefined designs have a receiver efficiency of ~84% which compares relatively well with the ~86% of the reference molten salts case presented in chapter 3. When factoring-in the Carnot efficiency and pressure drops, as in the first objective metric, these efficient receivers have M_1>0.56, much higher than the 0.3 value found for the reference receiver in the previous chapter.

Interestingly, the MOE-PMCE-O proved able to find geometries that are efficient and respect a maximum flux threshold with a simple and fixed annular aiming strategy. The impact of the temperature at which the flux is absorbed on the receiver overall efficiency is an added motivation to look at non-conventional geometries. This particular point is one that motivates the research developed in the next chapter that investigates the relation between geometrical parameters of optical concentrators and the quantity of useful work that can be converted by CSP systems.

4.5 Conclusions on receiver optimisation

In this chapter, two stochastic modelling techniques dedicated to stochastic optimisation have been presented and applied to receiver optimisation case studies. The first one, PMCE, is an evaluation technique that reduces the computational effort spent on MCRT in stochastic optimisation problems through the identification of the candidates that are competing to be optimal candidates in the population according to a single optimisation metric. The second contribution, MOE-PMCE-O is an optimisation method that includes an improved version of PMCE, adapted to constrained and multi-objective optimisation problems and in which the original population is small and evolves with added candidates during the optimisation.

Using a two-step optimisation method, the first of which includes PMCE in a random search algorithm, a new receiver design for the SG4 dish was established. PMCE demonstrated significant computational effort reduction in this problem compared to traditional parametric studies.

The application of MOE-PMCE-O to the optimisation of a receiver design for a surround field configuration was presented in a second case study. The method was used over a relatively unconstrained parameter space and with a relatively large precision criterion to provide geometrical exploration for receiver concept generation and provided insights into geometrical features that can benefit high-temperature receivers.

To the knowledge of the author of this work, it is the first application of a simulation-optimisation method to optimise the geometry of solar tower receivers using MCRT for the

simulation of the radiative component. The algorithm presented enables unsupervised optimisation of complex problems evaluated through statistical integration methods which are present in many research fields (eg. physics, information theory, signal processing, finance, cryptography). The possibilities offered by the MOE-PMCE-O are multiple:

- The method is derivative-free, enabling the evaluation of any optimisation metric.
- The case study presented in this work is a geometrical exploration; however, design refinement by setting the parameter space in a much more constrained manner around each geometrical node is a readily available application of MOE-PMCE-O.
- Interactive optimisation, where temporary results are interpreted externally and new, human-designed candidates introduced in the algorithm, are possible. This is particularly interesting in a design project situation where the different iterations of a concepts design can be tested through the method at each step, as it was the case in the USASEC project.

The current implementation of MOE-PMCE-O is not without caveats:

- The Pareto front is approximated using a convex hull algorithm. In future developments, this will be changed by replacing convex hull approximation with a more rigorous non-dominated sorting routine and therefore evaluate non-convex sets of objective metrics.
- The machine-learning aspect of the method is early-stage and consequently the method convergence and progression is slow. There are many candidate machine-learning methods that can be inserted in the progression step of the routine to improve it such as Artificial Neural Networks, Reinforcement Learning and meta-heuristics (genetic algorithms, particle swarm algorithms, simulated annealing, tabu search, etc.). Considering the large amount of data generated during the process, it is expected that the use of these methods would bring interesting capabilities and performance gains to MOE-PMCE-O.

The view-factor simulation algorithm represents most of the runtime of the optimisation method and is a real bottleneck in the context of non-convex receiver design geometries. There are potential solutions to mitigate this issue. The first solution is to use faster methods to generate the view-factors matrices such as analytical integration methods when possible [42] or pseudo/approximate Monte-Carlo approaches. Another solution is to use a “full Monte-Carlo” approach where the thermal emissions are simulated through ray-tracing at each step instead of being evaluated using the radiosity method. While this could speed-up the initialisation of each candidate geometry, there is a risk to slow down the convergence rate of

the objectives significantly. Finally, a hybrid method is possible where the view-factors matrix is first initialised with coarse precision and then updated during the optimisation when the uncertainty of the result becomes strongly dependent on this source of uncertainty.

Overall, the methods and case studies presented in this chapter demonstrate the possibility and potential of the geometrical optimisation of receiver design.

5 Applied exergy analysis in CSP

Exergy is the fraction of an energy quantity that can ultimately be converted into useful work. In solar thermal receivers, the exergy that is added to the heat carrier by conversion of the incident radiation into heat can be evaluated using a receiver model and traditional flow exergy methods [119]. The overall efficiency of the receiver in converting radiation into heat is dependent on the flux distribution on the receiver surface, which is in turn dependent on the concentrator design and properties. As a consequence, the exergy that is extracted by the receiver is dependent on the concentrator properties and the maximum exergy that can be extracted by the system is affected by the concentration process, before the absorption of the concentrated radiation by the receiver. To quantify the exergy loss during the concentration process requires an analysis of the exergy of radiation in between the source and the receiver.

In this chapter, the exergy loss caused by the concentrator subsystem is analysed with two objectives in mind:

- To understand the upper limit of the conversion of concentrated radiation into work by receivers.
- To be able to evaluate the consequences of concentrator properties on the work output of a concentrated solar system and therefore evaluate how critical some of the concentrator properties are in comparison with other parameters of the system.

Parts of this chapter are in publication (a) of the initial list of publications (p. ix). This chapter was submitted for review in the Applied Energy journal in January 2017.

5.1 The exergy of radiation

5.1.1 Historical development and controversies

The exergy of radiation has been independently established by Petela [114], Landsberg and Tonge [85] and Press [117], setting the upper bound for the conversion of radiative energy into work. The expression in Eq. 5-1 will be labelled the Petela equation, because of Petela being historically the first to derive it.

$$\gamma_{\mathrm{P}}\left(T_0, T_{\mathrm{b}}\right) = 1 - \frac{4}{3}\frac{T_0}{T_{\mathrm{b}}} + \frac{1}{3}\left(\frac{T_0}{T_{\mathrm{b}}}\right)^4 \tag{5-1}$$

with T_0 the temperature of the sink and the T_{b} temperature of a black-body source of radiation. Gribik and Osterle [50] supported a different formulation of the exergy of radiation

first proposed by Spanner as an approximation [139], and so did Jeter [67]. De Vos, Jeter and Gibrik, in De Vos and Pauwels [35], then discussed these results comparing the three available formulations at that time for exergy efficiency. Without agreeing completely they provide valuable insight into the intricacies of the thermodynamic derivation of radiation exergy. In this previous discussion, De Vos and Pauwels interestingly insist on the difference between the ideal conversion efficiency and maximum potential work output obtainable from a radiative energy source, thus discarding the possibility that the ultimate exergy content of radiative energy is equal to the Carnot efficiency as suggested by Jeter for real systems. Similarly, Bejan discussed three competing exergy efficiency formulations to highlight their limitations and underlying hypotheses [12]. He particularly focused on the thermodynamic system boundary definition which explains most of the discrepancies found in the literature: some authors study the exergy of radiation in an enclosed reversible system while others focus on an open system approach, more adapted to solar energy engineering.

Müser, followed by Castañs and De Vos, proposed a way to decouple the absorption process and the thermodynamic conversion process in photo-thermal systems, of direct relevance to CSP, leading to a simple and useful expression for solar engineering [23, 33].

More recently, Candau provided a demonstration of the radiation exergy formula proposed earlier and independently by Petela, Landsberg and Press using elementary thermodynamics [22]. Additionally, Candau provided formulations of non-blackbody radiation exergy and a demonstration of the Clausius law, interestingly linking the second law of thermodynamics to fundamental optics laws using only classical thermodynamics considerations.

5.1.2 Exergy-to-energy ratio of radiation

In designing and optimising devices that convert solar radiation into useful work, an important problem is how to estimate the maximum output achievable by such devices. This requires us to be able to estimate the exergy which is carried by the solar radiation, and how that exergy is affected by the various design parameters as the radiation passes through the device. This exergy content of radiation can be evaluated in a relative form using γ, the exergy-to-energy ratio defined as:

$$\gamma = \frac{\dot{W}''}{\dot{E}''} \tag{5-2}$$

where $\dot{W}''$ is the local work flux and $\dot{E}''$ the local energy flux. Selected results are summarised below, considering the case of unpolarised light only.

The Petela equation can be derived from the radiation pressure, energy and entropy within the cavity, together with the usual definition of exergy in a closed system. Calculated using Eq. 5-1, the exergy-to-energy ratio of extra-terrestrial (undiluted) solar energy is $\gamma = 0.93$ [117] ($T_b = 5800$ K, $T_0 = 300$ K).

Black-body radiation can be diluted either reversibly, such as when it spreads from a source and moves through space undisturbed, or irreversibly, such as when it is scattered as it travels through a participating medium or non-ideally emitted or reflected from 'real' surfaces [85, 86, 109, 111, 117, 150]. The local fluxes of energy $\dot{E}''$ and entropy $\dot{S}''$ of diluted black body radiation passing through an elemental area dA can be determined in general by integrating the incident radiation over solid angle and wavelength. A useful specific case for diluted black-body radiation is that of a Lambertian source providing uniform flux within a solid angle ω as seen from dA, with grey (spectrally uniform) dilution. In this case, the local fluxes of energy and entropy are:

$$\dot{E}'' = \frac{B}{\pi} \delta \sigma T_b^4 \tag{5-3}$$

$$\dot{S}'' = \frac{4}{3} \chi(\delta) \frac{\dot{E}''}{T_b} \tag{5-4}$$

where B is the geometric factor relating to the angular distribution of the incident rays, δ is the dilution factor relating to the loss of flux which has occurred due processes such as scatting or partial absorption and $\chi(\delta)$ is the entropy irreversibility factor, a function only of the dilution factor [155]. The geometric factor B:

$$B = \int_{\omega} \cos(\theta) \, d\omega \tag{5-5}$$

is obtained at dA by integrating the angle θ between the incident rays and the normal to dA over the range of incident solid angles. When the radiation passing through the elemental area dA occupies the entire hemisphere, the value of B is found to equal π. When the remote source subtends a solid angle ω originating from a circular isotropic radiation source centred on an axis normal to dA, the geometric factor can be shown to be [23, 83, 86]

$$B = \omega \left(1 - \frac{\omega}{4\pi} \right) = \pi^2 \sin^2(\theta_s) \tag{5-6}$$

where θ_s is the incident cone half-angle and is related to ω.

Landsberg and Tonge [85] found that for fully direct or fully diffuse diluted black-body radiation, an accurate approximation to the exergy to energy ratio (valid for $\delta > 10^{-4}$) is

obtained by using the Petela equation but with an effective temperature T_e substituted for the black body source temperature T_b:

$$T_e = \frac{T_b}{\chi(\delta)} \tag{5-7}$$

$$\gamma \approx \gamma_P(T_0, T_e) \quad \text{for } \delta > 10^{-4} \tag{5-8}$$

At least three equations have been advanced that explicitly seek to incorporate the angular distribution of the radiation incident at dA into the equation for γ: the equation of Parrott [109], still sometimes used, was retracted [111, 150]; the 'arbitrary radiation' equation of Petela [113] was refuted [85] for omitting $\chi(\delta)$; and the equation of Press [117, 151] can be seen to be a less accurate approximation to Eq. 5-7, using $\chi(\delta) \approx 0.9652 - 0.2777\ln(\delta)$ instead of $\chi(\delta) \approx 0.9652 - 0.2777\ln(\delta) + 0.0511\delta$.

Most studies considered the case of isotropic angular distribution radiation within a solid angle ω. However, Landsberg and Badescu [84] calculated a shape factor for the solar disc which included the effect of limb darkening, demonstrating that the formulation of the previous equations with B, δ and $\chi(\delta)$ could potentially be further generalised. Other studies considered the exergy of sunlight with direct and diffuse fractions [85] as two separate isotropic regions. There have not been any studies that seek to treat the exergy of reflected and concentrated sunlight with a realistic angular distribution. Regarding spectral effects, some studies have considered the exergy of arbitrary incident radiation spectra [22, 34, 153]. The present study, however, is limited to considering 'grey' distributions where the dilution factor is spectrally uniform.

Another approach to quantifying the exergy of radiation involves modelling it as two-step process, where the radiation arrives as a radiative energy flux $\dot{E}''$ which is absorbed as heat on an ideal black-body absorber at temperature T and suffers unavoidable losses, here considered only due to re-emission $\dot{E}''_{emi} = \sigma T^4$, and then converted to work per unit area $\dot{W}''$ in a reversible heat engine [7, 23, 86]. $\dot{W}''$ can then be expressed as the product of the net absorbed heat multiplied by the Carnot efficiency, resulting in the exergy-to-energy ratio for absorbed heat:

$$\gamma = \left(1 - \frac{\dot{E}''_{emi}}{\dot{E}''}\right)\left(1 - \frac{T_0}{T}\right) \tag{5-9}$$

The value of γ can then be maximised by solving $d\gamma/dT = 0$ for the optimal absorber temperature $T = T_{opt}$, solved numerically. Landsberg and Tonge [86] used this approach to

determine a maximum exergy-to-energy ratio of $\gamma = 0.8$ for a terrestrial solar-thermal receiver under 1000 suns of concentration, which was found with $T_{\text{opt}} = 1100$ K. Castañs et al. [23] used a similar approach to obtain a higher value $\gamma = 0.849$ using undiluted black body radiation at 5760 K as a source. Badescu [7] also used Eq. 5-9 to assert a revised exergy of diluted black body radiation,

$$\gamma \approx \gamma_{\text{P}}\left(T_0, T_{\text{b}}\sqrt[4]{\frac{B\delta}{\pi}}\right) \tag{5-10}$$

This equation results in much lower efficiencies for terrestrial radiation: for example, using $B\delta/\pi = 2.16\times10^{-5}$ [87], gives $\gamma = 0.097$. This result includes the effect of re-emission losses from the absorber when exposed to low irradiance, and discounts the possibility of further concentration. The result is also claimed only to be an upper bound for γ of Eq. 5-9, rather than an exact result.

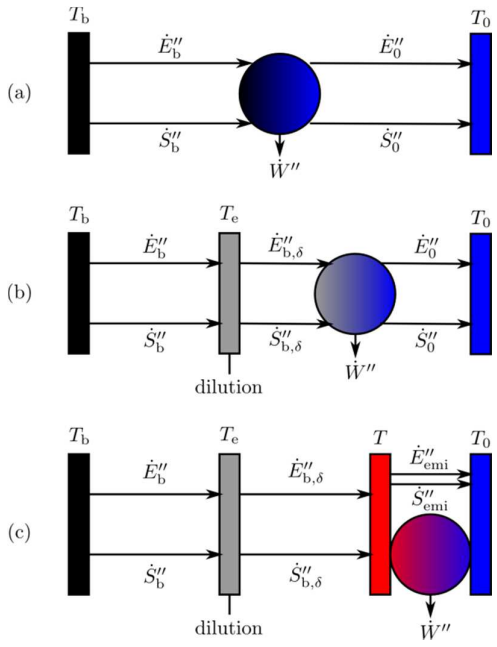

Figure 5-1. Conversion of radiation into work following (a) Eq. 5-1, (b) Eq. 5-8 and (c) Eq. 5-9.

Figure 5-1 aims to clarify the distinctions between the approaches above. Eq. 5-1, illustrated in Figure 5-1 (a), quantifies the exergy carried by incident black-body radiation; Eq. 5-8, illustrated in Figure 5-1 (b), is the same but for isotropic diluted radiation; Eq. 5-9, illustrated in Figure 5-1 (c), gives the actual value of $\dot{W}''$ for an assumed absorber temperature T, which can then be optimised as by Landsberg, allowing for 'inevitable' thermal losses $\dot{E}''_{\text{emi}}$. Eq. 5-10 is an upper bound to Eq. 5-9 assuming that $T = T_{\text{b}}\sqrt[4]{B\delta/\pi}$.

The value of the exergy-to-energy ratio γ of radiation itself should really be an intrinsic value; it should not be possible for the calculated value of exergy of radiation to *increase*, for

example by directing the radiation onto a focussing mirror, as can occur when using Eq. 5-9 [23, 91]. Hence Eq. 5-8 is a superior measure of γ for the local exergy of radiation, albeit limited to the case of isotropic radiation. Sun shape, imperfect mirrors, atmospheric attenuation and other factors will dilute the radiation and reduce the work that can be extracted even when it is optimally re-concentrated. It remains a challenge to calculate the variations in γ along a light-path in general and to properly account for the different irreversibilities. It is clear, however, that once radiation has been converted to heat, no further concentration is possible, and so Eq. 5-9 becomes entirely accurate as an estimate of the exergy of the radiation if it is to be converted to work via heat at that point.

5.1.3 Non-isothermal receivers

The spatial distribution of the radiation is modified as it propagates through the optical concentration process of a CSP system. This change in spatial distribution is expected to have an impact on the exergy content of the radiation reaching the receiver.

Ries et al [124] established that when local receiver temperatures are allowed to vary in response to the incident flux, significantly higher overall receiver efficiency is possible. However, this effect has not been considered in greater detail in the context of realistic concentrators with imperfections. Kribus et al [82] used this to develop a multi-cavity receiver using different isothermal regions for different levels of flux with success. Aside from adapting temperature profiles for thermodynamic optimisation, temperature profiles are often dictated by limits in the working fluid and containment materials, and such limits need to be included in the analysis. The high efficiency of non-isothermal receivers was demonstrated experimentally [120]. By confining high-temperature regions to those where the flux is highest, an experimental receiver energy efficiency (concentrated radiation to working-fluid enthalpy) of 97% at >500°C was demonstrated. This high efficiency depended on absorbing low-flux irradiance at low temperature, and high at high, as dictated by the optimisation of Eq. 5-9 as described above.

By applying the method presented in this chapter it is possible to quantify the exergy provided by a concentration process and evaluate where most of the distribution of exergy at the focus. This information can then be used to design receivers that harvest this exergy efficiently.

5.2 Dish concentrator exergy model

Among CSP concentrators, dish concentrators are the closest to the ideal point-focus paraboloid and potentially have the highest optical efficiency of all types [152]. In this study, the choice was made to consider only dish concentrators for simplicity: it is a concentrator

whose geometry and performance are independent of the sun position, in contrast to Fresnel based systems (heliostat fields and linear Fresnel concentrators) or single axis tracking trough concentrators. The analysis approach here, however, is portable to any other types of solar-thermal concentrator.

5.2.1 Paraboloidal dish model

The concentrator considered is a perfectly-shaped axisymmetric paraboloidal dish concentrator with a flat circular target positioned at the focal plane, and centred orthogonally on the axis. The geometry of the system is shown in Figure 5-2.

The aperture radius of the concentrator has a fixed value of $r_{\text{dish}} = 0.5$ m. The rim angle θ_{rim} is variable to study the effect of geometry changes as presented later. The target is a flat disc of radius r_{t} positioned at the focal length f and large enough to capture all the radiation coming from the dish surface in the simulations. The focal length of the dish is obtained by solving the second degree polynomial in Eq. 5-11 and selecting the positive root:

$$f^2 - f\left(\frac{r_{\text{dish}}}{\tan(\theta_{\text{rim}})}\right) - \frac{r_{\text{dish}}^2}{4} = 0 \tag{5-11}$$

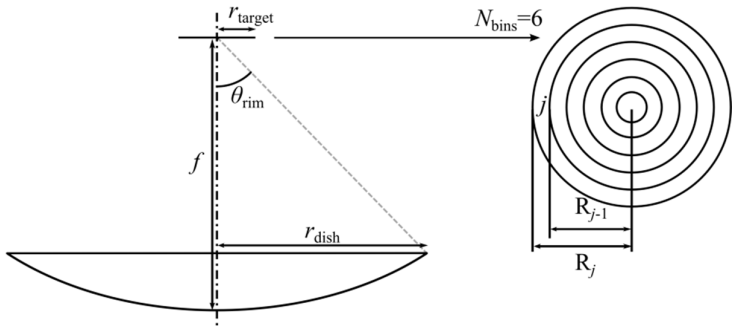

Figure 5-2. Schematic of the dish concentrator (left) and binned focal plane target (right).

The mirrored surface of the dish concentrator is opaque and has grey-body properties with a reflectivity of ρ, also used as a variable in a following section. Thermal emissions from mirror surfaces are assumed negligible. The total energy reflected by the mirror onto the target is $\dot{E}_{\text{tot}} = \rho G \pi r_{\text{dish}}^2$ since the target is large enough to intercept all reflected rays. Reflections are specular but with a Gaussian bivariate slope error distribution [151] with standard deviation σ. The value of σ is varied as a studied parameter.

5.2.2 Source and sunshape models

The source of radiation in the model is the sun. In order to provide a realistic geometrical configuration for the incoming radiative energy, angular distribution of intensity is considered. In the model, the source of radiation is a disc of diameter r_{dish} placed on the

aperture of the concentrator, shading from the focal plane target is consequently ignored here. The radiative flux emanating from the source G is set to 1000 W.m^{-2} and the angular distribution of the radiation intensity is alternatively established according to two different sunshape models, presented in Chapter 2:

- A pillbox "sunshape" source with uniform angular intensity distribution within the interval [0, ϑ_{ar}]. When ϑ_{ar}=0, the rays escape the source as a perfectly parallel beam.
- The "Buie" sunshape model that describes a more realistic angular distribution taking into account the circumsolar ratio (CSR), ratio of radiative energy coming from outside the sun's disc $q''_{S,aureole}$ to the total incoming solar radiation $q''_{S,tot}$ due to atmospheric interactions [21].

5.2.3 Focal plane target model

In order to capture the axisymmetric flux distribution, the focal plane target is divided into $j \in \{1...N_{bins}\}$ concentric rings. The radiative energy $\dot{E}_i$ transported by each traced ray $i \in \{1...N_{rays}\}$ is radially binned using r_i, the radial position of the ray hit location on the target, to an appropriate bin j with inner and outer radii $R_{j,in} < r_i < R_{j,out}$. Fluxes for each bin $\dot{E}''_j$ are determined by dividing the total accumulated ray energy in each bin $\dot{E}_j$ by the annular bin area $A_j = \pi\left(R^2_{j,out} - R^2_{j,in}\right)$. The total focal-plane energy rate is $\dot{E}''_{tot} = \int_A \dot{E}'' dA = \Sigma_{j=1}^{N_{bins}} \dot{E}_j$. The following additional assumptions are applied:

- The target is treated as a perfect black-body absorber. Reflective losses do not occur. This assumption is consistent with a desire to model, as far as possible, the exergy of the radiation rather than the exergy efficiency of a specific receiver design.
- For each bin on the target surface, an independent local temperature T_j is determined through optimisation as described below.
- Local re-emission fluxes are calculated as $\dot{E}''_{emi} = \sigma T_j^4$ on each bin.
- Each bin is perfectly isolated from the others. Any heat transfer between surfaces within the receiver would represent further exergy destruction and so is irrelevant in the estimation of focal-plane exergy.
- Convective and conduction losses are neglected.

The target is a theoretical construct used only to establish the focal plane exergy; it is not intended to be a realistic receiver design. Discretised with a sufficiently large number of radial bins N_{bins}, the continuous result will be approximated with good accuracy.

5.2.4 Focal plane exergy

The exergy transferred to the receiver as heat is calculated locally using Eq 5-9. The local energy-to-exergy ratios γ_j are calculated using the local absorbed radiative flux $\dot{E}_j''$ in each bin from the ray tracing. For each bin, the local temperature $T = T_j$ is optimised for $\dot{E}'' = \dot{E}_j''$ and T_0 by solving the fifth order polynomial in Eq. 5-12 resulting from $d\gamma/dT = 0$.

$$\begin{cases} T_{\text{opt}}\left(\dot{E}'', T_0\right) = T \\ 4T^5 - 3T_0T^5 - \dfrac{\dot{E}''}{\sigma}T_0 = 0 \end{cases} \tag{5-12}$$

The incident flux at the focal plane can be expressed in terms of the local optical concentration ratio C, so $\dot{E}'' = CG$. Results from Eq. 5-9 for a wide range of T and C are shown in Figure 5-3 along with the optimal temperatures $T_{\text{opt}}\left(CG, T_0\right)$ as obtained from Eq. 5-12. Results are calculated for ambient temperature $T_0 = 293.15\ \text{K} = 20\ ^\circ\text{C}$ and direct normal irradiance $G = 1{,}000\ \text{W.m}^{-2}$; these values are kept throughout the rest of the Chapter.

A curve-fit of $T_{\text{opt}}\left(CG, T_0\right)$, valid for $C \in [1, 30000]$, is given by Eq. 5-13, and also overlaid on Figure 5-3. The normalized root-mean-square error of the curve fit in Eq. 5-13 is 0.0016, making it a reasonably good fit under the range of parameters considered.

$$T_{\text{opt}} = T_0 C^{0.1919} \tag{5-13}$$

The values of γ calculated are lower than the exergy of diluted terrestrial radiation from Eq. 5-8, because of the conversion of radiation to heat, but will approach those values at very high concentration ratios.

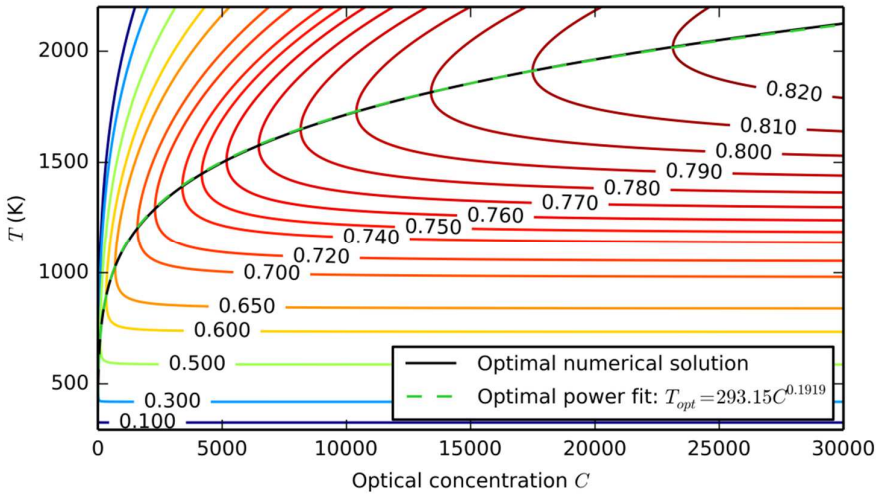

Figure 5-3. Local exergy-to-energy ratio γ (contours) as a function of local optical concentration C and temperature T, with optimal temperatures T_{opt} overlaid. The ambient temperature T_0 is 20°C and direct normal irradiance G is 1000 W.m^{-2}.

The overall exergy-to-energy ratio γ_C for the entire focal plane is defined as an energy-weighted average as shown in Eq. 5-14.

$$\gamma_C = \frac{\dot{W}_{target}}{\dot{E}''_{target}} = \frac{\int_{A_{target}} \gamma \dot{E}'' dA}{\rho G \pi r_{dish}^2} \tag{5-14}$$

Using the axi-symmetrical discretisation scheme presented in Figure 5-2, the numerical approximation is shown in Eq. 5-15:

$$\gamma_C \approx \frac{\sum_{j=1}^{N_{bins}} \gamma_j \dot{E}''_j A_j}{\rho G \pi r_{dish}^2} \tag{5-15}$$

With $\dot{E}''_j = C_j G$, where C_j is the average optical concentration ratio for bin j, this can also be written:

$$\gamma_C \approx \frac{\sum_{j=1}^{N_{bins}} \gamma_j C_j \left(R_j^2 - R_{j-1}^2\right)}{\rho r_{dish}^2} \tag{5-16}$$

With C_j determined from the sum of the energy $\dot{q}_i$ carried by each ray $i = \{1 \ldots N_{rays}\}$ intercepted in the axi-symmetrical bin j:

$$C_j = \frac{\sum_{i=1}^{N_{rays}} \dot{q}_i (r_i)}{\pi \left(R_j^2 - R_{j-1}^2\right) G} \text{ for } R_{j-1} < r_i \leq R_j \tag{5-17}$$

5.3 Dish concentrator exergy analysis

5.3.1 Influence of the sunshape

In this first simulation, the focus is on understanding how the source angular distribution variations influence the exergy output of dish concentrators.

In Figure 5-4, γ is shown for distinct radiative sources with the same perfectly specular and reflective 45° rim angle dish is exposed, no surface slope error is considered at this stage $\left(\rho = 1,\ \theta_{rim} = 40^\circ,\ \sigma = 0\right)$. Figure 5-4 (a) shows the radial variation of γ for three different sunshapes and in Figure 5-4 (b), γ_C, is displayed under a range of circumsolar ratios (CSR).

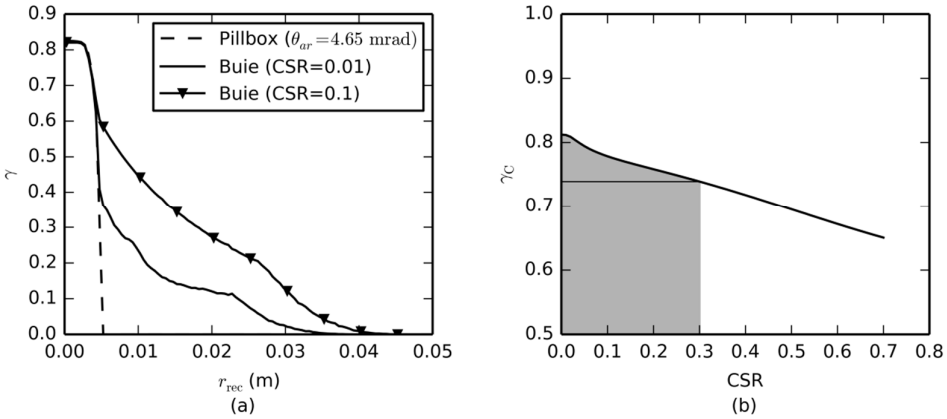

Figure 5-4. (a) Radially resolved exergy-to-energy ratio γ for three different sunshapes and (b) system exergy-to-energy ratio γ_C for Buie sunshapes from 0 to 70% CSR with a typical operational range of 0 to 30% highlighted in grey [15].

The relative influence of the sunshape on the local exergy efficiency at the target surface appears clearly in Figure 5-4 (a): higher values of γ in the central regions where concentration is the highest and gradually less for the less irradiated areas.

The system exergy-to-energy ratio γ_C decreases when the angular spread of the source increases (CSR increases) in Figure 5-4 (b). The exergy-to-energy ratio is locally higher on the outer regions of the target when the source angular range is wider due to an increase in local concentration of the flux. However, some of the flux in the center of the target has moved to the outer regions causing a decrease in overall concentrator exergy-to-energy ratio γ_C.

The sunshape has a relatively strong influence on the exergy available at the target. A clear day would usually be represented by a Buie sunshape with CSR<1% and concentrator exergy-to-energy ratio would be close to $\gamma_C = 0.8$. On a hazy day, with CSR=0.3 [15], The concentrator exergy-to-energy ratio falls to $\gamma_C = 0.74$.

5.3.2 Influence of mirror reflectance

The influence of the reflectance of the mirrors on the radial exergy-to-energy ratio is presented in Figure 5-5 $\left(\theta_{rim} = 45^\circ, \text{CSR}=0.01, \sigma = 0\right)$. The impact on local exergy-to-energy ratio γ (Figure 5-5 (a)) is seen to be greater further from the axis, due to the non-linear nature of the relationship between concentration and exergy. Similarly, the overall exergy to energy ratio is more strongly impacted for lower values of reflectivity (Figure 5-5 (b)). In the typical operational range, γ_C is relatively unchanged with a drop of 0.4% as the reflectivity drops from 0.98 to 0.85.

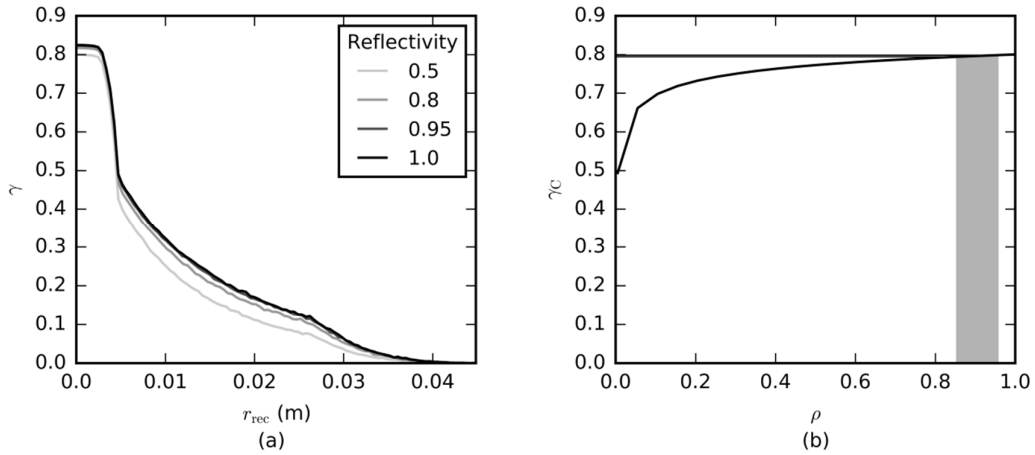

Figure 5-5. Influence of mirror reflectivity on (a) the local exergy-to-energy ratio radially at the target and (b) the concentrator exergy-to-energy ratio with the typical reflectance operational range of 0.85 to 0.98 highlighted in grey.

5.3.3 Influence of mirror slope error

The influence of surface slope error of the mirrors σ on the exergy efficiency is displayed in Figure 5-6 (a) and Figure 5-6 (b) $\left(\theta_{rim}=45^{\circ}, \text{CSR}=0.01, \rho=1\right)$.

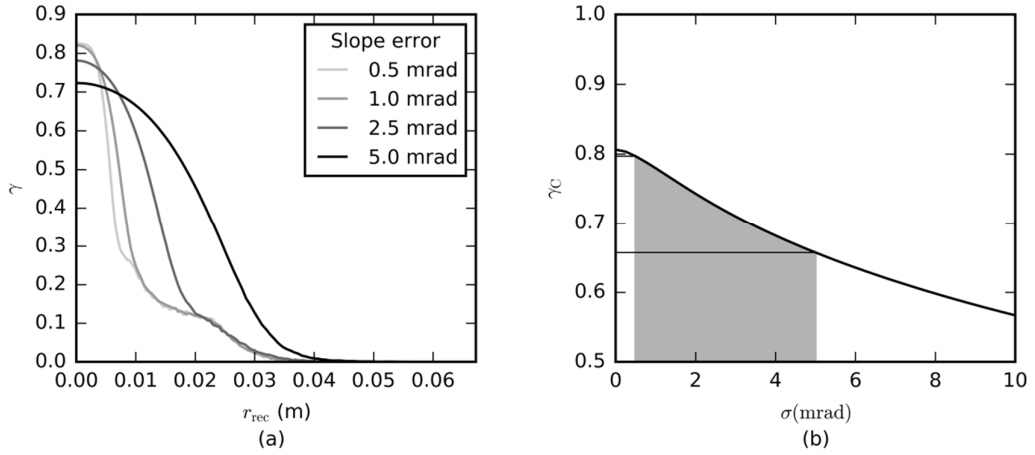

Figure 5-6. (a) Influence of mirror slope error on the local exergy to energy ratio γ, and (b) the effect of slope error on overall exergy-to energy ratio γ_C, with a typical operational range 0.4 to 5 mrad highlighted in grey.

The shaded area of Figure 5-6 (b) shows the range $\sigma\in\left[0.4,5\right]$ mrad, considered to be a typical range for real systems [91]. Larger slope errors cause reduced γ_C, as expected, since the focal plane distribution spreads and the locally optimal receiver temperatures are reduced. When the slope error increases from 0.4 to 5 mrad, the overall exergy-to-energy ratio drops from 0.8 to 0.66, a reduction of 14% absolute. This suggests that slope error is potentially the largest contributor to exergy losses amongst the factors considered in this study.

5.3.4 Influence of the collector geometry

The geometry of the concentrator has an influence on the spatial distribution of the reflected radiation. Different dish geometries will have different focal plane flux distributions.

The influence of the rim angle of the dish concentrator on the concentrator exergy-to-energy ratio is shown in Figure 5-7 $(\rho=1,\ \sigma=0)$. The source model used here is a pillbox sunshape with $\theta_{ar}=4.65$ mrad.

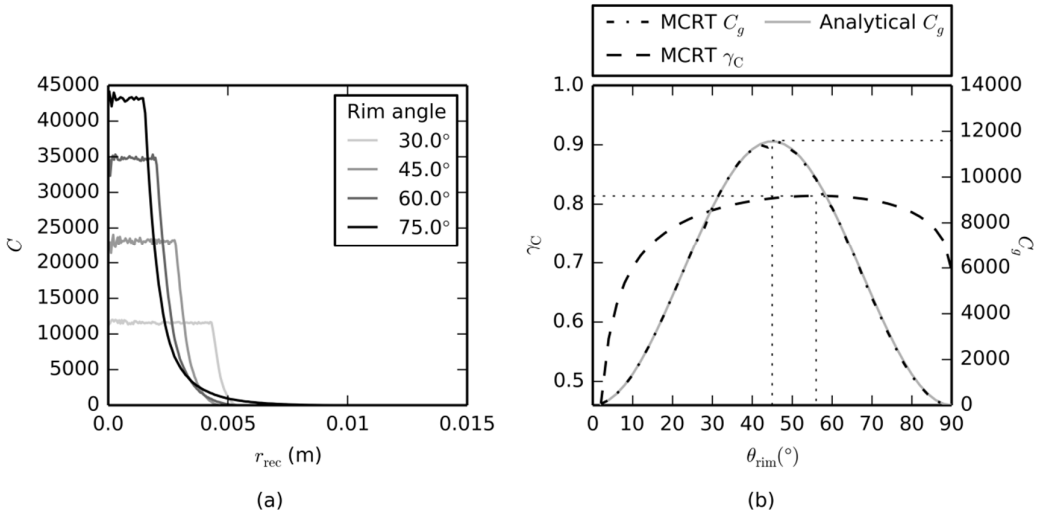

Figure 5-7. (a) Radial variation of concentration for 4 different rim angles and (b) comparison between concentrator exergy-to-energy and geometrical concentration ratio for rim angles from 1° to 90°. Geometrical concentration is determined both analytically and using MCRT for validation.

In the literature, the optimal rim angle of dish concentrators is usually defined as the rim angle at which the maximal geometrical concentration C_g with 100% capture ratio is obtained at the receiver aperture [92, 122]. This equation is given again here but was presented earlier in Chapter 2 Eq. 2-90.

$$C_g=\left(\frac{\sin(2\theta_{rim})}{2\sin(\theta_{ar})}\right)^2$$

C_g is maximised for $\theta_{rim}=45^\circ$ and reaches $C_g=11{,}600$ as observed in Figure 5-7 (b). When considering exergy, the maximal concentrator exergy-to-energy ratio is obtained at $\theta_{rim}\approx 56^\circ$ because the non-averaged concentration profile is now considered. The difference in concentrator exergy-to-energy ratio between $\theta_{rim}=45^\circ$ and $\theta_{rim}=56^\circ$ rim angles is marginal (an improvement of 0.5%) but the trend around the optimum changes greatly compared with the geometrical concentration approach.

5.3.5 Combined rim angle and slope error effects

Slope error has a strong impact on the concentration at the focal plane of the concentrator and the rim angle of a dish using mirrors with a known slope error should be adapted to take this variation into account [13, 55]. Figure 5-8 shows how the overall exergy-to-energy ratio γ_C varies with both slope error σ and rim angle θ_{rim}. The model assumes a pillbox sun shape with $\theta_{ar} = 4.65$ mrad, and perfectly reflective mirrors $\rho = 1$.

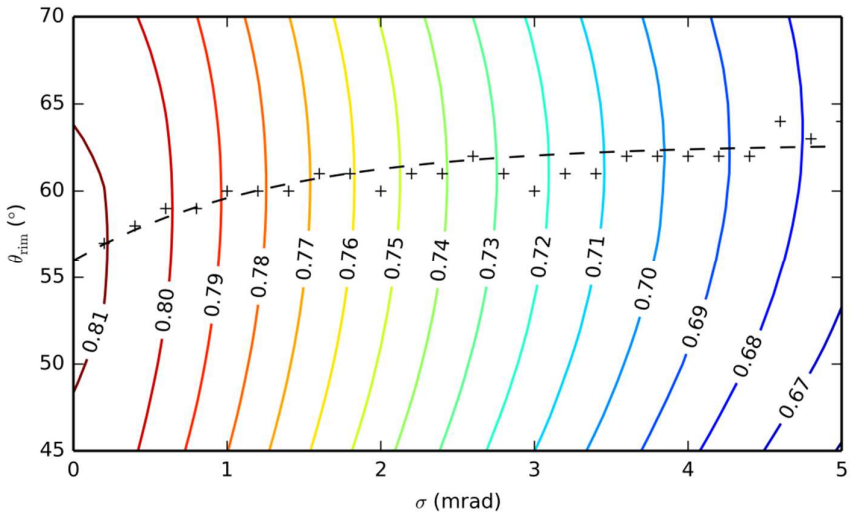

Figure 5-8. Optimal rim angle θ_{rim} as a function of the mirror slope error σ for maximised concentrator exergy-to-energy ratio, considering the optimal temperature profile at the target.

The exergetically optimal rim angle increases with increased slope error. This effect of increasing slope error leading to increased optimal rim angle has already been reported [56, 122] but had not been considered in the context of an exergy analysis with varying concentration in the focal plane.

5.4 Influence of the target temperatures

This section departs from the pure concentrator exergy efficiency analysis and considers the potential impacts of basic receiver design choices and constraints on the system performance, still evaluated using concentrator exergy-to energy ratio.

The exergy at the target of a "realistic" concentrator $\left(\rho = 0.95,\ \sigma = 3 \text{ mrad},\ \theta_{rim} = 56^\circ\right)$ is displayed for three temperature distributions:

1. Ideal non-isothermal target: The target is the perfect exergy receiver as presented earlier in this study where the temperature profile is optimised using the correlation presented in 5-13:

$$T_j = T_{opt}\left(\dot{E}''_j, T_0\right) \tag{5-18}$$

2. Temperature-constrained target: The target has a maximum temperature that cannot be exceeded T_{max}, imposed, for example, by material constraints:

$$\begin{cases} T_j = T_{opt} & \text{for } T_{opt}\left(\dot{E}_j'', T_0\right) < T_{max} \\ T_j = T_{max} & \text{for } T_{opt}\left(\dot{E}_j'', T_0\right) \geq T_{max} \end{cases} \tag{5-19}$$

3. Finite isothermal target: The target is set to maintain a specified uniform temperature T_{max} for radii within r_{cav} and T_0 for the rest of the target. The result is a temperature profile that emulates the behaviour of the aperture of an isothermal cavity receiver, a simplification commonly used in receiver studies.

$$\begin{cases} T = T_{max} & \text{for } r < r_{cav} \\ T = T_0 & \text{for } r \geq r_{cav} \end{cases} \tag{5-20}$$

With r_{cav} defined in two steps. First the optimal concentration for the temperature T_{max} is calculated using an inverted 5-13.

$$C_{cav} = \left(\frac{T_{max}}{T_0}\right)^{\frac{1}{0.1919}} \tag{5-21}$$

Then the target radius resulting in the ideal average concentration C_{cav} is determined using 5-22.

$$\begin{cases} \dfrac{2\pi}{G}\displaystyle\int_0^r \dot{E}'' dr = C_{cav} \\ r_{cav} = r \end{cases} \tag{5-22}$$

The temperature profiles of these targets are displayed in Figure 5-9 (a) and the radial exergy-to-energy ratios γ in Figure 5-9 (b).

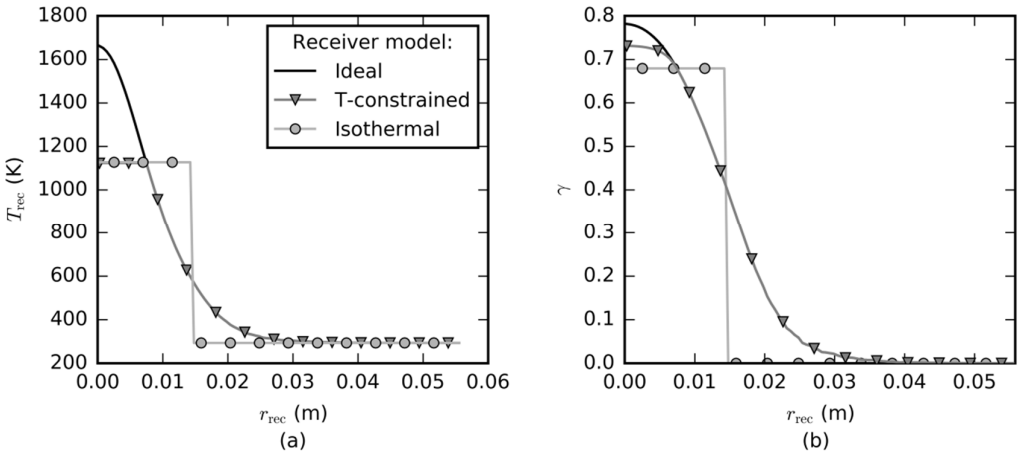

Figure 5-9: Influence of isothermal (850°C) and temperature-limited (max. 850°C) design constraints on the exergy at the focal plane, compared to the ideal (locally optimised temperature) case: (a) receiver temperature distribution and (b) radial exergy-to-energy ratios.

The values of concentrator exergy-to-energy ratio for the three targets are presented in Table 5-1. The concentrator exergy-to-energy ratio γ_C is the highest for the ideal non-isothermal target where $T = T_{opt}$. Limiting the temperature to $T_{max} = 850\ ^\circ C$ represents a 4.9% loss in focal plane exergy due to a lower exergy efficiency in the high radiative flux region at the centre of the target, now at a sub-optimal temperature. The isothermal target results in 7.2% exergy loss compared with the ideal. These results are consistent with the work of Ries et al [124] who found that non-isothermal receivers allow the maximum exergy to be extracted as heat from a flux distribution.

Table 5-1: Concentrator exergy –to-energy ratios for three targets with different temperature constraints.

	Ideal non-isothermal target	$T_{max} = 850\ ^\circ C$	
		Temperature-constrained target	Finite isothermal target
γ_C	0.710	0.662	0.638

5.5 Conclusions of focal-plane exergy analysis

The relative influence of the source, geometry and mirror properties on the exergy-to-energy ratio at the focal plane of solar-thermal dish concentrators was explored. The flux profile at the focal plane strongly influences the total amount of work that can be extracted via heat from the focal plane, as was demonstrated through variation of the parameters of sun shape, rim angle, reflectivity and slope error. The mirror surface slope error was identified as the largest potential contributor to concentrator exergy to energy ratio reduction when parameters are varied in typical ranges as shown in Table 5-2.

Table 5-2: Summary of the impact of circumsolar ratio CSR, rim angle θ_{rim}, mirror reflectance ρ and mirror slope error σ on the overall focal-plane exergy-to-energy ratio γ_{C} and exergy loss of the dish and target system $\rho\gamma_{\mathrm{C}}$.

Sensitivity	CSR $0 \rightarrow 0.3$	θ_{rim} $56° \rightarrow 45°$	ρ $0.98 \rightarrow 0.85$	σ $0.5\ \mathrm{mrad} \rightarrow 5\ \mathrm{mrad}$
Other parameters	$\theta_{\mathrm{rim}} = 45°$ $\rho = 1$ $\sigma = 0$	θ_{ar}=4.65 mrad $\rho = 1$ $\sigma = 0$	$CSR = 0.01$ $\theta_{\mathrm{rim}} = 45°$ $\sigma = 0$	$CSR = 0.01$ θ_{rim} =45° $\rho = 1$
$\Delta\gamma_C$	-7%	-0.5%	-0.4%	-14%
$\Delta\rho\gamma_C$			-10.7%	

The study also examined the impact of imposed temperature constraints in the focal plane, using a case study of a realistic dish concentrator. When an 850°C peak temperature constraint is imposed, the exergy-to-energy ratio for this dish reduces from 0.710 to 0.662. When an 850°C isothermal constraint is applied, the exergy-to-energy ratio drops further to 0.638. From this example, the reduction in the exergy-to-energy ratio of 7.2% shows that temperature constraints are also of major importance in system design.

Applied exergy analysis shows interesting potential in CSP systems design. A specific advantage of this approach is that it enables a fair comparison of thermal and optical design variables. In addition, the present method gives design insights for solar concentrators without the need to model a receiver system and subsequent processes.

The general approach of this study is not specific to dish concentrators, and can be applied to other types of concentrators such as central tower systems, which could greatly benefit from a deeper investigation in concentration strategies at the receiver. The use of this simple model provides the key information about the limitation imposed by the concentration process on the maximum work output of a concentrated solar thermal system.

6 Conclusions

The optimisation of the geometry of solar thermal receivers was identified as a gap in the existing research literature and an opportunity for the improvement of solar thermal receiver designs. To address this gap, a flexible modelling framework for concentrated solar receivers was first established and tested. Two methods, dedicated to “black box” problems involving uncertain evaluation of the objectives to optimise, were developed and presented. These two methods, PMCE and MOE-PMCE-O were used in conjunction with the receiver modelling framework to produce receiver design results. Finally, a more theoretical contribution to the field of concentrated solar research was developed in the form of a study of the exergy distribution at the focal plane of a concentrator depending on the concentrator geometry and optical properties.

In the area of geometrical optimisation of solar thermal receivers, the novel contributions of the author are:

- A new adaptive view-factor calculation method using Monte-Carlo ray-tracing and a statistically controlled ray-casting condition to minimise the number of rays used for a prescribed precision criterion.
- A method to store and reuse concentrator MCRT results, the “Intermediate Ray Emission Surface” (IRES) method that facilitates the optimisation of receiver problems with detailed concentrating optics modelling.
- The “Progressive Monte-Carlo Evaluation” (PMCE) method that minimises the computational effort spent in simulation in simulation-optimisation problems where the single objective metric is obtained via a statistical sampling technique.
- The “Multi-Objective and Evolutionary PMCE Optimisation” (MOE-PMCE-O) that extends the PMCE method to multi-objective optimisation problems and introduces dynamic population generation and evolution in order to mitigate the population initialisation effort and improve the convergence rate and overall quality of the results.

Conducting optimisation case studies, some findings in the area of receiver geometrical design were obtained. The contributions to the field of receiver geometry are:

- A robust definition of the receiver “aperture” in the context of concentrated solar applications was suggested. Using this new definition, the difference between “external” convex absorber geometries and “cavity” non-convex absorber geometries appears more clearly. Thanks to this definition, the calculation of light-trapping and

cavity effect was made possible in a more rigorous way on geometries that do not correspond to the traditional definition of “cavity” receivers.

- Led the radiative heat transfer modelling and geometric optimisation tasks for the development of a new dish receiver prototype which, when tested, showed an experimental thermal efficiency of 97.1% ±2.2% with an input of 60°C water and output of 500°C at ≈ 45 bar.
- The identification of geometrical shape concepts for high-flux and high-temperature liquid sodium receiver designs:
    - Upward and downward facing cones for flux mitigation
    - The annular “pseudo-cavities” for light trapping and cavity effect promotion as well as flux mitigation in high intensity regions.
    - The indication that the concentrated radiation should be absorbed at the highest possible temperature, within the operational range, to improve the receiver exergetic efficiency and that the geometrical design of receivers can be useful in achieving this.
- A method for the evaluation of the exergetic performance of solar concentrators and an evaluation of the impact of concentrator properties on the optimal temperature of receivers and consequently the upper bound of thermal receiver second-law efficiency. This study showed the dominant role of mirror surface slope error, and showed that the optimal concentrator geometry depends on the surface slope error for a dish concentrator.

Some further, relatively more minor contributions to the field of concentrated solar optics include:

- The development of a rigorous approach to Buie sunshape declaration for MCRT simulations and the identification of an imprecision related to the model for which a correction was given.
- A dual-region, slope-error-matched, dish concentrator model based on experimental measurements to enable fast simulation of realistic flux distributions on receiver surfaces.

Finally, all the modelling work developed during this dissertation was performed on open source code, and the author has contributed these codes to the public domain at: https://github.com/casselineau.

As a general concluding statement, the major contribution of the work developed is to enable the rigorous multi-objective optimisation of any receiver concept.

Further development of MOE-PMCE-O will focus on introducing machine-learning methods in the algorithm to improve the evolutionary aspect of the method. In the field of receiver modelling, the handling of thermal emissions remains an issue in terms of computational effort and some improvements are required to the existing method. The progressive evaluation of view-factor matrices, as part of the PMCE step of the optimisation is a potential improvement on the method, particularly if associated with efficient pseudo Monte-Carlo methods. In the light of the optimisation results obtained, receiver geometrical design will be explored further to establish promising concepts for the next generation of CSP systems. Future objective metrics to consider in that task will include an evaluation of the thermo-mechanical stresses to further improve the estimation of the reliability of the generated concepts.

Through further development of high-temperature receiver technologies and particularly their geometry, as demonstrated in this thesis, it is hoped that CSP technologies will continue improving their economical viability and play a role in our future cleaner and reliable energy mix.

Bibliography

[1] *LAPACK Users' Guide*. Society for Industrial and Applied Mathematics, Philadelphia, PA, third edition, 1999.

[2] T. Abe, N. Gokon, T. Izawa, and T. Kodama. Internally-circulating fluidized bed reactor using thermal storage material for solar coal coke gasification. *Energy Procedia*, 69: 1722 – 1730, 2015. ISSN 1876-6102. doi: 10.1016/j.egypro.2015.03.140. SolarPACES 2014.

[3] A. Agudelo and C. Cortés. Thermal radiation and the second law. *Energy*, 35 (2): 679–691, Feb. 2010. doi: 10.1016/j.energy.2009.10.024.

[4] S. Andradóttir. Chapter 20 An overview of simulation optimization via random search. In S. G. Henderson and B. L. Nelson, editors, *Simulation*, volume 13 of *Handbooks in Operations Research and Management Science*, pages 617 – 631. Elsevier, 2006. doi: 10.1016/S0927-0507(06)13020-0.

[5] C. E. Andraka, J. Yellowhair, and B. D. Iverson. A parametric study of the impact of various error contributions on the flux distribution of a solar dish concentrator, 2010.

[6] A. L. Ávila-Marín. Volumetric receivers in solar thermal power plants with central receiver system technology: A review. *Solar Energy*, 85 (5): 891 – 910, 2011. ISSN 0038-092X. doi: 10.1016/j.solener.2011.02.002.

[7] V. Badescu. On the thermodynamics of the conversion of diluted radiation. *Journal of Physics D: Applied Physics*, 23 (3): 289–292, mar 1990. doi: 10.1088/0022-3727/23/3/002.

[8] V. Badescu. Maximum reversible work extraction from a blackbody radiation reservoir. a way to closing the old controversy. *EPL*, 109 (4), 2015. doi: 10.1209/0295-5075/109/40008.

[9] J. Ballestrín and A. Marzo. Solar radiation attenuation in solar tower plants. *Solar Energy*, 86 (1): 388 – 392, 2012. ISSN 0038-092X. doi: 10.1016/j.solener.2011.10.010.

[10] C. B. Barber, D. P. Dobkin, and H. Huhdanpaa. The quickhull algorithm for convex hulls. *ACM Trans. Math. Softw.*, 22 (4): 469–483, Dec. 1996. ISSN 0098-3500. doi: 10.1145/235815.235821.

[11] O. Behar, A. Khellaf, and K. Mohammedi. A review of studies on central receiver solar thermal power plants. *Renewable and Sustainable Energy Reviews*, 23: 12 – 39, 2013. ISSN 1364-0321. doi: 10.1016/j.rser.2013.02.017.

[12] A. Bejan. Unification of three different theories concerning the ideal conversion of enclosed radiation. *Journal of Solar Energy Engineering, Transactions of the ASME*, 109 (1): 46–51, 1987.

[13] P. Bendt and A. Rabl. Optical analysis of point focus parabolic radiation concentrators. *Applied Optics*, 20 (4): 674–683, Feb. 1981. doi: 10.1364/AO.20.000674.

[14] H. Benoit, L. Spreafico, D. Gauthier, and G. Flamant. Review of heat transfer fluids in tube-receivers used in concentrating solar thermal systems: Properties and heat transfer coefficients. *Renewable and Sustainable Energy Reviews*, 55: 298 – 315, 2016. ISSN 1364-0321. doi: 10.1016/j.rser.2015.10.059.

[15] P. Blanc, B. Espinar, N. Geuder, C. Gueymard, R. Meyer, R. Pitz-Paal, B. Reinhardt, D. Renné, M. Sengupta, L. Wald, and S. Wilbert. Direct normal irradiance related definitions and applications: The circumsolar issue. *Solar Energy*, 110 (0): 561 – 577, 2014. ISSN 0038-092X. doi: 10.1016/j.solener.2014.10.001.

[16] M. Blanco-Muriel, D. Alarcón-Padilla, T. López-Moratalla, and M. Lara-Coira. Computing the solar vector. *Solar Energy*, 70 (5): 431–441, 2001. doi: 10.1016/S0038-092X(00)00156-0.

[17] M. Blanco-Muriel, D. Alarcón-Padilla, T. López-Moratalla, and M. Lara-Coira. Computing the solar vector. *Solar Energy*, 70 (5): 431–441, 2001. doi: 10.1016/S0038-092X(00)00156-0.

[18] N. Boerema, G. Morrison, R. Taylor, and G. Rosengarten. High temperature solar thermal central-receiver billboard design. *Solar Energy*, 97: 356 – 368, 2013. ISSN 0038-092X. doi: 10.1016/j.solener.2013.09.008.

[19] D. Brkic. Solutions of the CW equation for flow friction. *Ápplied Mathematics Letters*, 24 (8): 1379 – 1383, 2011. ISSN 0893-9659. doi: 10.1016/j.aml.2011.03.014.

[20] D. Buie and A. Monger. The effect of circumsolar radiation on a solar concentrating system. *Solar Energy*, 76 (1-3): 181 – 185, 2004. ISSN 0038-092X. doi: 10.1016/j.solener.2003.07.032. Solar World Congress 2001.

[21] D. Buie, A. Monger, and C. Dey. Sunshape distributions for terrestrial solar simulations. *Solar Energy*, 74 (2): 113–122, 2003. ISSN 0038-092X. doi: 10.1016/S0038-092X(03)00125-7.

[22] Y. Candau. On the exergy of radiation. *Solar Energy*, 75 (3): 241–247, 2003. ISSN 0038-092X. doi: 10.1016/j.solener.2003.07.012.

[23] M. Castañs, A. Soler, and F. Soriano. Theoretical maximal efficiency of diffuse radiation. *Solar Energy*, 38 (4): 267–270, 1987. ISSN 0038-092X. doi: 10.1016/0038-092X(87)90048-X.

[24] J. Chaves. *Introduction to nonimaging optics*. CRC Press, 2015.

[25] C.-H. Chen, M. C. Fu, and L. Shi. *Simulation and Optimization*, chapter 12, pages 247–260. INFORMS, 2008. doi: 10.1287/educ.1080.0050.

[26] Y. T. Chen, A. Kribus, B. H. Lim, C. S. Lim, K. K. Chong, J. Karni, R. Buck, A. Pfahl, and T. P. Bligh. Comparison of two sun tracking methods in the application of a heliostat field. *Journal of Solar Energy Engineering*, 126 (1): 638–644, Feb. 2004. ISSN 0199-6231. doi: 10.1115/1.1634583.

[27] A. Chinnici, M. Arjomandi, Z. F. Tian, Z. Lu, and G. J. Nathan. A novel solar expanding-vortex particle reactor: Influence of vortex structure on particle residence times and trajectories. *Solar Energy*, 122: 58 – 75, 2015. ISSN 0038-092X. doi: 10.1016/j.solener.2015.08.017.

[28] F. J. Collado and J. Guallar. Campo: Generation of regular heliostat fields. *Renewable Energy*, 46: 49 – 59, 2012. ISSN 0960-1481. doi: 10.1016/j.renene.2012.03.011.

[29] J. Coventry, J. Campbell, G. Burgess, J.-S. Kim, J. Pye, and W. Saw. Receiver performance scoping study. Technical report, ASTRI, October 2014.

[30] J. Coventry, C. Andraka, J. Pye, M. Blanco, and J. Fisher. A review of sodium receiver technologies for central receiver solar power plants. *Solar Energy*, 122: 749 – 762, 2015. ISSN 0038-092X. doi: 10.1016/j.solener.2015.09.023.

[31] K. Craig, P. Gauché, and H. Kretzschmar. Optimization of solar tower hybrid pressurized air receiver using cfd and mathematical optimization. *Energy Procedia*, 49: 324 – 333, 2014. ISSN 1876-6102. doi: 10.1016/j.egypro.2014.03.035.

[32] K. J. Daun, D. P. Morton, and J. R. Howell. Geometric optimization of radiant enclosures containing specular surfaces. *Journal of Heat Transfer*, 125 (5): 845–851, Sept. 2003. ISSN 0022-1481. doi: 10.1115/1.1599369.

[33] A. De Vos. Thermodynamics of radiation energy-conversion in one and in 3 physical dimensions. *Journal of Physics and Chemistry of Solids*, 49 (6): 725–730, 1988. ISSN 0022-3697.

[34] A. De Vos. *Thermodynamics of solar energy conversion*. Wiley, 2008.

[35] A. De Vos and H. Pauwels. Discussion on the second law efficiency of solar energy conversion. *Journal of Solar Energy Engineering*, 108 (1): 80–83, Feb. 1986. ISSN 0199-6231. doi: 10.1115/1.3268070.

[36] J. Delatorre, G. Baud, J. Bézian, S. Blanco, C. Caliot, J. Cornet, C. Coustet, J. Dauchet, M. E. Hafi, V. Eymet, R. Fournier, J. Gautrais, O. Gourmel, D. Joseph, N. Meilhac, A. Pajot, M. Paulin, P. Perez, B. Piaud, M. Roger, J. Rolland, F. Veynandt, and S. Weitz. Monte carlo advances and concentrated solar applications. *Solar Energy*, 103 (0): 653 – 681, 2014. ISSN 0038-092X. doi: 10.1016/j.solener.2013.02.035.

[37] J. Fang, J. Wei, X. Dong, and Y. Wang. Thermal performance simulation of a solar cavity receiver under windy conditions. *Solar Energy*, 85 (1): 126 – 138, 2011. ISSN 0038-092X. doi: 10.1016/j.solener.2010.10.013.

[38] J. K. Fink and L. Leibowitz. Thermodynamic and transport properties of sodium liquid and vapor. Technical report, Argonne national laboratory, 1995. ANL/RE-95/2.

[39] G. Flamant, D. Gauthier, H. Benoit, J.-L. Sans, R. Garcia, B. Boissière, R. Ansart, and M. Hemati. Dense suspension of solid particles as a new heat transfer fluid for concentrated solar thermal plants: On-sun proof of concept. *Chemical Engineering Science*, 102: 567 – 576, 2013. ISSN 0009-2509. doi: 10.1016/j.ces.2013.08.051.

[40] O. Flores, C. Marugán-Cruz, D. Santana, and M. García-Villalba. Thermal stresses analysis of a circular tube in a central receiver. *Energy Procedia*, 49: 354 – 362, 2014. ISSN 1876-6102. doi: 10.1016/j.egypro.2014.03.038. SolarPACES 2013.

[41] D. K. Fork, J. Fitch, S. Ziaei, and R. I. Jetter. Life estimation of pressurized-air solar-thermal receiver tubes. *Journal of Solar Energy Engineering*, 134 (4): 041016–041016, Oct. 2012. ISSN 0199-6231. doi: 10.1115/1.4007686.

[42] S. C. Francisco, A. M. Raimundo, A. R. Gaspar, A. V. M. Oliveira, and D. A. Quintela. Calculation of view factors for complex geometries using Stokes's theorem. *Journal of Building Performance Simulation*, 7 (3): 203–216, 2014. doi: 10.1080/19401493.2013.808266.

[43] L. Frederickson, M. Dordevich, and F. Miller. Lab-scale experimentation and {CFD} modeling of a small particle heat exchange receiver. *Energy Procedia*, 49: 363 – 372, 2014. ISSN 1876-6102. doi: 10.1016/j.egypro.2014.03.039. SolarPACES 2013.

[44] M. C. Fu, F. W. Glover, and J. April. Simulation optimization: A review, new developments, and applications. In *Proceedings of the 37th Conference on Winter Simulation*, WSC '05, pages 83–95. Winter Simulation Conference, 2005. ISBN 0-7803-9519-0. URL http://dl.acm.org/citation.cfm?id=1162708.1162728.

[45] P. Garcia, A. Ferriere, and J.-J. Bezian. Codes for solar flux calculation dedicated to central receiver system applications: A comparative review. *Solar Energy*, 82 (3): 189 – 197, 2008. ISSN 0038-092X. doi: 10.1016/j.solener.2007.08.004.

[46] V. Gnielinski. New equations for heat and mass transfer in turbulent pipe and channel flow. *Int. Chem. Eng*, 16 (2): 359–368, 1976.

[47] V. Gnielinski. On heat transfer in tubes. *International Journal of Heat and Mass Transfer*, 63: 134 – 140, 2013. ISSN 0017-9310. doi: 10.1016/j.ijheatmasstransfer.2013.04.015.

[48] A. Gogna and A. Tayal. Metaheuristics: review and application. *Journal of Experimental & Theoretical Artificial Intelligence*, 25 (4): 503–526, 2013. doi: 10.1080/0952813X.2013.782347.

[49] R. Grena. An algorithm for the computation of the solar position. *Solar Energy*, 82 (5): 462 – 470, 2008. ISSN 0038-092X. doi: 10.1016/j.solener.2007.10.001.

[50] J. Gribik and J. Osterle. Second law efficiency of solar energy conversion. *Journal of Solar Energy Engineering, Transactions of the ASME*, 106 (1): 16–21, 1984.

[51] D. Groeneveld. Post-dryout heat transfer at reactor operating conditions. Technical report, Atomic Energy of Canada Ltd., Chalk River, Ontario. Chalk River Nuclear Labs., 1973.

[52] C. Gueymard, D. Myers, and K. Emery. Proposed reference irradiance spectra for solar energy systems testing. *Solar Energy*, 73 (6): 443 – 467, 2002. ISSN 0038-092X. doi: 10.1016/S0038-092X(03)00005-7.

[53] M. Gupta and S. Kaushik. Exergy analysis and investigation for various feed water heaters of direct steam generation solar thermal power plant. *Renewable Energy*, 35 (6): 1228 – 1235, 2010. ISSN 0960-1481. doi: 10.1016/j.renene.2009.09.007.

[54] W. J. Gutjahr and A. Pichler. Stochastic multi-objective optimization: a survey on non-scalarizing methods. *Annals of Operations Research*, 236 (2): 475–499, 2016. ISSN 1572-9338. doi: 10.1007/s10479-013-1369-5.

[55] J. A. Harris and W. S. Duff. Focal plane flux distributions produced by solar concentrating reflectors. *Solar Energy*, 27 (5): 403–411, 1981. ISSN 0038-092X. doi: 10.1016/0038-092X(81)90005-0.

[56] J. A. Harris and T. G. Lenz. Thermal performance of solar concentrator/cavity receiver systems. *Solar Energy*, 34 (2): 135–142, 1985. ISSN 0038-092X. doi: 10.1016/0038-092X(85)90170-7.

[57] B. J. Hathaway, W. Lipinski, and J. H. Davidson. Heat transfer in a solar cavity receiver: Design considerations. *Numerical Heat Transfer, Part A: Applications*, 62 (5): 445–461, 2012. doi: 10.1080/10407782.2012.703471.

[58] A. F. Haught. Physics considerations of solar energy conversion. *Journal of Solar Energy Engineering*, 106 (1): 3–15, Feb. 1984. ISSN 0199-6231. doi: 10.1115/1.3267561.

[59] N. Hernández, D. Riveros-Rosas, E. Venegas, R. J. Dorantes, A. Rojas-Morín, O. Jaramillo, C. A. Arancibia-Bulnes, and C. A. Estrada. Conical receiver for a paraboloidal concentrator with large rim angle. *Solar Energy*, 86 (4): 1053 – 1062, 2012. ISSN 0038-092X. doi: 10.1016/j.solener.2011.09.008. {ISRES} 2010.

[60] D. Hirsch and A. Steinfeld. Solar hydrogen production by thermal decomposition of natural gas using a vortex-flow reactor. *International Journal of Hydrogen Energy*, 29 (1): 47 – 55, 2004. ISSN 0360-3199. doi: 10.1016/S0360-3199(03)00048-X.

[61] C. K. Ho and B. D. Iverson. Review of high-temperature central receiver designs for concentrating solar power. *Renewable and Sustainable Energy Reviews*, 29: 835 – 846, 2014. ISSN 1364-0321. doi: 10.1016/j.rser.2013.08.099.

[62] C. K. Ho, A. R. Mahoney, A. Ambrosini, M. Bencomo, A. Hall, and T. N. Lambert. Characterization of Pyromark 2500 paint for high-temperature solar receivers. *Journal of Solar Energy Engineering*, 136 (1): 014502–014502, July 2013. ISSN 0199-6231. doi: 10.1115/1.4024031.

[63] J. Holman. *Heat transfer*. Mechanical engineering series. McGraw-Hill, 1989. ISBN 9780071004879.

[64] T. Homem-de-Mello and G. Bayraksan. Monte carlo sampling-based methods for stochastic optimization. *Surveys in Operations Research and Management Science*, 19 (1): 56 – 85, 2014. ISSN 1876-7354. doi: 10.1016/j.sorms.2014.05.001.

[65] J. Howell, M. Menguc, and R. Siegel. *Thermal Radiation Heat Transfer, 6th Edition*. CRC Press, 2015. ISBN 9781498757744.

[66] H. W. Jensen, J. Arvo, P. Dutre, A. Keller, A. Owen, M. Pharr, and P. Shirley. Monte carlo ray tracing. In *ACM SIGGRAPH*, 2003.

[67] S. M. Jeter. Maximum conversion efficiency for the utilization of direct solar radiation. *Solar Energy*, 26 (3): 231 – 236, 1981. ISSN 0038-092X. doi: 10.1016/0038-092X(81)90207-3.

[68] L. Jianfeng, D. Jing, and Y. Jianping. Heat transfer performance of an external receiver pipe under unilateral concentrated solar radiation. *Solar Energy*, 84 (11): 1879 – 1887, 2010. ISSN 0038-092X. doi: 10.1016/j.solener.2009.11.015.

[69] L. Jianfeng, D. Jing, Y. Jianping, and Y. Xiaoxi. Exergetic optimization for solar heat receiver with heat loss and viscous dissipation. *Solar Energy*, 86 (9): 2273 – 2281, 2012. ISSN 0038-092X. doi: 10.1016/j.solener.2012.04.017.

[70] G. Johnston. Flux Mapping the 400 m2 Big Dish at the Australian National University. *Journal of Solar Energy Engineering*, 117 (4): 290–293, Nov. 1995. ISSN 0199-6231. doi: 10.1115/1.2847841.

[71] E. Jones, T. Oliphant, and P. Peterson. SciPy: Open source scientific tools for Python, 2001.

[72] S. Kabelac and F.-D. Drake. The entropy of terrestrial solar radiation. *Solar Energy*, 48 (4): 239 – 248, 1992. ISSN 0038-092X. doi: 10.1016/0038-092X(92)90097-T.

[73] S. Kandlikar. *Handbook of Phase Change: Boiling and Condensation*. Taylor & Francis, 1999. ISBN 9781560326342.

[74] S. G. Kandlikar. Development of a flow boiling map for subcooled and saturated flow boiling for different fluids inside circular tunnels. *Journal of Heat Transfer*, 113: 191–200, February 1991.

[75] S. Kaneff. The white cliffs solar thermal electric power systems. *Solar Engineering 1987*, pages 815–820, 1987.

[76] J. Karni, A. Kribus, B. Ostraich, and E. Kochavi. A high-pressure window for volumetric solar receivers. *Journal of Solar Energy Engineering*, 120 (2): 101–107, May 1998. ISSN 0199-6231. doi: 10.1115/1.2888051.

[77] S. Kaushik, R. Misra, and N. Singh. Second law analysis of a solar thermal power system. *International Journal of Solar Energy*, 20 (4): 239–253, 2000. doi: 10.1080/01425910008914358.

[78] B. Kistler. *A user's manual for DELSOL3: A computer code for calculating the optical performance and optimal system design for solar thermal central receiver plants*. Nov 1986.

[79] Kongsberg Oil & Gas Technologies. Coin 3d, 1998.

[80] A. Konstandopoulos, C. Pagkoura, and S. Lorentzou. 20 - solar fuels and industrial solar chemistry. In K. Lovegrove, , and W. Stein, editors, *Concentrating Solar Power Technology*, Woodhead Publishing Series in Energy, pages 620 – 661. Woodhead Publishing, 2012. ISBN 978-1-84569-769-3. doi: 10.1533/9780857096173.3.620.

[81] A. Kribus. Performance of the directly-irradiated annular pressurized receiver (diapr) operating at 20 bar and 1,200°C. *Journal of solar energy engineering*, 123 (1): 10–, 2001. ISSN 0199-6231.

[82] A. Kribus, P. Doron, R. Rubin, J. Karni, R. Reuven, S. Duchan, and E. Taragan. A multistage solar receiver: The route to high temperature. *Solar Energy*, 67 (1-3): 3–11, 1999. ISSN 0038-092X. doi: 10.1016/S0038-092X(00)00056-6.

[83] P. Landsberg and V. Badescu. Solar energy conversion: list of efficiencies and some theoretical considerations Part I - Theoretical considerations. *Progress in Quantum Electronics*, 22 (4): 211–230, 1998. ISSN 0079-6727. doi: 10.1016/S0079-6727(98)00012-3.

[84] P. T. Landsberg and V. Badescu. The geometrical factor of spherical radiation sources. *Europhysics Letters (EPL)*, 50 (6): 816–822, jun 2000. doi: 10.1209/epl/i2000-00554-7.

[85] P. T. Landsberg and G. Tonge. Thermodynamics of the conversion of diluted radiation. *Journal of Physics A: Mathematical and General*, 12 (4): 551, 1979. doi: 10.1088/0305-4470/12/4/015.

[86] P. T. Landsberg and G. Tonge. Thermodynamic energy conversion efficiencies. 51 (7), 1980. doi: 10.1063/1.328187.

[87] W. G. Le Roux, T. Bello-Ochende, and J. P. Meyer. A review on the thermodynamic optimisation and modelling of the solar thermal Brayton cycle. *Renew. Sust. Energ. Rev.*, 28: 677–690, 2013. doi: 10.1016/j.rser.2013.08.053.

[88] T. Lee, S. Lim, S. Shin, D. L. Sadowski, S. Abdel-Khalik, S. M. Jeter, and H. Al-Ansary. Numerical simulation of particulate flow in interconnected porous media for central particle-heating receiver applications. *Solar Energy*, 113: 14 – 24, 2015. ISSN 0038-092X. doi: https://doi.org/10.1016/j.solener.2014.12.017. URL https://-www.sciencedirect.com/science/article/pii/S0038092X14006082.

[89] Z. Li, D. Tang, J. Du, and T. Li. Study on the radiation flux and temperature distributions of the concentrator-receiver system in a solar dish/stirling power facility. *Applied Thermal Engineering*, 31 (10): 1780 – 1789, 2011. ISSN 1359-4311. doi: 10.1016/j.applthermaleng.2011.02.023.

[90] M. Loeve. *Probability Theory I*. Comprehensive Manuals of Surgical Specialties. Springer, 1977. ISBN 9780387902104. URL https://books.google.com.au/-books?id=_9xWBlvUEuIC.

[91] K. Lovegrove and J. Pye. *Concentrating Solar Power Technology*, chapter Fundamental Principles of Concentrating Solar Power (CSP) Systems, pages 16–67. Woodhead Publishing Series in Energy. Woodhead Publishing, 2012. ISBN 978-1-84569-769-3. doi: 10.1533/9780857096173.1.16.

[92] K. Lovegrove and J. Pye. 2 - Fundamental principles of concentrating solar power (CSP) systems. In K. Lovegrove and W. Stein, editors, *Concentrating Solar Power Technology*, Woodhead Publishing Series in Energy, pages 16 – 67. Woodhead Publishing, 2012. ISBN 978-1-84569-769-3. doi: 10.1533/9780857096173.1.16.

[93] K. Lovegrove, G. Burgess, and J. Pye. A new 500 m2 paraboloidal dish solar concentrator. *Sol. Energy*, 85 (4): 620–626, April 2011. doi: 10.1016/j.solener.2010.01.009.

[94] T. Markvart. From steam engine to solar cells: can thermodynamics guide the development of future generations of photovoltaics? *Wiley Interdisciplinary Reviews: Energy and Environment*, 5 (5): 543–569, mar 2016. doi: 10.1002/wene.204.

[95] G. Marsaglia and W. W. Tsang. The ziggurat method for generating random variables. *Journal of Statistical Software*, 5 (1): 1–7, 2000. ISSN 1548-7660. doi: 10.18637/jss.v005.i08.

[96] A. J. Marston, K. J. Daun, and M. R. Collins. Geometric optimization of concentrating solar collectors using monte carlo simulation. *Journal of solar energy engineering*, 132 (4): 41002–41002–9, 2010. ISSN 0199-6231.

[97] M. McKerns, L. Strand, T. Sullivan, A. Fang, and M. Aivazis. Building a framework for predictive science. In *10th Python in Science Conference*, 2011.

[98] A. Mecit, F. Miller, and A. Whitmore. Optical analysis and thermal modeling of a window for a small particle solar receiver. *Energy Procedia*, 49: 457 – 467, 2014. ISSN 1876-6102. doi: 10.1016/j.egypro.2014.03.049.

[99] Y. Meller. Tracer package: an open source, object oriented, ray-tracing library in python language. https://github.com/yosefm/tracer, 2013.

[100] G. Mie. Beiträge zur optik trüber medien, speziell kolloidaler metallösungen. *Annalen der Physik*, 330 (3): 377–445, 1908. ISSN 1521-3889. doi: 10.1002/andp.19083300302.

[101] M. F. Modest. *Radiative Heat Transfer*. Academic Press, 2003.

[102] A. Mwesigye, T. Bello-Ochende, and J. P. Meyer. Multi-objective and thermodynamic optimisation of a parabolic trough receiver with perforated plate inserts. *Applied Thermal Engineering*, 77: 42 – 56, 2015. ISSN 1359-4311. doi: 10.1016/j.applthermaleng.2014.12.018.

[103] M. Neber and H. Lee. Design of a high temperature cavity receiver for residential scale concentrated solar power. *Energy*, 47 (1): 481 – 487, 2012. ISSN 0360-5442. doi: 10.1016/j.energy.2012.09.005. Asia-Pacific Forum on Renewable Energy 2011.

[104] C. J. Noone, M. Torrilhon, and A. Mitsos. Heliostat field optimization: A new computationally efficient model and biomimetic layout. *Solar Energy*, 86 (2): 792 – 803, 2012. ISSN 0038-092X. doi: 10.1016/j.solener.2011.12.007.

[105] J. Noring, D. Grether, and A. Hunt. Circumsolar radiation data: The lawrence berkeley laboratory reduced data base. Technical report, Lawrence Berkeley Laboratory, University of California Berkeley, California 947209, December 1991.

[106] NREL. Solarpilot: Integrated layout and optimization tool for solar power towers, 2016.

[107] J. D. Ortega, J. M. Christian, and C. K. Ho. Structural analysis of a direct heated tubular solar receiver for supercritical co2 brayton cycle, 2015. URL 10.1115/ES2015-49464.

[108] S. Paitoonsurikarn, G. Hughes, J. Pye, and K. Lovegrove. Numerical investigation of natural convection loss from cavity receivers in solar dish applications, Mar. 2011. ISSN 0199-6231.

[109] J. Parrott. Theoretical upper limit to the conversion efficiency of solar energy. *Solar Energy*, 21 (3): 227–229, 1978. ISSN 0038-092X. doi: 10.1016/0038-092X(78)90025-7.

[110] J. Parrott. Theoretical upper limit to the conversion efficiency of solar energy. *Solar Energy*, 21 (3): 227 – 229, 1978. ISSN 0038-092X. doi: 10.1016/0038-092X(78)90025-7.

[111] J. Parrott. Letter to the editor. *Solar Energy*, 22 (6): 572–573, 1979. doi: 10.1016/0038-092x(79)90033-1.

[112] C. Pérez-Rábago, M. Marcos, M. Romero, and C. Estrada. Heat transfer in a conical cavity calorimeter for measuring thermal power of a point focus concentrator. *Solar Energy*, 80 (11): 1434 – 1442, 2006. ISSN 0038-092X. doi: 10.1016/j.solener.2006.03.006. European Solar Conference (EuroSun 2004)EuroSun Conference 2004.

[113] R. Petela. Exergy of Heat Radiation. *ASME Journal of Heat Transfer*, 86: 187–192, May 1964. doi: 10.1115/1.3687092.

[114] R. Petela. Exergy of undiluted thermal radiation. *Solar Energy*, 74 (6): 469 – 488, 2003. ISSN 0038-092X. doi: 10.1016/S0038-092X(03)00226-3.

[115] B. Petukhov and V. Popov. Theoretical calculation of heat exchange and frictional resistance in turbulent flow in tubes of an incompressible fluid with variable physical properties. *High Temperature*, 1: 69–83, 1963.

[116] B. D. Pomeroy, J. M. Roberts, and T. V. Narayanan. High-flux solar absorber concept for central receiver power plants. *Journal of Solar Energy Engineering*, 103 (1): 52–55, Feb. 1981. ISSN 0199-6231. doi: 10.1115/1.3266210.

[117] W. Press. Theoretical maximum for energy from direct and diffuse sunlight. *Nature*, 264 (5588): 734–735, 1976. doi: 10.1038/264734a0.

[118] J. Pye. Freesteam table properties. Simple placeholder for Freesteam reference, 2010.

[119] J. Pye, M. Zheng, J. Zapata, C.-A. Asselineau, and J. Coventry. An exergy analysis of tubular solar-thermal receivers with different working fluids. In *Proceedings of SolarPACES 2014*, Beijing, China, 2014.

[120] J. Pye, G. Hughes, E. Abbasi, C.-A. Asselineau, G. Burgess, J. Coventry, W. Logie, F. Venn, and J. Zapata. Development of a higher-efficiency tubular cavity receiver for direct steam generation on a dish concentrator. In *Proceedings of the SolarPACES 2015 conference*, Cape Town, South Africa, 2015.

[121] J. Pye, J. Coventry, F. Venn, J. Zapata, E. Abbasi, C.-A. Asselineau, G. Burgess, G. Hughes, , and W. Logie. Experimental testing of a high-flux cavity receiver. In *Proceedings of SolarPACES 2016*, Abu Dhabi, October 2016 2016.

[122] A. Rabl. Comparison of solar concentrators. *Solar Energy*, 18 (2): 93–111, 1976.

[123] A. Rabl and P. Bendt. Effect of circumsolar radiation on performance of focusing collectors. *Journal of Solar Energy Engineering*, 104 (3): 237–250, Aug. 1982. ISSN 0199-6231. doi: 10.1115/1.3266308.

[124] H. Ries, A. Kribus, and J. Karni. Nonisothermal receivers. *Journal of Solar Energy Engineering, Transactions of the ASME*, 117 (3): 259–261, 1995.

[125] M. Rodríguez-Sánchez, A. Soria-Verdugo, J. Z. A. A.-I. iez, A. Acosta-Iborra, and D. Santana. Thermal design guidelines of solar power towers. *Applied Thermal Engineering*, 63 (1): 428 – 438, 2014. ISSN 1359-4311. doi: 10.1016/j.applthermaleng.2013.11.014.

[126] M. Roldán, L. Valenzuela, and E. Zarza. Thermal analysis of solar receiver pipes with superheated steam. *Applied Energy*, 103: 73 – 84, 2013. ISSN 0306-2619. doi: 10.1016/j.apenergy.2012.10.021.

[127] M. Romero and A. Steinfeld. Concentrating solar thermal power and thermochemical fuels. *Energy and Environmental Science*, 5: 9234–9245, 2012. doi: 10.1039/C2EE21275G.

[128] W. L. Roux, T. Bello-Ochende, and J. Meyer. Operating conditions of an open and direct solar thermal brayton cycle with optimised cavity receiver and recuperator. *Energy*, 36 (10): 6027 – 6036, 2011. ISSN 0360-5442. doi: 10.1016/j.energy.2011.08.012.

[129] A. Sánchez-González, M. R. Rodríguez-Sánchez, and D. Santana. Aiming strategy model based on allowable flux densities for molten salt central receivers. *Solar Energy*, pages –, 2016. ISSN 0038-092X. doi: 10.1016/j.solener.2015.12.055.

[130] W. Schiel, M. Geyer, and R. Carmona. *The IEA/SSPS High Flux Experiment*. Springer-Verlag, 1987.

[131] W. J. Schiel and M. A. Geyer. Testing an external sodium receiver up to heat fluxes of 2.5 mw/m2: Results and conclusions from the iea-ssps high flux experiment conducted at the central receiver system of the plataforma solar de almeria (spain). *Solar Energy*, 41 (3): 255 – 265, 1988. ISSN 0038-092X. doi: 10.1016/0038-092X(88)90143-0.

[132] M. Schmitz, P. Schwarzbözl, R. Buck, and R. Pitz-Paal. Assessment of the potential improvement due to multiple apertures in central receiver systems with secondary concentrators. *Solar Energy*, 80 (1): 111 – 120, 2006. ISSN 0038-092X. doi: 10.1016/j.solener.2005.02.012.

[133] A. Segal and M. Epstein. Optimized working temperatures of a solar central receiver. *Solar Energy*, 75 (6): 503 – 510, 2003. ISSN 0038-092X. doi: 10.1016/j.solener.2003.08.036.

[134] N. Sendhil Kumar and K. Reddy. Numerical investigation of natural convection heat loss in modified cavity receiver for fuzzy focal solar dish concentrator. *Solar Energy*, 81 (7): 846 – 855, 2007. ISSN 0038-092X. doi: 10.1016/j.solener.2006.11.008.

[135] M. R. Shortis and G. Burgess. Photogrammetric monitoring of the construction of a solar energy dish concentrator. *Photogrammetric Engineering & Remote Sensing*, 78 (5): 519–527, 2012. ISSN 0099-1112. doi: doi:10.14358/PERS.78.5.519.

[136] Y. Shuai, X.-L. Xia, and H.-P. Tan. Radiation performance of dish solar concentrator/cavity receiver systems. *Solar Energy*, 82 (1): 13 – 21, 2008. ISSN 0038-092X. doi: 10.1016/j.solener.2007.06.005.

[137] P. L. Siangsukone. *Transient simulation and modelling of a dish solar thermal power system*. Thesis, 2005. Thesis (Ph.D.)–Australian National University, 2005.

[138] N. P. Siegel, C. K. Ho, S. S. Khalsa, and G. J. Kolb. Development and evaluation of a prototype solid particle receiver: On-sun testing and model validation. *Journal of solar energy engineering*, 132 (2): 21008–, 2010. ISSN 0199-6231.

[139] D. C. Spanner. The green leaf as a heat engine. *Nature*, 198 (4884): 934–937, June 1963.

[140] A. Steinfeld and M. Schubnell. Optimum aperture size and operating temperature of a solar cavity-receiver. *Solar Energy*, 50 (1): 19 – 25, 1993. ISSN 0038-092X. doi: 10.1016/0038-092X(93)90004-8.

[141] R. P. Taylor and R. Luck. Comparison of reciprocity and closure enforcement methods for radiation view factors. *Journal of Thermophysics and Heat Transfer*, 9 (4): 660–666, Oct. 1995. ISSN 0887-8722. doi: 10.2514/3.721.

[142] S. Ushak, A. Fernández, and M. Grageda. 3 - using molten salts and other liquid sensible storage media in thermal energy storage (TES) systems. In L. F. Cabeza, editor, *Advances in Thermal Energy Storage Systems*, Woodhead Publishing Series in Energy, pages 49 – 63. Woodhead Publishing, 2015. ISBN 978-1-78242-088-0. doi: 10.1533/9781782420965.1.49.

[143] S. van der Walt, S. C. Colbert, and G. Varoquaux. The numpy array: A structure for efficient numerical computation. *Computing in Science Engineering*, 13 (2): 22–30, March 2011. ISSN 1521-9615. doi: 10.1109/MCSE.2011.37.

[144] L. Vant-Hull. 8 - central tower concentrating solar power (CSP) systems. In K. Lovegrove, , and W. Stein, editors, *Concentrating Solar Power Technology*, Woodhead Publishing

Series in Energy, pages 240 – 283. Woodhead Publishing, 2012. ISBN 978-1-84569-769-3. doi: 10.1533/9780857096173.2.240.

[145] P. Vueghs. *Innnovative Ray Tracing Algorithms for Space Thermal Analysis*. PhD thesis, Universitry of Liege, Faculty of Applied Sciences, Department of Aerospace and Mechanics, 2009.

[146] T. Walker, S.-C. Xue, and G. W. Barton. Numerical determination of radiative view factors using ray tracing. *Journal of Heat Transfer*, 132 (7): 072702–072702–6, Apr. 2010. ISSN 0022-1481. doi: 10.1115/1.4000974.

[147] M. Wang and K. Siddiqui. The impact of geometrical parameters on the thermal performance of a solar receiver of dish-type concentrated solar energy system. *Renewable Energy*, 35 (11): 2501 – 2513, 2010. ISSN 0960-1481. doi: 10.1016/j.renene.2010.03.021.

[148] Y. Wang, C.-A. Asselineau, J. Coventry, and J. Pye. Optical performance of bladed receivers for csp systems, 2016.

[149] B. P. Welford. Note on a method for calculating corrected sums of squares and products. *Technometrics*, 4 (3): 419–420, 1962. ISSN 00401706.

[150] A. Wexler. Letter to the editor. *Solar Energy*, 22 (6): 572, 1979. doi: 10.1016/0038-092x(79)90032-x.

[151] C. Winter, R. Sizmann, and L. Vant-Hull. *Solar Power Plants: Fundamentals, Technology, Systems, Economics*. Springer Berlin Heidelberg, 1991. ISBN 9783642647598.

[152] C. Winter, R. Sizmann, and L. Vant-Hull. *Solar Power Plants: Fundamentals, Technology, Systems, Economics*. Springer Berlin Heidelberg, 2012. ISBN 9783642612459.

[153] S. Wright, M. Rosen, D. Scott, and J. Haddow. The exergy flux of radiative heat transfer with an arbitrary spectrum. *Exergy, An International Journal*, 2 (2): 69 – 77, 2002. ISSN 1164-0235. doi: 10.1016/S1164-0235(01)00041-3.

[154] S.-Y. Wu, L. Xiao, Y. Cao, and Y.-R. Li. Convection heat loss from cavity receiver in parabolic dish solar thermal power system: A review. *Solar Energy*, 84 (8): 1342 – 1355, 2010. ISSN 0038-092X. doi: 10.1016/j.solener.2010.04.008.

[155] W. Wu and Y. Liu. Radiation entropy flux and entropy production of the earth system. *Reviews of Geophysics*, 48 (2), May 2010. doi: 10.1029/2008rg000275.

[156] W. Wu, L. Amsbeck, R. Buck, R. Uhlig, and R. Ritz-Paal. Proof of concept test of a centrifugal particle receiver. *Energy Procedia*, 49: 560 – 568, 2014. ISSN 1876-6102. doi: 10.1016/j.egypro.2014.03.060.

[157] Y.-T. Wu, C. Chen, B. Liu, and C.-F. Ma. Investigation on forced convective heat transfer of molten salts in circular tubes. *International Communications in Heat and Mass Transfer*, 39 (10): 1550 – 1555, 2012. ISSN 0735-1933. doi: 10.1016/j.icheatmasstransfer.2012.09.002.

[158] C. Xu, Z. Wang, X. Li, and F. Sun. Energy and exergy analysis of solar power tower plants. *Applied Thermal Engineering*, 31 (17-18): 3904 – 3913, 2011. ISSN 1359-4311. doi: 10.1016/j.applthermaleng.2011.07.038. {SET} 2010 Special Issue.

[159] J. Yellowhair, J. M. Christian, and C. K. Ho. Evaluation of solar optical modeling tools for modeling complex receiver geometries. In *ASME 2014 8th International Conference on Energy Sustainability collocated with the ASME 2014 12th International Conference on Fuel Cell Science, Engineering and Technology*, pages V001T02A048–V001T02A048. American Society of Mechanical Engineers, 2014.

[160] C. Zamfirescu, I. Dincer, and W. R. Wagar. Evaluation of exergy and energy efficiencies of photothermal solar radiation conversion. *Applied Solar Energy*, 45 (4): 213–223, 12 2009. Copyright - Allerton Press, Inc. 2009; Last updated - 2014-08-30.

[161] J. Zapata, C.-A. Asselineau, J. Pye, M. Kaufer, and G. Hughes. An integrated optical and thermal model of cavity receivers for paraboloidal dish concentrators. In *Proceedings of the Asia Pacific Solar Research Conference 2014*, 2014.

[162] Y. Zhang, B. Lin, and J. Chen. Optimum performance characteristics of an irreversible solar-driven brayton heat engine at the maximum overall efficiency. *Renewable Energy*, 32 (5): 856 – 867, 2007. ISSN 0960-1481. doi: 10.1016/j.renene.2006.02.008.